Tidal interactions between planets and stars

Adrian John Barker

March 2011

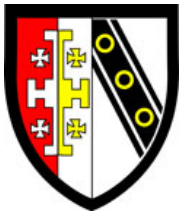

Selwyn College

University of Cambridge

THIS DISSERTATION IS SUBMITTED

FOR THE DEGREE OF

DOCTOR OF PHILOSOPHY

Tidal interactions between planets and stars

A.J. Barker, Selwyn College

Since the first discovery of an extrasolar planet around a solar-type star, observers have detected over 500 planets outside the solar system. Many of these planets have Jovian masses and orbit their host stars in orbits of only a few days, the so-called "Hot Jupiters". At such close proximity to their parent stars, strong tidal interactions between the two bodies are expected to cause significant secular spin-orbit evolution. This thesis tackles two problems regarding the tidal evolution of short-period extrasolar planets.

In the first part, we adopt a simple model of the orbit-averaged effects of tidal friction, to study the tidal evolution of planets on inclined orbits. We also analyse the effects of stellar magnetic braking. We then discuss the implications of our results for the importance of Rossiter-Mclaughlin effect observations.

In the second part, we study the mechanisms of tidal dissipation in solar-type stars. In particular, internal gravity waves are launched at the interface of the convection and radiation zones of such a star, by the tidal forcing of a short-period planet. The fate of these waves as they approach the centre of the star is studied, primarily using numerical simulations, in both two and three dimensions. We find that the waves undergo instability and break above a critical amplitude. A model for the tidal dissipation that results from this process is presented, and its validity is verified by numerical integrations of the linear tidal response, in an extensive set of stellar models. The dissipation is efficient, and varies by less than an order of magnitude between all solar-type stars, throughout their main-sequence lifetimes, for a given planetary orbit. The implications of this mechanism for the survival of short-period extrasolar planets is discussed, and we propose a possible explanation for the survival of all of the extrasolar planets currently observed in short-period orbits around F, G and K stars.

We then perform a stability analysis of a standing internal gravity wave near the centre of a solar-type star, to understand the early stages of the wave breaking process in more detail, and to determine whether the waves are subject to weaker parametric instabilities, below the critical amplitude required for wave breaking. We discuss the relevance of our results to our explanation for the survival of short-period planets

presented in the second part of this thesis.

Finally, we propose an alternative mechanism of tidal dissipation, involving the gradual radiative damping of the waves. Based on a simple estimate, it appears that this occurs even for low mass planets. However, it is in conflict with current observations since it would threaten the survival of all planets in orbits shorter than 2 days. We discuss some hydrodynamic instabilities and magnetic stresses which may prevent this process.

Preface

This thesis describes work done between October 2007 and December 2010 in the Astrophysical Fluid Dynamics & Nonlinear Patterns research group at the Department of Applied Mathematics & Theoretical Physics, University of Cambridge, under the supervision of Dr Gordon Ogilvie. No part of this thesis has been submitted for any qualification other than the degree of Doctor of Philosophy at the University of Cambridge.

Chapter 1 constitutes an introduction and review of relevant background material. Subsequent chapters contain original material, from which the following have been published in, submitted to, or in preparation for submission to, peer-reviewed journals:

Chapter 2: A.J. Barker & G.I. Ogilvie, "On the tidal evolution of Hot Jupiters on inclined orbits", MNRAS, 2009, 395, 2268-2287

Chapter 3: A.J. Barker & G.I. Ogilvie, "On internal wave breaking and tidal dissipation near the centre of a solar-type star", MNRAS, 2010, 404, 1849-1868

Chapter 4: A.J. Barker, "Three-dimensional simulations of internal wave breaking and the fate of planets around solar-type stars", MNRAS, accepted

Chapter 6: A.J. Barker & G.I. Ogilvie, "Stability analysis of a tidally excited internal gravity wave near the centre of a solar-type star", in preparation for submission to MNRAS

The remaining chapters represent work that is a reorganisation and refinement of some material contained in these publications.

This thesis is my own work and contains nothing which is the outcome of work done in collaboration with others, except as specified in the text and acknowledgements.

Cambridge, March 2011

Acknowledgements

Firstly, and most importantly, I would like to thank my PhD supervisor, Gordon Ogilvie, for invaluable advice and many useful suggestions, that have sustained me throughout the three years of my PhD, and made this research possible. In our collaboration in two published papers, Gordon contributed Figs. 2.9 & 5.8, as well as some of the original calculations in §3.4, 3.5 & 4.2.2, which are present in this thesis. I am also grateful for him taking the time to carefully read and helpfully criticise a draft of this thesis, and several of its chapters in earlier forms.

I would like to thank the Astrophysical Fluid Dynamics research group, for many stimulating discussions over coffee, or during seminars. Of those, I would particularly like to thank Geoffroy Lesur, for providing a version of his SNOOPY code, before it became publicly available, and for help with modifying the code, and visualisation of the results. I also have him to thank for correcting some of my coding errors, which were only spotted by me being reminded that his code "never fails". For many fascinating discussions, and for coping with being pestered about "simple" computer problems, as well as proof-reading several documents over the years, I would like to thank my fellow office resident, Hanno Rein.

For kindly taking the time to compute a set of stellar interior models, and assisting with their interpretation, I am grateful to Jørgen Christensen-Dalsgaard. For several extremely useful references, albeit to technical JFM papers from the 1960's and 70's, I would like to thank Michael McIntyre.

This work would not have been possible without the financial support of STFC, who funded my studentship[1] for three years, and the Cambridge Philosphical Society, who funded a studentship for the final three months. I have also received financial support for travel to various conferences and workshops from DAMTP, Selwyn College, Cambridge Philosophical Society, and the International Astronomical Union, to all of which I am grateful.

[1]Unfortunately, their postdoctoral fellowships are currently lacking such support...

Contents

Chapter 1

Introduction

It has now been more than a decade since the discovery of the first extrasolar planet orbiting a solar-type star (Mayor & Queloz 1995). The detection of this first Jovian-like planet 51 Peg b, and its 4 day orbit, certainly came as a surprise to the astrophysics community. To put this discovery in context, the closest planet in our solar system, Mercury, completes a single orbit of the Sun in 88 days, and so 51 Peg b is more than seven times closer to its host star than Mercury is to the Sun (and 100 times closer than Jupiter).

The discovery of 51 Peg b rapidly spurred further research into the detection, formation and evolution of planetary systems, making this one of the most exciting fields in astrophysics today. Since 1995, more than 500 planets have been detected around stars other than the Sun, and this total is increasing on an almost weekly basis[1]. This data set shows that the existence of planets in extraordinarily tight orbits (< 0.1 AU), such as 51 Peg b, is rather common. Indeed, from the current statistics, nearly a third of planets orbit within 0.1 AU of their host stars, making an explanation of the existence and properties of such planets an important goal of planet formation and evolution studies.

For such close-in planets, the stellar insolation that they receive could lead to the surface temperature of these worlds attaining values as high as 1500 K, which together with their roughly Jovian-masses, has led to them being dubbed "Hot Jupiters" (HJs). It is the purpose of this thesis to describe and understand some of the surprising

[1] see http://exoplanet.eu/ or http://www.exoplanet.hanno-rein.de/ for the latest updates

properties of these HJs, and their evolutionary history.

1.1 Observations of short-period extrasolar planets

We should perhaps not be surprised that the *first* planets detected be close-in and of Jovian mass, if we consider the observational biases of the currently favoured detection techniques. 51 Peg b, as with over 400 of the planets detected so far, was discovered using the radial velocity (RV) method (Mayor & Queloz 1995). This involves measuring the Doppler shift of stellar spectral lines, which are slightly blue-shifted and red-shifted by the orbital motion of the star around the centre of mass of the star-planet system, throughout the orbit. The RV method gives a measurement of the line-of-sight orbital velocity of the star (the velocity semi-amplitude K). In addition, the period of the Doppler shift fluctuations gives the orbital period (P), and the shape of the RV curve allows a determination of the eccentricity (e) of the orbit. These data allow a determination of $M_p \sin I_p$, which is a lower bound on the mass of the planet (M_p), where I_p is the angle of inclination of the orbital plane to the plane of the sky. The velocity semi-amplitude for a Keplerian orbit of eccentricity e is given by (Papaloizou & Terquem 2006)

$$K = \left(\frac{2\pi G}{P}\right)^{\frac{1}{3}} \frac{M_p}{(M_p + M_\star)^{\frac{2}{3}}} \frac{1}{\sqrt{1-e^2}}, \tag{1.1.1}$$

where $M_\star$ is the stellar mass. We see that a close-in, massive planet produces a larger velocity semi-amplitude, which is easier to detect above stellar jitter. It must be noted that most RV surveys concentrate on late-type, relatively chromospherically inactive stars which tend to be slow rotators, since stellar activity can cause significant jitter in RV data, which hinders the detection of planets.

In the last decade, the RV method has been supplemented by an additional technique for the detection of extrasolar planets, which when combined with RV spectroscopy, can provide much more information about a system. This is transit photometry, which involves looking for a reduction in stellar flux caused by the passage of a planet across the stellar disc in the plane of the sky (Charbonneau et al. 2000; Charbonneau et al. 2007). A Jupiter-mass planet on a short-period orbit can cause a

fractional dimming of the starlight by as much as 1% (see Fig. 1.1), and this can be readily observed. This technique gives us unprecedented access to the physical properties of the planet, such as a direct estimate of its mass and radius. These are both important for determining the interior structure of these planets, thereby constraining theoretical models (e.g. Fortney et al. 2007).

Another advantage to combining RV and photometric transit data is the possibility of detecting the Rossiter-McLaughlin (RM) effect (Rossiter 1924; McLaughlin 1924). The RM effect is a spectral distortion of the RV data that results from the planet occulting a spot on the rotating surface of the star as it transits the stellar disc. High-precision RV data during a transit allow a determination of the angle (λ) between the sky-projected angular momentum vectors of the planetary orbit ($\mathbf{h}$) and stellar spin ($\mathbf{\Omega}$), through the RM effect. This measured value λ is not necessarily the same as the inclination i (which is also called the stellar obliquity, given by $i = \arccos(\hat{\mathbf{\Omega}} \cdot \hat{\mathbf{h}})$) which is the angle between the equatorial plane of the star and orbital plane of the planet, since λ is just a sky-projection of this angle. These angles are related by $\cos i = \cos I_\star \cos I_p + \sin I_\star \sin I_p \cos \lambda$, where I_p and $I_\star$ are the angles of inclination of the planetary orbital plane and stellar equatorial plane, to the plane of the sky. For a transit, the orbit must be close to edge-on, so $I_p \approx 90°$, giving $\cos i \simeq \sin I_\star \cos \lambda$. In this case, λ gives a lower bound on the angle between these two vectors.

The RM effect has now been used to measure the degree of spin-orbit alignment in more than 30 systems (Triaud et al. 2010), and this number is expected to increase significantly over the next few years. The first systems were all consistent with λ being zero, with the exception of XO-3 b (Hébrard et al. 2008). We discuss a model for the survival and remnant misalignment of this planet in §2.6. In the past year, the misalignment of XO-3 b has been confirmed by Winn et al. (2009), and significant misalignments have been found in several additional systems: HD 80606 b (Moutou et al. 2009) WASP-14 b (Johnson et al. 2009), and possible retrograde orbital motion has been identified for HAT-P-7 b (Winn et al. 2009; Narita et al. 2009) and WASP-2 b, WASP-15 b, and WASP-17 b (Triaud et al. 2010), amongst others.

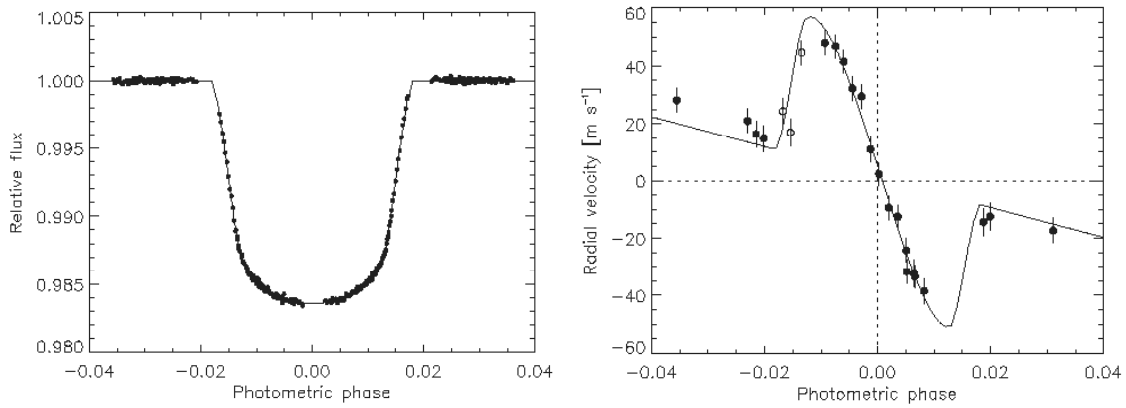

Figure 1.1: Left: Transit lightcurve for HD 209458, as a function of transit phase (defined to be zero when the planet passes the centre of the stellar disc). Right: Close-up of RV data throughout a transit for the same system, showing the RM effect as an "anomalous" spectral distortion. As expected for a prograde orbit, we first see a net red-shift, followed by a net blue-shift. The RM effect allows a determination of the sky-projected spin-orbit misalignment (λ) in a transiting system, which is found to be $\lambda = -4°.4 \pm 1°.4$ for HD 209458. This figure was taken from Winn et al. (2005).

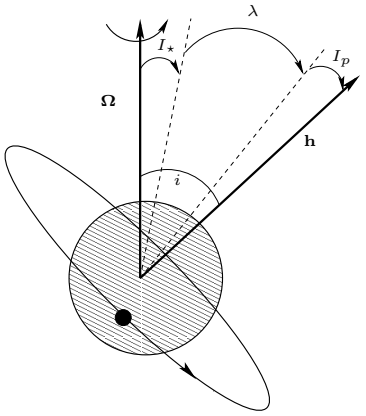

Figure 1.2: Angles involved in the calculation of the inclination i, from the sky-projected spin-orbit misalignment angle λ, given that $\mathbf{\Omega}$ is inclined to the line-of-sight by $I_\star$ degrees, and $\mathbf{h}$ is inclined to the line-of-sight by I_p degrees. λ is detectable through the RM effect, I_p can be determined for a transit (and is $\approx 90°$). For transiting planets λ gives a lower bound on the true spin-orbit misalignment i.

1.2 Formation and early migration of giant planets

Observations of the solar system show that the orbits of the planets all approximately lie within a common plane, whose normal is oriented only 6° from the solar rotation axis (Beck & Giles 2005). This observed coplanarity is what originally inspired Kant (1755)[2] and Laplace (1796) to propose that the Sun and its planets condensed from a spinning, flattened nebula, which is the so-called Nebular Hypothesis.

Since the time of Kant and Laplace our theories have complicated considerably (see Papaloizou & Terquem 2006 for a comprehensive review), but the main idea of the Nebular Hypothesis has remained unchanged. It is now generally believed that planets form out of the discs of gas and dust observed around young T-Tauri stars. These stars and their circumstellar discs are thought to have themselves formed from the collapse of molecular cloud material with appreciably nonzero angular momentum, in which centrifugal forces hinder collapse perpendicular to the rotation axis, resulting in the formation of a gaseous disc. These protoplanetary discs around T-Tauri stars last for up to 10 Myr, after which the discs appear to dissipate (Beckwith 1996). Planet formation theory must therefore explain the formation of the planets in the solar system, and their extrasolar analogues, within this window of opportunity.

There are two competing theories for the formation of giant planets. The first involves the coagulation and accumulation of small particles of ice and rock to form a solid core (Safronov 1969), which rapidly accretes gas from the protoplanetary disc. This is the core-accretion scenario (Pollack et al. 1996). The second relies on the gravitational instability of the gaseous disc (see Durisen et al. 2007, for a recent review) to produce the giant planet directly.

Both of these formation scenarios necessitate the formation of planets such as 51 Peg b in colder regions of the disc, much further out (with semi-major axes of several AU), before a migratory process that brings the planet in towards the star and to its present location (Lin et al. 1996). Planetary migration in gaseous protoplanetary discs had already been predicted prior to the 1980's (Goldreich & Tremaine 1979; Lin & Papaloizou 1979), and is thought to be driven by the dynamical interaction between

[2]The Nebular Hypothesis was first proposed in 1734 by Emanuel Swedenborg (Swedenborg 1734), though Immanuel Kant developed the theory further in 1755.

the planet and its gaseous protoplanetary disc. This migration occurs because the planet produces inward and outward propagating spiral density waves in the disc, which both interact gravitationally with the planet. These waves carry negative and positive angular momentum fluxes respectively, and a corresponding tidal torque acts on the orbit of the planet. This is referred to as type I migration, and is relevant for terrestrial planets and giant planet cores. When the mass of the planet grows, the density perturbation becomes non-linear and the planetary wake turns into a shock in its vicinity. This results in the formation of a gap in the disc, with the subsequent inward migration of the planet occurring on the disc viscous timescale. Research into both of these migration regimes is still underway, and there remain many unsolved problems (see Papaloizou et al. 2007 for a recent review), though a combination of both processes during the early stages of planet formation could potentially produce a population of HJs.

The formation of systems of giant planets can be thought of as occurring in two oversimplified stages (Jurić & Tremaine 2008).

- During stage 1 the cores of the giant planets are formed, they accrete gas and undergo migration, driven by the dynamical interaction between the planets and the gaseous protoplanetary disc. This stage lasts a few Myr until the gas dissipates, by which time a population of gas giants may exist. If these form sufficiently closely packed then stage 2 follows.

- Stage 2 lasts from when the disc has dissipated and continues until the present, and primarily involves gravitational interactions and collisions between the planets. Recent studies into stage 2 (Jurić & Tremaine 2008; Chatterjee et al. 2008; Ford & Rasio 2008) have shown that this is a chaotic era, in which planet-planet scatterings force the ejection of all but a few ($\sim 2-3$) planets from the system, in a period of large-scale dynamical instability lasting $\lesssim 10^8$yr.

Planet-planet scatterings can excite the eccentricities of the planets to levels required to explain observations. They tend also to excite the inclinations of the planets with respect to the initial symmetry plane of the system, though this has been found to be less efficient than the excitation of eccentricity. This could potentially lead to observable consequences via the RM effect.

It is possible for HJs orbiting a host star which has a distant and inclined stellar companion, or massive inclined outer planetary companion, to undergo another type of migration. This is Kozai migration (Wu & Murray 2003). The presence of such an outer companion to an exoplanet host star could cause Kozai oscillations, which produce periods of extreme eccentricity in the planet orbit, if various conditions are satisfied (e.g. see section 1.2 of Fabrycky & Tremaine 2007). The subsequent tidal dissipation that occurs during the periods of small pericentre distance leads to gradual inward migration of the planet. It has even been proposed that a combination of planet-planet scattering, tidal circularisation and the Kozai mechanism in outer planets, can produce HJs around single stars (Nagasawa et al. 2008). HJs produced from these processes generally have their orbital angular momentum vector misaligned with respect to the stellar spin axis by large angles – occasionally larger than 90° (Fabrycky & Tremaine 2007; Nagasawa et al. 2008).

Misaligned orbits are not predicted from stage 1 alone, so if λ is measured to be appreciably nonzero in enough systems, then it could be seen as evidence for planet-planet scattering or Kozai migration. This is because gas-disc migration does not seem able to excite orbital inclination (Lubow & Ogilvie 2001; Cresswell et al. 2007). Alternatively, if observed planets are all found with λ consistent with zero, this could rule out planet-planet scattering or Kozai migration as being of any importance.

One important consideration is that at such close proximity to their parent stars, strong tidal interactions between the star and planet are expected to cause significant long-term spin-orbit evolution, including changes to the value of λ (actually the true spin-orbit misalignment angle i) over time. If tides can change λ since the time of formation, then we may have difficulty in distinguishing migration caused by planet-planet scattering and Kozai oscillations, from gas-disc migration. The tidal evolution of such inclined orbits must therefore be considered an important goal in planetary evolution studies. In Part I, we study the effects of tidal friction on such inclined orbits.

1.3 Introduction to tidal friction

It has been known since the time of Newton that the gravitational interaction between the Earth and the Moon produces a tide in the seas. An early analysis of the nature of this tidal interaction was introduced by Darwin (1880)[3]. In his model, the Earth is treated as a homogeneous spherical fluid body, which continually adjusts to maintain a state of quasi-hydrostatic equilibrium in the time-varying gravitational potential of the Moon. Darwin calculated that viscosity would introduce a phase lag in the response of the Earth to the forcing potential of the Moon. This leads to a misalignment between the tidal bulge and the line connecting the centres of the Earth and Moon, resulting in the action of torques on the rotation of the Earth and on the orbit of the Moon. This concept is referred to as the equilibrium tide model (see Fig. 1.3). Significant spin-orbit evolution can occur over secular timescales through these tides, as can be inferred from Lunar Laser Ranging observations (Chapront et al. 2002), which show that the Moon is receding from the Earth at a current rate of 3.8 cm per year as the Earth spins down at a rate of 23 μs per year.

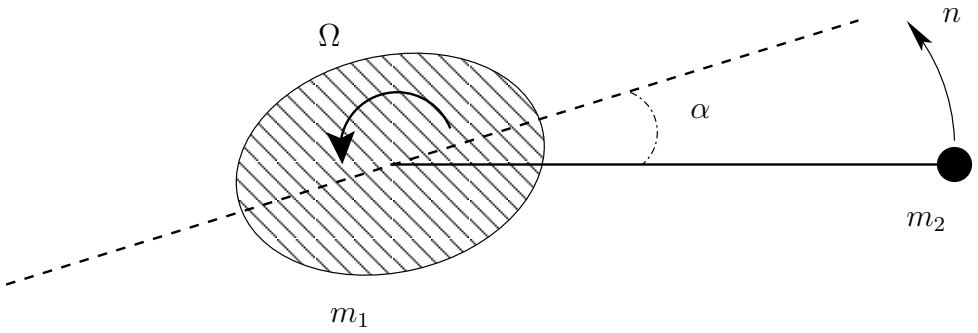

Figure 1.3: Illustration of the tidal torque on an asynchronously rotating primary. When the primary rotates faster than the orbital motion ($\Omega > n$), its mass distribution is shifted by an angle α from the line joining the centres of the two components, due to dissipation of energy. Since the forces applied to the two tidal bulges are not equal, a torque is exerted on the star, which tends to synchronise its rotation with the orbital motion ($\Omega \to n$). A similar picture emerges when $\Omega < n$; see §1.4 for a derivation of the torque in this case.

The tidal interaction between two orbiting bodies acts to continually change the orbital and rotational system parameters, and continually dissipates mechanical energy. Ultimately – in the absence of angular momentum loss from the system – either

[3]who also had happened to have a somewhat influential father...

an equilibrium state is asymptotically approached, or the two bodies spiral towards each other at an accelerating rate, and eventually collide. The equilibrium state is characterised by coplanarity (the equatorial planes of the bodies coincide with the orbital plane), circularity and corotation (rotational frequencies of each body match the orbital frequency) (Hut 1980).

Tidal forces are also thought to be important elsewhere in the solar system (see Goldreich & Soter 1966 for an old review and Peale 1999 for a more modern one), and are responsible for producing the spectacular vulcanism on Jupiter's moon Io. There also exist close-binary stars whose orbits appear to have been circularised, which shows that tidal friction is not only important for planets and their satellites in our solar system (e.g. Meibom & Mathieu 2005). In addition, a close-in planet with an orbital period shorter than the stellar spin period is subject to tidally induced inspiral into the star (the opposite evolution to that of the Earth-Moon system). The problem tackled in Part II is to explain the survival of the observed short-period planets, by understanding the efficiency of this process.

1.4 Simple calculation of the tidal torque

In this section we derive the torque on an asynchronously rotating star with a companion planet on a coplanar, circular orbit following the approach of Zahn (2008), for illustrative purposes. In the equilibrium tide model we assume that the star is in hydrostatic equilibrium, and that in the absence of dissipation its shape would adjust instantaneously to the time-dependent perturbing potential of its orbiting companion. We further assume that the star rotates slower than the planet revolves around the star, i.e., $\Omega < n$. Fig. 1.3 sketches the system under consideration, except that it shows the case $\Omega > n$, appropriate for the Earth-Moon system.

The relative height of the tidal bulge is given approximately by the ratio of the differential force exerted on the bulges (f_{tide}) to the surface gravity of the body (f_{bind})

$$\frac{\delta R_1}{R_1} \approx \frac{f_{tide}}{f_{bind}} \approx \frac{G m_2 m_1 R_1 / r^3}{G m_1^2 / R_1^2} \approx \frac{m_2}{m_1} \left(\frac{R_1}{r} \right)^3 . \tag{1.4.1}$$

In these expressions, r is the star-planet separation and R_1 is the stellar radius. If we

further assume that the star has a constant density, then its tidal bulges would have a mass $\delta m_1 \approx \frac{\delta R_1}{R_1} m_1$. This is not strictly correct for a realistic stellar model, due to the strong central condensation of the star (which can be taken into account by defining a Love number $k < 1$; it is also not exact for a homogeneous body), but it suffices for the present purpose.

When $\Omega \neq n$, dissipation of energy stored in the tide by any process will introduce a slight lag of the tidal bulges relative to the lines joining the centres of the star and the planet. The star therefore experiences a torque which acts to synchronise the spin of the star with the orbit. Due to conservation of total angular momentum, this is equal in magnitude and opposite in sign to the torque which acts on the orbit of the planet. In the weak friction approximation this lag is represented by a lag angle $\alpha \ll 1$, which is assumed to be proportional to the tidal frequency $\hat{\omega} = 2(n - \Omega)$. The tidal frequency is the Doppler shifted forcing frequency that is seen in the frame rotating with the star (with angular velocity Ω), and is twice the orbital angular frequency (n) because the dominant tide is quadrupolar, i.e., has two high tides and two low tides (see e.g. Murray & Dermott 1999). A common non-dimensional parametrisation of the lag angle is

$$\alpha = \frac{\hat{\omega}}{t_{diss}} \frac{R_1^3}{G m_1}, \tag{1.4.2}$$

where we have introduced the dynamical timescale $(R_1^3/Gm_1)^{1/2}$ to make α dimensionless. This gives a tidal torque acting to synchronise the star with the orbital motion of magnitude

$$\Gamma \approx \delta m_1 f_{tide} R_1 \sin\alpha \approx \frac{\hat{\omega}}{t_{diss}} \frac{m_2^2}{m_1} R_1^2 \left(\frac{R_1}{r}\right)^6, \tag{1.4.3}$$

when $\alpha \ll 1$. This expression is only valid if the dissipation is relatively inefficient, with large t_{diss} (and therefore $Q' \gg 1$, which we define in the next section). A torque of equal magnitude, but of opposite sign, acts on the orbit of the planet, which results in a transfer of angular momentum from the planetary orbit to the stellar spin. The consequences of this torque are that the star spins up as the planet falls into the star, until either the star is spun up to rotate with the angular frequency of the orbit, or the planet has plunged into the star.

1.5 Tidal quality factors and empirical estimates

The efficiency of tidal dissipation in a body is often parametrised by a dimensionless quality factor Q, which reflects the fact the body undergoes a forced oscillation and dissipates a small fraction of the associated energy during each oscillation period. This is analogous to the quality factor in a forced, damped harmonic oscillator (Murray & Dermott 1999; Feynman 1963), and is defined by

$$Q = 2\pi E_0 \left(\oint -\dot{E}\, \mathrm{d}t \right)^{-1},$$

where E_0 is the maximum energy stored in an oscillation and the integral represents the energy dissipated over one cycle. This is related to the time-lag τ in the response of the body to tidal forcing of frequency $\hat{\omega}$ by $Q^{-1} = \hat{\omega}\tau$. We further find it convenient to define $Q' = \frac{3Q}{2k}$, where k is the Love number of the body, since this combination always appears together in the evolutionary equations. The factor $k < 1$ if the body is centrally condensed, as is the case for stars and giant planets. Q' reduces to Q for a homogeneous fluid body, where $k = \frac{3}{2}$.

Typically assumed values of $Q' \sim 10^6$ for stars are roughly consistent with observational data regarding the circularisation periods of binary stars (Ogilvie & Lin 2007, hereafter OL07). This value can explain the observed circularity of the orbits of close binary stars with orbital periods shorter than the circularisation period (which increases with system age), if tidal friction is responsible for the circularisation. In addition, the magnitude of Q' for HJs is often assumed to be similar to that for Jupiter, which has been inferred to be in the range $2 \times 10^5 - 8 \times 10^6$ (Yoder & Peale 1981), since $k \approx 0.38$ for Jupiter (Gavrilov & Zharkov 1977). This estimate is based on a model of the tidal origin of the Laplace resonance among the Galilean satellites; however, it has been argued that even if the origin of the resonance is primordial, the average Q' cannot be far from these bounds (Peale & Lee 2002). This estimate also appears consistent with Jackson et al. (2008), who found that one can reproduce the outer planet (with semi-major axes wider than 0.2 AU) eccentricity distribution from integrating the tidal evolution equations backwards in time for the observed close-in planets (with semi-major axes smaller than 0.2 AU) quite well if $Q \sim 10^{5.5}$ for stars

and $Q \sim 10^{6.5}$ for HJs. However, the resulting stellar Q' is difficult to reconcile with the existence of the planets on the tightest orbits, such as WASP-12 b (Hebb et al. 2009) and OGLE-TR-56 b (Sasselov 2003), since it would imply that the inspiral time for these planets would be much less than the age of the system. That several planets have been found with similarly short periods makes this seem unlikely on probabilistic grounds. Additionally, Jackson et al. (2008) assume that Q' is the same for all exoplanet host stars. This may be a major oversimplification, which we discuss in Part II of this thesis.

In the model of § 1.4, the reciprocal of the tidal quality factor of the star is given by

$$\frac{1}{Q'} \propto \frac{1}{t_{diss}} \left(\frac{R_1^3}{G m_1} \right) |\hat{\omega}|. \tag{1.5.1}$$

If the dissipation of the equilibrium tide is solely due to an effective viscosity associated with turbulent convection, then t_{diss} can be calculated by integrating the turbulent viscosity (ν_t) over convective regions of the star. In the mixing length prescription, this turbulent viscosity is defined to be $\nu_t = vl$, where v is the eddy velocity and l is the mixing length. When the tidal period is shorter than the convective turnover time, i.e.,

$$\frac{2\pi}{\hat{\omega}} \equiv P_{tide} < t_{conv} \equiv \frac{l}{v}, \tag{1.5.2}$$

the turbulent viscosity should be reduced by some factor, over which there is uncertainty (see e.g. Zahn 1966; Goldreich & Nicholson 1977; Goodman & Oh 1997; Penev et al. 2007). Zahn reduces the turbulent viscosity by the following prescription with $p = 1$:

$$\nu_t = \frac{1}{3} vl \left[1 + B \left(|\hat{\omega}|\, t_{conv} \right)^p \right]^{-1}, \tag{1.5.3}$$

where B is a constant numerical factor. This prescription gives $t_{diss} \propto |\hat{\omega}|$. If this reduction is correct, then modelling the effects of tidal friction by a frequency-independent Q' would be reasonable. If on the other hand, ν_t is assumed to be independent of $\hat{\omega}$, then t_{diss} is frequency-independent. This is the constant time-lag

approach (Alexander 1973; Hut 1981), which is justified if the dissipative process acts instantaneously, i.e., the convective turnover time, which is the relaxation time of the turbulent stress, is zero (Ivanov & Papaloizou 2004). In Part I we outline a derivation of the constant lag-time model of tidal friction, in a model which is valid for arbitrary eccentricity and stellar and planetary obliquity.

1.6 Mechanisms of tidal dissipation

The problem of theoretically determining the efficiency of tidal dissipation, and therefore quantifying the evolution of a system, amounts to calculating Q' factors for each body. Q' is in principle a function of the tidal forcing frequency and (in nonlinear cases) the amplitude of the tidal disturbance, and is a result of complex dissipative processes in each body (Zahn 2008). For solid bodies such as the Earth, Q' is thought to be approximately constant over a wide range of frequency (Munk & MacDonald 1960), which together with computational simplicity, has led to most studies of tidal evolution for solar system bodies assuming a frequency-independent Q'. This assumption for gaseous stars and giant planets is questionable, and the nature of the response of such a body to tidal forcing remains under investigation.

The tidal disturbance can generally be decomposed into two parts: an equilibrium tide, and a dynamical tide. The equilibrium tide is the quasi-hydrostatic ellipsoidal tidal bulge. In the frame corotating with the fluid, the time-dependence of the equilibrium tide, or its associated velocity field, is dissipated through its interaction with turbulent convection. However, the damping rate is uncertain, particularly when the convective time exceeds the tidal period, as we discussed in the previous section. The dynamical tide consists of internal waves that are excited by low-frequency tidal forcing, and has received much recent interest with regard to its possible contribution to Q' (Witte & Savonije 2002; Ogilvie & Lin 2004, hereafter OL04; Wu 2005; Papaloizou & Ivanov 2005; Ivanov & Papaloizou 2007; OL07; Goodman & Lackner 2009). This is because if these waves have short wavelength, then they are more easily damped than the large-scale equilibrium tide by radiative diffusion (Zahn 1975; Zahn 1977), convective viscosity (Terquem et al. 1998; hereafter T98), or nonlinear breaking (Goodman & Dickson 1998; hereafter GD98). For rotating fluid bodies, calculations of the exci-

tation and dissipation of internal waves have indicated that Q' varies in a complicated way with the tidal frequency (Savonije et al. 1995a; Savonije & Papaloizou 1997a; Papaloizou & Savonije 1997a; OL04; OL07) – for an illustration see Fig. 1.4.

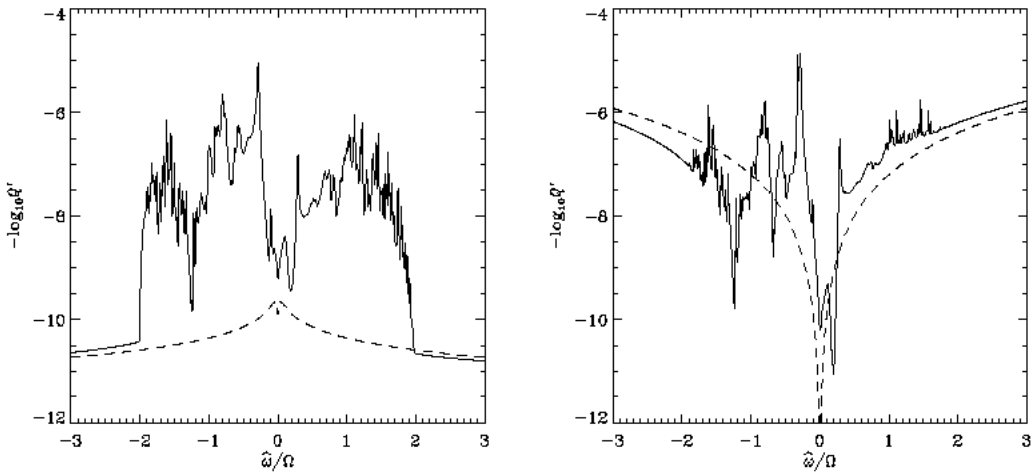

Figure 1.4: Q' as a function of the ratio of tidal frequency to spin frequency $\hat{\omega}/\Omega$. These results refer to tidal forcing by the $l = m = 2$ spherical harmonic in a model of the Sun with a spin period of 3 days. Left: Q' from the viscous dissipation of inertial waves in the CZ. Right: Q' from the excitation of internal inertia-gravity waves in the RZ. The dashed lines show the effect of omitting the Coriolis force, which has been found to be of great importance when $|\hat{\omega}| < 2|\Omega|$. The efficiency of tidal dissipation depends in a highly erratic way on the tidal forcing frequency. This figure was taken from OL07.

The tidal frequency is typically much lower than the dynamical frequency of the body, so the relevant internal waves must be approximately incompressible, restored not by pressure, but by buoyancy or rotation. OL04 found that the dissipation of tidally excited inertial waves, whose restoring force is the Coriolis force, can contribute significantly to the dissipation rate in a giant planet, whose interior is mostly convective (see also Wu 2005 and Ivanov & Papaloizou 2007). These waves can also contribute to the dissipation rate in convection zones (CZs) of stars (OL07). They are excited by tidal forcing of frequency $\hat{\omega}$, if this is less than the Coriolis frequency (2Ω), and this is true for many astrophysically relevant circumstances. However, these waves are not excited if the tidal frequency exceeds the Coriolis frequency, so this process is then not effective at dissipating the tide, and contributing to Q'.

In slowly rotating stars (with $\Omega < n$), such as those that host most of the short-period planets, the waves are primarily excited by tidal forcing in radiative regions, and are restored by buoyancy. These are commonly referred to as internal gravity

waves (IGWs). IGWs are damped by radiative diffusion, but this is only efficient if their frequencies are sufficiently low compared with the damping rate, which occurs if they have a short radial wavelength. However, in solar-type stars, the waves excited by planets with several-day orbital periods or less, are of sufficiently large wavelength that radiative diffusion is negligible in their attenuation (see § 7.1; GD98). It is therefore appropriate to ask whether there are any other mechanisms that can contribute to their dissipation (and to the stellar Q'), which would have implications for the survival of these short-period planets.

One such mechanism was proposed by GD98, and involves nonlinear effects becoming important near the centre of a solar-type star with a radiative core, where these waves become geometrically concentrated, and may attain large amplitudes. If nonlinear effects result in the absorption of the waves that propagate towards the centre, then this would be a relatively efficient mechanism of tidal dissipation, which could dominate over convective damping of the equilibrium tide. It is important to understand whether this process actually occurs, and if indeed it does, how efficient it is at affecting the orbits of the short-period planets. In Part II we study this mechanism in detail. We perform the first simulations of IGWs approaching the centre of a solar-type star, in both two and three dimensions, with the aim of studying how the reflection of waves from the centre is modified by nonlinearities as the amplitude is increased. We find that the waves break near the centre if they attain sufficient amplitude, and that this has important implications for the survival of short-period extrasolar planets.

We now summarise several mechanisms for dissipating energy stored in tidal oscillations in gaseous bodies, which have been found to be of considerable importance.

- Dissipation of the equilibrium tide by the turbulent viscosity of convective eddies in the convective envelopes of solar-type stars and the convective interiors of giant planets.

- The excitation and subsequent dissipation by turbulent viscosity of inertial waves in convective regions. These are excited when tidal frequencies are smaller than twice the spin frequency ($|\hat{\omega}| < 2|\Omega|$).

- The excitation of internal inertia-gravity waves – essentially IGWs modified

through Coriolis accelerations by rotation – in radiation zones (RZs) of stars and radiative envelopes of highly irradiated giant planets. These are dissipated by radiative diffusion, which is particularly strong near the surface of a giant planet or star. In addition, nonlinear effects may be important near the centre of a solar-type star, which could result in wave breaking and additional dissipation. This latter process is studied in detail in Part II.

1.7 Effects of tidal interactions on short-period planets

Following the discovery of 51 Peg b, it was realised that tidal interactions between a HJ and its host star could result in significant spin-orbit evolution over secular timescales (Rasio et al. 1996; Marcy et al. 1997). Rasio et al. (1996) showed that 51 Peg b is subject to orbital decay due to tides dissipated in the star, but has an inspiral time slightly longer than the main-sequence lifetime of the star in their model (though note that this timescale depends on the tidal quality factors of the star and planet). It is also expected that tides dissipated in the planet will synchronise the rotation of the planet with the orbital motion in a few Myr. In addition, Rasio et al. (1996) suggested that tidal dissipation in the planet may explain the negligible eccentricities of the shortest-period planets, and indeed observed planets with orbital periods shorter than 6 days primarily have circular orbits. This is illustrated in Fig. 1.5.

Dobbs-Dixon et al. (2004) proposed an explanation for the coexistence of both circular and eccentric orbits for the planets in the period range 7-21 days as the result of the variation in spin-down rates of young stars. Planets with orbits within this range are expected to be moderately affected by tides, whereas planets with orbital periods longer than 21 days are expected to be only negligibly affected, due to the strong dependence of the tidal force on separation. Recently Pont (2009) discussed empirical evidence for tidal spin-up of exoplanet host stars, and found indications of such a process occurring in the present sample of transiting planets. These works highlight the importance of stellar spin evolution on tidal evolution.

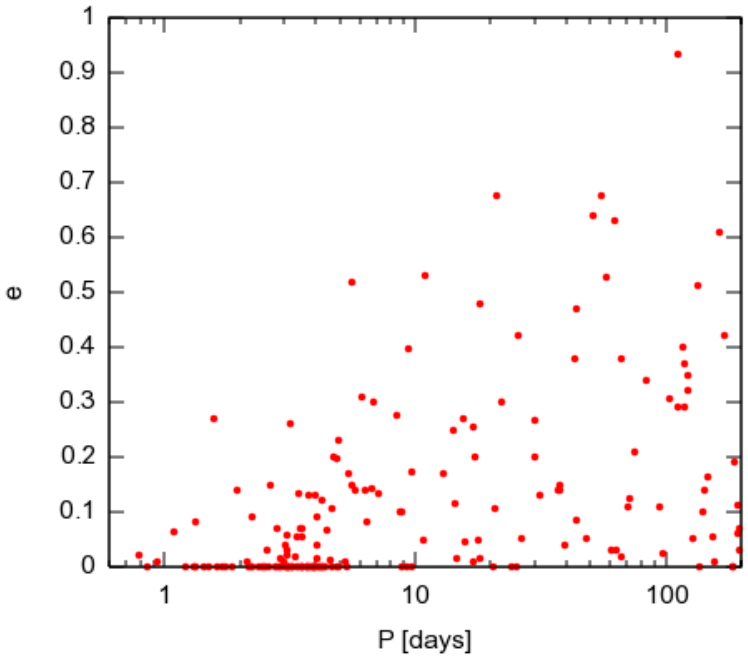

Figure 1.5: Orbital period-eccentricity distribution for the currently observed extrasolar planets. Orbits with $P \lesssim 6$ days have a smaller spread in e than those with larger orbital periods. This could be a result of circularisation due to dissipation of tides raised in the planet. This figure was taken from exoplanet.hanno-rein.de.

Jackson et al. (2008) found from considering coupled evolution of the eccentricity and semi-major axis that simple timescale considerations of circularisation may not accurately represent the true evolution. In addition, they found that it is inaccurate to neglect the combined effects of both the stellar and planetary tides. In Part I we study the accuracy of simple timescale estimates for tidal evolution, when coupled evolution of the orbital and rotational elements is considered, in a more general model of the long-term effects of tidal friction than Jackson et al. (2008) consider. We include stellar spin-down, and study its effects in a simplified system. In particular, we study the tidal evolution of inclination, since this has not been done in previous work.

1.8 Outline of this thesis

In Part I we study the tidal evolution of inclined orbits, using a variant of the simple "constant time-lag" model of tidal friction. We study the inclusion of stellar rotational spin-down and the accuracy of simple timescale estimates of tidal evolution. These

results have important consequences for the interpretation of observations of spin-orbit alignment angles using the RM effect, which will be discussed.

In Part II, we turn to the larger problem of understanding the mechanisms of tidal dissipation in solar-type stars. It is of particular interest to study the efficiency of tidal dissipation in these stars, since many have been found to harbour close-in planets, whose survival is determined by the stellar Q'. This is because a planet with an orbital period shorter than the stellar spin period is subject to tidally induced orbital decay, with an inspiral time that depends linearly on the stellar Q'. We study and extend a nonlinear model of tidal dissipation, initially proposed by GD98. In this model IGWs are excited at the interface of the convection and radiation zones of a solar-type star, which then propagate to the centre, where they can break if their amplitude is sufficiently large. We model the dynamics of the central regions of the star to study this process, primarily through the use of direct numerical simulations, in both two and three dimensions. Particular emphasis is made on analysing the resulting ingoing wave absorption which takes place near the centre. We then perform a detailed stability analysis of an IGW near the centre of a solar-type star to understand the breaking process in more detail, and to determine the existence and properties of any instabilities that onset for lower amplitude waves than were observed to break in the simulations. We also outline an additional mechanism of tidal dissipation involving the gradual attenuation of the waves by radiative diffusion, and discuss whether it is likely to operate in reality. The implications of these processes for the survival of short-period planets around solar-type stars is discussed throughout. This work allows us to propose a possible explanation for the survival of all short-period planets around F, G and K stars.

Part I

Constant lag time model of tidal friction

Chapter 2

Tidal evolution of Hot Jupiters on inclined orbits

In this chapter, we use a simple model of the orbit-averaged effects of tidal friction to study the evolution of close-in planets on inclined orbits, due to tides. We first analyse the effects of the inclusion of stellar rotational spin-down due to magnetic braking (hereafter MB). A phase-plane analysis of a simplified system of equations, including the MB torque is performed. We find that the inclusion of MB can lead to qualitatively different spin-orbit evolution; its neglect can result in a very different system history. We then present the results of numerical integrations of the tidal evolution equations, where we find that it is essential to consider coupled evolution of the orbital and rotational elements, including dissipation in both the star and planet, to accurately model the evolution. The main result of these integrations is that for typical HJs, tidal friction aligns the stellar spin with the orbit on a similar time as it causes the orbit to decay. This tells us that if a planet is observed to be aligned, then it probably formed coplanar. This reinforces the importance of Rossiter-McLaughlin effect observations in determining the degree of spin-orbit alignment in transiting systems. Finally, we apply these results to the first observed system with a spin-orbit misalignment, XO-3, and constrain the efficiency of tidal dissipation (i.e. the modified tidal quality factors Q') in both the star and the planet in this system.

2.1 Model of tidal friction adopted

In light of the uncertainties in Q', and the difficulty in calculating the spin-orbit evolution when Q' is a complicated function of $\hat{\omega}$, we adopt a simplified model, based on a frequency-independent lag time (with one modification discussed below). We adopt the model of Eggleton et al. (1998), which is based on the equilibrium tide model of Hut (1981). In this formulation, we calculate the evolution of the specific angular momentum of the planetary orbit

$$\mathbf{h} = \mathbf{r} \times \dot{\mathbf{r}} = na^2\sqrt{1-e^2}\,\hat{\mathbf{h}}, \tag{2.1.1}$$

together with its eccentricity vector $\mathbf{e}$, and the stellar and planetary spin vectors $\mathbf{\Omega}_1$ and $\mathbf{\Omega}_2$. The eccentricity vector has the magnitude of the eccentricity, and points in the direction of pericentre, and is defined by

$$\mathbf{e} = \frac{\dot{\mathbf{r}} \times \mathbf{h}}{Gm_{12}} - \hat{\mathbf{r}}, \tag{2.1.2}$$

where $m_{12} = m_1 + m_2$ is the sum of the stellar and planetary masses.

The evolutionary equations are derived by starting with the equation of relative motion of a planet of mass m_2 and its host star of mass m_1

$$\frac{d^2\mathbf{r}}{dt^2} = -\frac{Gm_{12}}{r^3}\mathbf{r} + \mathbf{f}, \tag{2.1.3}$$

where $\mathbf{r}$ is the separation and $\mathbf{f}$ represents a perturbing acceleration. The solution of the unperturbed equation (with $\mathbf{f} = \mathbf{0}$) is the ellipse

$$|\mathbf{r}| = \frac{a(1-e^2)}{1+e\cos f}, \tag{2.1.4}$$

where f is the angle referred to pericentre (the true anomaly). This is the Newtonian two-body problem (Murray & Dermott, 1999). Both $\mathbf{h}$ and $\mathbf{e}$ are conserved for an unperturbed Keplerian orbit; therefore under weak external perturbations their components vary slowly compared with the orbital period. This allows averaging of the effects of the tidal perturbation over a Keplerian orbit, resulting in a set of secular evolution equations for the rotational and orbital elements.

In Eggleton & Kiseleva-Eggleton (2001), $\mathbf{f}$ contains many contributions: the effects of general relativity, perturbing accelerations due to other planets and tidal and spin distortions of the star and planet, as well as tidal friction. In this chapter we solely consider the perturbing effects of tidal friction (see Appendix A.1 for the inclusion of the additional contributions) and set $\mathbf{f} = \mathbf{f}_{\rm tf} = \mathbf{f}^1_{\rm tf} + \mathbf{f}^2_{\rm tf}$, where

$$\mathbf{f}^{1,2}_{\rm tf} = -3\tau_{1,2}k_{1,2}n^2\left(\frac{m_{2,1}}{m_{1,2}}\right)\left(\frac{R_{1,2}}{a}\right)^5\left(\frac{a}{r}\right)^8\left[3(\hat{\mathbf{r}}\cdot\dot{\mathbf{r}})\hat{\mathbf{r}} + (\hat{\mathbf{r}}\times\dot{\mathbf{r}} - r\,\boldsymbol{\Omega}_{1,2})\times\hat{\mathbf{r}}\right]. \quad (2.1.5)$$

Here $n = \sqrt{\frac{Gm_{12}}{a^3}}$ is the orbital mean motion, $k_{1,2}$ are the second-order potential Love numbers for the star and planet respectively (which is twice the apsidal motion constant), and $\tau_{1,2}$ is the effective tidal lag time for each body. This form of the dissipative force of tidal friction is that derived under the assumption of a constant lag time in the equilibrium tide model (Eggleton et al., 1998). In this model, we assume that the body quasi-hydrostatically adjusts to the perturbing potential of its companion, but delayed by some small lag time (τ_1 for the star, τ_2 for the planet) that is proportional to the dissipation. Thus for each body, $Q = \frac{1}{\hat{\omega}\tau}$ is assumed to be inversely proportional to the tidal frequency $\hat{\omega}$, so that the lag time τ is independent of tidal frequency, thus the same for all components of the tide.

In the resulting equations we have chosen to parametrise the efficiency of tidal dissipation in each body by redefining $Q = \frac{1}{n\tau}$, and adopt a constant Q which does not change during the evolution, i.e., we assume effectively that the lag time scales with the orbital period (then Eq. 2.1.5 matches Eq. 4 in Mardling & Lin 2002, where this assumption was not made explicit). We also introduce the definition $Q' = \frac{3Q}{2k}$. This allows us to discuss "Q' values" for particular bodies, which do not change as the orbital and rotational elements vary. For the purposes of this work we *define* $Q' = \frac{3}{2kn\tau}$. This is equivalent to *assuming* that the relevant tidal frequency $\hat{\omega} = n$. Note that this may not give identical numerical factors in the resulting equations to other formulations of tidal friction (e.g. Goldreich & Soter 1966; Zahn 1977; Hut 1981), but we feel that this is the best way to study the general effects of tidal friction, given the uncertainties in the value of Q', and its dependence on $\hat{\omega}$, for realistic giant planets and stars.

The planet's specific orbital angular momentum $\mathbf{h}$ changes at a rate

$$\frac{d\mathbf{h}}{dt} = \mathbf{r} \times (\mathbf{f}_{\rm tf}^1 + \mathbf{f}_{\rm tf}^2), \tag{2.1.6}$$

with a corresponding rate of angular momentum transfer between the orbit and spin of each body given by

$$\dot{\mathbf{J}}_{1,2} = I_{1,2}\dot{\mathbf{\Omega}}_{1,2} = -\mu \mathbf{r} \times \mathbf{f}_{\rm tf}^{1,2}, \tag{2.1.7}$$

since total angular momentum is conserved, and where $\mu = \frac{m_1 m_2}{m_{12}}$ is the reduced mass of the system. The eccentricity vector evolves as

$$\frac{d\mathbf{e}}{dt} = \frac{[2(\mathbf{f}_{\rm tf} \cdot \dot{\mathbf{r}})\mathbf{r} - (\mathbf{r} \cdot \dot{\mathbf{r}})\mathbf{f}_{\rm tf} - (\mathbf{f}_{\rm tf} \cdot \mathbf{r})\dot{\mathbf{r}}]}{G m_{12}}. \tag{2.1.8}$$

Eqs. 2.1.6 and 2.1.8 are time-averaged over the orbit, and the resulting differential equations are given below. Numerical integration of these equations gives the secular evolution of the orbital elements. Note that we have written these equations so that they are regular at $e = 0$, unlike those in Eggleton & Kiseleva-Eggleton (2001) and Mardling & Lin (2002). To do this we have eliminated reference to $\hat{\mathbf{e}}$, which is undefined for a circular orbit, whereas $\mathbf{e}$ is perfectly well defined and equal to zero. The resulting equations read

$$\begin{aligned}
\frac{d\mathbf{h}}{dt} &= -\frac{1}{t_{f1}}\left[\frac{\mathbf{\Omega}_1 \cdot \mathbf{e}}{2n} f_5(e^2) h\mathbf{e} - \frac{\mathbf{\Omega}_1}{2n} f_3(e^2) h + \left(f_4(e^2) - \frac{\mathbf{\Omega}_1 \cdot \mathbf{h}}{2n}\frac{1}{h} f_2(e^2)\right)\mathbf{h}\right] \\
&\quad -\frac{1}{t_{f2}}\left[\frac{\mathbf{\Omega}_2 \cdot \mathbf{e}}{2n} f_5(e^2) h\mathbf{e} - \frac{\mathbf{\Omega}_2}{2n} f_3(e^2) h + \left(f_4(e^2) - \frac{\mathbf{\Omega}_2 \cdot \mathbf{h}}{2n}\frac{1}{h} f_2(e^2)\right)\mathbf{h}\right] \\
&= \left(\frac{d\mathbf{h}}{dt}\right)_1 + \left(\frac{d\mathbf{h}}{dt}\right)_2
\end{aligned} \tag{2.1.9}$$

$$\begin{aligned}
h\frac{d\mathbf{e}}{dt} &= -\frac{1}{t_{f1}}\left[\frac{\mathbf{\Omega}_1 \cdot \mathbf{e}}{2n} f_2(e^2)\mathbf{h} + 9\left(f_1(e^2) h - \frac{11}{18}\frac{\mathbf{\Omega}_1 \cdot \mathbf{h}}{n} f_2(e^2)\right)\mathbf{e}\right] \\
&\quad -\frac{1}{t_{f2}}\left[\frac{\mathbf{\Omega}_2 \cdot \mathbf{e}}{2n} f_2(e^2)\mathbf{h} + 9\left(f_1(e^2) h - \frac{11}{18}\frac{\mathbf{\Omega}_2 \cdot \mathbf{h}}{n} f_2(e^2)\right)\mathbf{e}\right]
\end{aligned} \tag{2.1.10}$$

$$\frac{d\mathbf{\Omega}_1}{dt} = -\frac{\mu}{I_1}\left(\frac{d\mathbf{h}}{dt}\right)_1 + \dot{\omega}_{\rm mb} \tag{2.1.11}$$

$$= \frac{\mu}{I_1 t_{f1}}\left[\frac{\mathbf{\Omega}_1 \cdot \mathbf{e}}{2n} f_5(e^2) h\mathbf{e} - \frac{\mathbf{\Omega}_1}{2n} f_3(e^2) h + \left(f_4(e^2) - \frac{\mathbf{\Omega}_1 \cdot \mathbf{h}}{2n}\frac{1}{h} f_2(e^2)\right)\mathbf{h}\right] + \dot{\omega}_{\rm mb}$$

$$\frac{d\mathbf{\Omega}_2}{dt} = -\frac{\mu}{I_2}\left(\frac{d\mathbf{h}}{dt}\right)_2 \tag{2.1.12}$$

$$= \frac{\mu}{I_2 t_{f2}} \left[\frac{\mathbf{\Omega}_2 \cdot \mathbf{e}}{2n} f_5(e^2) h\mathbf{e} - \frac{\mathbf{\Omega}_2}{2n} f_3(e^2) h + \left(f_4(e^2) - \frac{\mathbf{\Omega}_2 \cdot \mathbf{h}}{2n} \frac{1}{h} f_2(e^2) \right) \mathbf{h} \right]$$

We also need to define an inverse tidal friction timescale t_f^{-1} for each body (here for body 1, change $1 \rightarrow 2$ to get the corresponding expression for body 2), and the functions of the eccentricity (first derived in a similar form by Hut 1981).

$$\frac{1}{t_{f1}} = \left(\frac{9n}{2Q_1'} \right) \left(\frac{m_2}{m_1} \right) \left(\frac{R_1}{a} \right)^5 = \sqrt{Gm_{12}} \left(\frac{9}{2Q_1'} \right) \left(\frac{m_2}{m_1} \right) R_1^5 \, a^{-\frac{13}{2}} \quad (2.1.13)$$

$$f_1(e^2) = \frac{1 + \frac{15}{4}e^2 + \frac{15}{8}e^4 + \frac{5}{64}e^6}{(1-e^2)^{\frac{13}{2}}} \quad (2.1.14)$$

$$f_2(e^2) = \frac{1 + \frac{3}{2}e^2 + \frac{1}{8}e^4}{(1-e^2)^5} \quad (2.1.15)$$

$$f_3(e^2) = \frac{1 + \frac{9}{2}e^2 + \frac{5}{8}e^4}{(1-e^2)^5} \quad (2.1.16)$$

$$f_4(e^2) = \frac{1 + \frac{15}{2}e^2 + \frac{45}{8}e^4 + \frac{5}{16}e^6}{(1-e^2)^{\frac{13}{2}}} \quad (2.1.17)$$

$$f_5(e^2) = \frac{3 + \frac{1}{2}e^2}{(1-e^2)^5} \quad (2.1.18)$$

$$f_6(e^2) = \frac{1 + \frac{31}{2}e^2 + \frac{255}{8}e^4 + \frac{185}{16}e^6 + \frac{25}{64}e^8}{(1-e^2)^8} \quad (2.1.19)$$

In the absence of MB ($\dot{\omega}_{\rm mb} = \mathbf{0}$) the total angular momentum is conserved ($\frac{d\mathbf{L}}{dt} = \mathbf{0}$). With the inclusion of MB (see §2.2), the total angular momentum of the system decreases at a rate

$$\frac{d\mathbf{L}}{dt} = \frac{d}{dt} \left(\mu\mathbf{h} + I_1\mathbf{\Omega}_1 + I_2\mathbf{\Omega}_2 \right) = I_1 \dot{\omega}_{\rm mb} = -\alpha_{\rm mb} I_1 \Omega_1^2 \mathbf{\Omega}_1. \quad (2.1.20)$$

Tidal dissipation and MB result in a loss of energy from the system. The total rate of energy dissipated can be expressed as follows:

$$\dot{E}_{tot} = \frac{1}{2} \frac{Gm_1m_2}{a} \frac{\dot{a}}{a} + I_1\Omega_1\dot{\Omega}_1 + I_2\Omega_2\dot{\Omega}_2 \quad (2.1.21)$$

$$= -H_1 - H_2 - \alpha_{\rm mb} I_1 \Omega_1^4, \quad (2.1.22)$$

where the final term in the last expression is the energy dissipated by MB and

$$H_1 = \frac{\mu h}{n t_{f1}} \left[\frac{1}{2} \left(\Omega_1^2 f_3(e^2) + \frac{(\mathbf{\Omega}_1 \cdot \mathbf{h})^2}{h^2} f_2(e^2) - (\mathbf{\Omega}_1 \cdot \mathbf{e})^2 f_5(e^2) \right) - 2n \frac{(\mathbf{\Omega}_1 \cdot \mathbf{h})}{h} f_4(e^2) + n^2 f_6(e^2) \right],$$

$$H_2 = \frac{\mu h}{n t_{f2}} \left[\frac{1}{2} \left(\Omega_2^2 f_3(e^2) + \frac{(\mathbf{\Omega}_2 \cdot \mathbf{h})^2}{h^2} f_2(e^2) - (\mathbf{\Omega}_2 \cdot \mathbf{e})^2 f_5(e^2) \right) - 2n \frac{(\mathbf{\Omega}_2 \cdot \mathbf{h})}{h} f_4(e^2) + n^2 f_6(e^2) \right],$$

are the tidal heating rates in the star and planet, respectively. It has been proposed that H_2 can result in planetary inflation, if the energy is deposited deep in the interior of the planet (e.g. Bodenheimer et al. 2001). Note that these expressions approach zero as $e \to 0$, $\mathbf{\Omega}_{1,2} \cdot \mathbf{e} \to 0$ and $\mathbf{\Omega}_{1,2} \cdot \hat{\mathbf{h}} \to n$, i.e. tidal dissipation continues until the orbit becomes circular, and the spin of each body becomes coplanar and synchronous with the orbit.

This formulation is beneficial because it can treat arbitrary orbital eccentricities and stellar and planetary obliquities, unlike other models which are only valid to a given order in the eccentricity, or for small (or zero) orbital inclinations (Goldreich & Soter 1966; Hut 1981). Using the secular evolution equations allows us to perform integrations quickly that represent dynamical evolution over billions of years. The full set of equations are written in a form which is straightforward to numerically integrate.

2.2 Magnetic braking

Observations of solar-type stars have shown that the mean stellar rotational velocity decreases with time, following the relation $\Omega \propto t^{-1/2}$ (Skumanich, 1972). This is the empirical Skumanich relation, and can be interpreted as telling us that solar-type stars have been undergoing continuous spin-down since they first started on the main sequence. MB by a magnetised outflowing wind has long been recognised as an important mechanism for the removal of angular momentum from rotating stars (Weber & Davis, 1967), and such a mechanism seems able to explain most of the observed stellar spin-down (Barnes, 2003).

The surface layers of solar-type stars are convectively unstable, and turbulent motion and rotation can generate magnetic fields via a dynamo action, which heats the corona and produces a magnetically controlled stellar wind. Magnetic stresses impart angular momentum to the stellar wind, which forces the plasma to corotate with the star up to the Alfvén radius (r_A), which is where the kinetic and magnetic energy density of the outflowing plasma balance. This enhances the angular momentum loss via the stellar wind considerably over a non-magnetic case (by a factor $(r_A/R_\odot)^2 \sim 100$,

for the Sun). This mechanism is referred to as MB, and can be attributed to Schatzman (1962), though the first formulations of such a steady, magnetised, thermally driven outflow in the ideal-MHD limit were due to Weber & Davis (1967) and Mestel (1968).

The simplest models of MB, such as Weber & Davis (1967), involve a thermally-driven wind flowing out on magnetic field lines, which are essentially radial close to the star (split monopole). Magnetic stresses impart angular momentum to the outflowing gas, but the field weakens with the inverse square of distance from the star (see Fig. 2.1). This model gives an angular momentum loss rate of

$$\frac{dJ}{dt} = \frac{8\pi}{3\mu_0} \left(B_0 R_1^2\right)^2 \frac{\Omega}{v_A(r_A)}, \tag{2.2.1}$$

where $J = I\Omega$ is the spin angular momentum of the star, B_0 is the magnetic field at the surface of the star, R_1 is the radius of the star and $v_A(r_A)$ is the Alfvén speed evaluated at the Alfvén radius (given by $\frac{B(r_A)}{\sqrt{\mu_0 \rho(r_A)}}$). If we assume that the open-field magnetic flux scales linearly with the rotation rate, i.e. $4\pi B_0 R_1^2 \propto \Omega$, then we recover the commonly-used relation

$$\frac{d\Omega}{dt} \propto -\Omega^3. \tag{2.2.2}$$

Integration of this equation leads asymptotically to the Skumanich relation (Collier Cameron, 2002).

Although the Skumanich law is well established for stars with rotational velocities in the range $1 - 30$ km s^{-1}, it overestimates the spin-down rates of stars younger than 10^8 yrs, and thus cannot explain the presence of fast rotators in the Pleiades (Ivanova & Taam, 2003). As a resolution to this problem it has been suggested that the angular momentum loss rate for high rotation rates could be reduced, as a result of the saturation of the stellar dynamo (MacGregor & Brenner, 1991), or alternatively due to a reduction in the number of open field lines in a complex magnetic field topology (Taam & Spruit, 1989). These and similar approaches lead to modified models of the MB torque for fast rotators, and several such models have been proposed (e.g. Ivanova & Taam 2003; Holzwarth & Jardine 2005). Nevertheless, Barnes (2003) find that the Skumanich relation is remarkably accurate at modelling the spin-down of Sun-like

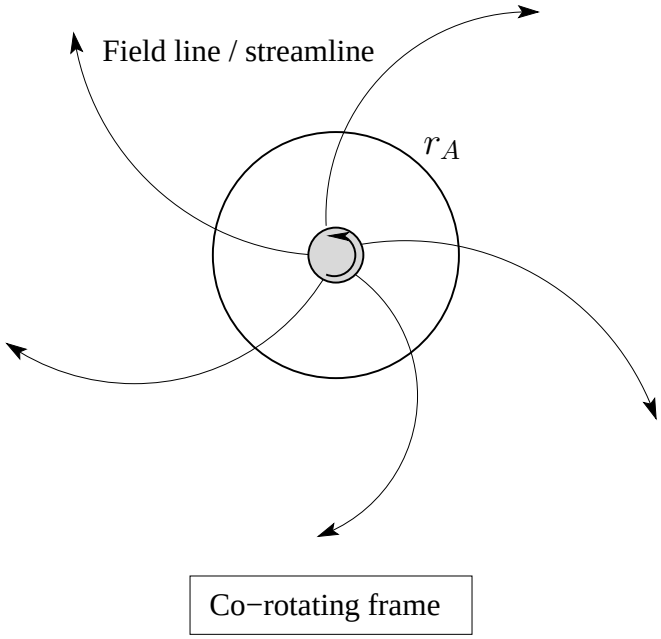

Figure 2.1: Sketch of the magnetic field lines and direction of flow of outflowing plasma in the equatorial plane of a stellar wind. Charged stellar wind particles flow out these on magnetic field lines, which are essentially radial close to the star. Magnetic stresses enforce corotation of the outflowing plasma up until r_A, which enhances the angular momentum loss rate over a non-magnetic case by $\sim (r_A/R_\odot)^2$.

stars that are not rapid rotators, so to a first approximation, a MB torque based on the empirical Skumanich law is best for our purposes.

In this chapter, we include the effects of MB in the equations written down in §2.1 in the tidal evolution equations, through the inclusion of the Verbunt & Zwaan (1981) braking torque, with the particular coefficients of Dobbs-Dixon et al. (2004),

$$\dot{\boldsymbol{\omega}}_{\rm mb} = -\alpha_{\rm mb}\, \Omega_1^2\, \boldsymbol{\Omega}_1, \tag{2.2.3}$$

where $\alpha_{\rm mb} = 1.5 \times 10^{-14}\gamma$ yrs. γ is a correction factor for an F-star, which takes the value 0.1 for an F star, but is unity for a G or K star. We can also define a MB timescale $\tau_{\rm mb} \equiv \frac{\Omega_1}{\dot{\omega}_{\rm mb}} = \frac{1}{\alpha_{\rm mb}} \frac{1}{\Omega_1^2}$, which is approximately 10^{10} yrs for the Sun.

2.3 Analysis of the effects of MB on tidal evolution in a simplified system

2.3.1 Circular, coplanar orbit with MB

We first study the effects of MB on a simplified system of a circular, coplanar orbit under the influence of only the tide that is raised on the star by the planet, and MB. We have neglected the tide in the planet here since the moment of inertia of the planet is much smaller than that of star and the orbit (i.e. $I_2 \ll I_1 \sim m_2 a^2$), so to a first aproximation we can neglect the effects of planetary spin; in any case the planetary spin is expected to synchronize rapidly with the orbit. The following set of dimensionless equations can be derived from the full set of equations in §2.1:

$$\frac{d\tilde{\Omega}}{d\tilde{t}} = \tilde{n}^4 \left(1 - \frac{\tilde{\Omega}}{\tilde{n}}\right) - A\,\tilde{\Omega}^3, \tag{2.3.1}$$

$$\frac{d\tilde{n}}{d\tilde{t}} = 3\,\tilde{n}^{\frac{16}{3}} \left(1 - \frac{\tilde{\Omega}}{\tilde{n}}\right), \tag{2.3.2}$$

where we have normalised the stellar spin frequency Ω_1 and orbital mean motion n to the orbital frequency at the stellar surface, together with a factor $C^{\frac{3}{4}}$. C is the ratio of the orbital angular momentum of a mass m_2 in an orbit with semi-major axis equal to the stellar radius R_1, to the spin angular momentum of an equally rapidly rotating star of radius R_1, mass m_1 and dimensionless radius of gyration r_{g1}. C is important for classifying the stability of the equilibrium curve $\tilde{\Omega} = \tilde{n}$ in the absence of MB, and it can be shown from energy and angular momentum considerations (see Appendix A.2), that this equilibrium is stable if $\tilde{n} \leq 3^{-\frac{3}{4}}$. This is equivalent to the statement that no more than a quarter of the total angular momentum can be in the form of spin angular momentum for stability (Hut, 1980). We have thus defined the following dimensionless quantities:

$$\tilde{\Omega} = \Omega_1 \left(\frac{R_1^3}{G m_{12}}\right)^{\frac{1}{2}} C^{-\frac{3}{4}}, \tag{2.3.3}$$

$$\tilde{n} = n \left(\frac{R_1^3}{G m_{12}}\right)^{\frac{1}{2}} C^{-\frac{3}{4}}, \tag{2.3.4}$$

$$C = \frac{\mu R_1^2}{I_1} = \frac{\mu}{r_{g1}^2\, m_1}, \tag{2.3.5}$$

$$\tilde{t} = \left(\frac{G m_{12}}{R_1^3}\right)^{\frac{1}{2}} \left(\frac{9}{2Q_1'}\right) \left(\frac{m_2}{m_1}\right) C^{\frac{13}{4}}\, t, \tag{2.3.6}$$

$$A = \alpha_{\rm mb} \left(\frac{G m_{12}}{R_1^3}\right)^{\frac{1}{2}} \left(\frac{2Q_1'}{9}\right) \left(\frac{m_1}{m_2}\right) C^{-\frac{7}{4}}. \tag{2.3.7}$$

There is only one parameter (A) that completely characterises the solution in the $(\tilde{n}, \tilde{\Omega})$-plane, and its value may be estimated as

$$A \simeq 100\, \gamma \left(\frac{Q_1'}{10^6}\right), \tag{2.3.8}$$

for a Jupiter-mass planet orbiting a Sun-like star undergoing MB (with standard $\alpha_{\rm mb}$ and with $Q' = 10^6$). The size of this term shows that in general MB dominates the stellar spin evolution. Note that in the absence of MB ($A = 0$), Eqs. 2.3.1 and 2.3.2 do not contain reference to the masses of the star and planet or to the tidal Q' of the star. The parameter A, together with the initial conditions $(\tilde{n}_0, \tilde{\Omega}_0)$, completely determines the evolution.

We plot some solutions on the $(\tilde{n}, \tilde{\Omega})$-plane in Fig. 2.2 by integrating Eqs. 2.3.1 and 2.3.2 for various initial conditions. Fig. 2.2 shows two phase portrait plots, which show the general qualitative behaviour of the solutions to Eqs. 2.3.1 and 2.3.2, for a given value of the parameter A. The arrows on each curve show the direction of time evolution from the initial state. For prograde orbits we restrict ourselves to studying the region, $0 \leq \tilde{n} \leq 10, 0 \leq \tilde{\Omega} \leq 10$, in the $(\tilde{n}, \tilde{\Omega})$-plane. This is because $\Omega_1 = \sqrt{G m_{12}/R_1^3}$ corresponds to stellar breakup velocity and $n \geq \sqrt{G m_{12}/R_1^3}$ means that the planet would be orbiting at, or beneath, the stellar surface. For a HJ with a mass of M_J orbiting a star of mass $M_\odot$, $C \sim 0.01$, so $\tilde{n} \simeq 10$ corresponds to an orbital semi-major axis of $a \simeq 0.01$ AU, and $\tilde{n} \simeq 0.1$ corresponds to $a \simeq 0.2$ AU, so these plots represent the full range of orbits of the HJs. The top panel of Fig. 2.2 is for $A = 100$, which corresponds to canonical MB for a G/K star ($\gamma = 1$) and Q_1' of 10^6.

In the absence of MB ($A = 0$) we recover the standard tidal evolution equations for a coplanar, circular orbit. These have been well studied in the literature (e.g. Counselman 1973; Hut 1981). These equations have an equilibrium of coplanarity and

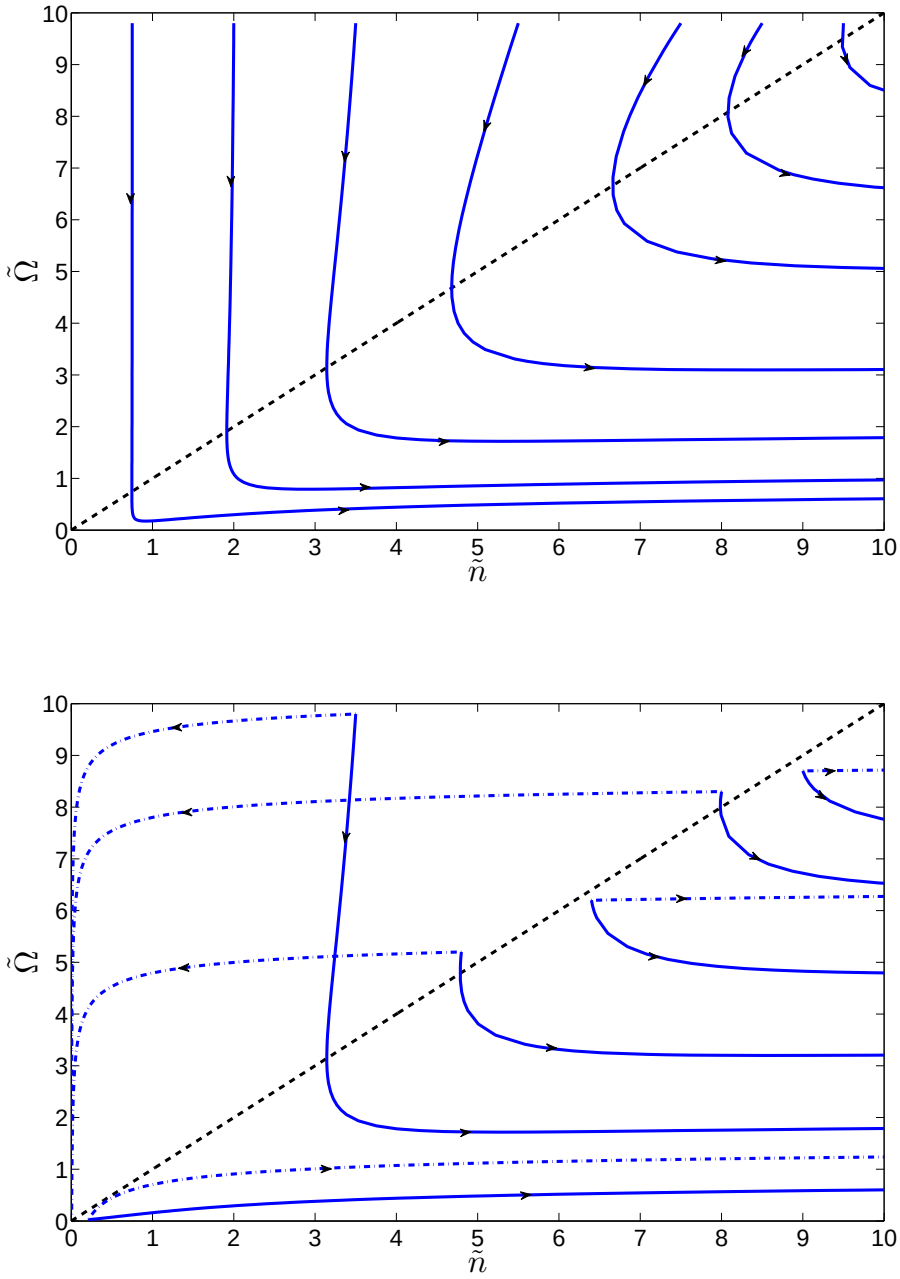

Figure 2.2: $(\tilde{n}, \tilde{\Omega})$-plane with $A = 100$ for a HJ orbiting a Sun-like star. The diagonal dashed line in each plot corresponds to corotation ($\tilde{\Omega} = \tilde{n}$). Top: MB spins the star down so that the planet finds itself inside corotation, where the sign of the tidal torque changes, and planet is subject to tidally induced orbital decay. For an initially high $\tilde{n}$ outside corotation tidal friction efficiently transfers angular momentum from spin to orbit, which pushes the planet outwards. Bottom: Solutions with the same initial conditions are plotted with and without MB for a HJ around a solar-type star, with dot-dashed lines having $A = 0$ and solid lines have $A = 100$. The dot-dashed lines are also curves of constant total angular momentum. This shows that the inclusion of MB is extremely important in determining the secular evolution of the system, and its absence results in a very different evolutionary history unless $\tilde{\Omega} \ll \tilde{n}$ in the initial state.

corotation, i.e. $i = 0$ and $\tilde{\Omega} = \tilde{n}$, where the orbital inclination (or stellar obliquity) i is defined by $\cos i = \hat{\mathbf{\Omega}}_1 \cdot \hat{\mathbf{h}}$ and $i \geq 0$. The system will approach this equilibrium if both the spin angular momentum is less than a quarter of the total angular momentum, and the total angular momentum exceeds some critical value (Greenberg 1974; Hut 1980). With no braking, orbits initially outside corotation ($\tilde{\Omega} > \tilde{n}$) are not subject to tidally induced orbital decay, and asymptotically approach a stable equilibrium $\tilde{\Omega} = \tilde{n}$, with $\tilde{n} \leq 3^{-\frac{3}{4}}$. Orbits initially inside corotation can evolve in two different ways, depending on the stability of the equilibrium state on the solution's closest approach to $\tilde{\Omega} = \tilde{n}$. If $\frac{d\tilde{\Omega}}{dt} > \frac{d\tilde{n}}{dt} > 0$ near corotation, then $\tilde{n} \leq 3^{-\frac{3}{4}}$, and the equilibrium state is locally stable (though no such curves are plotted in Fig. 2.2, since they occur only in the far bottom left of the plot, near the origin). This is when the corotation radius moves inwards faster than the orbit shrinks due to tidal friction, which can result in a final stable equilibrium state for the system if the corotation radius "catches up" with the planet. On the other hand, orbits inside corotation for which this condition is not satisfied are subject to tidally induced orbital decay, since tidally induced angular momentum exchange enhances the difference between $\tilde{\Omega}$ and $\tilde{n}$, which leads to further orbital evolution, and the spiralling in of the planet. This evolution can be seen from the dot-dashed lines in the bottom panel of Fig. 2.2.

Including MB ($A \neq 0$) means that $\tilde{\Omega} = \tilde{n}$ is no longer an equilibrium state, and the total angular momentum of the system is not conserved. For an orbit initially not subject to spiralling into the star via tidal transfer of angular momentum from orbit to spin ($\tilde{\Omega} \geq \tilde{n}$) we see from the top panel in Fig. 2.2, that MB will spin the star down so that the planet finds itself inside the corotation radius of the star. Passing through corotation changes the sign of the tidal torque and causes the planet to spiral into the star. Note that, if we ignore the age of the system, any bound orbit will eventually decay in a finite time since the system has no stable equilibrium. The effect of MB is to increase the minimum semi-major axis at which the orbit is not subject tidally induced orbital decay over the nuclear lifetime of the star.

This means that an initially rapidly rotating G-type star hosting a close-in Jupiter mass companion will lose significant spin angular momentum through MB (over a time $\sim \tau_{\rm mb}$). During this stage of spin-down the spin frequency of the star may temporarily

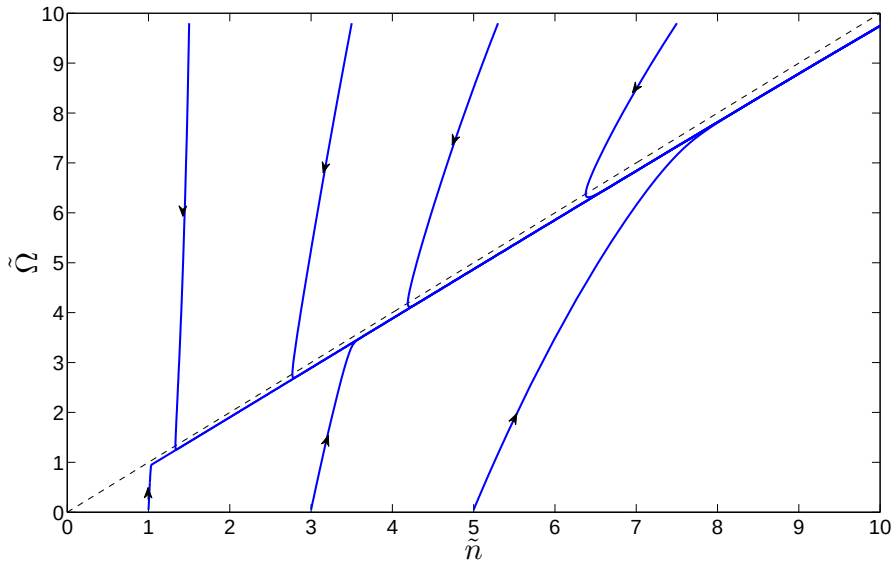

Figure 2.3: $(\tilde{n}, \tilde{\Omega})$-plane showing the effects of reducing the stellar mass fraction participating in angular momentum exchange (by a factor $\epsilon_\star = 10^{-2}$) with the orbit, while the braking rate is unchanged, with $A = 100$. This has been proposed to apply to F stars like τ Boo.

equal the orbital frequency of its close-in planet, but the rate of angular momentum loss through MB will exceed the tidal rate of transfer of angular momentum from orbit to spin. The stellar spin continues to drop well below synchronism until the efficiency of transfer of tidal angular momentum from orbit to spin can compensate or overcompensate for the braking. If $\frac{d\tilde{\Omega}}{d\tilde{t}} > \frac{d\tilde{n}}{d\tilde{t}} > 0$ inside corotation, then tides will act to spin up the star, though the timescale for this to cause significant spin-up may be much longer than the stellar lifetime, and this only occurs if the orbit has sufficient angular momentum to noticeably spin up the star. Otherwise, the planet continues to spiral inwards once it moves inside corotation, and $\tilde{\Omega} \simeq$ const.

So far we have considered the whole star to participate in tidal angular momentum exchange with the orbit. For an F-star (like τ Boo), it has been proposed that only the outer convective envelope (of mass fraction $\epsilon_\star$) participates in angular momentum exchange with the orbit (Marcy et al. 1997; Dobbs-Dixon et al. 2004; Donati et al. 2008). If the core and envelope of such a star can decouple, then tides would only have to spin up the outer layers of the star, which would reduce the spin-up time by $\epsilon_\star$. In

this case the system could remain in a state with $\tilde{\Omega} \simeq \tilde{n}$ just inside corotation, with the resulting torque on the orbit small. This may explain the spin-orbit synchronism of stars such as τ Boo, as noted by Dobbs-Dixon et al. (2004). Fig. 2.3 shows the phase plane for a simplified system in which the moment of inertia of the star acted on by tides is reduced by a factor $\epsilon_\star = 10^{-2}$, but the braking rate is unchanged, i.e., we multiply the first term on the right-hand side of Eq. 2.3.1 by $\epsilon_\star^{-1}$. Note that this may be too simple a model to describe such core-envelope decoupling, and we have ignored associated changes to the braking rate.

2.3.2 Extending the analysis to eccentric coplanar orbits

We can extend the simplified system in §2.3.1 to arbitrary eccentricity. If the orbit is eccentric but still coplanar, then we have three coupled nonlinear ODEs:

$$\frac{de}{d\tilde{t}} = 9e\,\tilde{n}^{\frac{13}{3}}\left[\frac{11}{18}\frac{\tilde{\Omega}_1}{\tilde{n}}f_2(e^2) - f_1(e^2)\right] \tag{2.3.9}$$

$$\frac{d\tilde{\Omega}}{d\tilde{t}} = \tilde{n}^4\left[f_4(e^2) - \frac{\tilde{\Omega}}{2\tilde{n}}\left(f_3(e^2) + f_6(e^2)\right)\right] - A\,\tilde{\Omega}^3 \tag{2.3.10}$$

$$\frac{d\tilde{n}}{d\tilde{t}} = 3\tilde{n}^{\frac{16}{3}}\left[f_4(e^2) - \frac{\tilde{\Omega}}{\tilde{2}n}\left(f_3(e^2) + f_6(e^2)\right)\right] \tag{2.3.11}$$

The polynomials in e^2 are as before, and we have used the dimensionless quantities defined in §2.3.1.

The solutions to these equations in the absence of MB have been studied in Hut (1981), so we move on to analyse the effects of MB. Fig. 2.4 we plot the phase plane for $A = 100$ with $e = 0.2$ initially (top), and $A = 10$ with $e = 0.6$ initially (bottom) to represent cases of moderate and highly eccentric orbits. A smaller value of A is chosen in order to show the effects of tides more clearly, since reducing A is equivalent to reducing Q'. Tidal effects become more important for smaller $\tilde{n}$ as e is increased since this reduces the pericentre distance $r_p = a(1-e)$. This is shown in Fig. 2.4. The evolution is otherwise similar to that for a circular orbit. Eq. 2.3.9 exhibits the eccentricity instability, where e is excited if $\tilde{\Omega} \geq \frac{18}{11}\frac{f_1(e^2)}{f_2(e^2)}\tilde{n}$. The evolution of e is not plotted, and will in general be different for different curves, but is found to decay once $\tilde{\Omega} < \frac{18}{11}\frac{f_1(e^2)}{f_2(e^2)}\tilde{n}$.

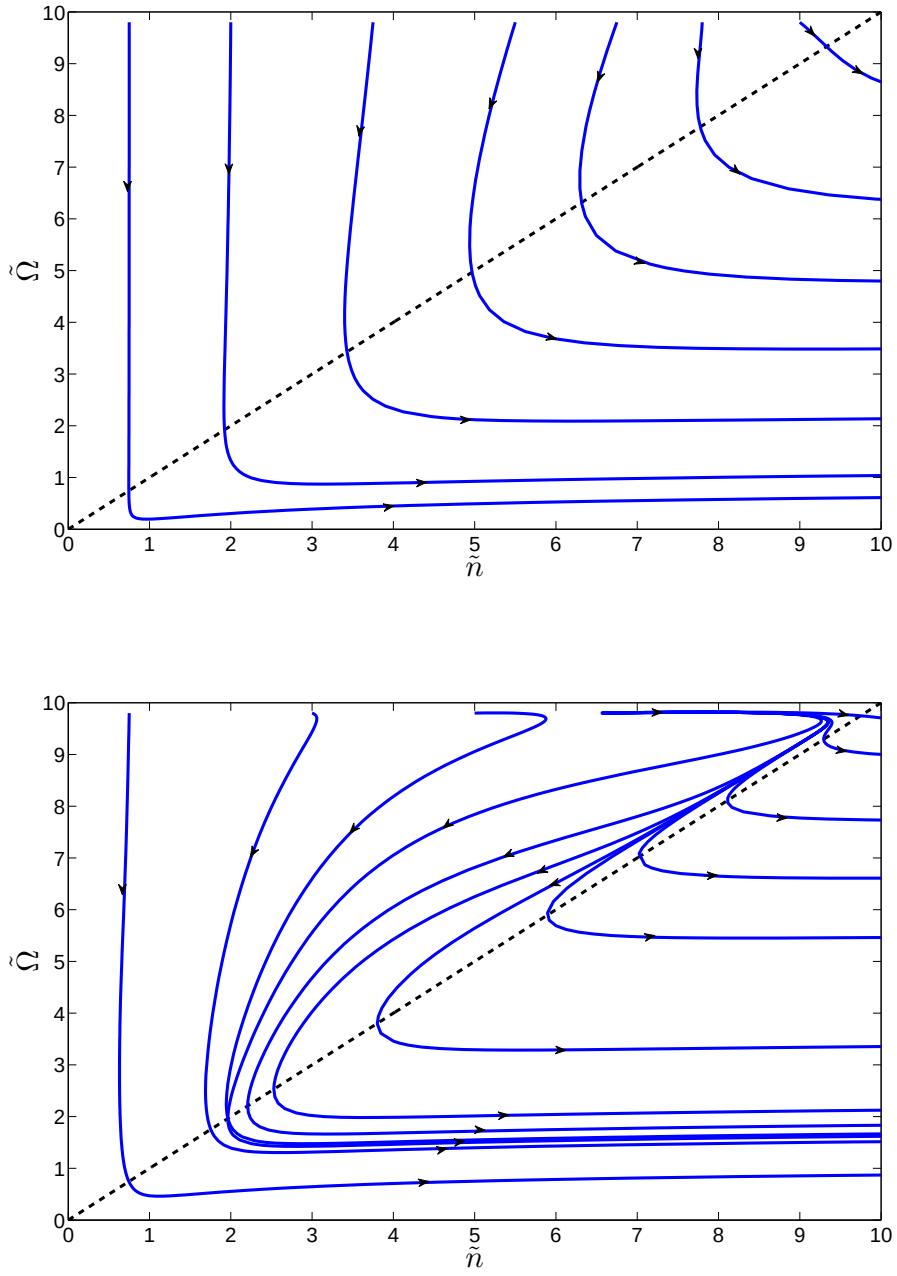

Figure 2.4: Top: $(\tilde{n}, \tilde{\Omega})$-plane with $A = 100$ and $e = 0.2$ initially, where the dashed line corresponds to $\tilde{\Omega} = \tilde{n}$. This is qualitatively similar to Fig. 2.2, showing that moderate eccentricity does not affect the evolution significantly. This is partly due to the decay of the eccentricity after the star has spun down so that $\tilde{\Omega} \leq \frac{18}{11}\frac{f_1(e^2)}{f_2(e^2)}\tilde{n}$. Bottom: $(\tilde{n}, \tilde{\Omega})$-plane with $A = 10$ and $e = 0.6$ initially. This differs from the top panel since the eccentricity remains appreciably nonzero until after corotation is passed (eccentricity evolution not shown). Finite eccentricity increases the slope of $\frac{d\tilde{n}}{dt}$ over the circular case, since tidal friction becomes much more important with decreasing pericentre distance. In addition, the eccentricity is excited when $\tilde{\Omega} \geq \frac{18}{11}\frac{f_1(e^2)}{f_2(e^2)}\tilde{n}$.

2.3.3 Extending the analysis to inclined circular orbits

We can extend the simplified system of equations analysed in §2.3.1 to arbitrary inclination (i) of the orbital plane with respect to the equatorial plane of star:

$$\frac{d\tilde{\Omega}}{d\tilde{t}} = \tilde{n}^4 \left[\cos i - \frac{\tilde{\Omega}}{2\tilde{n}}\left(1+\cos^2 i\right)\right] - A\,\tilde{\Omega}^3, \tag{2.3.12}$$

$$\frac{d\tilde{n}}{d\tilde{t}} = 3\,\tilde{n}^{\frac{16}{3}}\left[1 - \frac{\tilde{\Omega}}{\tilde{n}}\cos i\right], \tag{2.3.13}$$

$$\frac{di}{d\tilde{t}} = -\tilde{n}^4\tilde{\Omega}^{-1}\sin i\left[1 - \frac{\tilde{\Omega}}{2\tilde{n}}\left(\cos i - \tilde{n}^{\frac{1}{3}}\tilde{\Omega}\right)\right], \tag{2.3.14}$$

For small inclination, Eq. 2.3.14 reproduces Eq. 13 from Hut (1981), with the exception that we have used a constant Q_1' rather than a constant time-lag in the equations (i.e., replace time lag τ by $\frac{1}{2}\frac{3}{2k_1 n Q_1'}$, and note that k_1 is twice the apsidal motion constant of the star).

From Eq. 2.3.13 the orbit begins to decay if

$$\tilde{\Omega}\cos i < \tilde{n}, \tag{2.3.15}$$

which is always satisfied for a retrograde orbit ($i \geq 90^\circ$). This is just a generalisation of the corotation condition $\tilde{\Omega} = \tilde{n}$, to a non-coplanar orbit. The inclination grows if

$$\tilde{\Omega} > \tilde{\Omega}_{crit} = 2\tilde{n}\left(\cos i - \tilde{n}^{\frac{1}{3}}\tilde{\Omega}\right)^{-1}, \tag{2.3.16}$$

where we have assumed the quantity in brackets is positive, i.e., $\cos i > \tilde{n}^{\frac{1}{3}}\tilde{\Omega}$. This agrees with the condition from Hut (1981) when $i \sim 0$. For sufficiently close-in orbits that tidal friction is important, MB will rapidly spin down the star such that this condition is not satisfied, so we can safely conclude that the inclination is not likely to grow appreciably by tidal friction. When this condition is not satisfied, the inclination decays to zero, on a timescale τ_i (defined in the next section). Note that $i = 180^\circ$ is an unstable equilibrium value of the inclination.

In the absence of MB we recover the evolution considered by Greenberg (1974), so we move on to concentrate on the inclusion of MB. The top panel in Fig. 2.5 plots the $(\tilde{n}, \tilde{\Omega})$-plane for $A = 10$ for an initial inclination of $i = 90^\circ$. The evolution of i

is not plotted (and will in general be different for each curve), but is found to decay once the stellar spin decays sufficiently that Eq. 2.3.16 is not satisfied. The bottom panel in Fig. 2.5 shows the effect of increasing the inclination in steps to illustrate the behaviour as i is increased, on various curves with otherwise the same initial conditions, with $A = 10$. The orbit begins to decay for smaller $\tilde{n}$, and decays at a faster rate as i is increased. This peaks for a perfectly retrograde orbit ($i = 180°$), with anti-parallel spin and orbit, where the rates of change of spin and orbital angular frequencies are maximum. Fig. 2.5 shows that the orbit generally begins to decay outside corotation, once $\tilde{\Omega}\cos i < \tilde{n}$. This has implications for the tidal evolution of close-in planets on inclined orbits, in that if this condition is satisfied, the planet will be undergoing tidally induced orbital decay – though the inspiral time may be longer than the expected stellar lifetime, depending on the value of Q'_1.

In this section we have seen that MB can only be reasonably neglected for a coplanar orbit when $\Omega \ll n$. For an inclined orbit, this condition must be generalised to $\Omega\cos i \ll n$ – obvious from Eq. 2.3.13. Neglecting $\dot{\omega}_{\rm mb}$ for stars for which this condition is not satisfied can result in a qualitatively different evolution, as already seen in the bottom panel of Fig. 2.2 for a coplanar orbit.

2.4 Tidal evolution timescales

It is common practice to interpret the effects of tidal evolution in terms of simple timescale estimates. The idea behind these is that if the rate of change of a quantity X is exponential, then $\dot{X}/X$ will be a constant, so we can define a timescale $\tau_X = X/\dot{X}$. If $\dot{X}/X \neq$ const, then these may not accurately represent the evolution. Here we reproduce the timescales that can be derived from the equations in §2.1.

A tidal inspiral time can be calculated from the equation for $\dot{a}$, by considering only the effects of the tide raised on the star by the planet (not unreasonable since $I_2 \ll I_1 \sim m_2 a^2$). Here $\dot{a}/a \sim a^{-13/2} \neq$ const, so a more accurate estimate of the inspiral time for a circular coplanar orbit is

$$\tau_a \equiv -\frac{2}{13}\frac{a}{\dot{a}} \tag{2.4.1}$$

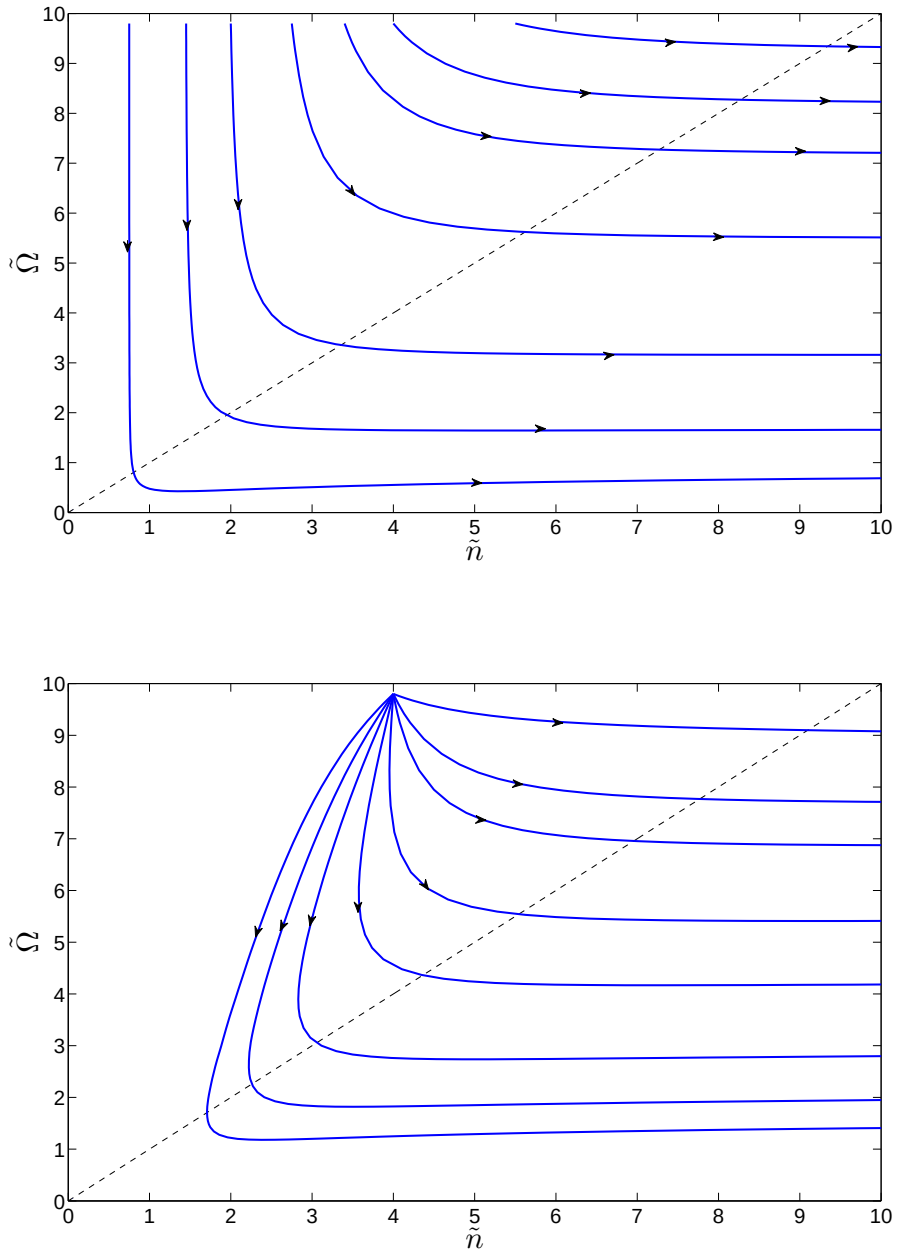

Figure 2.5: Top: $(\tilde{n}, \tilde{\Omega})$-plane for an orbit with an initial $i = 90°$, with $A = 10$, where the dashed line corresponds to $\tilde{\Omega} = \tilde{n}$. This is similar to Fig. 2.2, except that the orbit decays once $\tilde{\Omega} \cos i < \tilde{n}$, which can occur above the dashed line, in contrast with the circular case. The evolution of i is not plotted, and is in general different for each curve, but is found to decay once the stellar spin drops below that given by Eq. 2.3.16. Bottom: various initial inclinations, with $A = 10$, where the dashed line corresponds to $\tilde{\Omega} = \tilde{n}$. The bottom trajectory has $i = 0$, and the inclination is increased in steps towards the top curve, which has $i = 180°$, to illustrate the behaviour. Note that orbits with larger initial i decay for smaller $\tilde{n}$, once $\tilde{\Omega} \cos i < \tilde{n}$ is satisfied.

$$\simeq \quad 12 \text{ Myr} \left(\frac{Q_1'}{10^6}\right) \left(\frac{m_1}{M_\odot}\right)^{\frac{8}{3}} \left(\frac{M_J}{m_2}\right) \left(\frac{R_\odot}{R_1}\right)^5 \left(\frac{P}{1\text{d}}\right)^{\frac{13}{3}} \left(1-\frac{P}{P_\star}\right)^{-1}, \quad (2.4.2)$$

Here P and $P_\star$ are the orbital and stellar spin periods, respectively. We have already seen in §2.3 that it is unreasonable to assume that Ω is fixed unless $\Omega \ll n$, due to MB.

If the orbit is inside corotation, angular momentum will be transferred from the orbit to the spin of the star, giving a tidal spin-up time of

$$\tau_{\Omega_1} \equiv -\frac{\Omega_1}{\dot{\Omega}_1} \simeq \frac{13\tau_a}{2\,\alpha}, \quad (2.4.3)$$

where $\alpha = \frac{\mu h}{I\Omega}$ is the ratio of orbital to spin angular momentum. For the HJ problem, $\tau_{\Omega_1} \geq \tau_a$ since $\alpha = O(1)$, though this neglects the spin-down effects of MB. The planetary spin Ω_2 will tend to synchronise much faster, since the moment of inertia of the planet is much less than that of the orbit (by $\sim 10^5$), and will not be considered further, i.e., we assume $\Omega_2 = n$.

A circularisation time can be derived from the equation for $\dot{\mathbf{e}}$, and is given for a coplanar orbit by

$$\tau_e \equiv -\frac{e}{\dot{e}} \quad (2.4.4)$$

$$\simeq 17 \text{ Myr} \left(\frac{Q_1'}{10^6}\right) \left(\frac{m_1}{M_\odot}\right)^{\frac{8}{3}} \left(\frac{M_J}{m_2}\right) \left(\frac{R_\odot}{R_1}\right)^5 \left(\frac{P}{1\text{d}}\right)^{\frac{13}{3}}$$
$$\times \left[\left(f_1(e^2) - \frac{11}{18}\frac{P}{P_\star} f_2(e^2)\right) + \beta\left(f_1(e^2) - \frac{11}{18} f_2(e^2)\right)\right]^{-1}, \quad (2.4.5)$$

where we have included both the stellar and planetary tides, as these have been shown to both contribute to the tidal evolution of e (Jackson et al., 2008). Note that $\dot{e}/e \sim$ const only if $P \sim$ const and $e \ll 1$, where $f_{1,2}(e^2) \simeq 1$. The factor

$$\beta = \frac{Q_2'}{Q_1'}\left(\frac{m_1}{m_2}\right)^2 \left(\frac{R_2}{R_1}\right)^5 \sim 10\frac{Q_2'}{Q_1'}, \quad (2.4.6)$$

for the HJ problem.

If the orbital and stellar equatorial planes are misaligned, then dissipation of the

tide raised on the star by the planet would align them on a timescale

$$\tau_i \equiv -\frac{i}{\frac{di}{dt}} \tag{2.4.7}$$

$$\simeq 70 \text{ Myr} \left(\frac{Q'_1}{10^6}\right)\left(\frac{m_1}{M_\odot}\right)\left(\frac{M_J}{m_2}\right)^2\left(\frac{R_\odot}{R_1}\right)^3\left(\frac{P}{1\text{d}}\right)^4 \times \left(\frac{\Omega_1}{\Omega_0}\right)\left[1-\frac{P}{2P_\star}\left(1-\frac{1}{\alpha}\right)\right]^{-1}, \tag{2.4.8}$$

where we have assumed that the orbit is circular and made the small i approximation. We take $\Omega_0 = 5.8 \times 10^{-6}\text{s}^{-1}$, which corresponds to a spin period of ~ 12.5 d.

The validity of these timescales to accurately represent the tidal evolution of the orbital and rotational elements is an important subject of study, since these timescales are commonly applied to observed systems. In a recent paper, Jackson et al. (2008) found that it is essential to consider the coupled evolution of e and a in order to accurately model the tidal evolution, and that both the stellar and planetary tides must be considered. They showed that the actual change of e over time can be quite different from simple circularisation timescale considerations, due to the coupled evolution of a. In the following we will consider the validity of the spin-orbit alignment timescale to accurately model tidal evolution of i.

2.5 Numerical integrations of the full equations for an inclined orbit

We perform direct numerical integrations of the equations in §2.1 with a 4th/5th order Runge-Kutta scheme with adaptive stepsize control, using a scheme with Cash-Karp coefficients similar to that described in Press et al. (1992). Our principal aim is to study inclination evolution and to determine the accuracy of the spin-orbit alignment timescale τ_i for close-in planets.

We choose a "standard" system of a HJ in orbit around an FGK star. We have $m_1 = M_\odot, m_2 = M_J, R_1 = R_\odot, R_2 = R_J$, and we modify[1] a, i, e. We choose the initial ratio $\Omega_1/n = 10$, and include MB in all simulations, setting $\gamma = 1$ unless stated

[1]We take $\mathbf{\Omega}_1 \cdot \mathbf{e} = 0$, though this need not be assumed. We find negligible difference between integrations for which $\mathbf{\Omega}_1 \cdot \mathbf{e} = 0$ and $\mathbf{\Omega}_1 \cdot \mathbf{e} \neq 0$

otherwise. We also take $Q'_1 = Q'_2 = 10^6$, and $\Omega_2/n = 1$. The dimensionless radii of gyration are chosen to be $r_{g1}^2 = 0.076$ and $r_{g2}^2 = 0.261$, which are values appropriate for polytropic stellar and planetary models with respective indices 3 and 1.

2.5.1 Inclusion of MB and the importance of coupled evolution of a and i

For a prograde orbit ($i < 90°$) initially outside corotation, MB rapidly spins the star down sufficiently to ensure that inclination is not excited through tidal friction (so that Eq. 2.3.16 is not satisfied), and the inclination begins to decay. Subsequent spin-down moves the orbit-projected corotation radius beyond the orbit of the planet (so that $\Omega \cos i < n$), and the resulting tidal inspiral accelerates as the difference between $\Omega \cos i$ and n is enhanced. The associated reduction in a increases the rate of stellar spin-orbit alignment. Thus the inclusion of $\dot{\omega}_{\rm mb}$ increases the rate of alignment, and reduces τ_i from the simple estimate, which ignores MB and coupled a and i evolution.

The effect of MB on a retrograde orbit ($i \geq 90°$) is qualitatively different. A retrograde orbit is always subject to tidally induced inspiral since $\Omega \cos i < n$ for all $i \geq 90°$. MB acts to reduce Ω, thereby reducing the difference $|\Omega \cos i - n|$, making the tidal torque smaller. This acts to *increase* the timescale for alignment of the stellar spin and orbit, though the effect is found to be small.

The most important effect of including MB is simply that of reducing the stellar spin sufficiently so that $\Omega \cos i < n$, where the semi-major axis can then decay through tidal friction. As a subsequently decreases, the tidal torque increases, resulting in a faster tidal evolution. MB can only be neglected if $|\Omega \cos i| \ll n$. If the orbit is already highly inclined, such as $i \geq 90°$, then the inclusion of MB is not so important, since $\Omega \cos i < n$ regardless of the spin rate.

For an orbit initially at $a = 0.05$ AU, the simple estimate of the stellar spin-orbit alignment timescale gives $\tau_i \simeq 2 \times 10^{10}$ yrs. Fig. 2.6 shows the evolution of i and a for various initial inclinations for an orbit at $a = 0.05$ AU and $a = 0.08$ AU respectively. The outer orbit a changes only slightly over 10 Gyr, and i evolves as expected from the simple estimate of $\tau_i \simeq 3 \times 10^{11}$ yrs. The inner orbit, on the other hand, is subject to tidally induced orbital decay, with an inspiral time of $1 - 3$ Gyr, and this reduction

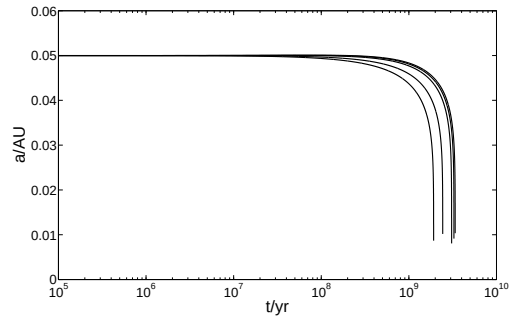

(a) a evolution for $a = 0.05$ AU

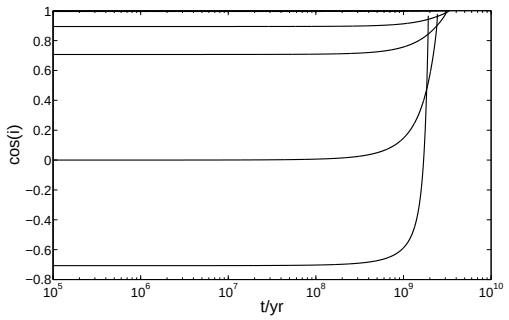

(b) $\cos i$ evolution for $a = 0.05$ AU

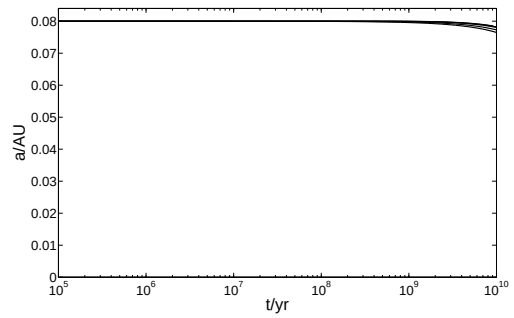

(c) a evolution $a = 0.08$ AU

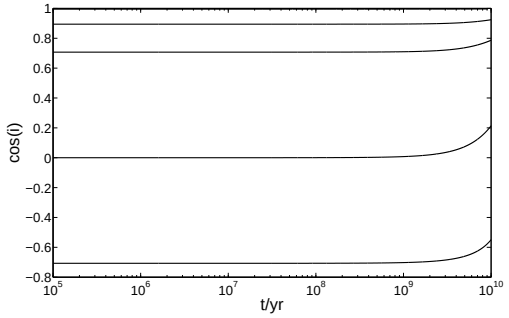

(d) $\cos i$ evolution $a = 0.08$ AU

Figure 2.6: Tidal evolution for a circular, inclined orbit at $a = 0.05$ AU and $a = 0.08$ AU, with various initial inclinations: $i = 6°, 26°, 45°, 90°, 180°$. (a) and (c) show their respective semi-major axis evolutions (with the highest inclination orbit decaying first – the bottom curve – and the lowest inclination orbit decaying last – the top curve), and (b) and (d) show the respective inclination evolution for these systems. The outer orbit a changes only slightly over 10 Gyr, and i evolves as expected from simple estimates of τ_i. The inner orbit, on the other hand, is tidally shrunk, and this reduction in a means that the true evolution is much faster than the simple timescale estimates predict. This highlights the importance of considering coupled evolution of a and i.

in a increases the rate of inclination evolution. This highlights the importance of considering coupled evolution of a and i, especially for large initial inclinations, where inspiral occurs for higher stellar spin rates. The difference between the simple estimate of τ_i and the true timescale can be up to an order of magnitude different for orbits whose a changes appreciably.

2.5.2 Inclined and eccentric orbits

Jackson et al. (2008) highlighted the importance of coupled a and e evolution for a coplanar orbit. We will now consider how e might affect i evolution for a non-coplanar orbit, which is the subject of this section.

A nonzero eccentricity reduces the pericentre distance $r_p = a(1-e)$, which increases the tidal torque over a circular orbit, since the tidal torque $\sim r^{-6}$. Although the planet spends less time near pericentre, the torque there is much greater, so dominates the orbit-averaged torque. We therefore expect the stellar spin-orbit alignment time to be reduced as we increase e. In addition, we expect that an orbit at large e would more strongly affect the rate of alignment over a circular orbit, than one at large i would over a coplanar orbit, because e reduces r_p, whereas i only changes the difference $(\Omega \cos i - n)$. The tidal torque $\sim r^{-6}(\Omega \cos i - n)$, which depends more strongly on r than Ω. This behaviour can be seen in Figs. 2.6(d) and 2.7(b) which shows that the ratios of stellar spin-orbit alignment times for an orbit with small i and large i is $\sim O(1)$, whereas the ratios of stellar spin-orbit alignment times for an orbit with small e and large e can be up to several orders of magnitude.

From Fig. 2.7 we can compare the simple estimate of $\tau_i \simeq 3.0 \times 10^{11}$ yrs for an orbit at $a = 0.08$ AU, with the coupled evolution of the orbital and rotational elements from integration of the full equations. We see that the simple estimate gives a misleadingly long stellar spin-orbit alignment time compared with that obtained from integrating the full equations in cases where e is initially non-negligible – as a result of the strong functions of the eccentricity in this model of tidal friction. This confirms the conclusion of Jackson et al. (2008), in that it is essential to consider coupled evolution of a and e in order to determine an accurate system history. We also find that the associated changes in semi-major axis strongly affect stellar spin-orbit alignment. A

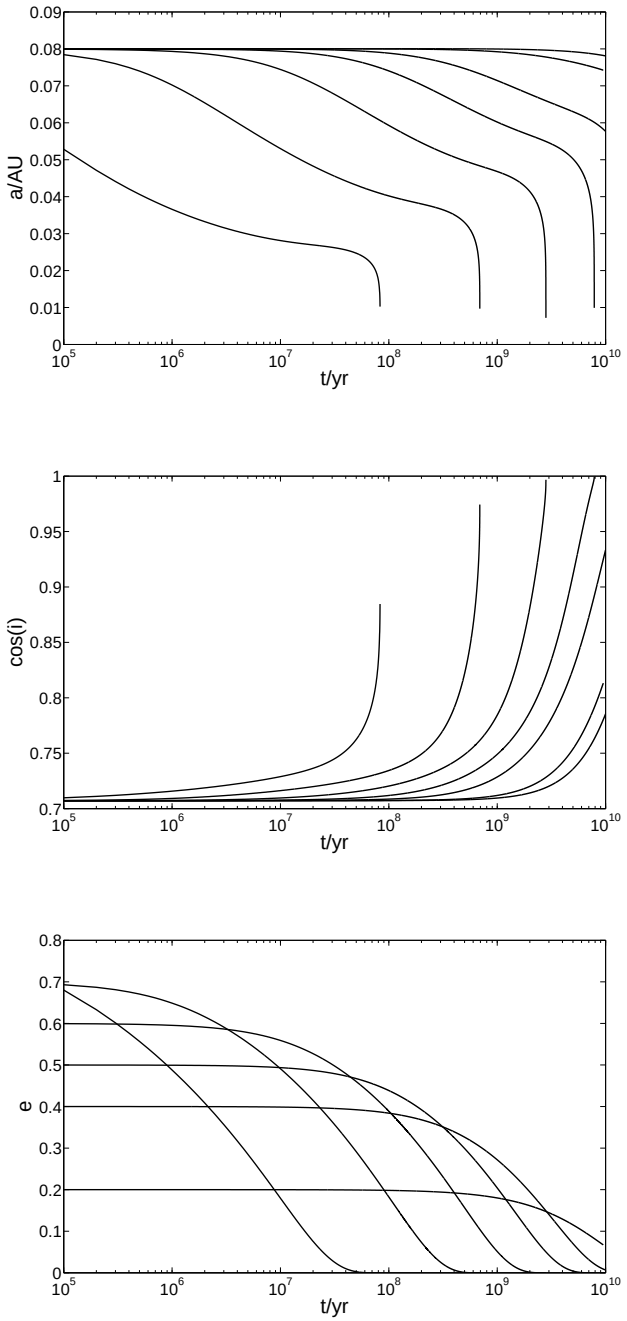

Figure 2.7: Top: Semi-major axis evolution for an inclined orbit with initial $i = 45°$ at $a = 0.08$ AU for various initial e, with $e = 0, 0.2, 0.4, 0.5, 0.6, 0.7, 0.8$. Middle and bottom: Inclination and eccentricity evolution for the same systems. Solutions with the smallest initial e have the smallest change in a and i. Solutions with the largest initial e undergo much more rapid tidal evolution (note that for $e = 0.8$, e decays to less than 0.7 within 10^5 yrs) – curves can be distinguished by noting that the curves corresponding to the fastest evolution have the largest initial e. Increasing the eccentricity can be seen to reduce the inspiral time by up to several orders of magnitude over the circular case. In contrast, increasing the inclination in Fig. 2.6 only reduces the inspiral time by a factor $\sim O(1)$ over a coplanar orbit. Also note that $\tau_e < \tau_i$ for all integrations.

marginally better estimate for τ_i can be made by replacing the orbital period with the orbital period around periastron (equivalent to replacing a by r_p), though this is still inadequate since it neglects evolution of a.

2.5.3 Discussion

For typical HJs, we find that the stellar spin-orbit alignment time is comparable to the inspiral time, i.e. $\tau_i \sim \tau_a$. This means that if we observe a planet, then its survival implies that tides are unlikely to have aligned its orbit. For planets on an accelerating inspiral into the star, the rate of inclination evolution will have been much lower in the past. Therefore if we observe a planet well inside corotation ($\Omega \cos i < n$), with a roughly coplanar orbit, we can assume that it must have started off similarly coplanar – unless we are lucky enough to be observing a planet on its final rapid inspiral into the star after it has undergone most of the evolution, where it is now in a very short-period orbit, close to being consumed.

We expect $\tau_i \sim \tau_a$ when $\alpha \ll 1$ – which is true for close-in terrestrial planets – since $\mathbf{\Omega}$ can be considered fixed, with the inclination changing only due to changes in $\mathbf{h}$. For typical values of $\alpha = O(1)$ for HJs, the inclination changes due to rotations of both $\mathbf{\Omega}$ and $\mathbf{h}$, so the timescales are not exactly the same, but would be expected to be of the same order of magnitude.

Hut (1981) showed by considering only the tide in the star, that the stellar spin-orbit alignment timescale is longer than the circularisation timescale ($\tau_i > \tau_e$) unless $\alpha > 6$. This was based on exponential decay estimates for small e and i, but nevertheless holds for the systems integrated in this work, as can be seen from Fig. 2.7. This makes intuitive sense, since $\alpha = O(1)$ means that spin angular momentum is important, and circularisation involves only a property of the orbit, whereas alignment involves both the spin and the orbit. For typical HJs $\alpha < 6$; we therefore expect $\tau_e < \tau_i$, especially when the eccentricity damping effect of the tide in the planet is taken into account, which further enhances this inequality. The tide in the planet is completely negligible in changing the stellar obliquity since $I_2 \ll I_1 \sim m_2 a^2$.

This means that if an orbit is initially inclined and eccentric as a result of planet-planet scattering or Kozai migration into a short-period orbit, we would expect the

orbit to become circular before it aligns with the spin of the star. We should therefore observe fewer eccentric orbits than inclined orbits, *if those systems start with a uniform distribution in e, i–space*. This also means that if we observe a close-in planet on a circular orbit with non-zero i, we cannot rule out a non-negligible eccentricity in the past.

2.6 Application to an observed system: an explanation for the misaligned spin and orbit of XO-3 b

The first system observed with a spin-orbit misalignment was XO-3 (Hébrard et al. 2008; Winn et al. 2009), which has a sky-projected spin-orbit misalignment angle of $\lambda = 37.3^\circ \pm 3.7^\circ$ (after being revised down from $\lambda \simeq 70^\circ$). This system has a very massive $m_2 = 12.5\,M_J$ planet on a moderately eccentric $e = 0.29$, $P = 3.2$ d orbit around an F-type star of mass $m_1 = 1.3\,M_\odot$. Its age is estimated to be $\tau_\star \simeq (2.4 - 3.1)$ Gyr. Note that even if the star is rotating near breakup velocity ($P_\star \sim 1$ d), the planet is still subject to tidal inspiral, since $P_\star > P\cos i$ (where we henceforth assume $i = \lambda$, which may slightly *underestimate* i). If we assume that the angle of inclination of the stellar equator to the plane of the sky is $\sim 90^\circ$, then $P_\star = 3.3$ d $\sim P$, i.e., $\Omega \sim n$.

Hébrard et al. (2008) quote a stellar spin-orbit alignment timescale of $\sim 10^{12}$ yr for this system, but we find that this is in error by $\sim 10^5$. We believe that the reason for this discrepancy is that their estimate was based on assuming that the spin-orbit alignment time for XO-3 b is the same as for HD17156 b (Narita et al. 2008; Cochran et al. 2008), which is a less massive planet on a much wider orbit. We find $\tau_i \sim 30$ Myr (using the expression in §2.4) assuming $Q'_1 = 10^6$ to align the whole star with the orbit. Circularisation time of $\tau_e \sim 10$ Myr and the inspiral time is estimated to be $\tau_a \sim 16$ Myr from simple estimates.

Integrations for this system are given in Fig. 2.8 for a variety of stellar and planetary Q' values. These integrations again highlight the importance of considering coupled evolution of the orbital and rotational elements, since timescales for tidal evolution can be quite different from the simple estimates. Indeed, the actual spin-orbit alignment

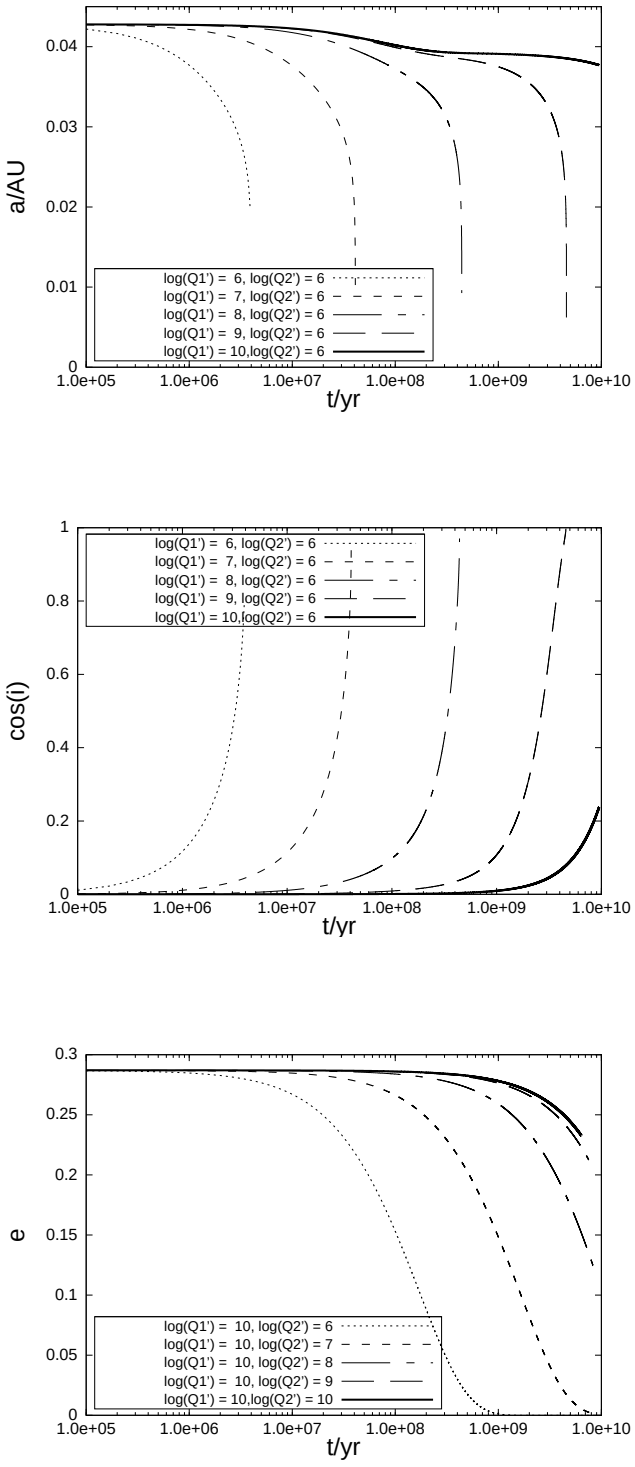

Figure 2.8: Tidal evolution of XO-3 b taking current values for the orbital properties of the system, except that $i = 90°$. MB is included with $\gamma = 0.1$, and $\Omega_1/n = 2$ initially (results do not depend strongly on this choice). From the top and middle plots we require $Q'_1 \geq 10^{10}$ for the planet to survive for several Gyr, and maintain its high inclination. From the bottom plot we see that if $Q'_1 \geq 10^{10}$, we require $Q'_2 \geq 10^8$ to maintain the current eccentricity for a few Gyr. Tidal dissipation in both the planet and star must therefore be weak to explain the current configuration of the system.

time from integrating the full set of equations is about an order of magnitude smaller than that from the simple decay estimate, due to the semi-major axis evolution. We choose an initial $i = 90°$ to make the evolution clearer (this is not unreasonable since λ, in any case, gives a lower bound on i, and the results do not depend strongly on the non-zero value of i).

For the cases considered, the system can only survive and remain with its current inclination for ~ 3 Gyr if $Q'_1 \geq 10^{10}$. An explanation for the survival and remnant orbital inclination of XO-3 b could therefore be the inefficiency of tidal dissipation in the host star. The host star is an F-star of mass $m_1 = 1.3 \pm 0.2 M_\odot$, so it will contain a small convective core and a very thin outer convection zone (OCZ) separated by a RZ. Dissipation in the convective core will only weakly affect the tide, and dissipation in the RZ will also be weak (Zahn, 2008). This is because internal inertia-gravity waves excited at the interface between convective and radiative regions cannot reach the photosphere, where they can damp efficiently, as supposed for high-mass stars. In addition, nonlinear effects due to geometrical concentration of the waves near the centre of the star (studied in detail in Part II) cannot occur because the waves will reflect from the outer boundary of the inner convection zone well before they become nonlinear.

We expect that most dissipation occurs in the OCZ of the star. A calculation of Q' for the dissipation of the equilibrium tide and inertial modes, in the thin OCZ, using a stellar model[2] appropriate for this star (note that the metallicity of the star is subsolar, with $Z \sim 0.01$), was performed (see OL04 for details of the numerical method). It must be noted that these calculations involve uncertainties regarding the effective viscosity of turbulent convection, though the general trends in the results below (and those discussed in §5.7) are likely to be quite robust. The results for the $m = 0, 1, 2$ components of the tide are plotted in Fig. 2.9. In Appendix A.3, we show that a combination of the $m = 0, 1, 2$ components of the tide are relevant for spin-orbit alignment and inspiral for an inclined orbit, and so we must calculate Q' for all components of the $l = 2$ (quadrupolar) tide. The relevant tidal frequencies, assuming $\Omega \sim n$ currently, would be those of integer $\hat{\omega}/\Omega$. However, since the angle of inclination of the stellar equatorial plane to the plane of the sky has not been

[2]for which we use EZ Web at http://shayol.bartol.udel.edu/∼rhdt/ezweb/

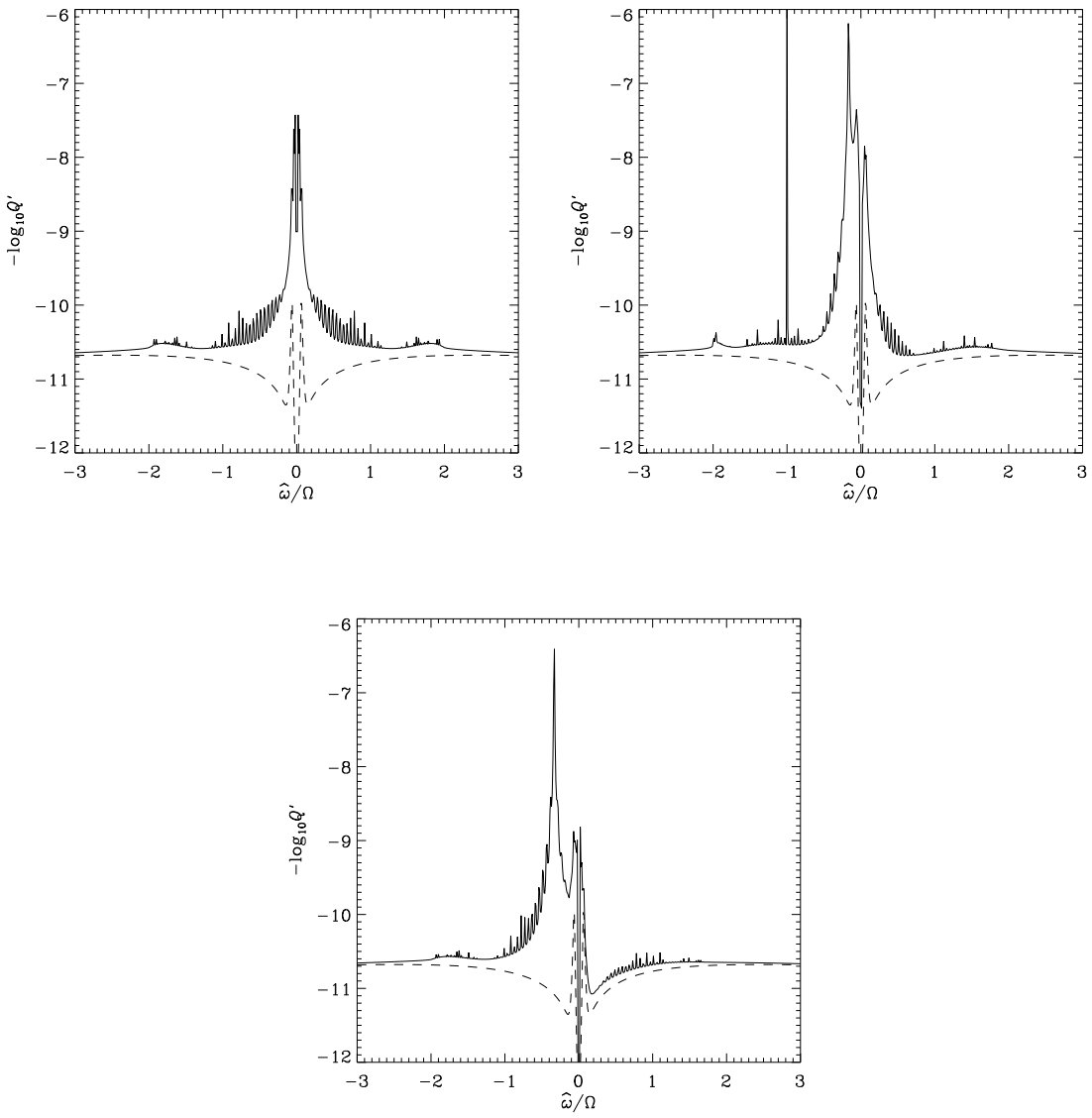

Figure 2.9: Q' as a function of the ratio of tidal frequency to spin frequency $\hat{\omega}/\Omega$, from dissipation of the $l = 2$, $m = 0$, 1, 2 components respectively, of the equilibrium tide and dissipation of inertial modes in the OCZ of an F-type star (see OL07 for details of this calculation). This used a stellar model appropriate for XO-3 to model the convection zone. The dashed lines represent the effect of omitting the Coriolis force, and therefore inhibiting inertial waves. The prominent features in each figure (which occur for $\hat{\omega}/\Omega = -1$ and $-1/6$ for $m = 1$ and $\hat{\omega}/\Omega = -1/3$ for $m = 2$) are Rossby wave resonances, which probably occur for tidal frequencies not relevant for the XO-3 system. For most tidal frequencies $Q' \geq 10^{10}$, which could explain the survival and remnant orbital inclination of XO-3 b.

determined, the relevant tidal frequencies cannot be calculated with any certainty. Nevertheless, $Q' \geq 10^{10}$ for most tidal frequencies for the host star XO-3. This can explain the survival and remnant inclination of XO-3 b, since both τ_a and τ_i would be longer than the age of the system.

In addition, the remnant eccentricity could be maintained due to weak damping of the tide in the star for the same reasons. However, we must also explain the inefficient damping of the tide in the planet, if indeed the reason for the eccentricity is that $\tau_e > \tau_\star$. The planet in this system is massive, and may be a low-mass brown dwarf. If it formed without a core, then the dissipation of inertial modes may be reduced if they are able to form global modes, as found in OL04.

2.7 Conclusions

In this chapter we have investigated the long-term tidal evolution of HJs in a simple model of tidal friction. We have studied the effects of MB on tidal evolution in a simplified system, and then performed numerical integrations for a variety of HJ systems, with particular emphasis on inclination evolution. We now summarise the main results of this work.

MB moves the corotation radius of the star outwards such that any close-in planets will eventually orbit inside corotation ($\Omega \cos i < n$), and be subject to orbital decay due to tides. MB is found to be important for the tidal evolution of HJs unless $\Omega \cos i \ll n$, in which case the orbit is already well inside the orbit-projected corotation radius. MB is particularly important when it comes to interpreting the tidal evolution of observed systems from formation to the present day, since the star may have been rotating much more rapidly in the past. Nevertheless, it is probably not a bad approximation to neglect MB for calculating the *future* tidal evolution of most observed HJs, if the star has already spun down so that $\Omega \ll n$.

Combining our results with Jackson et al. (2008), we find that coupled evolution of the orbital and rotational elements is essential to accurately model tidal evolution. This is especially true for highly eccentric orbits.

We find that the timescale for stellar spin-orbit alignment is comparable to the inspiral time for HJs, therefore the orbits of most close-in planets have probably not

aligned with the spin of the star. Observed inclinations are likely to be a relic of the migration process. This means that RM observations of transiting planets can potentially distinguish between migration caused by planet-planet scattering or Kozai oscillations combined with tidal dissipation in the star, and that produced by tidal interaction with the gas disc. If the majority of candidates are found with $\lambda \sim 0$, this strongly disfavours planet-planet scattering or Kozai migration, since they are expected to produce significantly inclined orbits, and we have found that tides are unlikely to have aligned orbits without causing inspiral. Alternatively, if systems are found with significantly nonzero λ, then some planet-planet scattering or Kozai migration could have occurred to produce these orbital inclinations.

The population of planets whose spin-orbit alignments have been observed with the RM effect can be statistically analysed to give a distribution of i for HJs (Fabrycky & Winn, 2009). Collecting all RM observations together, this indicates the surprising result that most HJs appear to be misaligned, possessing a wide variety of spin-orbit angles (Triaud et al., 2010). This distribution of i appears consistent with that predicted by the process of Kozai cycles with tidal friction (Fabrycky & Tremaine, 2007) (see §1.2). Together with our result that the spin-orbit angle is not likely to change appreciably over the lifetime of the system due to tides, *if future observations can confirm this i distribution*, then it would indicate that Kozai migration may indeed be an important formation mechanism of HJs. However, it is unlikely to work in all cases. These observations do appear to disfavour disk migration as the sole mechanism for producing HJs.

For most HJs, tides tend to circularise the planet's orbit before spin-orbit alignment or inspiral occurs. Therefore, if we observe a planet on an inclined, circular orbit, we cannot rule out a non-negligible eccentricity in the past. This means that we should observe fewer eccentric orbits than inclined orbits *if those systems start with a uniform distribution of points in (e, i)-space*, due to tidal friction. This should be considered when comparing the observed (e, i) distribution with those predicted from theoretical work on Kozai migration or planet-planet scattering, before we can further constrain these theories (Fabrycky & Tremaine 2007; Jurić & Tremaine 2008).

The misaligned spin and orbit of the XO-3 system could potentially be explained

in terms of inefficient tidal dissipation inside the host star. The required stellar $Q'_1 \gtrsim 10^{10}$ required for the survival and remnant misalignment is predicted from theoretical calculations of tidal dissipation in the OCZ of an F-star. In addition, the remnant eccentricity poses constraints on the planetary $Q'_2 \gtrsim 10^8$, in the absence of perturbing forces that could excite the eccentricity.

In this part of the thesis we have adopted a simple model of the effects of tidal friction and examined some of its consequences. In Part II we turn to studying in detail the mechanisms of tidal dissipation in solar-type stars, to try to understand the importance of tides in the evolution of short-period planets and their host stars.

Part II

Internal gravity waves and tidal dissipation in solar-type stars

Chapter 3

Internal wave breaking near the centre of a solar-type star: Boussinesq-type model and 2D simulations

We study the fate of IGWs approaching the centre of an initially non-rotating solar-type star, primarily using two-dimensional numerical simulations based on a cylindrical model. A train of IGWs is excited by tidal forcing at the interface between the convection and radiation zones of such a star. We derive a Boussinesq-type model of the central regions and obtain a nonlinear wave solution. We then use spectral methods to integrate the system of equations numerically, with the aim of studying at what amplitude the wave is subject to instabilities. These instabilities lead to wave breaking whenever the amplitude exceeds a critical value. Below this critical value, the wave reflects perfectly from the centre of the star. Wave breaking leads to mean flow acceleration, which corresponds to a spin up of the central region of the star, and the formation of a critical layer, which acts as an absorbing barrier for subsequent ingoing waves. As these waves continue to be absorbed near the critical layer, the star is spun up from the inside out. This has implications for the fate of short-period planets orbiting solar-type stars, which will be discussed in Chapter 5.

3.1 Introduction

IGWs are thought to account for the efficient tidal dissipation inferred from the circularisation of early-type binary stars (Zahn 1975; Zahn 1977; Zahn 2008; Savonije & Papaloizou 1983; Papaloizou & Savonije 1985; Savonije et al. 1995b; Savonije & Papaloizou 1997b; Papaloizou & Savonije 1997b), which are massive enough to have a convective core and an exterior radiative envelope. In these stars, IGWs are excited near the boundary between these two regions, where the buoyancy frequency (or Brunt-Väisälä frequency, see § 3.2) matches the tidal forcing frequency. These propagate outwards into the stably stratified RZ, towards the surface, where they are fully or partially damped by radiative diffusion. In this picture, these stars are tidally synchronized from the outside in, since angular momentum is deposited in the regions of the star where these waves damp. Goldreich & Nicholson (1989) propose that a corotation resonance (or critical layer, which we define in the next section) forms near the surface, which absorbs outward propagating waves. This is analogous to the picture that we will describe later in this chapter, except that our model has the star spinning up from the inside out.

The above model only works for stars with an exterior RZ, which is unlike that of the Sun and other stars of solar type, which have radiative cores and convective envelopes. It is of particular interest to study the efficiency of tidal dissipation in these stars, since many have been found to harbour close-in planets, whose survival is determined by the stellar Q'. This is because a planet with an orbital period shorter than the stellar spin period is subject to tidally induced orbital decay, with an inspiral rate that depends linearly on dissipation in the star. In these stars, a train of IGWs are again excited at the interface between the convective and radiative regions, but here it propagates towards the stellar centre. If they can coherently reflect from the centre, global standing modes can form in the RZ. In this case, tidal dissipation is efficient only when the tidal frequency matches that of a global standing mode (which are commonly referred to as g-modes; Terquem et al. 1998; Savonije & Witte 2002). When this occurs, the dissipation can be very large, leading to rapid evolution of the system out of resonance. This would not contribute appreciably to the time-averaged Q' because the transition through resonance is relatively fast, unless the system gets

locked into resonance by evolutionary processes, such as stellar evolution or MB (Witte & Savonije 1999; Witte & Savonije 2001). On the other hand, if these waves do not reflect coherently from the centre, and are either strongly dissipated there, or are reflected with a perturbed phase, then efficient dissipation is possible over a broad range of tidal frequencies (GD98; OL07). The extent of nonlinearity in the waves near the centre is likely to be the factor that determines whether these waves reflect coherently, and this is controlled by the amplitude and frequency of the tidal forcing, as well as the properties of the stellar centre.

In this chapter we study the problem of IGWs approaching the centre of a solar-type star, primarily using two-dimensional numerical simulations. We first derive a Boussinesq-type system of equations appropriate for the stellar centre, which are ideal for integrating numerically using spectral methods. An exact solution for tidally forced waves in 2D is derived, and some of its properties are discussed. Our numerical set-up is described and results are presented for both linear and nonlinear forcing amplitudes, including an analysis of the reflection coefficient and a study of the growth of different azimuthal wavenumbers in the disturbance. The simulations in this chapter are extended to three dimensions in Chapter 4. This is followed by a discussion of the results, especially their relevance to Q' for solar-type stars, and to the survival of close-in giant planets in orbit around such stars, in Chapter 5. We study the stability of the nonlinear wave derived in this chapter in Chapter 6. Finally, in Chapter 7 we present and discuss an alternative mechanism of tidal dissipation involving the gradual radiative damping of the waves being able to produce a critical layer.

3.2 Internal gravity waves: elementary properties, wave breaking and critical layers

IGWs are a family of dispersive waves that are ubiquitous in nature. They propagate in any fluid with a stable density stratification, due to the restoring force of buoyancy. Their influence can be observed in the oceans and atmosphere of the Earth on a range of spatial and temporal scales, from the visual undulations of striated cloud structures, to the complex interplay between these waves and shearing flows, which

produces the large-scale Quasi-Biennial Oscillation in the equatorial stratosphere. It is widely recognised that IGWs play a prominent role in the transport of energy and angular momentum in geophysical and astrophysical flows (McIntyre 2000; Bühler 2009). IGWs are thought to be important in stably stratified RZs of stars. When excited by turbulent convection, they were at one stage put forward as potential explanations for maintaining the solid body rotation of the radiative interior of the Sun (Schatzman 1993; Zahn et al. 1997). However, it was pointed out that the "antidiffusive" nature of IGWs tends to enhance local shear rather than reduce it (Gough & McIntyre 1998). IGWs are still thought to produce angular velocity variations in the RZ (Rogers & Glatzmaier 2006). They have also been invoked to explain the Li depletion problem in F-stars (Garcia Lopez & Spruit 1991), affecting solar neutrino production (Press 1981), and possibly having an effect on the solar cycle (Kumar et al. 1999).

Observations of oscillations on the solar surface are able to provide information about the interior properties of the Sun (Christensen-Dalsgaard 2002). IGWs in the radiative interior of the Sun can form global standing modes, commonly referred to as g-modes, if their frequency matches that of a free mode of oscillation. These are known to have their amplitude largest close to the centre (see § 3.5 & 5.2) and would therefore seem ideal probes of the deep interior. Unfortunately for observers, the standing g-modes are effectively trapped in the radiative interior, where the stratification is stable, and are evanescent in the CZ, and so are unlikely to be visible at the solar surface. Nevertheless, modes of sufficiently low degree, with high enough amplitude, may have already been observed at the surface by García et al. (2007), though it must be noted that thus far there is no undisputed evidence for observations of g-modes (Appourchaux et al. 2010).

The frequencies of the largely incompressible internal waves lie in ranges controlled by the buoyancy frequency (or Brunt-Väisälä frequency) N, and the Coriolis frequency 2Ω. The square of the buoyancy frequency in a spherically symmetric star is defined by

$$N^2(r) = -\frac{1}{\rho}\frac{dp}{dr}\left(\frac{1}{\Gamma_1}\frac{d\ln p}{dr} - \frac{d\ln\rho}{dr}\right), \tag{3.2.1}$$

where ρ, p are the density and pressure, and $\Gamma_1 = \left(\frac{\partial \ln p}{\partial \ln \rho}\right)_s$, is the first adiabatic

exponent (derivative taken at constant specific entropy s and constant chemical composition). The local dispersion relation for linear noncompressive internal waves in a fluid body rotating with angular velocity $\mathbf{\Omega}$ is

$$\omega^2 = N^2 \sin^2\alpha + 4\Omega^2 \cos^2\beta, \tag{3.2.2}$$

where α is the angle between the wavevector $\mathbf{k}$ and the gravitational acceleration $\mathbf{g}$, and β is the angle between $\mathbf{k}$ and $\mathbf{\Omega}$. The frequency of these waves is independent of wavelength (in the absence of viscosity or thermal conduction), and only depends on the direction of the wavevector. This is different from waves whose restoring force is due to compressibility, which have frequency inversely proportional to wavelength. When $N = 0$, Eq. 3.2.3 describes inertial waves, which have frequencies in the range $(0, 2\Omega)$. If the body is non-rotating ($\mathbf{\Omega} = 0$), then these waves are IGWs, and possess frequencies in the range $(0, N)$. In the presence of nonzero $\mathbf{\Omega}$ and N, these waves are intermediate between inertial waves and IGWs and are referred to as inertia-gravity waves. For waves in a spherical star, at a given latitude there is a minimum frequency for inertia-gravity wave propagation. Near the equator, waves can propagate with arbitrarily low frequency. From here on we neglect the bulk rotation, and assume that $\mathbf{\Omega} = 0$, i.e., we consider only IGWs. The local dispersion relation for IGWs can be rewritten

$$\omega^2 = N^2 \frac{k_h^2}{k_r^2 + k_h^2}, \tag{3.2.3}$$

where k_h and k_r are the horizontal and radial wavenumbers.

The phase and group velocities of these waves can be calculated from Eq. 3.2.3 to give

$$\mathbf{c}_p = \frac{\omega}{|\mathbf{k}|}\frac{\mathbf{k}}{|\mathbf{k}|} = \frac{N k_h}{(k_r^2 + k_h^2)^{\frac{3}{2}}}\left(k_r \mathbf{e}_r + k_h \mathbf{e}_h\right) \tag{3.2.4}$$

$$\approx \frac{N k_h}{k_r^3}\left(k_r \mathbf{e}_r + k_h \mathbf{e}_h\right), \tag{3.2.5}$$

$$\mathbf{c}_g = \nabla_{\mathbf{k}}\omega = -\frac{N k_r}{(k_r^2 + k_h^2)^{\frac{3}{2}}}\left(k_h \mathbf{e}_r - k_r \mathbf{e}_h\right) \tag{3.2.6}$$

$$\approx -\frac{N}{k_r^2}\left(k_h \mathbf{e}_r - k_r \mathbf{e}_h\right), \tag{3.2.7}$$

in the tidally relevant limit that the radial wavelength of the waves is much shorter than the horizontal wavelength, i.e., $k_h \ll k_r$ (which is true except near a turning point, or within the last few wavelengths from the centre of a star). In this limit, $\mathbf{c}_g \cdot \mathbf{e}_r = -N\frac{k_h}{k_r^2} = -\mathbf{c}_p \cdot \mathbf{e}_r$, i.e., the radial wave pattern moves in the opposite direction to the radial energy flux. Since ω is independent of $|\mathbf{k}|$, $\mathbf{c}_g \cdot \mathbf{k} = 0$, meaning that the energy in IGWs propagates along surfaces of constant phase.

For waves on a non-zero horizontal background shear flow $\mathbf{U}$, Eq. 3.2.3 still applies if the Richardson number $Ri = \frac{N^2}{|\partial \mathbf{U}/\partial r|^2} \gg 1$, if we replace ω by the Doppler shifted frequency $\hat{\omega}$, and similarly for the phase and group velocity of the waves,

$$\hat{\omega} = \omega - \mathbf{k} \cdot \mathbf{U}, \quad \hat{\mathbf{c}}_p = \mathbf{c}_p - \mathbf{U}, \quad \hat{\mathbf{c}}_g = \mathbf{c}_g - \mathbf{U}. \tag{3.2.8}$$

We now have the possibility of the wave frequency being Doppler shifted upwards to N, in which case $\hat{\mathbf{c}}_g \cdot \mathbf{e}_r$ reverses, giving total internal reflection.

The other extreme, $\hat{\omega} \to 0$, occurs when the horizontal velocity in the shear matches the horizontal phase velocity. This occurs at a so-called "critical layer", which is defined as the layer in which the wavelength of the waves would be Doppler shifted to zero, if they were ever to reach it. Note though, that $\hat{\mathbf{c}}_g \cdot \mathbf{e}_r \to 0$ as $\hat{\omega} \to 0$, so in linear theory the waves never reach the critical layer in a finite time. Early work on IGWs in a background shear, including a study of critical layers, can be found in Booker & Bretherton (1967) and Hazel (1967). They find that an IGW propagating through a critical layer is attenuated by a factor $\sim \exp\left(-2\pi(Ri - 1/4)^{1/2}\right)$. If $Ri \gg 1/4$, the wave is fully absorbed, and irreversibly transfers its energy to the mean flow. However, it must be noted that at the critical layer, linear theory predicts that the wave steepness

$$s = \frac{\max(\mathbf{u} \cdot \mathbf{e}_h)}{\hat{\mathbf{c}}_p \cdot \mathbf{e}_h}, \tag{3.2.9}$$

where $\mathbf{u}$ is the velocity perturbation, of these waves goes to infinity, as the Doppler shifted horizontal phase speed $\hat{\mathbf{c}}_p \cdot \mathbf{e}_h$ goes to zero, i.e., the waves become strongly nonlinear at the critical layer (which McIntyre 2000, refers to as linear theory predicting its own breakdown). Since wave breaking is expected to occur whenever $s > 1$, the waves are likely to break before they reach the critical layer. Nonlinear effects have

been studied in early simulations by Winters & D'Asaro (1994), who find that the of initial wave energy on encountering a critical layer, roughly one third reflects, one third results in mean flow acceleration, and the remainder cascades to small scales where it is dissipated. This implies that wave absorption by the mean flow need not be complete, in contrast with the prediction from linear theory. This is discussed further in § 3.9.2, in relation to the results of our simulations.

Wave breaking is defined as any wave-induced process that leads to the rapid and irreversible deformation of "otherwise wavy" material contours (McIntyre 2000), and it leads to the production of turbulence and irreversible energy dissipation. The breaking process results from the growth of an instability upon a basic state composed of a wave with $s > 1$. The susceptibility of a wave to breaking can be enhanced by resonant triad interactions, in which a primary wave resonantly interacts with a pair of low-amplitude secondary waves. This process transfers energy to the secondary waves, whose steepness can then grow beyond the critical value required for breaking to occur, even though the primary steepness may not be sufficient for breaking on its own (Staquet & Sommeria 2002). Previous work has shown that the process leading to the wave steepening is two-dimensional, but that breaking is a three-dimensional process (Klostermeyer 1991; Winters & D'Asaro 1994). Nevertheless, the mechanisms responsible for breaking and the final outcome of the breaking process are likely to be similar in 2D.

Here we are interested in studying what happens when IGWs excited by tidal forcing approach the centre of a star with an inner RZ, i.e. G-type stars such as the Sun, which do not possess a convective core. We are primarily concerned with the efficiency of tidal dissipation for solar-type stars, resulting from breaking of these waves near the centre. Throughout the rest of this chapter we restrict our problem to 2D, and postpone study of any 3D effects until Chapter 4. We now describe our basic problem in more detail.

3.3 Basic description of the problem

3.3.1 Tidal potential

Consider a star and a planet in a mutual Keplerian orbit (though we make no assumptions about the relative masses at this stage). The tidal potential experienced by the star can be written as a sum of rigidly rotating spherical harmonics (e.g. OL04). For the simplest case of a planet on a circular orbit, that is coplanar with the equatorial plane of the star, we can consider a two-dimensional restriction of the problem to this plane. This allows us to write the time-dependent part of the quadrupolar ($l = 2$) tidal potential in the equatorial plane of the star as

$$\Psi(r, \phi, t) = -\frac{3}{4}\frac{G m_p}{a^3} r^2 \cos(2\phi - \hat{\omega} t), \tag{3.3.1}$$

in spherical polar coordinates (r, θ, ϕ) with origin at the centre of the star, in the plane $\theta = \pi/2$. Here m_p is the planet mass, a is the orbital semi-major axis, and $n > 0$ is the mean motion. The relevant tidal frequency is $\hat{\omega} = 2n - 2\Omega$, for a star rotating with angular velocity Ω. From here on we assume that the star is non-rotating, i.e., we assume that $\Omega = 0$, which is a reasonable assumption if the star is spinning much slower than the orbit. This is appropriate if a short-period planet orbits a solar-type star, that has been spun down by MB for the duration that it has spent on the main-sequence, to rotate with a spin period of several tens of days.

We consider a restriction of the full three-dimensional problem, in which the tidal potential is composed of many different spherical harmonic components for an orbit of arbitrary eccentricity and inclination, to instead consider a simplified two dimensional model of a star, forced by this single component of the tide. In Chapter 4 we will carry out fully three-dimensional simulations of this problem, which find that the two dimensional approximation is indeed reasonable.

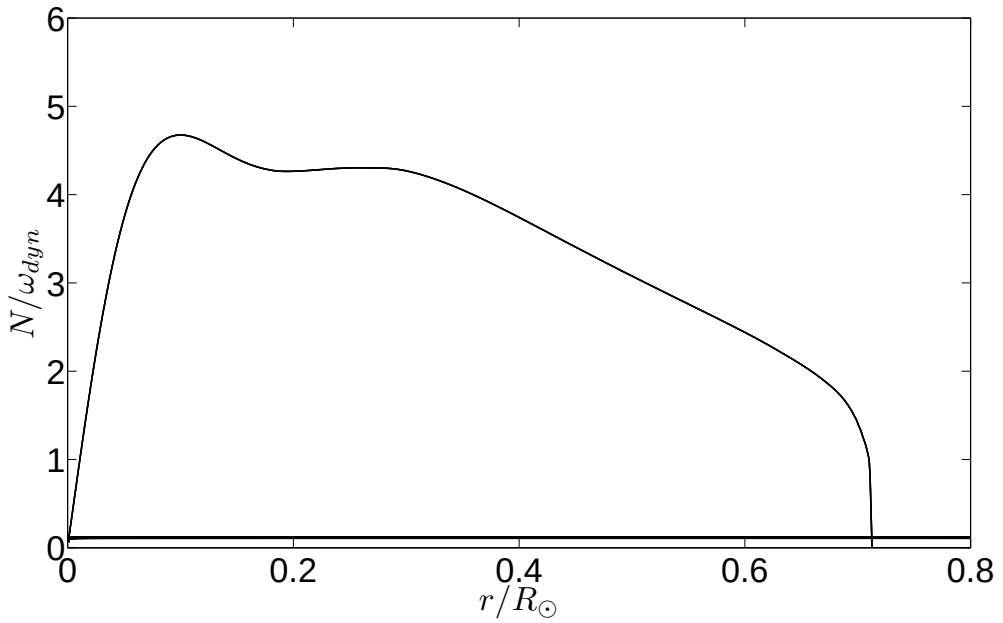

Figure 3.1: Buoyancy frequency N normalised to dynamical frequency ω_{dyn} versus radius, based on Model S of the current Sun. Also plotted is the frequency $2\pi/0.5\text{day} \sim 0.1\omega_{dyn}$, corresponding with the tidal frequency for a one-day orbit. Note that $\hat{\omega} \ll N$ throughout the bulk of the RZ. Only near the centre and at the CZ/RZ interface, does $\hat{\omega} \sim N$.

3.3.2 Central regions of a star

The buoyancy frequency is real and comparable with the dynamical frequency of the star

$$\omega_{dyn} = \left(\frac{Gm_\star}{R_\star^3}\right)^{\frac{1}{2}}, \tag{3.3.2}$$

throughout the bulk of the RZ, where $m_\star$ and $R_\star$ are the stellar mass and radius, respectively. In Fig. 3.1 we plot N normalised to ω_{dyn} in the RZ for Model S of the current Sun, which is a high-resolution standard solar model developed for helioseismology (Christensen-Dalsgaard et al. 1996). For our problem, the tidal frequencies of interest $\hat{\omega} \ll N$, which implies $k_r \gg 2\pi/r$, except near the centre. IGWs are excited at the top of the RZ by a combination of tidal forcing in that region, together with the pressure of inertial waves acting at the interface if $|\hat{\omega}| < 2\Omega$ (OL07). It is within this transition region that N increases linearly with distance into the RZ, so there is a point at which $N \sim \hat{\omega}$, and IGWs are efficiently excited. These propagate towards the centre with radial wavelengths $\lambda_r \sim 10^{-3} - 10^{-2} R_\odot$, for typical tidal frequencies.

Expanding the standard equations of stellar structure about $r = 0$, we obtain the density stratification $\rho \approx \rho_0 + \rho_2 r^2$. For sufficiently small r, g is linear in r, and $N \approx Cr$, where C is a constant that varies with stellar model, and main-sequence age. For the current Sun, $C \equiv C_\odot \approx 8.0 \times 10^{-11}\mathrm{m}^{-1}\mathrm{s}^{-1}$. This is valid throughout only the inner $\lesssim 3\%$ of the Sun. However, even considering the largest radial wavelength produced by a HJ, this region contains multiple wavelengths.

3.4 Derivation of a Boussinesq-type system of equations

The ideal compressible fluid equations in 2D plane polar (r, ϕ) coordinates are

$$Du_r - \frac{u_\phi^2}{r} = -\frac{1}{\rho}\partial_r p - \partial_r \Phi, \tag{3.4.1}$$

$$Du_\phi + \frac{u_r u_\phi}{r} = -\frac{1}{\rho r}\partial_\phi p - \frac{1}{r}\partial_\phi \Phi, \tag{3.4.2}$$

$$D\rho + \rho\left[\frac{1}{r}\partial_r(ru_r) + \frac{1}{r}\partial_\phi u_\phi\right] = 0, \tag{3.4.3}$$

$$Dp - \frac{\gamma p}{\rho}D\rho = 0, \tag{3.4.4}$$

$$\nabla^2\Phi = 4\pi G\rho, \tag{3.4.5}$$

$$D = \partial_t + u_r\partial_r + \frac{u_\phi}{r}\partial_\phi. \tag{3.4.6}$$

The basic state is static and circularly symmetric. Near the centre, we pose the expansion

$$\rho = \rho_0 + \rho_2 r^2 + \rho_4 r^4 + O(r^6), \tag{3.4.7}$$

and similarly for p and Φ. The coefficients are related by the condition for the background to be in hydrostatic equilibrium, together with Poisson's equation, giving

$$p_2 = -\rho_0\Phi_2, \quad p_4 = -\rho_0\Phi_4 + \frac{p_2\rho_2}{2\rho_0}, \tag{3.4.8}$$

$$\Phi_2 = \pi G\rho_0, \quad \Phi_4 = \frac{\pi G\rho_2}{4}, \tag{3.4.9}$$

and so on for the coefficients of higher-order terms.

We are interested in a region where $r/R_\star = O(\epsilon)$, where $\epsilon \ll 1$, so let $r = \epsilon x$. Now introduce a slow time $\tau = \epsilon t$, then the solution including the basic state, and a slow nonlinear density perturbation, has the form

$$\rho = \underbrace{\rho_0 + \epsilon^2\rho_2 x^2 + \epsilon^4\rho_4 x^4 + ...}_{\text{basic state}} + \underbrace{\epsilon^2\rho_2'(x,\phi,\tau) + ...}_{\text{nonlinear perturbation}}, \tag{3.4.10}$$

$$p = \underbrace{p_0 + \epsilon^2 p_2 x^2 + \epsilon^4 p_4 x^4 + ...}_{\text{basic state}} + \underbrace{\epsilon^4 p_4'(x,\phi,\tau) + ...}_{\text{nonlinear perturbation}}, \tag{3.4.11}$$

$$\Phi = \underbrace{\Phi_0 + \epsilon^2\Phi_2 x^2 + \epsilon^4\Phi_4 x^4 + ...}_{\text{basic state}} + \underbrace{\epsilon^4\Phi_4'(x,\phi,\tau) + ...}_{\text{nonlinear perturbation}}, \tag{3.4.12}$$

$$u_r = \underbrace{\epsilon^2 u_{r2}(x,\phi,\tau) + ...}_{\text{nonlinear perturbation}}, \tag{3.4.13}$$

$$u_\phi = \underbrace{\epsilon^2 u_{\phi 2}(x,\phi,\tau) + ...}_{\text{nonlinear perturbation}}, \tag{3.4.14}$$

In the Boussinesq approximation, the fractional pressure perturbation is small compared with the fractional density perturbation because this is a low-frequency disturbance, with $\omega \ll \omega_{dyn}$, for which acoustic effects are negligible. For such short-wavelength perturbations, the gravitational perturbation is also small (Christensen-Dalsgaard 2002). These two points explain the absence of terms in the above solutions proportional to ϵ^2 for p and Φ in the nonlinear perturbation. This corresponds to looking for small density constrasts and weak material accelerations compared with gravity.

Substituting these expansions into the basic equations, and subtracting terms that arise only in the basic state, we obtain at leading order

$$D_1 u_{r2} - \frac{u_{\phi 2}^2}{x} = -\frac{1}{\rho_0}\partial_x p_4' + \frac{2x p_2 \rho_2'}{\rho_0^2} - \partial_x \Phi_4', \tag{3.4.15}$$

$$D_1 u_{\phi 2} + \frac{u_{r2}u_{\phi 2}}{x} = -\frac{1}{\rho_0 x}\partial_\phi p_4' - \frac{1}{x}\partial_\phi \Phi_4', \tag{3.4.16}$$

$$\rho_0\left[\frac{1}{x}\partial_x(x u_{r2}) + \frac{1}{x}\partial_\phi u_{\phi 2}\right] = 0, \tag{3.4.17}$$

$$2x p_2 u_{r2} - \frac{\gamma p_0}{\rho_0}\left(D_1\rho_2' + 2x\rho_2 u_{r2}\right) = 0, \tag{3.4.18}$$

$$\nabla^2\Phi_4' = 4\pi G\rho_2', \tag{3.4.19}$$

$$D_1 = \partial_\tau + u_{r2}\partial_x + \frac{u_{\phi 2}}{x}\partial_\phi. \tag{3.4.20}$$

We can rewrite these equations in a more natural notation, removing the asymptotic scalings to find

$$Du_r - \frac{u_\phi^2}{r} = -\partial_r q + rb, \tag{3.4.21}$$

$$Du_\phi + \frac{u_r u_\phi}{r} = -\frac{1}{\rho r}\partial_\phi q, \tag{3.4.22}$$

$$\frac{1}{r}\partial_r(ru_r) + \frac{1}{r}\partial_\phi u_\phi = 0, \tag{3.4.23}$$

$$Db + C^2 r u_r = 0, \tag{3.4.24}$$

$$D = \partial_t + u_r\partial_r + \frac{u_\phi}{r}\partial_\phi, \tag{3.4.25}$$

where

$$b = \frac{2p_2}{\rho_0^2}\rho_2', \tag{3.4.26}$$

$$q = \frac{1}{\rho_0}p_4' + \Phi_4', \tag{3.4.27}$$

are a buoyancy variable and a modified pressure variable, and

$$C^2 = 4\Phi_2\left(\frac{p_2}{\gamma p_0} - \frac{\rho_2}{\rho_0}\right), \tag{3.4.28}$$

is related to the buoyancy frequency N by $N = Cr$, with $C^2 > 0$ for a stable stratification. Note that Poisson's equation is no longer required, since we have separated out the gravitational potential perturbation in this approximation.

We can write these equations in the vector-invariant form (which can be used in two or three dimensions)

$$D\mathbf{u} = -\nabla q + \mathbf{r}b, \tag{3.4.29}$$

$$Db + C^2\mathbf{r}\cdot\mathbf{u} = 0, \tag{3.4.30}$$

$$\nabla\cdot\mathbf{u} = 0, \tag{3.4.31}$$

$$D = \partial_t + \mathbf{u}\cdot\nabla. \tag{3.4.32}$$

These equations are similar to the standard Boussinesq system for a slab of fluid in Cartesian geometry (see e.g. Bühler 2009, Ch. 6) with a uniform stratification, with the exception that our problem is in cylindrical geometry, with g and N proportional

to r. Note also that the buoyancy variable defined here is related, but not identical, to that of the standard Boussinesq approximation used in atmospheric sciences and oceanography (see e.g. Bühler 2009). The buoyancy variable is proportional to the density and entropy perturbation.

An energy equation for our system can be derived by contracting Eq. 3.4.29 with $\mathbf{u}$:

$$\partial_t \left(\frac{1}{2}|\mathbf{u}|^2 + \frac{b^2}{2C^2} \right) + \nabla \cdot \left[\left(\frac{1}{2}|\mathbf{u}|^2 + \frac{b^2}{2C^2} + q \right) \mathbf{u} \right] = 0. \tag{3.4.33}$$

Thus $E = \frac{1}{2}\rho_0|\mathbf{u}|^2 + \rho_0 \frac{b^2}{2C^2}$ is the energy density per unit volume, and
$\mathbf{F}^E = \rho_0 \left(\frac{1}{2}|\mathbf{u}|^2 + \frac{b^2}{2C^2} + q \right) \mathbf{u}$ is the energy flux density.

If the fluid is at rest, with $b = 0$, then the stratification surfaces are circles (spheres in 3D), and C^2 measures the strength of the stable stratification. If we disturb the fluid from rest, then a positive (negative) buoyancy is associated with an inward (outward) radial displacement of particles, resulting in an outward (inward) acceleration of the fluid due to buoyancy, to restore the system to equilibrium. From the energy equation Eq. 3.4.33, the state $b = 0$ is seen to be that of minimum gravitational potential energy, since the available potential energy density $\rho_0 \frac{b^2}{2C^2}$ is minimised. This makes sense, since this corresponds to having a background state with no wave-like disturbance.

3.5 Linear theory of IGWs approaching the stellar centre

3.5.1 Linear solution steady in a frame rotating with the pattern speed of forcing

If the RZ is forced from above then this will excite waves which propagate to the centre of the star. If the incoming wave has frequency ω and azimuthal wavenumber m, then we can assume that the response is steady in a frame rotating with the angular pattern speed $\Omega_p = \omega/m$, in the absence of instabilities. The dependence on ϕ and t is then

only through the combination

$$\xi = m(\phi - \Omega_p t). \tag{3.5.1}$$

We can choose Ω_p/C as a unit of length, and Ω_p^{-1} as a unit of time[1], to allow us to write the equations in the dimensionless form

$$Du_r - \frac{u_\phi^2}{r} = -\partial_r q + rb, \tag{3.5.2}$$

$$Du_\phi + \frac{u_r u_\phi}{r} = -\frac{m}{\rho r}\partial_\xi q, \tag{3.5.3}$$

$$\frac{1}{r}\partial_r(ru_r) + \frac{m}{r}\partial_\xi u_\phi, \tag{3.5.4}$$

$$Db + ru_r = 0, \tag{3.5.5}$$

$$D = u_r\partial_r + m\left(\frac{u_\phi}{r} - 1\right)\partial_\xi. \tag{3.5.6}$$

The energy equation (Eq. 3.4.33) allows us to infer that the radial energy flux

$$F_r^E = \rho_0 \int_0^{2\pi} \left[\frac{1}{2}\left(|\mathbf{u}|^2 + b^2\right) + q\right] ru_r d\xi, \tag{3.5.7}$$

is independent of r for disturbances steady in this frame of reference, since the solutions are periodic in ξ with period 2π.

The radial angular momentum flux is

$$F_r^L = \frac{m}{\omega}F_r^E. \tag{3.5.8}$$

We can obtain a solution to these equations by linearization, assuming that the solution is proportional to $e^{i\xi}$, obtaining (where real parts are assumed to be taken)

$$-imu_r = -\partial_r q + rb, \tag{3.5.9}$$

$$-imu_\phi = -\frac{imq}{r}, \tag{3.5.10}$$

$$\frac{1}{r}\partial_r(ru_r) + \frac{im}{r}u_\phi = 0, \tag{3.5.11}$$

$$-imb + ru_r = 0. \tag{3.5.12}$$

The incompressibility constraint allows expression of the velocity in terms of the

[1]Note that these units are only used in this section, §4.2, §7.2, and in Appendix A.4.

streamfunction $\psi(r,\phi)$, defined by

$$\mathbf{u} = \nabla \times (\psi \mathbf{e}_z) = \left(\frac{1}{r}\partial_\phi \psi\right)\mathbf{e}_r + (-\partial_r \psi)\,\mathbf{e}_\phi, \tag{3.5.13}$$

so we can write

$$u_r = \mathrm{Re}\left[\frac{im}{r}\psi\right], \tag{3.5.14}$$

$$u_\phi = \mathrm{Re}\left[-\partial_r \psi\right]. \tag{3.5.15}$$

This enables us to reduce the system to Bessel's equation of order m,

$$L_m \psi = \partial_r(r\partial_r \psi) + r\left(1 - \frac{m^2}{r^2}\right)\psi = 0 \tag{3.5.16}$$

with solution regular at the origin $\psi \propto J_m(r)$. This represents a wave that approaches from infinity, reflects perfectly from the centre and goes out to infinity. Pure ingoing and outgoing wave solutions are described by $J_m(r) \pm iY_m(r)$, with the appropriate sign explained below.

3.5.2 Properties of the (non-)linear solution

The general solution can be written in the form of a sum of ingoing and outgoing waves, with complex amplitudes A_{in} and A_{out}, as follows:

$$\psi_{in}(r,\xi) = [J_m(r) + iY_m(r)]e^{i\xi}, \tag{3.5.17}$$

$$\psi_{out}(r,\xi) = [J_m(r) - iY_m(r)]e^{i\xi}, \tag{3.5.18}$$

$$\psi(r,\xi) = A_{in}\psi_{in}(r,\xi) + A_{out}\psi_{out}(r,\xi). \tag{3.5.19}$$

We can check that ψ_{in} corresponds to an ingoing wave by calculating its phase and group velocities. A simple calculation shows that the radial phase velocity is directed outward if we adopt the convention that $\omega = m\Omega_p > 0$, and the group velocity is directed inward. This highlights one of the peculiarities of IGWs – that the phase and group velocities are oppositely directed, as discussed in § 3.2. For these linear waves, we have

$$F_r^E = \rho_0 \pi m r \mathrm{Im}[\psi \partial_r \psi^*] = 2m\rho_0\left(|A_{out}|^2 - |A_{in}|^2\right). \tag{3.5.20}$$

The solution for a wave that perfectly reflects from the centre is

$$\psi(r,\xi) = 2A_{in}J_m(r)e^{i\xi}, \tag{3.5.21}$$

and has $F_r^E = 0$, since $A_{in} = A_{out}$.

If we take the curl of Eq. 3.4.29, we obtain

$$\partial_t(\nabla \times \mathbf{u}) = \nabla \times (\mathbf{r}b) - \nabla \times (\mathbf{u} \cdot \nabla \mathbf{u}), \tag{3.5.22}$$

which has eliminated the modified pressure perturbation q. The z-component of this equation, expressed in terms of the streamfunction, is

$$\partial_t(-\nabla^2\psi) = -\partial_\phi b + J(\psi, -\nabla^2\psi), \tag{3.5.23}$$

and the buoyancy equation is

$$\partial_t b = -\partial_\phi \psi + J(\psi, b). \tag{3.5.24}$$

The nonlinear terms take the form of Jacobians,

$$J(A,B) = \frac{1}{r}\frac{\partial(A,B)}{\partial(r,\phi)} = (\partial_r A)(\frac{1}{r}\partial_\phi B) - (\frac{1}{r}\partial_\phi A)(\partial_r B). \tag{3.5.25}$$

For the solution above, we have

$$J(\psi, -\nabla^2\psi) = J(\psi, b) = 0, \tag{3.5.26}$$

which expresses the surprising result that the solutions derived are exact nonlinear solutions of the system. This follows from the fact that $-\nabla^2\psi = b = \psi$ for these waves. This arises because although the nonlinear terms $\mathbf{u}\cdot\nabla\mathbf{u} \neq 0$, they are balanced by the modified pressure term in the equations of motion. We also have $\mathbf{u}\cdot\nabla b = 0$.

This is distinct from, but analogous to, the result that a single propagating plane IGW in a uniform stratification is a nonlinear solution of the standard Boussinesq system (Drazin 1977; Klostermeyer 1982). This is a consequence of the fact that $\mathbf{k}\cdot\mathbf{u} = 0$ for these waves, which implies that the advective operator $\mathbf{u}\cdot\nabla$ annihilates any disturbance belonging to the same plane wave. A useful consequence of this is that

a stability analysis can be performed on finite-amplitude propagating IGWs, allowing detailed understanding of the initial stages of the breaking process for these waves (Drazin 1977; Klostermeyer 1982; Klostermeyer 1991). Such studies have shown that a single propagating IGW solution is *always* unstable whatever its amplitude, since it undergoes resonant triad interactions. One important difference in our problem is that the nonlinearity is spatially localized to the innermost wavelengths, whereas the nonlinearity is present everywhere in the plane IGW problem. We postpone a detailed study of the stability of our nonlinear standing wave until Chapter 6. However, we expect waves of sufficiently large amplitude to be unstable if they overturn the stratification.

The amplitude required to overturn the stratification can be derived using Eq. 3.5.21. The entropy (or more precisely, a quantity proportional to the entropy) is $s = b + (1/2)r^2$, in these units. Overturning the stratification means that the entropy profile, perturbed by a wave with buoyancy perturbation b, must satisfy $\partial_r s < 0$, which implies $(1/r)\partial_r b < -1$. Since $b = \psi$ for these nonlinear waves, this can be expressed in terms of the streamfunction as $(1/r)\partial_r \psi < -1$. Reintroducing dimensional variables, and substituting for u_ϕ, modifies this criterion to $(u_\phi/r) > \Omega_p$, i.e., overturning occurs if the angular velocity in the wave exceeds the angular pattern speed. Equivalently, wave breaking occurs if

$$\max(u_\phi) \gtrsim \frac{\omega^2}{4C}, \tag{3.5.27}$$

whose largest value occurs where the amplitude of $\partial_r J_2(r)$ is largest, which is one wavelength from the centre.

3.6 Numerical methods

We solve the system of equations 3.4.29-3.4.32 using a Cartesian spectral code, SNOOPY (Lesur & Longaretti 2005; Lesur & Longaretti 2007). It is advantageous to use a Cartesian code over one in the more natural (for the problem) cylindrical geometry, because of the absence of a coordinate singularity at the origin, near to which is the region of the flow that we are most interested in. We also avoid the timestep issues close

to the centre that would be present in a time-explicit cylindrical code. These arise from the Courant–Friedrichs–Lewy (CFL) condition, because the grid spacing becomes very small near the origin. In addition, using a Boussinesq-type model has the major advantage, over a fully compressible calculation, that it does not resolve sound waves. Since the ratio of the sound speed to a typical IGW radial group velocity is $c_s/c_{g,r} \sim 10^4 \gg 1$, fully compressible simulations would spend most of their time resolving sound waves, and are therefore impractical for use on this problem. We found that this was the case from preliminary low-resolution calculations using ZEUS-2D (Stone & Norman 1992), which nevertheless confirm our main results, and which are described in Appendix A.5, for completeness.

This code is a 3D Eulerian spectral Fourier code based on FFTW libraries, which was written by G. Lesur, for studying hydrodynamic and magnetohydrodynamic turbulence in accretion discs in the shearing box. The code has been parallelized using both the MPI protocol and OPEN-MP. The algorithm is a pseudo-spectral method which will now be briefly described. Spatial derivatives are computed in Fourier space, which means that they are extremely accurate down to the grid scale, which is one of the principle advantages of spectral methods (Boyd 2001). However, the nonlinear terms, and those in which the coefficients have spatial dependence, are computed in real space, since a real space product is a convolution in Fourier space. This procedure is more efficient than a direct convolution product since the FFT computation time scales as $N \log N$, where N is the number of grid cells, whereas a convolution in Fourier space scales as N^2. The only drawback with this procedure is that the finite resolution generates a numerical artifact commonly known as the aliasing effect, which is the apparition of non-physical waves near the Nyquist frequency. This effect can be handled through a de-aliasing procedure, in which the non-linear terms (and those with spatially variable coefficients) are computed with a resolution 3/2 higher than the effective resolution used in the source terms (Peyret 2002). This is implemented by setting components of the solution with wavenumbers larger than 2/3 times the maximum wavenumber to zero during every timestep, using a de-aliasing mask. Time evolution is computed using a 3rd-order Runge-Kutta scheme.

Since this is a Fourier spectral code, the problem must be periodic in space. We

solve our non-periodic problem using this code by setting up a region near the outer boundary, in which the fluid variables are smoothed to zero as we approach the boundary, using a parabolic smoothing function. We find it is quite acceptable to do this over a region about 1/10 of the total box size. For this value there is negligible interaction between neighbouring boxes. This approach is one that may be useful in many applications which would benefit from the use of spectral methods, but have non-Cartesian geometry and/or non-periodic boundary conditions. The obvious drawback of such an approach is the slight increase in computational cost, since the smoothing region is additional to the flow in the region of interest. Interior to this we have a thin ring in which we implement a forcing term in the radial momentum equation of the form $f_r \cos(2\phi - \omega t)$. This is designed to excite IGWs with $m = 2$, but is not designed to accurately describe the excitation of IGWs at the top of the RZ, since we are only interested in the dynamics of the central region. Our forcing is non-potential, which reflects the fact that the tidal forcing of waves is indirect (e.g. see Chapter 5; OL04). A potential force would be absorbed in this model by a hydrostatic adjustment of q. Note that for uniform rotation $\mathbf{\Omega} = \Omega \mathbf{e}_z$, $2\mathbf{\Omega} \times \mathbf{u} = \nabla(2\Omega\psi)$, so the resulting Coriolis force is also a potential force, and would have no effect.

We solve the equations

$$D\mathbf{u} = -\nabla q + \mathbf{r}b + \nu\nabla^2\mathbf{u} + \begin{cases} 0, & 0 \le r < r_{force}, \\ \mathbf{f}, & r_{force} \le r < r_{smooth}, \end{cases} \tag{3.6.1}$$

$$Db + C^2\mathbf{r} \cdot \mathbf{u} = 0, \tag{3.6.2}$$

$$\nabla \cdot \mathbf{u} = 0, \tag{3.6.3}$$

$$D = \partial_t + \mathbf{u} \cdot \nabla, \tag{3.6.4}$$

where $\mathbf{f} = -f_r \cos(2\phi - \omega t)\, \mathbf{e}_r$. We use a parabolic smoothing function $d(r) = \left(\frac{r - r_{smooth}}{r_{box} - r_{smooth}}\right)^2$, to instantaneously smooth u_r, u_ϕ and b to zero as we approach the outer boundary. We do this by multiplying the variables in the region $r_{smooth} \le r < r_{box}$ by $d(r)$ during every timestep. We also solve a Poisson equation for the modified pressure during each timestep.

Our choice of units for length and time are arbitrary. We study a region $-1.5 < x < 1.5$, $-1.5 < y < 1.5$ and set $r_{force} = 0.85\ r_{box}$, $r_{smooth} = 0.9\ r_{box}$, with $r_{box} = 1.5$.

We choose a typical IGW radial wavelength of $\lambda_r = 0.1$, so that we are resolving ~ 12 wavelengths within the box. The radial wavelength of these waves is not strictly constant, but its variation for large r is small, and can be reasonably approximated by a constant value in that region. We choose a forcing frequency $\omega = 1$. These choices are arbitrary, and are made to ensure that we are resolving a sufficient number of wavelengths within the box.

Explicit viscosity is added to Eq. 3.4.29, since the code has no intrinsic dissipation. This is necessary for stability – to ensure that we have no unphysical growth of energy at small scales. The value of the viscosity is chosen such that it dissipates disturbances on the grid scale, and a value of $\nu = 2 \times 10^{-6}$, is chosen for all simulations. Viscous terms are implemented in a time-implicit manner. We do not include thermal diffusion in the buoyancy equation since this was found to be unnecessary for stability (however, thermal diffusion is considered in §7.3).

The velocity components are normalised with respect to a typical radial phase velocity of the wave $\omega\lambda_r/2\pi$,

$$u_{r,\phi} = \tilde{u}_{r,\phi} \left(\frac{\omega \lambda_r}{2\pi} \right), \tag{3.6.5}$$

in which $\tilde{u}_\phi$ is equivalent to the wave steepness s, and is a measure of the nonlinearity in the wave. This condition for overturning the stratification in Eq. 3.5.27, is then

$$\tilde{u}_\phi > \frac{1}{2}. \tag{3.6.6}$$

Since we have chosen to specify the radial wavelength λ_r and frequency ω of the waves that we wish to study, we have already constrained the stratification

$$C = \frac{\pi \omega}{\lambda_r}. \tag{3.6.7}$$

There is now only one further parameter, f_r to fully specify the problem. We set

$$f_r = \tilde{f}_r \left(\frac{\omega \lambda_r}{2\pi} \right) \omega \tag{3.6.8}$$

and vary the normalised amplitude $\tilde{f}_r$, to model the effects of different tidal forcing amplitudes. From preliminary investigation, it is found to be appropriate to choose

values between 10^{-2} and 10^3, since these result in central amplitudes that range from $\tilde{u}_r \ll 1$ to $\tilde{u}_r = O(1)$ (higher central amplitudes are not observed, as is described in the results, owing to wave breaking above a critical amplitude). This represents a vast range of amplitudes of tidal forcing, from cases in which the secondary body is a low-mass planet to a solar-mass binary companion, in a close orbit.

Our background is a hydrostatic equilibrium with no wave, with $b = 0$ in the initial state. We use a resolution of 512×512 for most simulations, though higher resolution runs have been performed using 1024×1024 and 1536×1536. We confirm that the results are not dependent on the numerical method (and that our system Eqs. 3.4.29-3.4.32 correctly describes the relevant physics) by reproducing the basic results using ZEUS-2D. We describe our implementation of the problem in this code in Appendix A.5. ZEUS reproduces the same basic results as the SNOOPY code, which indicates that the effects of nonzero compressibility are unimportant. In light of this, we only discuss the SNOOPY results below.

3.7 Numerical results

We use the set-up described in § 3.6 for a set of simulations with a variety of forcing amplitudes $\tilde{f}_r$. The typical radial group velocity and wave crossing time are, respectively,

$$c_{g,r} = \frac{C\lambda_r^2}{2\pi^2}, \tag{3.7.1}$$

$$t_c = \frac{r_{box}}{c_{g,r}}. \tag{3.7.2}$$

For the initial conditions described in the previous section, $t_c \sim 90$. We define a "wave" to be a non-axisymmetric oscillatory flow represented by a single azimuthal wavenumber $m \neq 0$, whereas a "mean flow" is an axisymmetric azimuthal flow with $m = 0$.

We perform several different quantitative analyses of the results. We separate the amplitudes of the waves into an ingoing wave (IW) and an outgoing wave (OW), and calculate a reflection coefficient, using the method described in Appendix A.4. The reflection coefficient $\mathcal{R}$ is defined as the ratio of the absolute amplitudes of the OWs

(A_{out}) and IWs (A_{in}) for a given radial ring,

$$\mathcal{R} = \left| \frac{A_{out}}{A_{in}} \right|, \tag{3.7.3}$$

and measures the amplitude decay for a wave travelling from r to the centre and back to r. We can relate it to the phase change on reflection ($\Delta\phi$) by

$$\Delta\phi = i \left[\ln \mathcal{R} - \ln \left(\frac{A_{out}}{A_{in}} \right) \right] \tag{3.7.4}$$

For perfect standing waves, $A_{in} = A_{out}$, and $\mathcal{R} = 1$. If the IW is entirely absorbed at the centre, then $\mathcal{R} = 0$. Thus, $\mathcal{R}$ is a measure of how much the wave has been attenuated on reflection from the centre.

We also Fourier analyse the solution, to study the temporal evolution of different azimuthal wavenumbers in the flow. This is done by selecting a ring of cells in the grid at a particular radius, which is chosen to be at $r = 0.1$, since this is probably close enough to the centre to detect the effects of nonlinear wave couplings, if they occur. Since this is a Cartesian grid, we do this by selecting all cells within a particular radial ring to within a tolerance width comparable with the size of a grid cell. We then compute the Discrete Fourier Transform of the velocity components, and from this calculate the power spectral density,

$$P_m = \frac{1}{N} \left| \sum_{k=0}^{N-1} u_{r,k} \exp \left(-imk \left(\frac{2\pi}{N} \right) \right) \right|^2 \tag{3.7.5}$$

and similarly for u_ϕ, where N is the number of grid points in the ring – which depends on r and the resolution, though $10^2 < N < 10^3$, for all adopted resolutions at $r = 0.1$. From this we can determine which components of the solution grow or decay as a result of viscous damping, instabilities or nonlinear wave-wave interactions. Note that this is only a rough approximation to the azimuthal power spectral density because the points are irregularly spaced around the ring, yet we have assigned an even weighting to each point. Nevertheless, this is justified in practice because this method works well when tested on low-amplitude solutions that are well described by the standing wave in § 3.5, for which we know that the solution is an $m = 2$ wave for both u_r and u_ϕ. Note also that $P_m = P_{-m}$ since $\mathbf{u}$ is real, so we cannot distinguish between waves with

wavenumbers m and $-m$, without also observing the time-dependence of the flow.

The main result that will be discussed in more detail below is that we find that there exists a critical wave amplitude beyond which wave breaking occurs near the centre. Below this amplitude, the waves reflect coherently from the centre, and a steady state is reached in the reference frame rotating with Ω_p, consisting of an $m = 2$ standing wave solution. This is the outcome inferred from linear theory (see §3.5), and we will discuss these cases first, followed by those in which nonlinear effects start to become important. We refer to the former as "low-amplitude" cases, and the latter as "high-amplitude" cases.

3.8 Low-amplitude forcing: coherent reflection

When the simulations are started, transients are excited by the forcing at many different frequencies (and radial wavelengths), centred around $\omega = 1$ in frequency space. As more inward propagating waves are excited by the forcing, an IW train propagates toward the centre. At this stage in the time evolution, the solution is composed of many different frequencies, so our decomposition of the solution into a single IW and OW does not work well. As transients escape the region and are damped, the primary response of the fluid is in the form of waves with frequency $\omega = 1$ and azimuthal wavenumber $m = 2$.

As the waves approach the centre and reflect, an OW is produced. As this process continues, the amplitude of the OW matches that of the IW near the centre. For these low-amplitude cases, the phase change on reflection is negligible. This means that we have coherent reflection from the centre, which allows standing waves to be produced. These waves are stationary in a frame rotating with Ω_p, as expected from linear theory. We confirm that our simulations produce the correct standing wave solution, by plotting an example of a comparison between the simulation and the wave solution in Fig. 3.2. We plot the velocity components in two dimensions for an example simulation in which standing waves have formed, with $\max(\tilde{u}_\phi) \sim 0.3$, in Fig. 3.3.

After a few wave crossing times, the reflection coefficient increases to values approaching unity throughout the grid, though its value decreases with radius, shown in

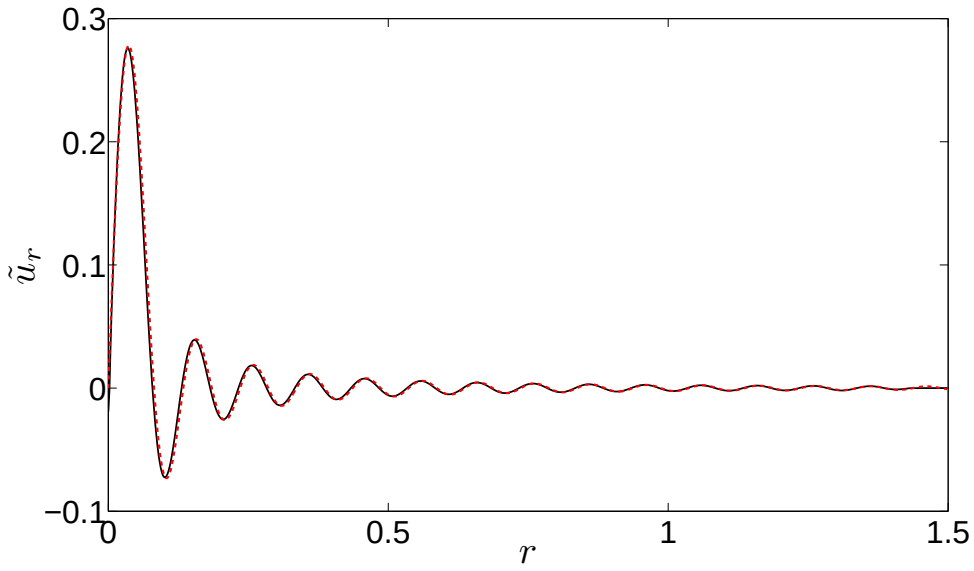

Figure 3.2: Radial velocity along the x-axis for a simulation with forcing amplitude insufficient to cause breaking. The amplitude of this wave is largest within the innermost wavelength. Also plotted is the corresponding analytic standing wave Eq. 3.5.21, converted into a radial velocity using Eq. 3.5.14. This illustrates that our simulations accurately describe the waves for the case in which the waves reflect coherently from the centre.

Fig. 3.4 for a low-amplitude case, with $\max(\tilde{u}_\phi) \sim 0.3$. In this figure we also plot the results of our IW/OW decomposition in a small-amplitude simulation with a resolution 1536×1536. Our reconstructed solutions match the data well except very close to the centre, thus showing that our decomposition works well for these cases.

The decay in $\mathcal{R}$ with radius is a result of the nonzero viscosity, which results in a decay of wave amplitude with time (and therefore distance from where they are excited). The OW has been damped for longer, which results in the amplitude of the OW being smaller than that of the IW. A simple estimate of the amplitude decay due to viscosity with propagation from radius r and then reflected back to r again gives

$$\frac{u_r}{u_{r,0}} \propto \exp\left(-2\int_0^r \frac{\nu k^2}{c_{g,r}} dr\right) \approx \exp\left(-\frac{16\pi^3\nu}{\omega\lambda_r^3} r\right), \tag{3.8.1}$$

since $k \sim k_r$, except near the centre, and $c_{g,r} \simeq \omega\lambda_r/2\pi$, throughout the box. This roughly matches the amplitude decay between A_{in} and A_{out} at $r = 1.2$, implying that the decay in amplitude is indeed due to viscous damping of the waves. In addition, our inviscid exact solution is not exact in the presence of viscosity (see Chapter 7), so

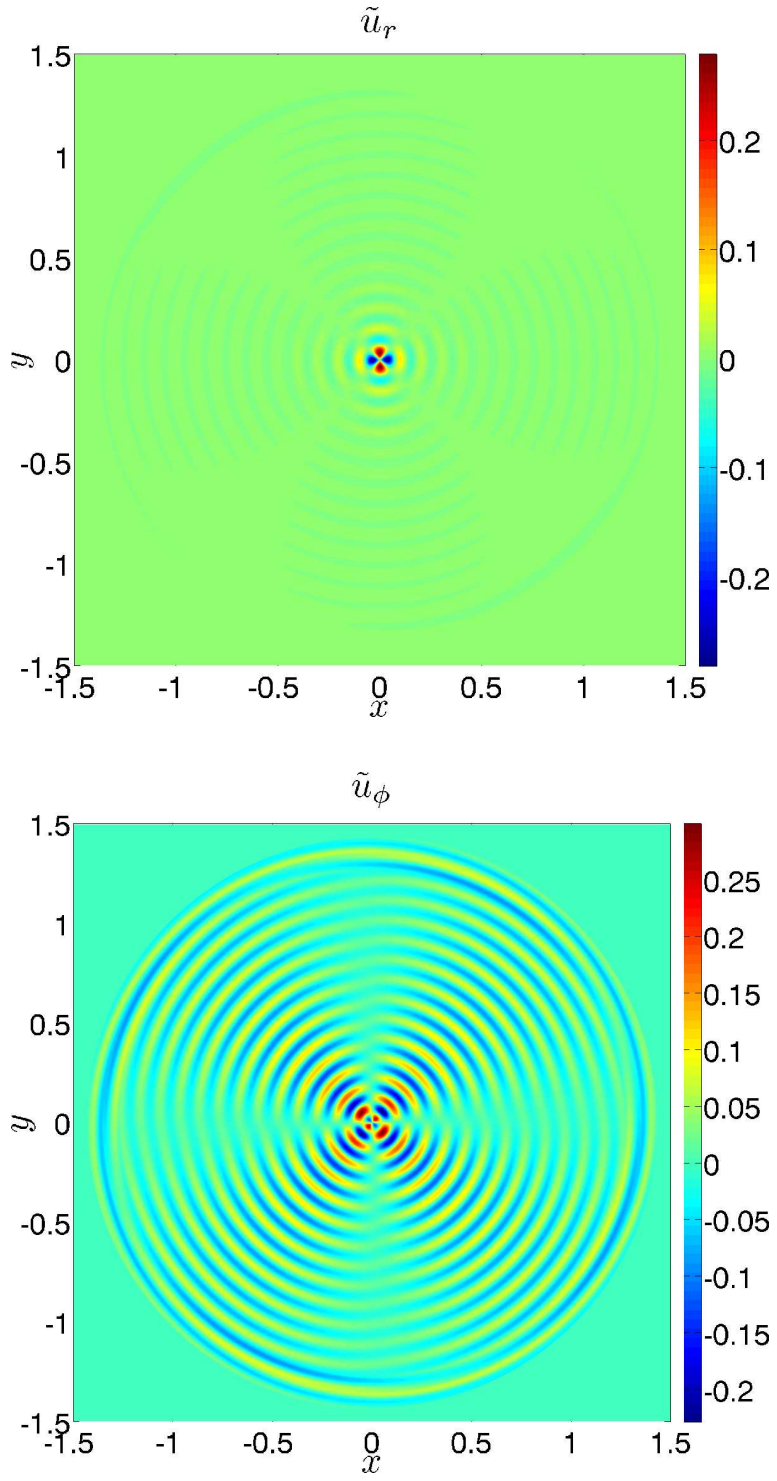

Figure 3.3: 2D plot of the radial (top) and azimuthal (bottom) velocity in the equatorial plane of the star for small-amplitude waves. This is at a time $t = 36t_c$, once standing waves have formed, in a simulation with $\max(\tilde{u}_\phi) \sim 0.3$, in which we have coherent reflection from the centre. In the outer part of the grid, the solution is smoothed to zero to satisfy periodic boundary conditions.

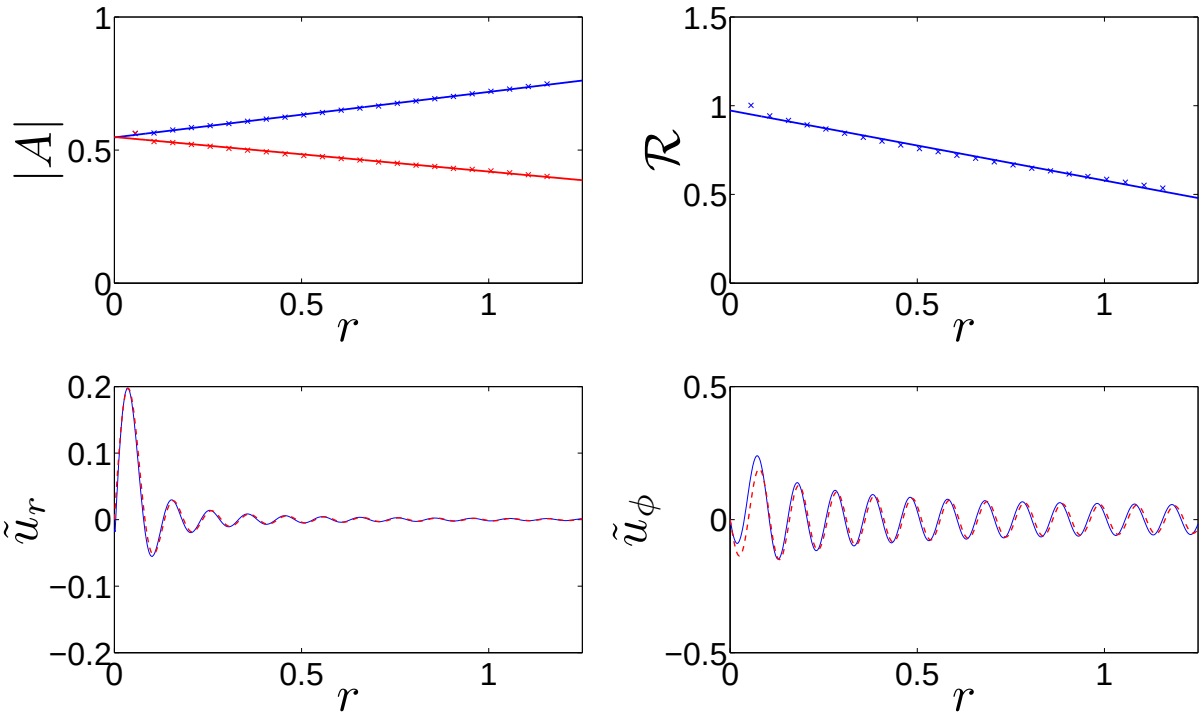

Figure 3.4: Radial velocity along the y-axis (bottom left) and azimuthal velocity along the line $y = x$ (bottom right) in a small-amplitude simulation, after standing waves have been set up at $t = 36t_c$, with $\max(\tilde{u}_\phi) \sim 0.3$ (solid blue lines). Also plotted is the reconstructed solution using A_{in} and A_{out} obtained using the method described in Appendix A.4 (dashed red lines). These are well matched everywhere except near the centre, showing that our decomposition works well for these cases. In the top left we plot $|A_{in}|$ (solid blue line) and $|A_{out}|$ (dashed red line) versus radius, together with a linear fit to each curve. The waves damp as they propagate due to viscosity. In the top right we plot $\mathcal{R}$ versus radius.

nonlinear terms do not vanish for this wave, though their effects are found to be small. We verified that this amplitude decay was due to viscosity by running a low-amplitude simulation with $\nu = 0$, in which case A_{in} and A_{out} no longer decay with radius, once standing waves have formed.

We find that the wave reflects coherently from the centre when $\tilde{u}_\phi \lesssim 0.5$. Long-term simulations ($t \sim$ several hundred t_c) do not show the development of any instabilities that act on waves with $\tilde{u}_\phi \lesssim 0.5$, though there is a slow growth of $m = 0$ components of $\tilde{u}_\phi$ in the solution, as can be seen in Fig. 3.5. In this figure, we plot P_m for the first few even wavenumbers in the flow from an example low-amplitude simulation. Negligible growth in odd m-values is observed, which is consistent with the symmetry of the basic wave, and the quadratic nonlinearities of the Boussinesq-type system. The growth in $m = 0$ is a result of viscosity, which acts to damp the waves and transfer angular momentum from $m = 2$ to the mean flow. This can distinguished from a process resulting from nonlinear interactions, because it is found to depend on ν. To conclude, no instability is observed for waves with $\tilde{u}_\phi \lesssim 0.5$.

3.9 High-amplitude forcing: wave breaking and critical layer formation

If we increase the value of $\tilde{f}_r$, then the above picture changes considerably when a critical wave amplitude is exceeded. Once $\tilde{u}_\phi > \tilde{u}_{\phi,crit} \approx 0.5$, wave breaking occurs near the centre within several wave periods (a few $2\pi/\omega$), and the outcome of the simulations is very different from the small-amplitude case. This occurs when the wave overturns the stratification – see Eqs. 3.5.27 and 3.6.6. In Fig. 3.6 we plot the 2D velocity components after wave breaking has occurred, in a simulation with $\tilde{f}_r = 15$.

For highly nonlinear forcing, for example with $\tilde{f}_r > 20$, the waves break as they reach the centre with sufficient amplitude before there has been any significant reflection. For $\tilde{f}_r \sim 10$, the amplitude of the IW alone is insufficient to cause breaking, and we must wait for reflection at the centre to produce an OW of comparable amplitude before $\tilde{u}_\phi > \tilde{u}_{\phi,crit}$. Once this critical value is exceeded, the waves break. This is an irreversible deformation of the otherwise wavy material contours.

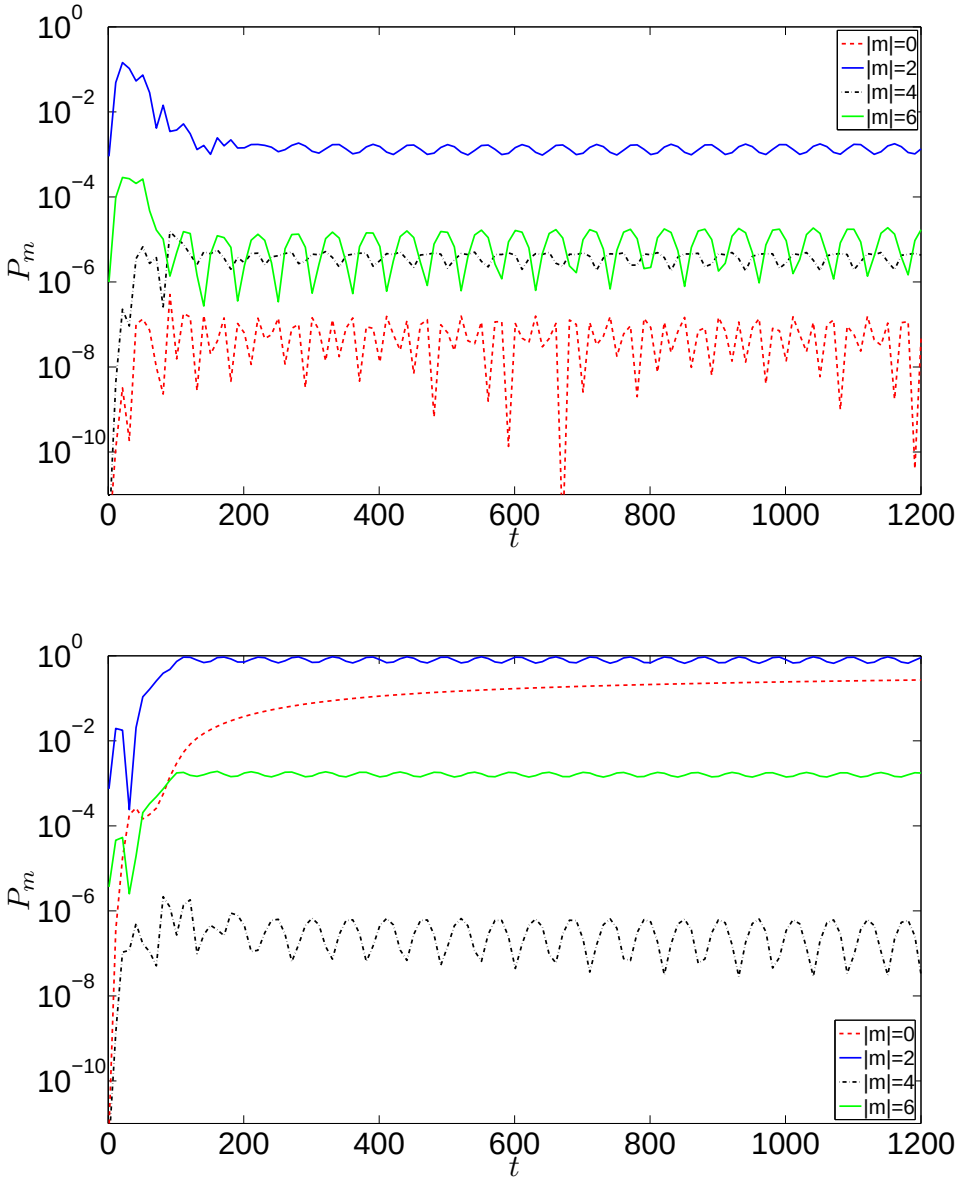

Figure 3.5: Temporal evolution of the power spectral density P_m at $r = 0.1$, in the lowest four azimuthal wavenumbers m in the solution for u_r (top) and u_ϕ (bottom), in a low-amplitude simulation with $\tilde{u}_\phi \sim 0.3$ near the centre, for grid resolution 512×512. The solution is in the form of $m = 2$ waves, and reaches a steady state in the frame rotating with Ω_p. Growth of $m = 0$ is nonzero as a result of viscous damping of the waves. No wave breaking occurs because $\tilde{u}_\phi < 0.5$ in the solution. The $m = 6$ components are most likely due to errors in the Fourier analysis.

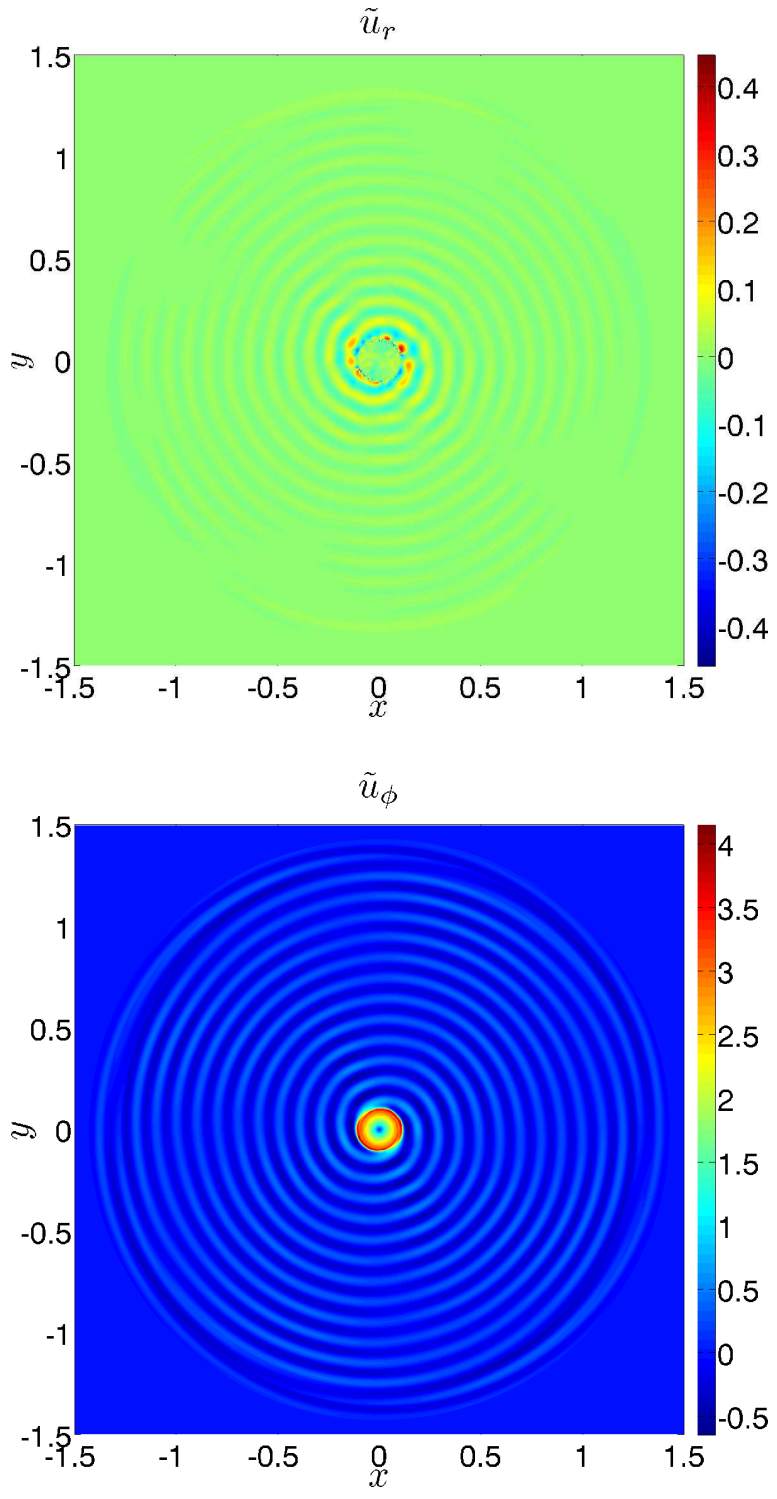

Figure 3.6: Radial velocity (top) and azimuthal velocity (bottom) in a high-amplitude simulation with $\tilde{f}_r = 15$ at $t = 7t_c$, after wave breaking has occurred, from a simulation with a resolution 1536×1536.

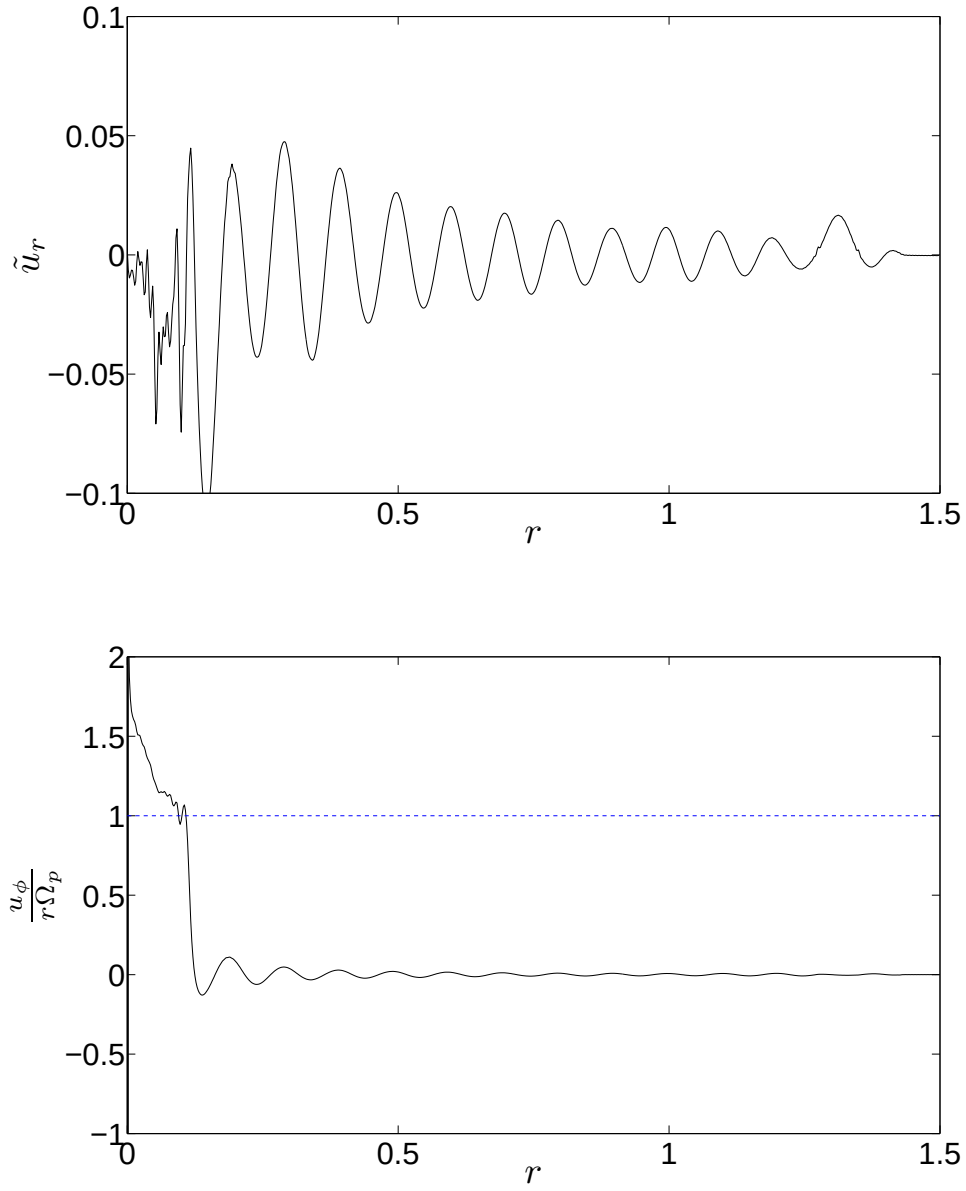

Figure 3.7: The top panel shows the radial velocity along $y = x$ for the same case as Fig. 3.6. The bottom panel shows the angular velocity of the fluid normalised to the angular pattern speed of the forcing Ω_p along the x-axis, at the same time in the simulation. This shows that the central regions after wave breaking are spun up to slightly exceed Ω_p. The critical layer occurs where $u_\phi/(r\Omega_p) = 1$.

Once breaking occurs, we observe consequent mean flow acceleration (i.e. growth of $m = 0$ components of u_ϕ), as the angular momentum of the waves is deposited locally where the wave breaks. This acts to spin up (if $\Omega_p > 0$) the central regions, which at this stage contain a sufficiently small fraction of the angular momentum of the star that their spin can be readily affected by these waves. Once this process has begun, the central regions spin up to $\sim \Omega_p$ (which corresponds with the orbital angular frequency of the planet), and a critical layer is formed, at which the Doppler shifted frequency of the waves goes to zero. At this location, the azimuthal phase velocity of the waves would equal that of the local rotation of the fluid, if they were ever to reach it intact. In reality, as subsequent IWs approach the critical layer, nonlinearities dominate, and the waves undergo breaking before they reach it – though see the discussion in § 3.9.2. We plot the angular velocity of the fluid normalised to Ω_p in the bottom panel of Fig. 3.7.

As IWs approach the critical layer, their radial wavelength decreases, and they slow down, i.e. $\hat{c}_{g,r} \to 0$ as $\hat{\omega} \to 0$. This causes a buildup of wave energy just above the critical layer, in which nonlinearities become important. In this thin region, the quadratic nonlinearities produce higher wavenumber disturbances with even m-values – see § 3.9.1. These are produced by the self-nonlinearity of the primary IW ($m = 2$) as it approaches the critical layer – these self-nonlinearities vanish in the absence of a mean flow. Daughter waves are damped faster than the primary wave because they have lower frequencies and therefore shorter radial wavelengths, which is a result of the theorem proved by Hasselmann (1967). Thus the IW is irreversibly deformed, and transfers its angular momentum to either the mean flow or to daughter waves that are then more easily dissipated by viscosity. The angular momentum carried by these waves must be given to the mean flow when they are dissipated. This process acts to spin up the fluid just above the critical layer to $\sim \Omega_p$. As subsequent IWs are absorbed by the critical layer, the spatial extent of the mean flow expands outwards, i.e. the star is spun up from the inside out. We envisage that this process will continue until the mean flow encompasses the bulk of the RZ, or the planet plunges into the star – this is discussed further in Chapter 5. Long-term simulations, lasting for several hundred t_c, show that this appears to be the case.

This picture is analogous to Goldreich & Nicholson (1989), who propose that early-type stars in close binaries would spin down (if $\Omega > n$, or spin up if $\Omega < n$) from the outside in, once a critical layer has formed near the surface as a result of strong radiative damping of the waves. In our problem, an instability of the primary wave, which occurs once the wave overturns the stratification, causes wave breaking. This results in angular momentum deposition and spin-up (for the case in which $\Omega < n$, spin-down if $\Omega > n$) of the central regions, which causes the formation of a critical layer near the centre of a solar-type star. The rate of expansion of the spatial extent of this region depends on the forcing amplitude; for larger amplitudes it expands faster. The critical layer moves outwards when the dissipation of subsequent IWs deposits sufficient angular momentum to spin up the fluid to $\sim \Omega_p$. In this picture, there is a front of synchronisation which gradually moves outwards.

3.9.1 Growth of different azimuthal wavenumbers in the flow

We now discuss the results of a spectral analysis of the simulation data, to study the growth of the mean flow ($m = 0$), and daughter waves produced by breaking (other $|m| \neq 2$ wavenumbers). We plot P_m for the first few even wavenumbers for a set of examples in Figs. 3.8 and 3.9. Negligible growth in odd m-values is observed, which is consistent with the symmetry of the basic wave and the quadratic nonlinearities (though it is possible in principle for the wave to be unstable to odd-m perturbations).

At the beginning of the simulations $m = 2$ dominates until the primary wave breaks and transfers angular momentum to the mean flow. When subsequent waves approach the critical layer, the primary IW transfers angular momentum to higher m-value disturbances – this can be seen from Fig. 3.8 prior to $t \sim 100$, after which the ring $r = 0.1$ is enveloped by the mean flow. After this, $m = 0$ dominates u_ϕ. On the other hand, u_r is then primarily in the form of $|m| = 2$ disturbances, which from examination of simulation output, counter-rotate with the forcing, and have angular pattern speed $-\Omega_p$. The excitation of these waves could explain the counter-intuitive effect of the most central regions spinning slightly faster than Ω_p, since they carry negative angular momentum. These waves appear to *reflect* from both the $m = 2$ critical layer (though note that these waves do not see this as a critical layer) and

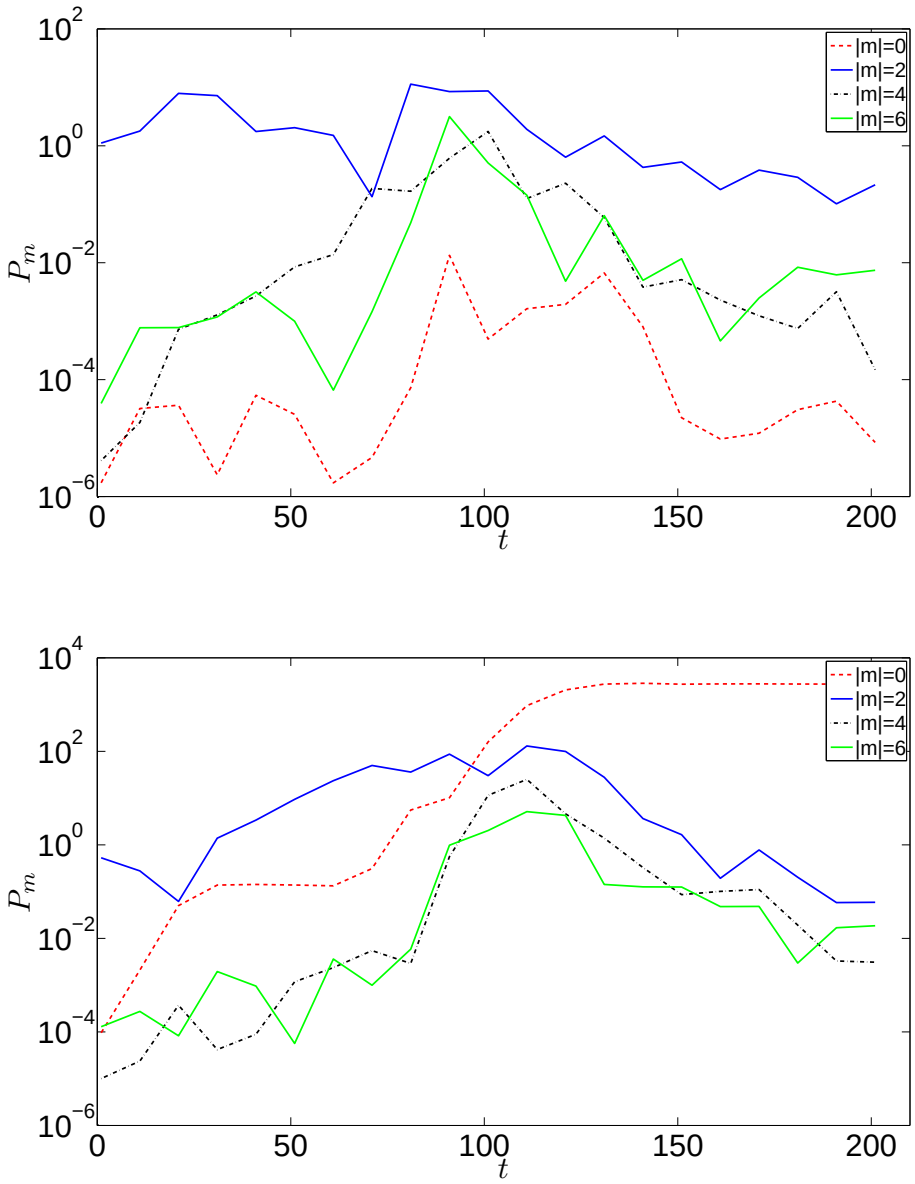

Figure 3.8: Temporal evolution of the power spectral density P_m at $r = 0.1$, in the lowest four even azimuthal wavenumbers m in the solution for u_r (left) and u_ϕ (right), in a simulation with $\tilde{f}_r = 15$ and resolution 1536×1536. The solution is primarily in the form of $m = 2$ waves, until growth of even-m disturbances occurs as the wave breaks. Note that $m = 0$ grows strongest for u_ϕ, i.e., angular momentum is transferred from the primary waves to the mean flow. Once $r = 0.1$ is located inside the rotating region, u_r is primarily composed of $|m| = 2$.

the centre. As these waves approach the $m = 2$ critical layer, since they are counter-propagating waves, their frequency is Doppler shifted upwards towards N, and they undergo total internal reflection. These waves appear to reflect back and forth from the critical layer and the centre.

We also note the appearance of oscillations in the energy in $m = 6$ in the solution. This is most likely due to errors in the Fourier analysis, because we are not sampling the solution with evenly spaced points. Oscillations in $m = 4$ could be due to nonlinearitesthe resulting from the presence of viscosity, since they are also present to some degree in the low-amplitude simulations. The amplitude of these oscillations is much smaller than that of the $m = 2$ or $m = 0$ waves, so should not affect any conclusions drawn from these results.

We experimented with the forcing amplitude to study cases in which the waves were of insufficient amplitude to cause breaking, and ran the simulation for $\sim 100t_c$. We find that, although breaking does not occur, a critical layer can eventually form through the gradual spin-up of the central regions by viscous damping of the primary waves. The results of our spectral analysis of the results of such a simulation are plotted in Fig. 3.9. We clearly see evidence for viscous damping in producing growth of energy in $m = 0$. This can be distinguished from the sudden growth at $t \approx 2200$ which results once a critical layer forms within the first wavelength. We discuss this mechanism further in Chapter 7.

3.9.2 Discussion of wave reflection from the critical layer

Once the critical layer has formed, we find that a large fraction of the IW angular momentum is absorbed near the centre. First, we confirmed this naively, by watching animations of the time dependence of the velocity components. For both components, the wave pattern moves outwards, which corresponds to inward propagating IGWs, so at least a significant fraction of the solution is in the form of IWs. This is quantified by performing our IW/OW decomposition. The results of this for a typical simulation are plotted in Fig. 3.10, where $\tilde{f}_r = 15$. The time has been chosen after the critical layer has formed, and the mean flow has been accelerated near the centre. The IW/OW wave decomposition does not work well near the centre, as we might expect, since

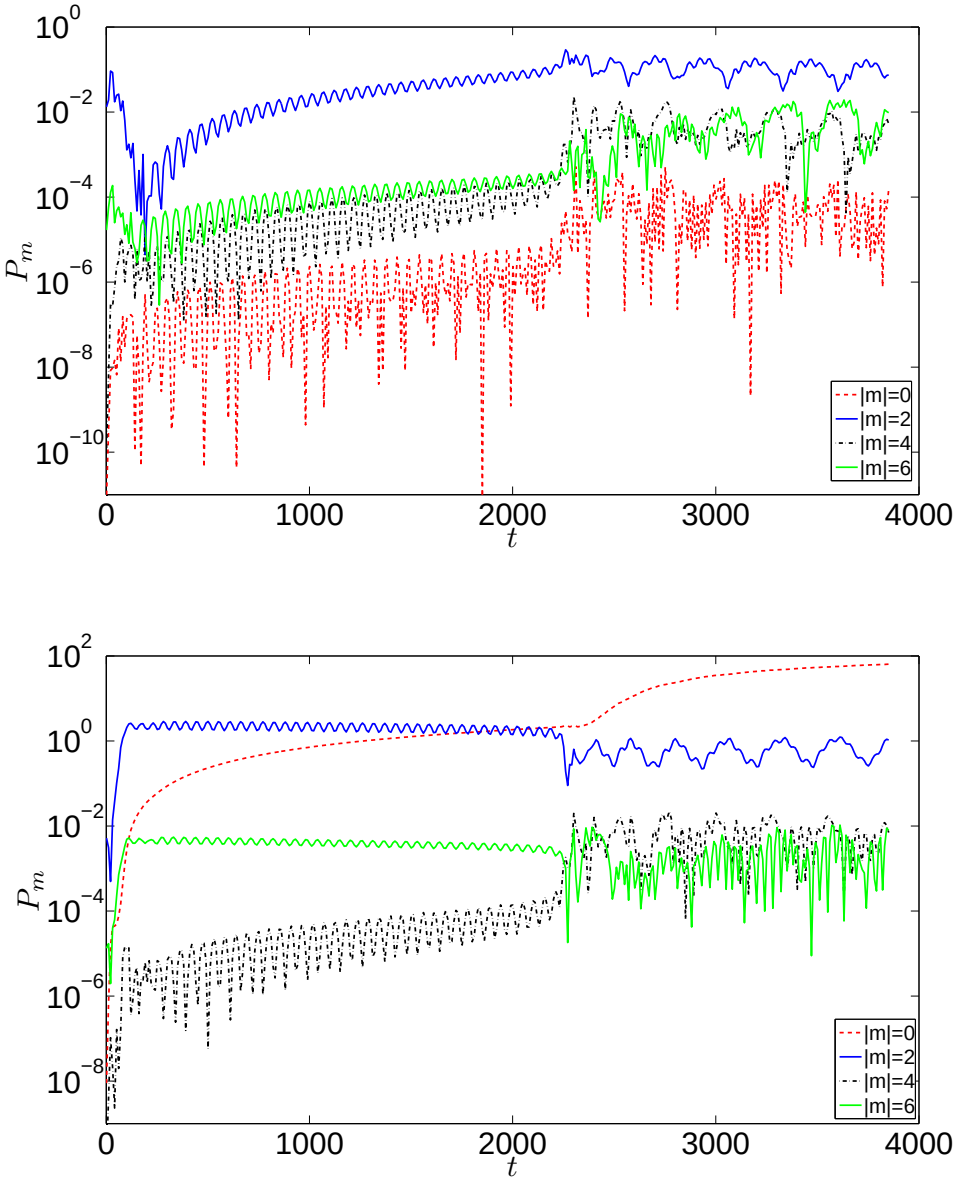

Figure 3.9: Temporal evolution of the power spectral density P_m at $r = 0.1$, in the lowest four even azimuthal wavenumbers m in the solution for u_r (top) and u_ϕ (bottom), in a simulation with $\tilde{f}_r = 2.5$ and resolution 512×512. Until $t = 2200$, viscous damping acts on the waves and transfers angular momentum to the mean flow. A critical layer forms at $t \approx 2200$, resulting in a jump in the growth of $m = 0$, and a drop of energy in $|m| = 2$.

here the disturbance is primarily the mean flow ($m = 0$), though there are also other components. Several wavelengths from the critical layer, in the region $0.3 < r < 1.2$, the reconstructed solution matches the simulation output quite well. The matching is much noisier than in Fig. 3.4, since the solution contains contributions from $m \neq 2$ wavenumbers and $\omega \neq 1$ frequencies, in addition to $m = 2$, $\omega = 1$ waves.

Fig. 3.10 shows that the amplitude of the IW decays as it propagates towards the centre. There is significant absorption of wave angular momentum near the critical layer, as the IW propagates through the mean shear. This results in $|A_{out}| \ll |A_{in}|$, though the reflection is nonzero, so $|A_{out}| \neq 0$. This leads to $\mathcal{R} \ll 1$, in the region where the decomposition works well, which implies that most of the angular momentum in IWs is absorbed near the centre – also note that the energy flux ratio $\propto \mathcal{R}^2 \ll 1$. In addition, the phase of the OW is perturbed with respect to the IW, which inhibits the formation of standing waves. $\mathcal{R}$ oscillates with radius, mainly because the solution is composed of some $\omega \neq 1$ and $m \neq 2$ components, which are not filtered by our IW/OW decomposition.

When a single propagating wave approaches a critical layer, the outcome has previously been found to depend on the ratio of the strength of nonlinear wave-wave couplings to linear viscous and radiative damping. Nonlinear wave-wave couplings occur over a timescale (Booker & Bretherton 1967)

$$t_{NL} = O\left(k_h^{-\frac{2}{3}} |\partial_r U_h|^{-\frac{1}{3}} U_r^{-\frac{2}{3}}\right), \tag{3.9.1}$$

and linear viscous and radiative damping occur over a timescale

$$t_L = O\left(k_h^{-\frac{2}{3}} \chi^{-\frac{1}{3}} |\partial_r U_h|^{-\frac{2}{3}}\right). \tag{3.9.2}$$

The ratio of these terms define the parameter (Maslowe 1986; Koop 1981)

$$\lambda \equiv \frac{t_{NL}}{t_L} \sim \left(\frac{\chi |\partial_r U_h|}{U_r^2}\right)^{1/3}. \tag{3.9.3}$$

where k_h is the horizontal wavenumber, $\partial_r U_h$ is the typical shear in the mean flow, U_r is a typical radial velocity in the wave, and χ is a diffusivity – which for the centre of a star is likely to be primarily radiative diffusion rather than viscosity, so χ will be

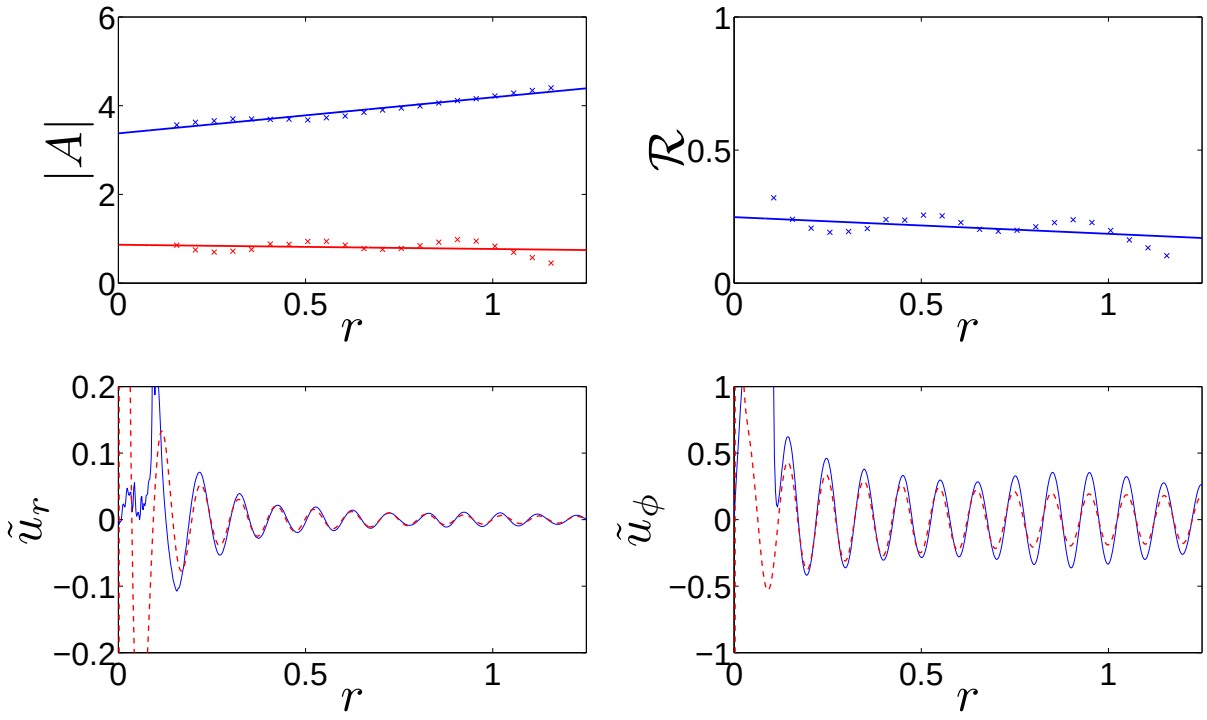

Figure 3.10: Radial velocity along the line $y = x$ (bottom left) and azimuthal velocity along the x-axis (bottom right) in a large-amplitude simulation after wave breaking, at $t = 7t_c$, with $\tilde{f}_r = 15$. These are plotted (blue solid lines) together with the reconstructed solution using A_{in} and A_{out} obtained from the method described in Appendix A.4 (red dashes lines) – these are quite well matched for $r \in [0.3, 1.2]$. The top left panel shows A_{in} (top line) and A_{out} (bottom line) versus radius. There is significant absorption of IWs near the critical layer at $r \sim 0.1$, resulting in $|A_{out}| \ll |A_{in}|$. The top right panel shows $\mathcal{R}$ versus radius. $\mathcal{R} \ll 1$ in the region where the decomposition works well.

primarily the thermal conductivity κ.

Nonlinearity acts to promote energy transfer away from the critical layer through the generation of daughter waves, and linear damping acts to suppress this resonant wave production. If $\lambda \gg 1$, then the time required for nonlinear effects to become important is long compared with that for linear damping to become important. In this limit, there is negligible wave reflection, and nearly all incoming wave energy is absorbed by the critical layer, as predicted by Hazel (1967). In the opposite limit, when $\lambda \ll 1$, nonlinear effects become manifest prior to the time when they become suppressed by linear damping. In this case, the flow can be extremely complicated, and nonlinearity in the critical layer region can lead to wave reflection, with ampltiudes $O\left(\exp\left(-\pi(Ri-1/4)^{1/2}\right)\right)$ or less (Breeding 1971). In this limit, nonlinear wave-wave couplings lead to the generation of many smaller-scale daughter waves, some of which propagate away from the critical layer, carrying a fraction of the wave energy (Fritts 1979). Experiments of internal waves approaching a critical layer have been performed by Koop (1981) and Koop & McGee (1986), in which $\lambda = O(1)$. For this value, the effects of both nonlinearity and linear damping become manifest at approximately the same time. Their laboratory experiments show that wave reflection, in the form of daughter waves produced by nonlinear couplings, that propagate away from the critical layer, is suppressed by viscosity for this value of λ.

Relating these results to our simulations, we find typical values of the parameter $\lambda \sim 10^{-1}$ near the critical layer, due to the explicit viscosity ($\nu = 2\times10^{-6}$) added in the code, since $|\partial_r U_h| \sim O(10^1)$ and $U_r = \tilde{u}_r \sim 0.1$. In this limit nonlinearities are likely to become important before viscous diffusion. Since this is the limit in which we would be expected to find wave reflection, if any occurs at all, and we find little reflection of waves from the critical layer, it is likely that most of the IWs are absorbed near to the centre, and not reflected. In any case, the reflected waves will not have the same frequency and horizontal wavenumber as the primary wave. Instead, reflected waves will be in the form of disturbances with smaller frequencies, and therefore shorter radial wavelengths, as well as higher m-values, as a result of wave-wave coupling (Hasselmann 1967). Such disturbances will be more easily dissipated by radiative diffusion, since the rate of energy dissipation $\sim m^3/\omega^4$.

We conclude that if wave breaking and critical layer formation occurs, it is probably reasonable to assume that the IWs are entirely absorbed in the RZ, primarily near to the critical layer. This is inferred from our simulations, as can be seen in the example in Fig. 3.10, in which $|A_{out}| \ll |A_{in}|$. The result of this is that if wave breaking and critical layer formation occurs, it is not possible for global standing modes to develop in the RZ. It would then be appropriate to calculate the tidal dissipation rate using the method of GD98. This is discussed in Chapter 5.

3.10 Conclusions

In this chapter, we have presented a study of the fate of IGWs approaching the centre of a solar-type star, primarily using two-dimensional numerical simulations. A train of IGWs is excited which propagates towards the centre. These waves break if they reach the centre with steepness sufficient to overturn the stratification, which in 2D corresponds to $\tilde{u}_\phi \gtrsim 0.5$. Once this occurs, nonlinear effects cause the subsequent formation of a critical layer, as the waves transfer their angular momentum to the mean flow, bringing the central regions of the star into corotation with the tidal forcing. This acts as an absorbing barrier for subsequent IWs, which continue to be absorbed near the critical layer, resulting in an expansion of the spatial extent of the mean flow. By decomposing the numerical solutions into an IW and OW, we find that *if critical layer formation occurs*, most of the angular momentum of the IW is absorbed near the centre, and is not reflected. This has very important implications for tidal dissipation in solar-type stars. These issues will be discussed in detail in Chapter 5. If critical layer formation, by wave breaking, does not occur, the wave is approximately perfectly reflected from the centre, and global standing modes can be set up in the RZ.

The general picture of this process is that the star spins up (or down) from the inside out, until either the planet has plunged into the star, or the RZ of the star has spun up (or down) to match that of the evolving orbit. This is discussed further in Chapter 5. In Chapter 6 we study the stability of the nonlinear gravity wave derived in § 3.5 to understand the instability that leads to wave breaking in more detail, and to determine what instabilities may set in for waves with insufficient amplitudes to overturn the stratification. In the next chapter, we extend these simulations to three

dimensions.

Chapter 4

Internal wave breaking near the centre of a solar-type star: 3D simulations

In the previous chapter, we derived a Boussinesq-type system of equations that is relevant for describing the dynamics of IGWs approaching the centre of a solar-type star. We then performed numerical simulations, solving these equations in two dimensional cylindrical geometry. In this chapter, we extend these simulations to three-dimensional spherical geometry, and confirm that the most important results of the previous chapter are not affected by this extension.

4.1 Tidal potential

The tidal potential experienced by a star hosting a short-period planet can be written in standard spherical polar coordinates (r, θ, ϕ) as a sum of rigidly rotating spherical harmonics

$$\mathrm{Re}\left[\Psi_{l,m} r^l Y_l^m(\theta,\phi) e^{-i\omega t}\right], \tag{4.1.1}$$

in a non-rotating (but non-inertial) reference frame centred on the star, where Y_l^m is a spherical harmonic (normalised such that the integral of $|Y_l^m|^2$ over solid angles is unity) and $\Psi_{l,m}$ is an amplitude. Here ω is the frequency in that frame, related to the

tidal frequency by $\hat{\omega} = \omega - m\Omega$, where Ω is the spin angular frequency of the star. In this paper we consider the waves excited by planets on circular, coplanar orbits, as in Chapter 3. In this case the dominant component of the tidal potential is quadrupolar ($l = 2$), with $m = 2$, and takes the form

$$\Psi(r, \theta, \phi, t) = -\sqrt{\frac{6\pi}{5}} \frac{G m_p}{a^3} r^2 Y_2^2(\theta, \phi - \frac{\hat{\omega}}{2} t), \tag{4.1.2}$$

where m_p is the planetary mass and a is its orbital semi-major axis. Since most short-period planets orbit faster than their stars spin, as a result of stellar magnetic braking, we take the star to be (initially) non-rotating, so that $\hat{\omega} = \omega = 2n$, where n is the orbital angular frequency of the planet.

4.2 Linear theory

In this section we derive a linear wave solution, starting from the Boussinesq-type system Eqs. 3.4.29–3.4.32, that was derived in 2D but is equally valid in 3D. Using the non-dimensionalisation of §3.5, we can then linearise about hydrostatic equilibrium in 3D spherical geometry, seeking solutions steady in the frame rotating at the angular rate Ω_p, proportional to $e^{im\xi}$, where $\xi = \phi - \Omega_p t$ is the azimuthal coordinate in this frame. This leads to the following equations:

$$-imu_r = -\partial_r q + rb, \tag{4.2.1}$$

$$-imu_\theta = -\frac{1}{r}\partial_\theta q, \tag{4.2.2}$$

$$-imu_\phi = -\frac{im}{r\sin\theta} q, \tag{4.2.3}$$

$$-imb = -ru_r, \tag{4.2.4}$$

$$\frac{1}{r^2}\partial_r(r^2 u_r) + \frac{1}{r\sin\theta}\partial_\theta(\sin\theta u_\theta) + \frac{im}{r\sin\theta} u_\phi = 0. \tag{4.2.5}$$

To obtain the linear solution, we expand scalar quantities (i.e. q and b) in spherical harmonics $Y_l^m(\theta, \xi)$, since the problem is separable in both angular coordinates. In Eqs. 4.2.1–4.2.5 we have already included the ξ-dependence of these functions ($e^{im\xi}$).

We thus take

$$q = \hat{q}(r) Y_l^m(\theta, 0), \tag{4.2.6}$$

so that the total functions are expanded onto $Y_l^m(\theta, \xi)$, and similarly for b and u_r, where from now on we drop the hats on the radial functions. The remaining velocity components are expanded onto angular functions as appropriate to satisfy Eqs. 4.2.1–4.2.5. The relation

$$q = \frac{im}{l(l+1)} \partial_r (r^2 u_r), \tag{4.2.7}$$

follows from incompressibility and the result

$$\left[\frac{1}{\sin\theta} \partial_\theta \sin\theta \partial_\theta Y_l^m + \frac{1}{\sin^2\theta} \partial_\phi^2 Y_l^m \right] = -l(l+1) Y_l^m. \tag{4.2.8}$$

This enables us to derive the linear differential equation

$$\partial_r^2 (r^2 u_r) - \frac{l(l+1)}{m^2} (m^2 - r^2) u_r = 0, \tag{4.2.9}$$

whose solutions can be written in terms of Bessel functions of half-integer order (alternatively these can be written as spherical Bessel functions, or they can be reduced to elementary functions). The corresponding (total) linear solution for a standing wave in 3D can be written (where real parts are assumed to be taken)

$$\begin{aligned}
u_r(r, \theta, \xi) &= B r^{-\frac{3}{2}} J_{l+\frac{1}{2}}(kr)\, Y_l^m(\theta, \xi), & (4.2.10)\\
u_\theta(r, \theta, \xi) &= \frac{B}{l(l+1)} \frac{1}{r} \partial_r \left[r^{\frac{1}{2}} J_{l+\frac{1}{2}}(kr) \right] \partial_\theta Y_l^m(\theta, \xi), & (4.2.11)\\
u_\phi(r, \theta, \xi) &= \frac{imB}{l(l+1)} \frac{1}{r} \partial_r \left[r^{\frac{1}{2}} J_{l+\frac{1}{2}}(kr) \right] \frac{1}{\sin\theta} Y_l^m(\theta, \xi), & (4.2.12)\\
b(r, \theta, \xi) &= -\frac{iB}{m} r^{-\frac{1}{2}} J_{l+\frac{1}{2}}(kr)\, Y_l^m(\theta, \xi), & (4.2.13)
\end{aligned}$$

where $B \in \mathbb{C}$ is an amplitude, and

$$k = \frac{1}{m} \sqrt{l(l+1)}. \tag{4.2.14}$$

IW and OW solutions can be obtained by replacing the Bessel function of the first kind by equivalent Hankel functions of the first $(J_\nu + iY_\nu)$ and second kinds $(J_\nu - iY_\nu)$, respectively. Note also that

$$\frac{1}{r}\partial_r\left[r^{\frac{1}{2}}\left(J_{l+\frac{1}{2}}(kr) \pm iY_{l+\frac{1}{2}}(kr)\right)\right] = r^{-\frac{3}{2}}\left[(1+l)\left(J_{l+\frac{1}{2}}(kr) \pm iY_{l+\frac{1}{2}}(kr)\right)\right.$$
$$\left. -kr\left(J_{(l+1)+\frac{1}{2}}(kr) \pm iY_{(l+1)+\frac{1}{2}}(kr)\right)\right]. \quad (4.2.15)$$

Starting from Eq. 3.4.33, we can calculate a conserved energy flux. Integrating this equation over ξ from 0 to 2π, eliminates the terms containing derivatives in t and ϕ due to periodicity in ξ, as a result of the fundamental theorem of calculus. This allows the definition of a conserved quantity proportional to the energy flux,

$$F = \int_0^\pi \int_0^{2\pi} r^2 \sin\theta u_r (E+q) d\xi d\theta. \quad (4.2.16)$$

For linear waves, terms involving products are small, so $E \ll q$, to this order. This leaves

$$F = \pi r^2 \int_0^\pi \mathrm{Re}\left[u_r q^*\right] \sin\theta d\theta. \quad (4.2.17)$$

Whether this is positive or negative depends on whether the wave is ingoing or outgoing.

Substituting the linear solution Eq. 4.2.10 into Eq. 4.2.17 provides a simple expression for the flux of a single l, m wave:

$$F = \frac{m}{\pi l(l+1)}(|A_{out}|^2 - |A_{in}|^2), \quad (4.2.18)$$

with corresponding energy flux $F_r^E = \rho_0 F$, and angular momentum flux $F_r^L = \frac{\rho_0 m}{\omega} F$. This follows from the orthonormality of spherical harmonics and the Wronskian of the Hankel functions

$$\int_0^{2\pi}\int_0^\pi Y_l^m(\theta,\xi)[Y_{l'}^{m'}(\theta,\xi)]^* \sin\theta d\theta d\xi = \delta_l^{l'}\delta_m^{m'}, \quad (4.2.19)$$

$$W[J_\nu(kr) + iY_\nu(kr), J_\nu(kr) - iY_\nu(kr)] = \frac{4}{i\pi r}. \quad (4.2.20)$$

In particular, the $l = m = 2$ wave has the components

$$u_r(r,\theta,\xi) = Br^{-\frac{3}{2}} J_{\frac{5}{2}}(kr)\, Y_2^2(\theta,\xi), \tag{4.2.21}$$

$$u_\theta(r,\theta,\xi) = \frac{B}{l(l+1)} \frac{1}{r} \partial_r \left[r^{\frac{1}{2}} J_{\frac{5}{2}}(kr) \right] \partial_\theta Y_2^2(\theta,\xi), \tag{4.2.22}$$

$$u_\phi(r,\theta,\xi) = \frac{imB}{l(l+1)} \frac{1}{r} \partial_r \left[r^{\frac{1}{2}} J_{\frac{5}{2}}(kr) \right] \frac{1}{\sin\theta} Y_2^2(\theta,\xi), \tag{4.2.23}$$

$$b(r,\theta,\xi) = -\frac{iB}{m} r^{-\frac{1}{2}} J_{\frac{5}{2}}(kr)\, Y_2^2(\theta,\xi), \tag{4.2.24}$$

where $k = \sqrt{6}/2$.

4.2.1 Criterion for overturning isentropes

A condition in 3D for isentropic overturning can be derived from considering when the radial gradient of the entropy $s = b + \frac{1}{2}r^2$ becomes negative. This occurs when $|\frac{1}{r}\partial_r(ru_r)| > |m|$. To correlate our notation with the appendix of OL07, we define the dimensionless nonlinearity parameter A, such that overturning occurs if $|A| > 1$. This is defined such that the radial velocity is the real part of

$$u_r = 40Ar^{-4} \left[\frac{1}{\sqrt{6}} \left(1 - \frac{1}{2}r^2 \right) \sin kr - \frac{1}{2} r \cos kr \right] \sin^2\theta e^{im\xi}, \tag{4.2.25}$$

in the dimensionless units that we have been using in this section (this is equivalent to Eq. 4.2.21).

Overturning is achieved at the centre when the radial velocity in the wave takes a maximum value $u_r = 1.27$ at its innermost peak at $r = 2.04$. This value is used to compare it to the magnitude of the radial velocity achieved in numerical simulations at the onset of wave breaking. In these dimensionless units, we similarly require $u_\phi \gtrsim 0.99$ or $b \gtrsim 0.38$. If we instead normalise the dimensional fluid velocity with the constant (asymptotic) radial group velocity, then we obtain a different non-dimensionalisation[1], that we previously used in Chapter 3. In those units, the criterion is modified to $\tilde{u}_\phi \gtrsim 0.49$. Note that there is not such a simple interpretation of the criterion on u_ϕ as in 2D, though the value is quantitatively very similar. From the results of the 2D simulations in the previous chapter, we expect the waves to undergo instability and

[1]In the figures below, we also use this nondimensionalisation. This is identical to Chapter 3, and gives values exactly 1/2 of those in the units of this section.

break within several wave periods after these criteria begin to be satisfied.

4.2.2 Weakly nonlinear theory

The linear solution written down in Eqs. 4.2.10–4.2.13 is not a nonlinear solution, unlike the equivalent in 2D. This can be shown by computing the nonlinear terms in the full Boussinesq-type system using the linear solution, in Mathematica, for example. We find that $\mathbf{u} \cdot \nabla b \neq 0$, in general, and similarly for the nonlinear terms in the momentum equation. This means that the reflection of the waves from the centre could be different than in 2D, since nonlinearities do not vanish for this wave. In this section we perform a weakly nonlinear analysis to determine the dominant nonlinear effects for small amplitudes. Since these nonlinearities do not vanish, this highlights the importance of numerical simulations for these waves approaching the centre. We describe the results of such simulations in § 4.4.

We propose a weakly nonlinear solution of the form

$$\begin{aligned} u_r(r,\theta,\xi) &= \frac{\epsilon}{2}\{u_{r1}(r,\theta)e^{i\xi} + u^*_{r1}(r,\theta)e^{-i\xi}\} \\ &\quad +\epsilon^2\{u_{r20}(r,\theta) + \frac{1}{2}\left(u_{r22}(r,\theta)e^{2i\xi} + u^*_{r22}(r,\theta)e^{-2i\xi}\right)\} \\ &\quad +\epsilon^3 u_{r3}(r,\theta,\xi) + O(\epsilon^4), \end{aligned} \tag{4.2.26}$$

and similarly for the other variables, where $\epsilon \ll 1$. Here we write $u_{r1}(r,\theta)e^{i\xi} = u_r(r,\theta,\xi)$ from Eq. 4.2.21, for the $l = m = 2$ wave above, and similarly for other variables. We substitute these expansions into the Boussinesq-type system and equate powers of ϵ. At each order we also equate coefficients of $e^{in\xi}$. At leading order only one mode is present, and we obtain the previously derived linear solution. The incoming wave generates harmonics through the quadratic nonlinearities. These additional waves (other than $m = 0$) will escape to infinity and carry away a portion of the energy flux. After some algebra the solution at $O(\epsilon^2)$ can be computed to give

$$u_{r22}(r,\theta,\xi) = A_{22}r^{-\frac{3}{2}}\left[J_{9/2}\left(\sqrt{5/6}kr\right) + iY_{9/2}\left(\sqrt{5/6}kr\right)\right]Y_4^4(\theta,\xi), \tag{4.2.27}$$

which is an $l = m = 4$ wave with complex amplitude A_{22}, which has been computed using Mathematica and given in terms of A.

For the wave described by Eq. 4.2.27, F can be computed. The ratio of the energy flux in the outgoing $l = m = 4$ wave to the ingoing $l = m = 2$ wave can be shown to be approximately $1.2 \times 10^{-5}|A|^2$, so the reflection coefficient for reflection from the centre, for a weakly nonlinear $l = m = 2$ wave, is

$$|\mathcal{R}|^2 \approx 1 - 1.2 \times 10^{-5}|A|^2. \tag{4.2.28}$$

This means that a weakly nonlinear primary wave (with $|A| \ll 1$), will reflect approximately perfectly from the centre, with a reflection coefficient that is close to unity. However, a small fraction of the IW energy flux is transferred to waves with higher l and m-values, reinforcing the fact that Eqs. 4.2.10–4.2.13 is not an exact solution, contrary to the analogous solution in 2D.

4.3 Numerical set-up

We solve the Boussinesq-type system in three dimensions using the Cartesian pseudospectral code SNOOPY, as in Chapter 3. However, we modify the forcing and damping to take into account the z-direction, and instead of forcing an $m = 2$ wave in the equatorial plane, we now have

$$\begin{aligned} \mathbf{f} &= -f_r \mathrm{Re}\left[Y_2^2(\theta, \phi - \frac{\omega}{2}t)\right] \mathbf{e}_r, \\ &= -f_r \frac{1}{4}\sqrt{\frac{15}{2\pi}}\frac{1}{r^2}\left\{\left(x^2 - y^2\right)\cos\omega t - 2xy \sin\omega t\right\} \mathbf{e}_r, \end{aligned} \tag{4.3.1}$$

in Cartesian coordinates (with $r^2 = x^2 + y^2 + z^2$), which is applied in the region $0.85 r_{box} \leq r \leq 0.9 r_{box}$. We study a region $x, y, z \in [-r_{box}, r_{box}]$, where $r_{box} = 1.5$, in arbitrary units (not the same as § 4.2). For $r > 0.9 r_{box}$ the solution is damped to zero by using a parabolic smoothing function.

We primarily use a resolution of 256^3, for which the simulations were possible to run on a single Intel Core i7 machine, utilising all 8 cores, with a typical run time of several weeks to resolve a hundred wave crossing times. We set $\omega = 1, \lambda_r = 0.15, \nu = 4 \times 10^{-6}, \kappa = 0$. An otherwise identical setup is used as in Chapter 3, except using spherical geometry instead of cylindrical geometry. A typical IGW wavelength of

$\lambda_r = 0.15$ is chosen, which is slightly larger than that for most of the 2D calculations. This increases the number of grid points within a wavelength of the primary wave, partially offsetting the reduction in resolution that results from using a smaller number of grid points per dimension than in 2D. Choosing larger wavelengths than this is found to result in unwanted effects from the proximity of the forcing region, which modifies the linear solution. We have confirmed that the linear solution is well reproduced with this numerical setup.

4.4 Numerical results

In this section we describe the results of the numerical simulations. We find that $\tilde{f}_r \equiv f_r 2\pi/(\omega^2 \lambda_r) \gtrsim 0.2$ is required for breaking, so a variety of simulations are performed with forcing amplitudes either side of this value. The basic results of these simulations are that the wave reflects approximately perfectly from the centre of the star if the amplitude of the wave is smaller than a certain critical value, which is found to correspond with that required for isentropic overturning. Above this value, wave breaking and critical layer formation occur. This picture is identical to that in 2D.

4.4.1 Low-amplitude simulations

For a low-amplitude simulation, with $\max(\tilde{u}_r)$ below the critical value for isentropic overturning (using $\tilde{f}_r = 0.1$), we plot the variation in amplitudes of the IWs and OWs, and also the reconstructed solutions in Fig 4.1. We analyse the results using the method described in Appendix A.4, choosing a time once transients have been sufficiently damped and standing waves have formed. The decay in radius is roughly (though slightly smaller than) that which would be expected from viscous damping, by the fractional amount

$$\frac{u_r}{u_{r,0}} \approx \exp\left(-2\int_0^r \frac{\nu k^2}{c_{g,r}} dr\right), \tag{4.4.1}$$

where $c_{g,r} = C\lambda_r^2/(2\pi^2)$ is the (constant asymptotic) radial group velocity, for a wave of the given wavelength. As in 2D, we have confirmed this explanation by running simulations without viscosity, which are found to not exhibit this decay (though these

simulations eventually become numerically unstable if $\nu = \kappa = 0$). Using a smaller viscosity is also found to reduce the wavelength-scale oscillations around the mean slope. These result from the fact that the linear solution to the forced wave problem is no longer exact in the presence of viscosity. We find that increasing the number of grid points within each shell (by reducing the values of i_{step}, j_{step} and k_{step}) slightly reduces the vertical extent of these oscillations, because this averages out the errors that result from the assumption that the inviscid linear solution is exact. However, increasing the number of grid points within each shell has negligible effect on the mean slope.

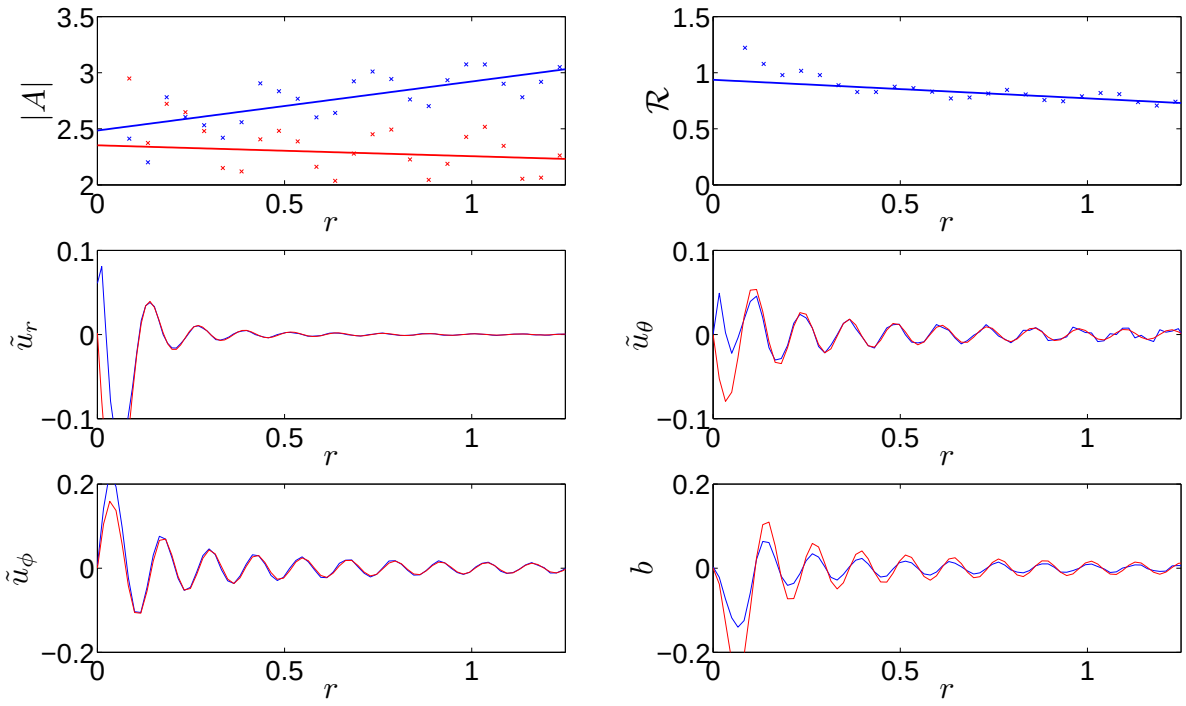

Figure 4.1: In the top left panel we plot A_{in} (blue) and A_{out} (red) vs. r, from a low-amplitude simulation in which the primary wave approximately perfectly reflects from the centre, with $\mathcal{R}$ displayed in the top right panel. Below, are the velocity components and the buoyancy variable (blue), plotted together with the reconstructed linear solution (red), against radius. This is taken from a simulation with $\tilde{f}_r = 0.1$ at $t = 250$, once standing waves have formed. The amplitude decay with radius can be explained as due to viscous damping.

The spatial structure of the solutions in three dimensions in the xy-plane is very similar to that in two dimensions, as can be seen in Fig. 4.2 (which can be compared

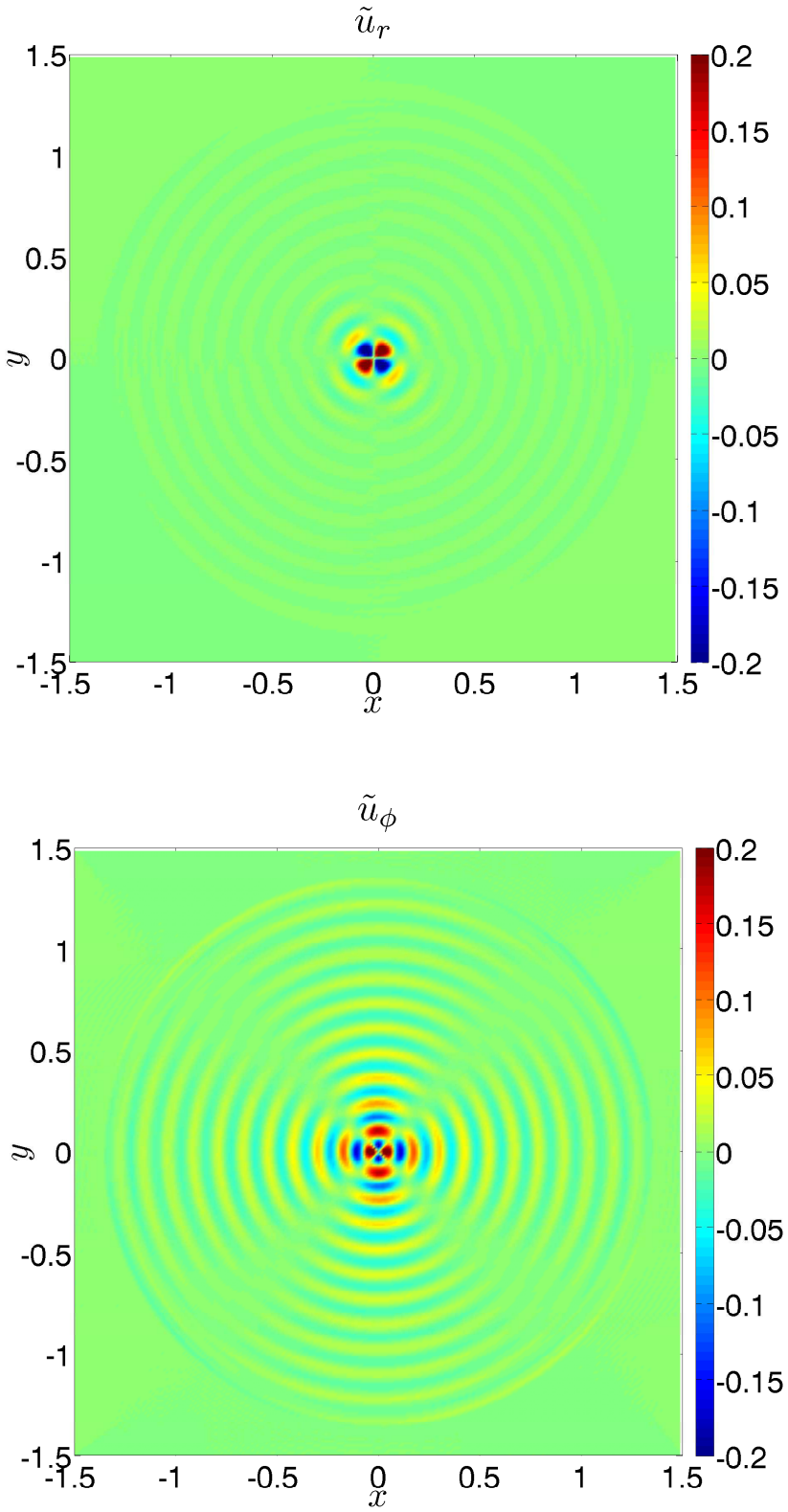

Figure 4.2: 2D plots of $\tilde{u}_r$ (top) and $\tilde{u}_\phi$ (bottom) on the xy-plane for a simulation in which the wave perfectly reflects from the centre, for which $\tilde{f}_r = 0.1$. This can be qualitatively compared with Fig. 3.3.

with Fig. 3.3). In Fig. 4.3, we plot $\tilde{u}_\phi$ on the xz-plane. This shows that the magnitude of the azimuthal velocity peaks at $\theta = \pi/2$, due to the latitudinal form of Y_2^2.

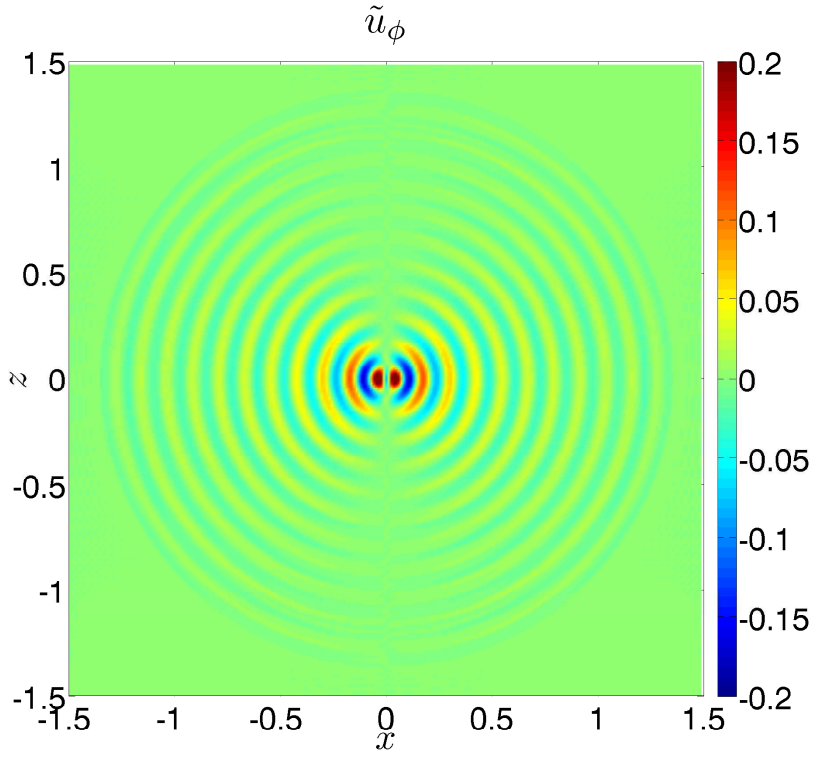

Figure 4.3: 2D plot of $\tilde{u}_\phi$ on the xz plane for a simulation in which the wave perfectly reflects from the centre, for which $\tilde{f}_r = 0.1$. $\tilde{u}_\phi$ is of largest magnitude in the equatorial plane, where $|Y_2^2|$ peaks.

From the calculation in § 4.2.2, we expect the effects of nonlinearity to be much weaker than the effects of viscosity for small-amplitude waves which do not cause isentropic overturning. Since the effects of weak nonlinearity are very small, it is difficult to quantitatively confirm the results in § 4.2.2, using, for example, an extension of the method described in Appendix A.4 for multiple l and m values. Nevertheless, we have qualitatively confirmed the result that the reflection is coherent and nearly perfect (in that $\mathcal{R} \approx 1$) for amplitudes below that required for overturning the stratification. As in 2D we do not observe any instabilities that act on the waves when they have insufficient amplitude to overturn the stratification. In this case, the waves can form global modes in the RZ.

4.4.2 High-amplitude simulations

In high-amplitude simulations, in which the wave amplitude exceeds the overturning criterion, the wave overturns the stratification during part of its cycle and a rapid instability acts on the wave, which leads to wave breaking within $1-3$ wave periods. This causes the rapid (within several wave periods) deposition of primary wave angular momentum, which spins up the mean flow to Ω_p and produces a critical layer. This critical layer acts as an absorbing barrier for IWs, as is shown from Fig. 4.4, which plots the variation in amplitude of the IW and OW, and also the reconstructed wave solutions (which can be contrasted with Fig. 4.1). Once the critical layer has formed, we find $|A_{out}| \ll |A_{in}|$. The central regions are not well described by the linear model, as we would expect. However, the region outside of $r \approx 0.25$ is well described by the linear solution, with $|A_{out}| \ll |A_{in}|$. In this region, $\mathcal{R} \ll 1$, so it is reasonable to assume that the IWs are efficiently absorbed near the centre. This picture is identical to that in 2D.

The picture in 3D in the xy-plane is very similar to that in 2D, as can be seen in Fig. 4.5 (to compare with Fig. 3.6). However, one noticeable difference is that the primary wave preferentially transfers its angular momentum at low latitudes, close to the equatorial plane. This can be seen in Fig. 4.6, where we plot the angular frequency of the flow normalised to Ω_p once a critical layer has formed, in both the xy and xz planes. This is a consequence of the latitudinal form of Y_2^2, whose magnitude peaks at $\theta = \pi/2$, as is illustrated in Fig. 4.3. The critical layer absorption is observed to continue as the wave forcing is ongoing, so this differential rotation is continually reinforced by the absorption of $l = m = 2$ IWs. Since there are wave motions in the region of fluid interior of the critical layer, parts of these regions spin slightly faster than Ω_p (this is not seen in Fig. 4.6 due to the adopted colour scale). This was also observed in the 2D simulations.

4.5 Conclusions

In this chapter, we have demonstrated that the fate of IGWs approaching the centre of a solar-type star is unaffected by the extension to three dimensions. We first derived

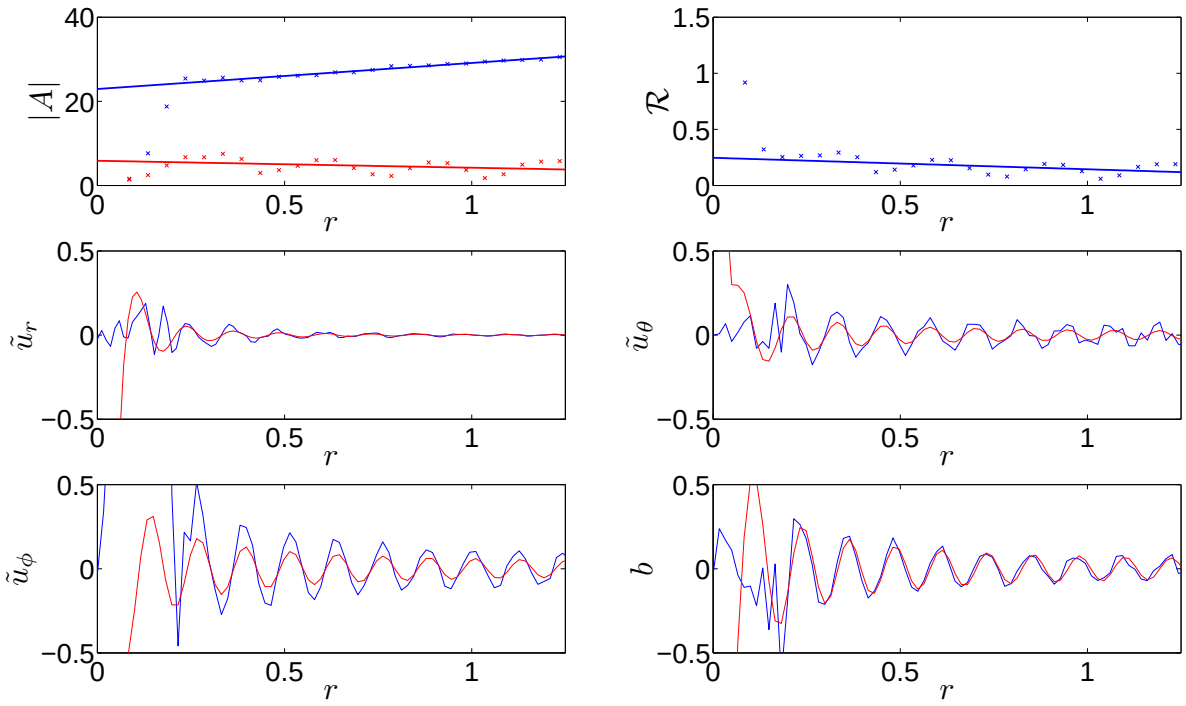

Figure 4.4: In the top left panel we plot A_{in} and A_{out} vs. r in a high-amplitude simulation in which the primary wave breaks ($\tilde{f}_r = 1$) at $t = 450$, with $\mathcal{R}$ in the top right panel. Below these are the velocity components and the buoyancy variable (blue), plotted together with the reconstructed linear solution (red), against radius. The central regions are not well described by the linear model, as expected.

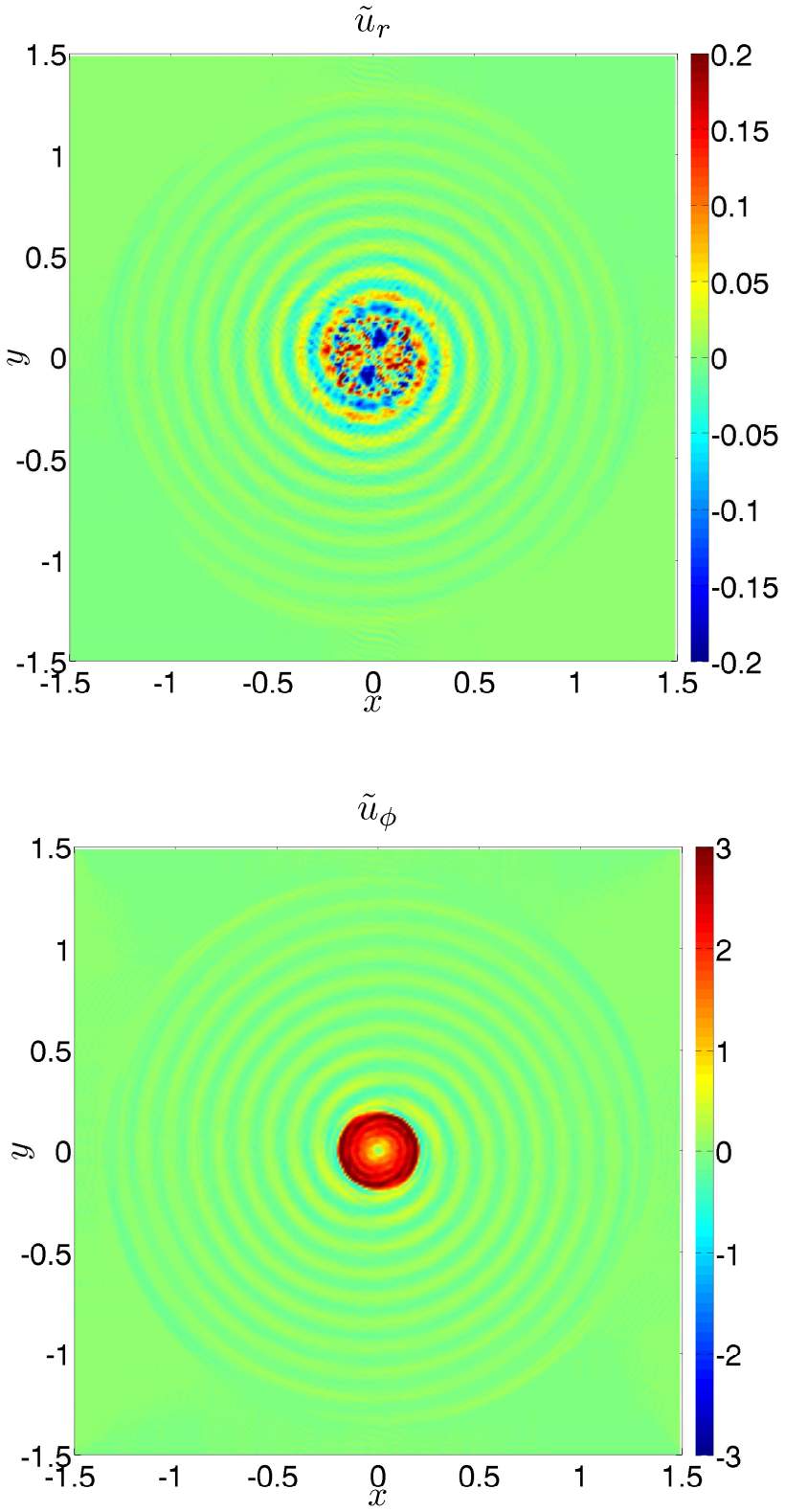

Figure 4.5: 2D plot of $\tilde{u}_r$ (top) and u_ϕ (bottom) on xy-plane for a simulation in which breaking occurs with $\tilde{f}_r = 1$, at $t = 450$.

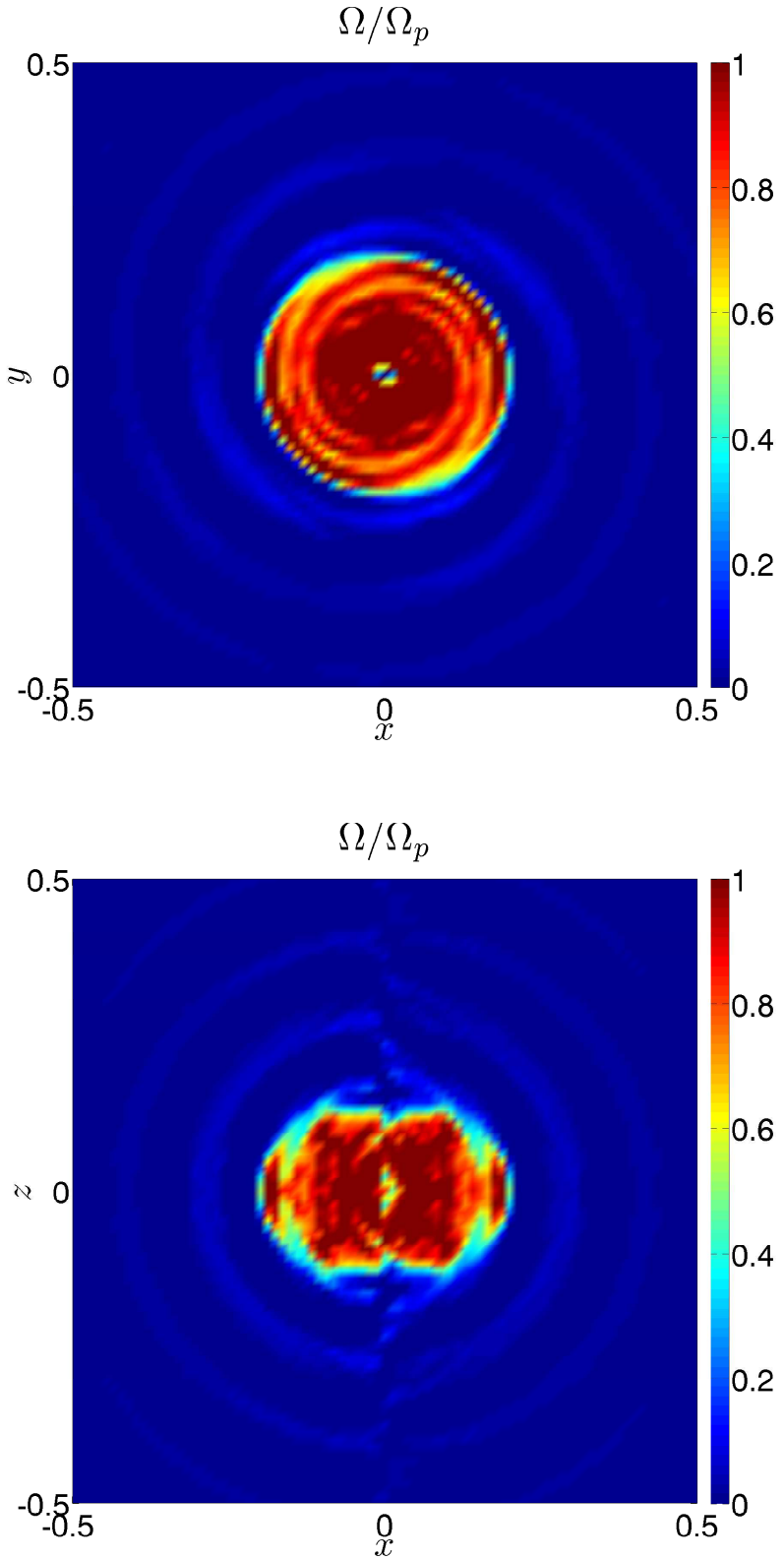

Figure 4.6: 2D plot of the angular velocity u_ϕ/R of the central regions in the xy (left) and xz (right) planes, normalised to the angular pattern speed (i.e., orbital angular frequency), in a large-amplitude simulation with $\tilde{f}_r = 1$, at $t = 450$. Latitudinal differential rotation is produced by absorption of ingoing $l = m = 2$ waves.

a linear wave solution in 3D, and found that nonlinearities do not vanish for this wave, unlike the 2D solution, which is exact. Nevertheless, these waves are found to reflect approximately perfectly for moderate amplitudes, a result which we have qualitatively confirmed in numerical simulations of moderate-amplitude tidal forcing. In this case global modes may form in the RZ, and an appreciable contribution to the tidal dissipation will only occur when the system enters a resonance with a global mode of oscillation.

The general picture for high-amplitude forcing is that IGWs break within the innermost wavelengths of a star, if they reach the centre with sufficient amplitude to overturn the stratification. If this occurs, they form a critical layer, which we have confirmed from the simulations, efficiently absorbs ingoing wave angular momentum. This results in the star being spun up to the orbital angular frequency of the planet, from the inside out. This could be very important to the survival of massive planets in short-period orbits around solar-type stars, which we will discuss in the following chapter.

One noticeable difference in 3D is that the absorption of $l = m = 2$ IWs results in the formation of latitudinal differential rotation. This is perpetually reinforced by critical layer absorption. Instabilities may act on this rotation profile, which could homogenise the horizontal angular momentum distribution. These include shear instabilities, which can be linear (Watson, 1981) or nonlinear instabilities, that set in at a critical Reynolds number (Richard & Zahn, 1999). These have growth times comparable to the tidal period, and could transfer angular momentum latitudinally. There are also doubly diffusive instabilities (Goldreich & Schubert 1967; Knobloch & Spruit 1982), or magnetic instabilities, such as the magnetorotational instability (Balbus & Hawley, 1994). However, these mechanisms are unlikely to be able to prevent the critical layer absorption, and thus prevent the tidal engulfment of a short-period planet.

As in Chapter 3, our simulations do not show any instabilities to act on the waves when they have insufficient amplitude to overturn the stratification. However, it may be that weaker parametric instabilities operate for waves with lower amplitudes (suggested by GD98). A detailed stability analysis of the 2D exact wave solution written

down in Chapter 3 is presented in Chapter 6, and will shed some light on this matter.

Chapter 5

Implications

In Chapters 3 and 4, we have studied a mechanism of critical layer formation due to wave breaking at the centre of a solar-type star. If such a critical layer forms, then ingoing wave angular momentum is efficiently absorbed at the centre. In this chapter we examine the consequences of this process for the orbital evolution of a close planetary companion. We determine the amplitude of the waves at the centre required to cause wave breaking, in terms of the star and planet parameters. We also calculate the tidal quality factors $Q'_\star$ that result, in a range of solar-type star models. This involves a discussion of the launching region at the top of the RZ, for which we present numerical calculations of the linearised adiabatic tidal response, together with a semi-analytic approximation for the angular momentum flux transported in IGWs. We discuss the relevance of this mechanism to the survival of short-period extrasolar planets, such as WASP-18 b, WASP-12 b and OGLE-TR-56 b. These results allow us to propose a possible explanation for the survival of all currently observed short-period planets around F, G and K-type stars.

5.1 Introduction

The main motivation for our work is to study $Q'_\star$ for solar-type stars, and in particular to connect this with the survival of close-in extrasolar planets. We have demonstrated in Chapters 3 & 4 that if IGWs approach the centre of a solar-type star with sufficient amplitude to break and form a critical layer, wave absorption is efficient, and global

modes (of any frequency very similar to the orbital frequency) are prevented from being set up in the RZ. The tidal torque can then be computed from assuming that the IWs are entirely absorbed. In this case a calculation along the lines of GD98 for the ingoing angular momentum flux of the waves excited at the top of the RZ is required. This estimates the tidal torque, and thus the orbital evolution of the planetary companion. In this section, we perform numerical integrations of the linearised tidal response in an extensive set of stellar models of solar-type stars with masses in the range $0.5 \leq m_\star/M_\odot \leq 1.1$, throughout their main sequence lifetimes. We aim to determine the tidal torque numerically, and compare it with a simple model of the launching region at the top of the RZ, previously derived in GD98.

If the ingoing energy flux in IGWs is F, then converting to an angular momentum flux, and assuming all wave angular momentum is deposited in the star, the torque is

$$\Gamma = \frac{m}{\omega} F = \frac{9}{4} \frac{1}{Q'_\star} \left(\frac{m_p}{m_\star + m_p} \right)^2 \frac{m_\star R_\star^2}{\omega_{dyn}^2} n^4. \tag{5.1.1}$$

Given a value of F, we can compute the tidal quality factor

$$Q'_\star = \frac{9}{4} \frac{\omega}{mF} \left(\frac{m_p}{m_\star + m_p} \right)^2 \frac{m_\star R_\star^2}{\omega_{dyn}^2} n^4. \tag{5.1.2}$$

In addition, if we are sufficiently far from resonance with a global mode, the amplitude at the centre required for wave breaking is

$$A = \left(\frac{72\sqrt{6}F}{5\pi} \frac{C^5}{\rho_c \omega^8} \right)^{\frac{1}{2}}. \tag{5.1.3}$$

Note, however, that if we are close to a resonance, then A may be much larger than this estimate would predict. In this chapter we will discuss calculations of F in models of solar-type stars, and then discuss the implications of our results in Part II for the survival of short-period extrasolar planets.

5.2 Numerical computation of the linearised tidal response throughout the star

In this section we solve the linearised equations governing the adiabatic tidal response throughout the star, computing the excitation of both the equilibrium and dynamical tides numerically. This allows us to determine the ingoing energy and angular momentum fluxes in IGWs launched at the top of the RZ, and to check the validity of approximate semi-analytic formulae for these quantities, presented in the next section. This is important because the orbital evolution of a planetary companion is determined by the ingoing angular momentum flux absorbed at the critical layer.

We solve the following coupled ODEs for the radial and horizontal displacements:

$$\frac{d\xi_r}{dr} = -\left[\frac{2}{r} + \frac{N^2}{g} + \frac{d\ln\rho}{dr}\right]\xi_r + \left[\frac{l(l+1)}{r} - \frac{\omega^2 r\rho}{\Gamma_1 p}\right]\xi_h + \frac{fr^2\rho}{\Gamma_1 p}, \tag{5.2.1}$$

$$\frac{d\xi_h}{dr} = \left[\frac{1}{r} - \frac{N^2}{r\omega^2}\frac{d\ln p}{d\ln\rho}\right]\xi_r - \left[\frac{1}{r} - \frac{N^2}{g}\right]\xi_h - \frac{fN^2 r}{\omega^2 g}. \tag{5.2.2}$$

An outline of the derivation of these equations is presented in T98. Note that we are ignoring the self-gravity of the entire tidal response, which is reasonable because most of the mass of the star is concentrated near the centre. This assumption is certainly valid for the dynamical tide, and is approximately valid for the equilibrium tide. In these equations, we take the tidal potential in the frame rotating with Ω_p to be equal to Eq. 4.1.2 with $\phi = \xi$ and $\omega = 0$, so that[1]

$$f = -\sqrt{\frac{6\pi}{5}}\frac{m_p}{(m_\star + m_p)}n^2. \tag{5.2.3}$$

This is the amplitude of the largest tide for a circular orbit. In this frame, the displacement field is separated into radial and horizontal (non-radial) components

$$\boldsymbol{\xi} = \xi_r Y_l^m(\theta,\xi)\mathbf{e}_r + \xi_h r\nabla Y_l^m(\theta,\xi). \tag{5.2.4}$$

We can further decompose the tidal response of a fluid body, which in this section we take to mean a solar-type star, into an equilibrium and a dynamical tide, defined

[1]Note that we are defining spherical harmonics in a standard manner, normalised so that the integral of $|Y_l^m|^2$ over solid angles is unity, unlike T98.

such that the total displacement is the sum of these two displacements, i.e, that $\boldsymbol{\xi} = \boldsymbol{\xi}^d + \boldsymbol{\xi}^e$. The equilibrium tide is a quasi-hydrostatic bulge defined by

$$\xi_r^e = -\frac{\Psi}{g}, \quad \text{and} \quad \nabla \cdot \boldsymbol{\xi}^e = 0, \tag{5.2.5}$$

in stratified regions (Goldreich & Nicholson 1989), where Ψ is the tidal gravitational potential experienced by the body and g is the gravitational acceleration. The total displacement is not well described by Eqs. 5.2.5 in convective regions (GD98; T98; OL04). This is because in a barotropic flow (with adiabatic stratification) vorticity is conserved, so we must have $\nabla \times \boldsymbol{\xi} = 0$, whereas $\nabla \times \boldsymbol{\xi}^e \neq 0$, in general. The presence of a convection zone (hereafter CZ) thus implies that a dynamical tide must exist. The dynamical tide $\boldsymbol{\xi}^d$ is defined as the residual response that results from the equilibrium tide not being the exact (linearised) solution to the problem, when the tidal frequency is nonzero.

The equations governing the adiabatic equilibrium and dynamical tides are

$$0 = -\frac{1}{\rho}\nabla\delta p^e + \frac{\delta\rho^e}{\rho^2}\nabla p - \nabla\Psi, \tag{5.2.6}$$

$$-\omega^2\boldsymbol{\xi}^d = -\frac{1}{\rho}\nabla\delta p^d + \frac{\delta\rho^d}{\rho^2}\nabla p + \underbrace{\omega^2\boldsymbol{\xi}^e}_{\text{Forcing}}, \tag{5.2.7}$$

from which it is clear that the dynamical tide is not forced directly by the tidal potential, only by the inertial terms in the equation of motion.

We impose a free upper boundary, i.e., take the Lagrangian pressure perturbation $\Delta p = 0$ at $r = R_\star$, so that the Eulerian pressure perturbation $\delta p = -\xi_r \frac{dp}{dr}$. Since the relation

$$\xi_h = \frac{1}{\omega^2 r}\left(\frac{\delta p}{\rho} + fr^2\right), \tag{5.2.8}$$

follows from the non-radial equation of motion, this relates our variables at the surface of the star. We take an IW BC at the inner boundary at $r \approx 0.02R_\star$, where we match ξ_r and ξ_h onto the analytic solution for an IW derived in §4.2,

$$\xi_r(r) = A_\xi r^{-\frac{3}{2}}(J_{\frac{5}{2}}(kr) + iY_{\frac{5}{2}}(kr)), \tag{5.2.9}$$

$$\xi_h(r) = \frac{A_\xi}{6} r^{-\frac{3}{2}} \Big[3(J_{\frac{5}{2}}(kr) + iY_{\frac{5}{2}}(kr)) - kr(J_{\frac{7}{2}}(kr) + iY_{\frac{7}{2}}(kr)) \Big] , \tag{5.2.10}$$

where $k = \frac{mC}{\omega}$. We take A_ξ to be a free parameter, so that these equations relate the ratio of ξ_r and ξ_h. This solution is quite accurate when $r/R_\star \lesssim 5\%$ since $\boldsymbol{\xi}^e$ is negligible in this region. This BC is meant to represent the IW absorption at a critical layer.

We solve Eqs. 5.2.1–5.2.2 using data interpolated from a stellar model at points required by a 4th/5th order adaptive step Runge-Kutta integrator, using a cubic spline interpolation. In particular, the coefficients of ξ_r, ξ_h, in Eqs. 5.2.1–5.2.2 are singular at the origin, so we first multiply these quantities by r *before* interpolating their values to the locations required by the ODE integrator, using the stellar model parameters. We then divide by r, after the interpolation. This is done to get the correct behaviour for small r.

Our method of solution is a shooting method to an intermediate fitting point (Press et al. 1992), which we take to be the CZ/RZ interface, where we enforce continuity of the solution. The freely specifiable initial conditions for each ODE integration are chosen to be ξ_r at the surface, and A_ξ at the inner boundary. We use $\xi_r = \xi_r^e$ as our starting "freely specifiable" estimate at the surface, which is an accurate approximation since $|\xi_r^d| \ll |\xi_r^e|$ at $r = R_\star$.

The Eulerian pressure perturbation for the dynamical tide is

$$\delta p^d = \rho\omega^2 r \left(\xi_h^e + \xi_h^d \right) , \tag{5.2.11}$$

from the horizontal component of Eq. 5.2.7. The radial energy flux at each radius is

$$F = \frac{\omega r^2}{2} \mathrm{Im} \left[(\delta p^d)^* \xi_r^d \right] , \tag{5.2.12}$$

which follows from manipulating Eqs. 5.2.6 and 5.2.7 to derive an energy equation.

From Eq. 5.2.7, we derive the relation

$$\nabla \cdot \mathrm{Im} \left\{ \delta p^d (\boldsymbol{\xi}^d)^* \right\} = \rho\omega^2 \mathrm{Im} \left\{ (\boldsymbol{\xi}^d)^* \cdot \boldsymbol{\xi}^e \right\} , \tag{5.2.13}$$

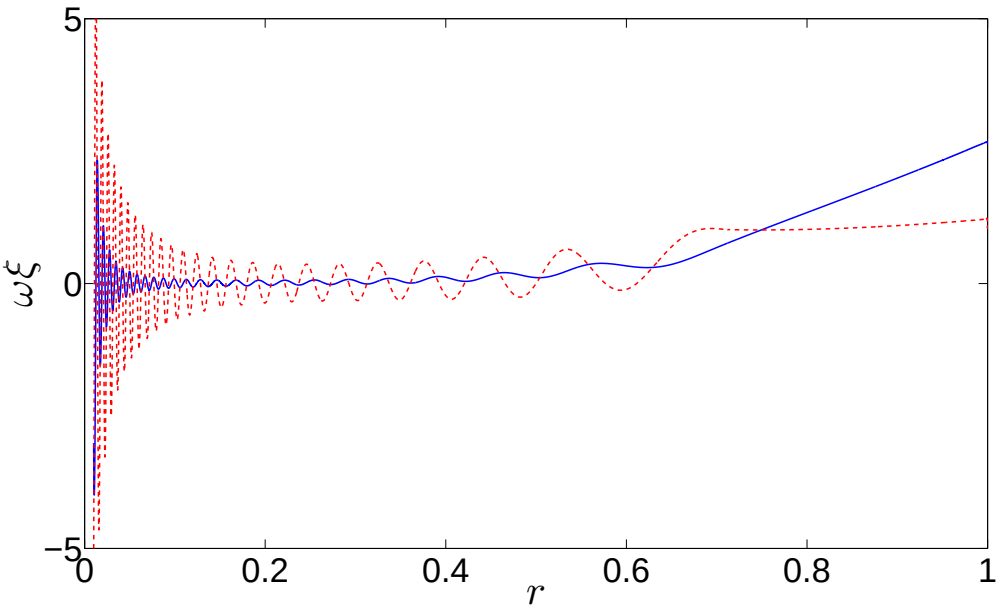

Figure 5.1: Typical values of the real parts of the radial ($\omega\xi_r$, in blue solid lines) and horizontal ($\omega\xi_h$, in red dashed lines) velocity components, in $\mathrm{m\,s^{-1}}$. We use Model S of the current Sun, and consider the tidal perturber to be a $P = 1$ d, $m_p = 1M_J$, planet orbiting the current Sun.

which can be integrated over solid angle to give

$$\mathrm{Im}\left\{\partial_r\left(r^2\delta p^d(\xi_r^d)^*\right)\right\} = \rho r^2\omega^2\mathrm{Im}\left\{(\xi_r^d)^*\xi_r^e + l(l+1)(\xi_h^d)^*\xi_h^e\right\}. \tag{5.2.14}$$

This is telling us that the equilibrium tide does work to excite the dynamical tide. As part of the validation of our numerical code, we have confirmed that this is accurately satisfied from the numerical solutions computed with an ingoing BC. This should adequately convince ourselves that the code is able to accurately compute the energy flux in the dynamical tide.

5.2.1 Results

As an illustration, we present the results of our integrations for a fiducial case with a $P = 1$ d, $m_p = 1M_J$ planet orbiting the current Sun (for which we use Model S, described in Christensen-Dalsgaard et al. 1996) in Fig. 5.1. We plot the real parts of $\omega\xi_r$ (solid blue) and $\omega\xi_h$ (dashed red) throughout the star, which represent typical

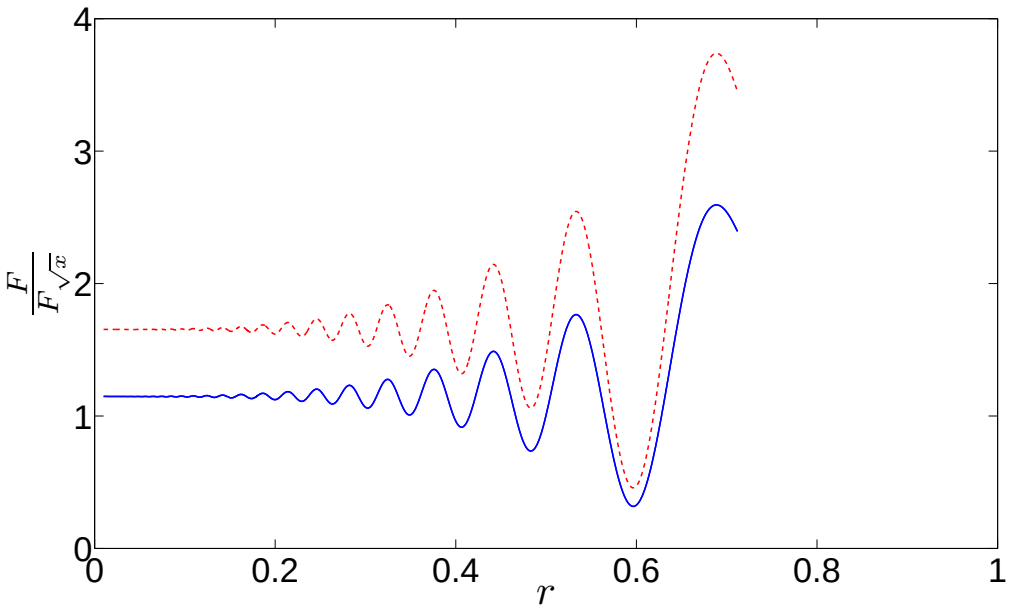

Figure 5.2: Numerically computed F, normalised to the prediction from the analytic theory in Eq. 5.2.24 (solid blue line) and Eq. 5.2.18 (red dashed line). Eq. 5.2.24 overestimates F by less than 10%, and is thus a good approximation of the ingoing energy flux.

values of the radial and horizontal velocity components. The radial wavelength of the waves decreases as the waves propagate deeper into the RZ, where N^2 increases. The large increase in the velocity amplitude near the centre is evident, as predicted from the linear solutions in § 4.2. This can be compared with a similar calculation in T98, displayed in their Fig. 1, which our code correctly reproduces for the given planetary orbital period when a regularity condition in applied at the centre. The only difference between our calculations and theirs is that we use an IW BC, whereas they allow the waves to perfectly reflect from the centre.

In Fig. 5.2 we plot the ingoing energy flux, normalised to both the semi-analytic prediction of GD98 (red dashed lines), and a revised expression derived in Appendix A.6 (blue solid lines), which will be discussed in the next section. This illustrates that the ingoing energy flux oscillates about its final asymptotic value, which it eventually approaches deep in the RZ.

5.2.2 Semi-analytical calculation of the ingoing energy flux

In this section we compare the numerically computed F with the semi-analytic estimate of GD98, and present a slight refinement which is found to be appropriate for solar-type stars.

In the launching region at the top of the RZ, there is a location at which $N = 0$ at $r = r_b \approx 0.71 R_\odot$, near to which it follows from the dispersion relation that the radial wavenumber of gravity waves vanishes. Near this turning point we can approximate the solution in this region by assuming a functional form for N^2. GD98 take $N^2 \propto r_b - r \equiv x$, in which case the problem in the launching region reduces to the solution of Airy's differential equation for ξ_r^d:

$$\frac{d^2\xi_r^d}{dx^2} - x\xi_r^d \approx 0, \tag{5.2.15}$$

if we define $\kappa x = r - r_b$, where

$$\kappa = \left(\frac{l(l+1)}{\omega^2 r_b^2} \frac{dN^2}{dx} \right)^{\frac{1}{3}}. \tag{5.2.16}$$

The reciprocal $L_{launch} = \kappa^{-1}$ is the radial lengthscale of the launching region, and is roughly equal to the first wavelength of the gravity waves launched. This approximation is valid only if $\frac{1}{\kappa^2 r^2} \ll 1$, otherwise Eq. 5.2.15 must be forced on the right hand side. In this model the wave is assumed to be excited in a thin shell of radial extent L_{launch}, at a radius $r \sim r_b$, within which $N^2 \propto r_b - r$.

If the solution is an IW, then the relevant solution of Airy's equation is

$$\xi_r^d(x) \propto \mathrm{Bi}(x) - i\mathrm{Ai}(x). \tag{5.2.17}$$

The energy flux F in IWs excited at the interface ($r = r_b$) in a non-rotating star, is (see Appendix A.6 for a similar derivation)

$$F \equiv F_x = \frac{3^{\frac{2}{3}}}{8\pi} \left[\Gamma\left(\frac{1}{3}\right) \right]^2 [l(l+1)]^{-\frac{4}{3}} \left[\rho_b r_b^5 \left| r_b \frac{dN^2}{dx} \right|^{-\frac{1}{3}} \left| \frac{\partial \xi_r}{\partial x} \right|^2 \right] \omega^{\frac{11}{3}}, \tag{5.2.18}$$

where $\omega = 2n$ is the frequency of IGWs excited by a planet in a circular, nonsyn-

chronous orbit, and

$$r_b \frac{dN^2}{dx} \approx -100\omega_{dyn}^2, \tag{5.2.19}$$

for the current Sun. The quantity

$$\frac{\partial \xi_r}{\partial x} \approx \sigma_c \frac{\Psi}{\omega_{dyn}^2}, \tag{5.2.20}$$

and σ_c is a constant whose value depends primarily on the thickness of the convection zone, and is equal to -1.2 for the current Sun. The values of these quantities depend on the stellar model. To calculate σ_c, we numerically solve GD98 Eq. 3, which we reproduce below, for the dynamical tide in the CZ using a linear shooting method, with $N^2 = 0$. We use the BCs that $\xi_r^d = 0$ at the top and bottom of the CZ. The motivation behind these choices is that the surface is roughly an equipotential, and we want to enforce continuity of the solution at the top of the RZ, where $\xi_r^d \sim 0$ (from the perspective of the solution in the CZ). The equation we solve is

$$L\xi_r^d(r) = f(r), \tag{5.2.21}$$

with the linear differential operator acting on the dynamical tide

$$L\xi_r^d(r) = \frac{d^2}{dr^2}\left(r^2\xi_r^d\right) + \frac{d}{dr}\left(\frac{d\ln\rho}{dr} r^2 \xi_r^d\right) + \frac{l(l+1)}{\omega^2}\left(N^2 - \omega^2\right)\xi_r^d, \tag{5.2.22}$$

and the forcing by the equilibrium tide given by

$$f(r) = l(l+1)\xi_r^e - \frac{d^2}{dr^2}\left(r^2\xi_r^e\right). \tag{5.2.23}$$

We find that a slightly better approximation is to take $N^2 \propto \sqrt{x}$ over the launching region[2], since this is valid over $\sim 0.15 R_\odot$ from the interface, as we illustrate in Fig. 5.3. The slope of the curve $\sqrt{x}$ can be obtained through fitting to the profile of N^2 in the stellar model. This allows a slightly more accurate calculation of F based on the stellar model than is obtained through direct application of F_x (where the gradient dN^2/dx is not uniquely defined). Nevertheless, the differences are only a factor of two at most.

[2]However, no simple physical arguments for such a profile have been found, which is perhaps to be expected since stellar models contain complicated combinations of physics.

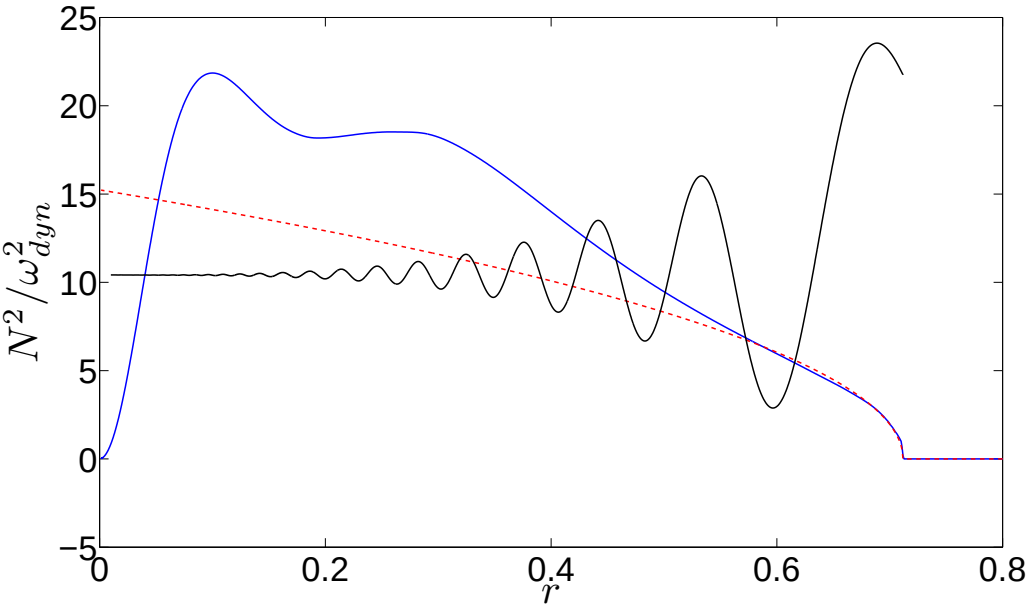

Figure 5.3: N^2 normalised to ω^2_{dyn} (solid blue line), together with our local approximation $N^2 \propto (r_b - r)^{1/2}$ (red dashed line). This approximation is reasonable over a region of size $\sim 0.15 R_\odot$. We also plot an arbitrarily scaled profile of F, to compare its radial profile with the profile of N^2, for $P = 1$ d.

In Appendix A.6 we calculate the solution in the launching region and the resulting F, for any power law profile of N^2 with a positive exponent, using the framework of OL04. Using our approximation, the radial extent of the launching region $L_{launch} \sim 0.03 R_\odot$.

For the case $N^2 \propto \sqrt{x}$, we obtain, for a non-rotating background,

$$F \equiv F_{\sqrt{x}} = \frac{\left(\frac{2}{5}\right)^{\frac{1}{5}} \pi}{2\left[\Gamma\left(\frac{3}{5}\right)\right]^2} \left[l(l+1)\right]^{-\frac{7}{5}} \omega^{\frac{19}{5}} \left[\rho_b r_b^5 \left|\sqrt{r_b}\frac{dN^2}{d\sqrt{x}}\right|^{-\frac{2}{5}} \left|\frac{\partial \xi_r}{\partial x}\right|^2\right]. \tag{5.2.24}$$

This matches the numerically computed asymptotic value of F for the current Sun quite well, to within 10% (see Fig. 5.2). The remaining discrepancy is due to the slight variation in background density, and the magnitude of the equilibrium tide, over the launching region. We note that the main change in the energy flux from modifying the profile of N^2 in the transition region is to change its frequency dependence.

To illustrate the refinement for short-period forcing, in the top panel of Fig. 5.4 we compare the numerically computed dynamical tide in the launching region (black solid lines) with Eq. 5.2.17 and Eq. A.6.16. It is clear that the Airy function approximation (blue dashed lines), using Eq. 5.2.19 for the slope at the interface, does not correctly represent the solution in first wavelength, whereas the solution derived in Appendix A.6 (red dashed lines), with a best fit $\sqrt{r_b}\frac{dN^2}{d\sqrt{x}} = 15\omega_{dyn}^2$, matches the solution in this region quite well. However, this discrepancy can be rectified by choosing a shallower slope at the interface for the Airy function approximation, as can be seen in the bottom panel, where both solutions match the numerically computed dynamical tide quite well. In the bottom panel we have used a slope $r_b\frac{dN^2}{dx} = 20\omega_{dyn}^2$, for computing the blue dashed line using Eq. 5.2.17.

As can be seen from Fig. 5.2, the numerically computed asymptotic value of F differs from F_x by a factor $\lesssim 2$, even in the case of short-period forcing. We would expect F_x to be correct to within a factor ~ 2 even if the slope varies by an order of magnitude, since it is only raised to the power $-\frac{1}{3}$. However, our slight refinement improves this estimate by $\sim 50\%$ for $P = 1$ d.

We have performed numerical integrations for several different forcing frequencies (planetary orbital periods), for which we find $F \propto P^{-8.06}$ for fixed stellar and planetary properties (other than the orbital period). If we take into account the fact that $\partial_x \xi_r^d \sim \Psi \sim P^{-2}$, and then consider a fixed tidal potential, we find that $F \propto \omega^{4.06}$, which is

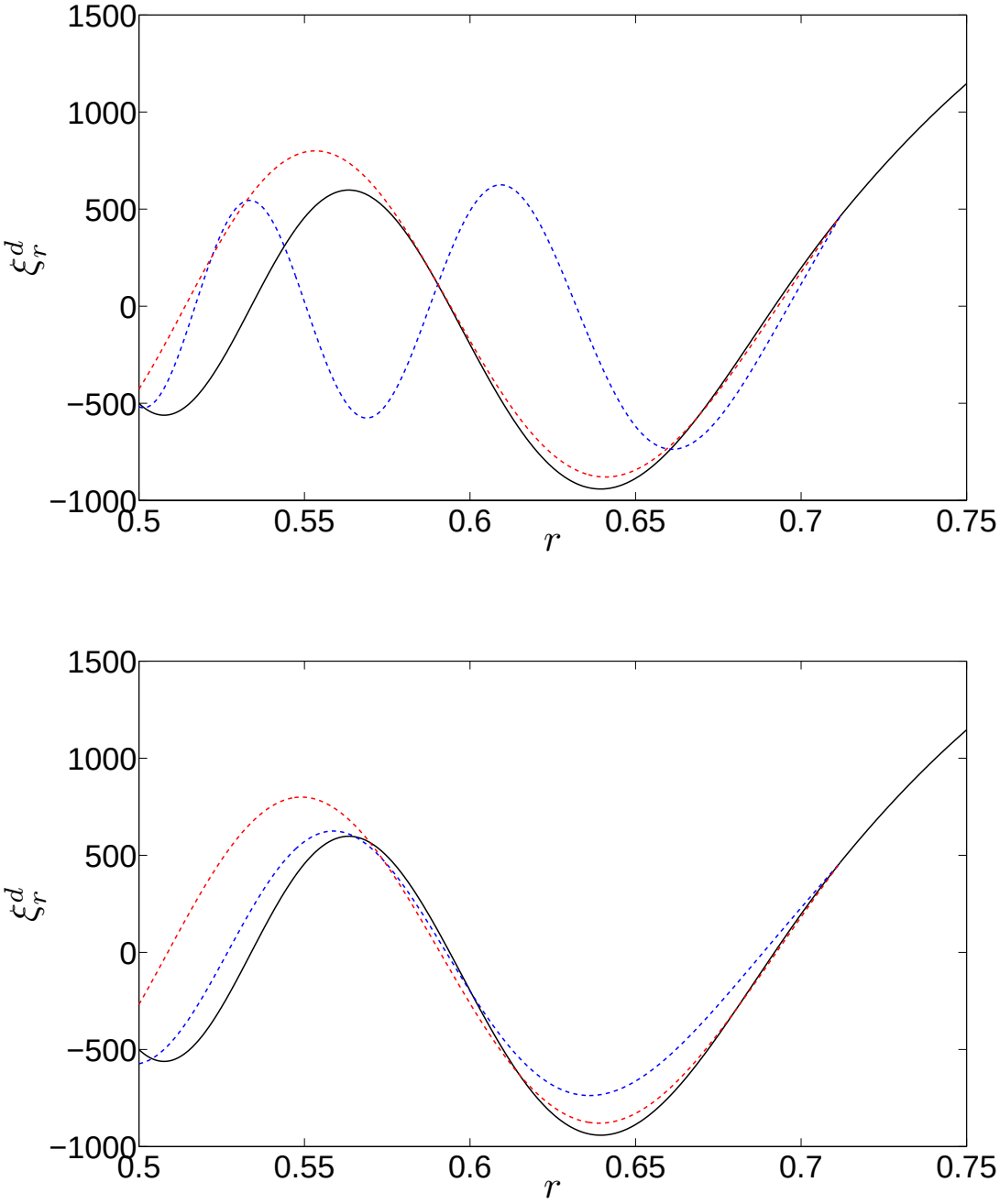

Figure 5.4: Top: ξ_r^d from numerical integrations (black solid line), compared with the Airy function approximation (blue dashed line) and the Bessel function approximation of Appendix A.6 (red dashed line). Bottom: Same, but with $\frac{dN^2}{dx}$ reduced by a factor of 5 for Airy function approximation (blue dashed line).

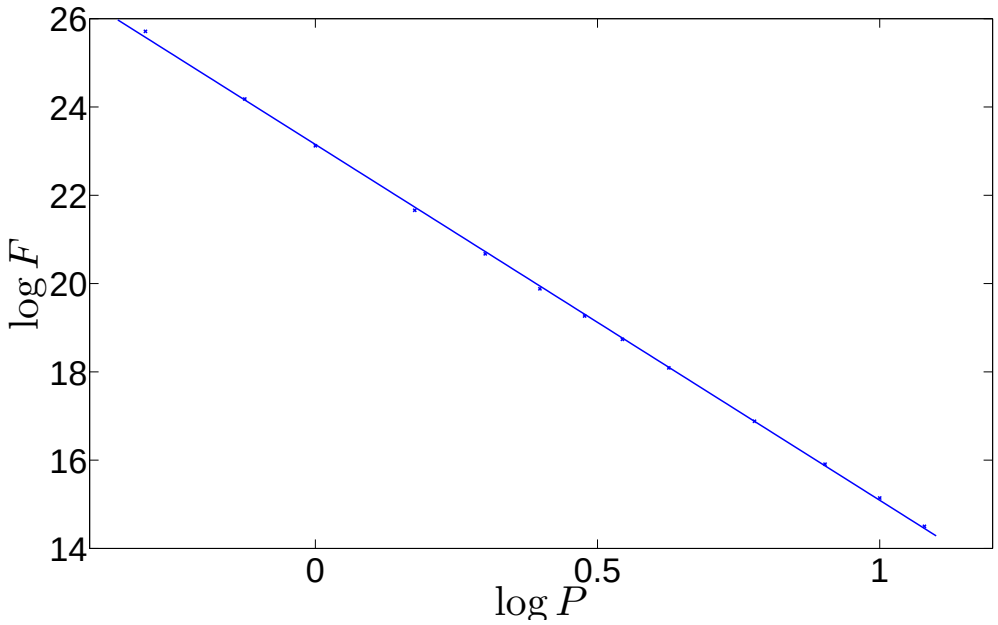

Figure 5.5: Power law dependence of F on P, for fixed stellar and planetary properties (other than the orbital period). This has slope -8.06.

slightly different from the power law dependence in Eq. 5.2.24. The discrepancy most likely results from the variation in the background density, and the magnitude of the equilibrium tide (which forces the dynamical tide), within this region.

For $P \lesssim 2 - 3$ d, which is the relevant regime for which this process is potentially important for the survival of close-in planets, as we discuss later, there is a few per-cent variation in background parameters over a lengthscale L_{launch}. This means that our calculation of $F_{\sqrt{x}}$ differs from the numerically computed value of F, by an amount that increases as P is made smaller to a maximum of 20% when $P = 0.5$ d. Nevertheless, this discrepancy is small, and our semi-analytic estimate $F_{\sqrt{x}}$ is a good approximation to F for all cases that we have modelled. This is used to provide an estimate of $Q'_\star$, and thus the tidal torque, in § 5.4.

5.2.3 Variation between different stellar models

Eq. 5.2.24, matches the numerically computed value to within a few per-cent for a variety of solar-type stars. This is because it generally arises that $N^2 \propto x^\alpha$, with $\alpha \sim 0.5$, when the launching region is a few percent of the stellar radius. This occurs

for the waves excited by planets in short-period orbits. We have confirmed this by computing F in a number of stellar models with masses in the range $0.5 \leq m_\star/M_\odot \leq 1.1$, and ages that represent the range of main-sequence ages expected for these stars. These were computed using ASTEC (Christensen-Dalsgaard 2008).

We collect all terms in Eq. 5.2.24, that depend on the properties of the launching region, into a single parameter

$$\mathcal{G} = \rho_b r_b^5 \left| \frac{dN^2}{d\ln\sqrt{x}} \right|^{-\frac{2}{5}} \sigma_c. \tag{5.2.25}$$

This parameter has been computed in each of the stellar models in our study. This involved integrating Eq. 5.2.21 throughout the CZ in each of these models, where $N^2 \sim 0$, using a linear shooting method, to determine σ_c. The result of this study is that $\mathcal{G} \sim \mathcal{G}_\odot \approx 1.2 \times 10^{48} \mathrm{kg\,m^2 s^{2/3}}$, to within a factor of 5 for all solar-type stars, throughout their main-sequence lifetimes. This is true even taking into account the evolution of the position of the CZ/RZ interface, and the resulting change in the density of the star at the interface.

The main uncertainty in these models is the profile of N^2 within the launching region, especially since the slope within $0.02R_\odot$ of the interface is not well constrained by theory or observations. Helioseismic observations are not yet able to constrain the stratification within this region, owing to the lack of observed g-modes (Ellis 1984; Appourchaux et al. 2010). In addition, the relevant physics included in the stellar models is also uncertain, particularly as a result of changes to the compositional gradient from convective overshoot. The inclusion of helium settling tends to make the interface profile sharper, and the inclusion of turbulent diffusion, that results from convective overshoot, and often parameterised using a simplified 1D model of this process, tends to smooth out the profile near the interface (Jørgen Christensen-Dalsgaard, private communication). However, these changes are small and occur only within a region smaller than the launching region for $P \lesssim 3$ d. This means that uncertainties in the observations, and the physics, at the interface, are unlikely to significantly change $\mathcal{G}$ (and therefore F) for $P \lesssim 3$ d, which are the planets whose survival could be threatened by our mechanism (as we discuss below). In addition, $\left|\frac{dN^2}{d\sqrt{x}}\right|$ is only raised to the -2/5 power in our model.

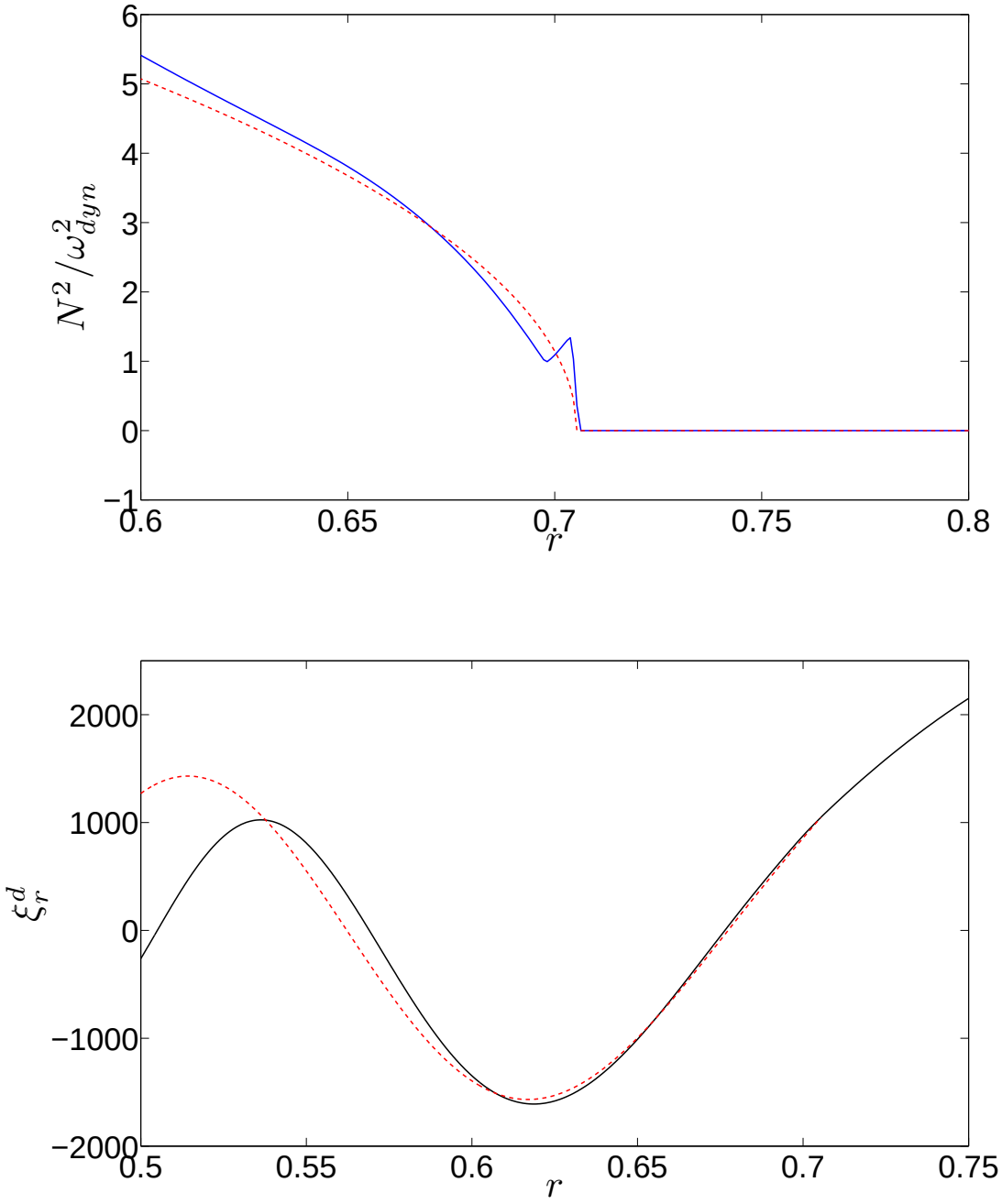

Figure 5.6: In the top panel we plot N^2 in a $1.0M_\odot$ star at $t = 6.95$ Gyr, with our fitted solutions in the bottom panel. This model has a "bump" in the N^2 profile, but this occurs over a region smaller than L_{launch}, and so does not reduce the accuracy of our analytic model in the launching region (or the corresponding energy flux), shown in the bottom panel.

For Model S, the compositional gradient (∇_μ) is unimportant in the launching region, and N^2 primarily results from temperature gradients. As the star evolves, the settling of elements heavier than H, produces a compositional gradient at the top of the RZ, which can produce "bumps" in the profile of N^2. In Fig. 5.6 we plot an example of the profile of N^2 for a $1M_\odot$ model (with $Z = 0.02$) at $t = 6.95$ Gyr, together with the best fit solution in the launching region. For $P \lesssim 3$ d, L_{launch} is generally much larger than these "bumps", so the wave launching process does not notice such departures from a smooth stratification profile, and Eq. 5.2.24 remains a good approximation for the energy flux. However, if the frequency is sufficiently low ($P \gtrsim 6$ d), the radial extent of the launching region can become comparable with the size of these "bumps", and the numerical solution can depart appreciably from our analytical model. Planets in such orbits are very unlikely to be affected by stellar tides at such orbital distances, so we do not consider such effects worthy of further consideration. To summarise, we have confirmed that Eq. 5.2.24 is a good approximation for the energy flux for planets on orbits of a few days throughout the range of solar-type stars in our study.

5.2.4 Are 1D linear hydrodynamic calculations reasonable?

The calculations done in § 5.2 are performed under the assumption of linearity. We have demonstrated in Chapters 3 and 4, that this is not a valid assumption near the centre of a star. A simple estimate of the nonlinearity in IGWs in the launching region, for want of a better measure, compares the radial displacement to the radial wavelength, for which $\xi_r^d/\lambda_r \sim 10^{-4}$, for a hot Jupiter orbiting the Sun on a one-day orbit (this estimate can be obtained from Fig. 5.1). This value increases linearly with the mass of the planet, but we are still in the linear regime even if we have a close-binary perturber, which indicates that linearity is likely to be a good approximation in the launching region (and throughout the RZ, except for the central regions).

However, it remains to be seen whether F for the 1D calculations is the same as that in 2D or 3D numerical simulations of realistic tidal forcing in a model including both a CZ and a RZ. Such simulations as Rogers et al. (2006) could be performed of the whole star subject to tidal forcing. The turbulent convection in these simulations will produce a spectrum of waves at the top of the CZ, in addition to those excited by

tidal forcing. It may be that the interaction of these waves reduces the ingoing energy flux. Alternatively, the profile of N^2 in the transition region could be modified by realistic modelling of convective overshoot, altering the strength of the stratification within a few percent of a pressure scale height from the interface. This would affect F if the overshoot region is comparable with the size of the launching region, though probably not significantly, as we discussed in the previous section.

A toroidal magnetic field in the launching region could also affect the amplitudes of these waves, and the value of F. Rogers & MacGregor (2010) find that when the IGW frequency is approximately equal to the Alfvén frequency (ω_A), strong wave reflection occurs. This behaviour follows from the dispersion relation for IGWs in the presence of a magnetic field (e.g. Kumar et al. 1999), and could have important consequences for F, if the magnetic field is sufficiently strong. However, for $\omega \approx \omega_A$ in the launching region, we require $B_\phi = 2\pi\sqrt{\mu_0\rho_b}r_b/P \gtrsim 6$ MG, when $P = 1$ d, which is close to being ruled out on empirical grounds, from measurements of the solar oblateness (Friedland & Gruzinov 2004). If $\omega_A < \omega$, little attenuation of wave energy over the non-magnetic case is found by Rogers & MacGregor (2010), so this seems unlikely to affect F in our case.

In the innermost wavelength, a strong magnetic field would be able to reflect IGWs before they reach the centre, if $\omega \approx \omega_A$ in this region. This requires a toroidal field of strength $B_\phi \gtrsim 6$ MG, or a poloidal (radial) field of strength $B_r \gtrsim 28$ MG. Since it is unlikely that such fields could exist in the RZ (Friedland & Gruzinov, 2004), a magnetic field will probably not affect the reflection of IGWs (excited by short-period planets) in the RZ. It is therefore appropriate to ask whether the waves will break on reaching the centre.

5.3 When does wave breaking occur?

In this section we estimate the orbital and stellar properties required to excite waves that are sufficiently nonlinear near the centre for breaking to occur, using the linear solution in Chapter 4. The nonlinearity parameter is defined so that for $|A| > 1$, the wave overturns the stratification during part of its cycle. Assuming we are not close to resonance with a global g-mode, we can estimate the amplitude near the centre,

assuming standing waves have formed, by using Eq. 5.2.24, to give

$$|A| = \frac{3}{10}\frac{\left(\frac{3}{2}\right)^{\frac{1}{20}}\pi^{\frac{2}{5}}}{5^{\frac{1}{10}}\Gamma(\frac{3}{5})}\frac{\mathcal{G}^{\frac{1}{2}}}{\omega_{dyn}^2}\left(\frac{C^5}{\rho_c}\right)^{\frac{1}{2}}\left(\frac{m_p}{m_\star+m_p}\right)P^{\frac{1}{10}} \quad (5.3.1)$$

$$\approx 0.4\left(\frac{\mathcal{G}}{\mathcal{G}_\odot}\right)^{\frac{1}{2}}\left(\frac{C}{C_\odot}\right)^{\frac{5}{2}}\left(\frac{m_p}{M_J}\right)\left(\frac{M_\odot}{m_\star}\right)\left(\frac{P}{1\text{ day}}\right)^{\frac{1}{10}}, \quad (5.3.2)$$

for the current Sun, where $\mathcal{G}_\odot \approx 1\times10^{48}\text{kg m}^2\text{s}^{2/3}$, and $C_\odot \approx 8\times10^{-11}\text{m}^{-1}\text{s}^{-1}$.

We can therefore write the following criterion for wave breaking:

$$\left(\frac{\mathcal{G}}{\mathcal{G}_\odot}\right)^{\frac{1}{2}}\left(\frac{C}{C_\odot}\right)^{\frac{5}{2}}\left(\frac{m_p}{M_J}\right)\left(\frac{M_\odot}{m_\star}\right)\left(\frac{P}{1\text{ day}}\right)^{\frac{1}{10}} \gtrsim 3.6. \quad (5.3.3)$$

A Jupiter-mass planet in a one-day orbit around the current Sun would not raise tides of sufficient amplitude near the centre for breaking to occur, and would presumably survive, because it does not satisfy this criterion. Indeed, all of the HJs currently observed around G or K type stars[3] do not satisfy this criterion, so this could be an important explanatation for their survival.

Note, however, that sufficiently long-period planets may be able to satisfy this criterion around the current Sun, due to the (weak) period dependence of the nonlinearity. The waves excited by such planets would be of very low amplitude, but they are also of very low frequency. This means that their wavelength is extremely short, so the energy of these waves would be concentrated into an extremely small volume near the centre of the star, if they were to reach it. However, radiative diffusion is certain to damp these waves before they reach the centre, since they are of such short wavelength. This process would, in any case, contribute negligibly to the orbital evolution of such long-period planets.

The variation in $|A|$ is primarily dependent on C, since $|A| \propto \mathcal{G}^{\frac{1}{2}}C^{\frac{5}{2}}$. The strong dependence on C means that as a star evolves the tide could become nonlinear at a critical age, since C increases with evolution on the main-sequence. In Fig. 5.7 we plot the variation in C versus main-sequence age, normalised to its value in the current Sun, from a sequence of solar models that pass through Model S. The increase in C with age is due both to the increasing central condensation, and the build-up of a gradient in the hydrogen abundance (there is a small drop around 8 Gyr when hydrogen is

[3]Contained in the catalogue at http://exoplanet.eu/catalog.php

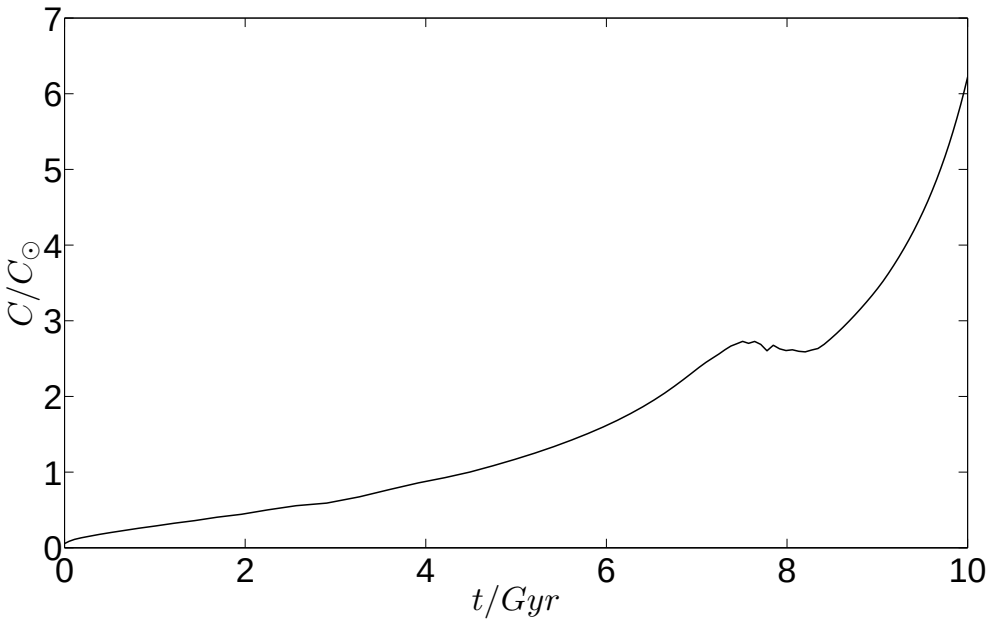

Figure 5.7: Coefficient C in the expansion $N \approx Cr$ near the centre of the Sun normalised to its current value versus main-sequence age, for a sequence of solar models that pass through Model S of the current Sun. The stratification steepens as the star evolves.

nearly used up and the contribution from the composition gradient decreases, after which the central density increases rapidly).

For a given age, C is larger in more massive stars, due to their greater central condensation. In addition, stars with lower metallicity also have a greater central condensation for a given age, and so have larger C values over stars with higher metallicity. Over the range of stars considered in this study, C is found to take values between $0.1 - 10\ C_\odot$. This leads to a large variation in A values, for fixed orbital parameters. As a result, C is critical in determining whether wave breaking occurs at the centre. We have stated that a short-period Jupiter-mass planet does not satisfy Eq. 5.3.3 around the current Sun. However, such a planet around a similar-age $1.0M_\odot$ star with a metallicity $Z = 0.01$, will cause wave breaking at the centre, since C is larger by a factor of 3. Thus, there is a strong dependence of the breaking criterion on the stellar model, primarily through the parameter C.

5.4 $Q'_\star$ for solar-type stars

The main motivation for our work is to study $Q'_\star$ for solar-type stars, and to connect this with the survival of close-in extrasolar planets. If a critical layer forms by wave breaking (or radiative diffusion, as we discuss in Chapter 7), then we can assume that the entire ingoing angular momentum flux is absorbed in the RZ. In that case, we use Eq. 5.1.2, together with Eq. 5.2.24, to write

$$Q'_\star = \frac{9}{32}\frac{\left(\frac{3}{2}\right)^{\frac{2}{5}}\left[\Gamma(-\frac{2}{5})\right]^2}{5^{\frac{4}{5}}\pi^{\frac{24}{5}}}\frac{1}{\mathcal{G}}m_\star R_\star^2\omega_{dyn}^2 P^{\frac{14}{5}} \tag{5.4.1}$$

$$\approx 0.9\times 10^5\left[\frac{P}{1\text{ day}}\right]^{\frac{14}{5}}. \tag{5.4.2}$$

Note that the exact value depends on the stellar model adopted – in particular the value of $\mathcal{G}$, which is determined from the stellar properties in the launching region, and the thickness of the convection zone. The given value applies to a stellar model of the current Sun. However, we stated in §5.2.3 that $\mathcal{G}$ varies by only a factor of 5 throughout the range of main-sequence stars in our study. Taken together with changes in stellar mass and radius, our estimate of $Q'_\star$ varies by only a similar amount, thus Eq. 5.4.2 can be considered quite robust, if critical layer absorption occurs near the centre. This is approximately true for all stars within the mass range $0.5 \leq m_\star/M_\odot \leq 1.1$, throughout their main-sequence lifetimes.

As the star evolves on the main-sequence, the position of the interface r_b moves inwards towards higher density material, which slightly increases F. This means that $Q'_\star$ tends to decrease with main-sequence age, though by only a factor of 5 or so. The dissipation that results from wave absorption at a critical layer thus becomes more effective as the star evolves.

5.5 Orbital evolution of the planetary companion

Tidal dissipation of the quadrupolar tide raised in the star leads to evolution of the semi-major axis at the rate

$$\frac{\dot{a}}{a} = -\frac{9}{2}\frac{m_p}{m_\star}\left(\frac{R_\star}{a}\right)^5 n\left[\frac{\text{sgn}(2n-2\Omega)}{Q'_\star}\right]. \tag{5.5.1}$$

The inspiral time for a planet into the current Sun is then

$$\tau_a = -\frac{10}{107}\frac{a}{\dot{a}} \approx 1.03 \text{ Myr} \left(\frac{M_J}{m_p}\right) \left(\frac{m_\star}{M_\odot}\right)^{\frac{8}{3}} \left(\frac{R_\odot}{R_\star}\right)^5 \left(\frac{P}{1 \text{ day}}\right)^{\frac{107}{15}}, \tag{5.5.2}$$

since $\dot{a}/a \propto a^{-107/10}$. Note that the strong frequency dependence of $Q'_\star$ means that this mechanism could be very important for short-period systems. This predicts that a planet spiralling into its star will undergo rapid acceleration as it migrates inwards. This is a consequence not only of the reduction in semi-major axis, but also the decrease in $Q'_\star$, as the tidal frequency increases with the inspiral. It must be noted that simple timescale estimates do not accurately reflect the evolution if the orbit is eccentric, inclined, or if the stellar spin is not much slower than the orbit (see Chapter 2), but this estimate shows that this mechanism can be very efficient in contributing to the tidal evolution of hot Jupiters on the tightest orbits. Indeed, $\tau_a \lesssim O(1)$ Gyr for a Jupiter-mass planet in an orbit of less than about three days around the current Sun, if a critical layer were to form near the centre.

We can crudely estimate the maximum orbital period of a planet that can be pulled into the star by this process, by equating the moments of inertia of the RZ, to that of the orbit $\mu a^2 = r_g^2 m_\star$, giving

$$P \simeq 1.8 \text{ d} \left(\frac{m_\star}{M_\odot}\right)^{\frac{1}{2}} \left(\frac{r_b}{0.7 R_\odot}\right) \left(\frac{M_J}{\mu}\right)^{\frac{1}{2}}, \tag{5.5.3}$$

where $\mu = \frac{m_p m_\star}{m_p + m_\star}$ is the reduced mass, and $r_g^2 = 0.076$ is the squared dimensionless radius of gyration for a polytrope of index 3.

A Jupiter-mass planet on a ~ 1 day orbit will spin up a substantial fraction of the RZ on infall. If the ratio of the orbital moment of inertia to the spin moment of inertia of the RZ $\gtrsim 1$, then the above process alone will be unable to cause the planet to spiral into the star. However, if this ratio is smaller than unity for such a short-period planet, the whole of the RZ must be spun up to cause the planet to completely spiral into the star. Once the entire RZ has spun up to the orbital frequency, this process becomes ineffective, and the corresponding tidal torque will vanish. However, the tidal torque is nonzero due to dissipation of the equilibrium tide by turbulent convection, and so even if this process stops, it does not guarantee the survival of the

planet. In addition, magnetohydrodynamic coupling between the CZ and RZ could act to partially counteract the spin-up of the interior, if the CZ is spinning slower than the orbit. Magnetic braking of the star through the interaction of its magnetic field with a stellar wind acts to spin down the CZ, which would also gradually spin down the RZ through these couplings. If the coupling between the CZ and RZ of the star is efficient, then our mechanism would again become effective. In the case that the coupling timescale balances the timescale for spin up of the RZ due to IGW absorption at a critical layer, then the planet would migrate into the star on the magnetic braking timescale. A detailed study of these effects is not currently possible, since there are many uncertainties, but this is worthy of future consideration.

5.6 Long-term evolution of the RZ

As the planet migrates inwards due to the IGWs it excites being absorbed at a critical layer, ω increases, since $\dot{n} > 0$. If we assume that the tidal frequency increases from ω_1 at a time t_1 to $\omega_2 > \omega_1$ at a slightly later time t_2, then since $\omega_2 > \omega_1$, the waves excited at t_2 no longer see the critical layer for ω_1 waves. If the change in frequency is sufficiently small, we would still expect significant attenuation by the shear as the waves approach the critical layer for ω_1 waves. This would transfer angular momentum from the waves to the mean flow, and may spin up the region near the original critical layer to the pattern speed for ω_2 waves, hence producing a critical layer for these waves. If this process occurs, then a weak radial differential rotation profile could be set up in the RZ, with $\frac{d\Omega(r)}{dr} > 0$. Similarly, if the planet migrates outwards for the case of a rapidly rotating star, then a profile with $\frac{d\Omega(r)}{dr} < 0$ could be set up (which would be unstable). If the flow does not have time to adjust to the change in frequency of the forcing, and cannot spin up sufficiently to produce a critical layer for ω_2 waves, then the dissipation rate may be reduced. However, it seems plausible that the change in the orbit will be gradual enough so that IGWs reaching the centre will be significantly attenuated. This is because their radial wavelengths get Doppler-shifted downwards by the shear, making them more susceptible to radiative damping.

We have so far restricted our investigation to $m = 2$ waves. If the orbit of the planet is eccentric or inclined with respect to the stellar equator, then IGWs with

other m-values could be excited. If these break, then they could each have their own critical layer. It would be interesting to study the effects of tidal forcing with several different frequencies and m-values to see how this would affect the reflection of the different waves. In addition, Rogers & Glatzmaier (2006) found that IGWs excited by turbulent convection at the top of the RZ, which had $1 < m < 15$ and typical frequencies $\omega \sim 20\mu$Hz, could reach the centre with sufficient amplitude to undergo breaking and spin up the central regions. If this commonly occurs in solar-type stars, then we might expect the core to be differentially rotating, even in the absence of tidal forcing. For most m-values the resulting spin frequency of the central regions is probably slower than that of the relevant pattern speed for tides raised by a close-in planet, so we expect that this would minimally attenuate any tidally excited low-m waves. Nevertheless, the interactions of multiple waves near the centre warrants further study.

5.7 Tidal dissipation in F-stars

In this chapter we have discussed the implications of the formation of a critical layer near the centre of a solar-type star, which can occur due to wave breaking. However, many planets orbit F-type stars, which have convective cores and thinner OCZs. Our calculation of $Q'_\star$ for XO-3 in Chapter 2 indicates that it would be worthwhile to study the range of $Q'_\star$ expected for F-stars, and how these may differ from the solar-type stars that we have considered so far in Part II of this thesis.

We have performed calculations of tidal dissipation in the OCZs of a variety of F-stars between the masses of $1.2 - 1.6\,M_\odot$, using the numerical method of OL04/OL07, and the stellar models of EZ-Evolution. These stars contain convective cores surrounded by a RZ and an OCZ. Since these stars are not stably stratified near the centre, the process of wave breaking and critical layer formation will not occur in such stars, because IGWs reflect from the core before they become nonlinear. This removes the possibility of the efficient mechanism of tidal dissipation that we have so far discussed, with damping of the dynamical tide in the RZ being due only to inefficient radiative diffusion (which is discussed further in §7.1). For this reason, we expect that tidal dissipation in the OCZ will dominate the dissipation.

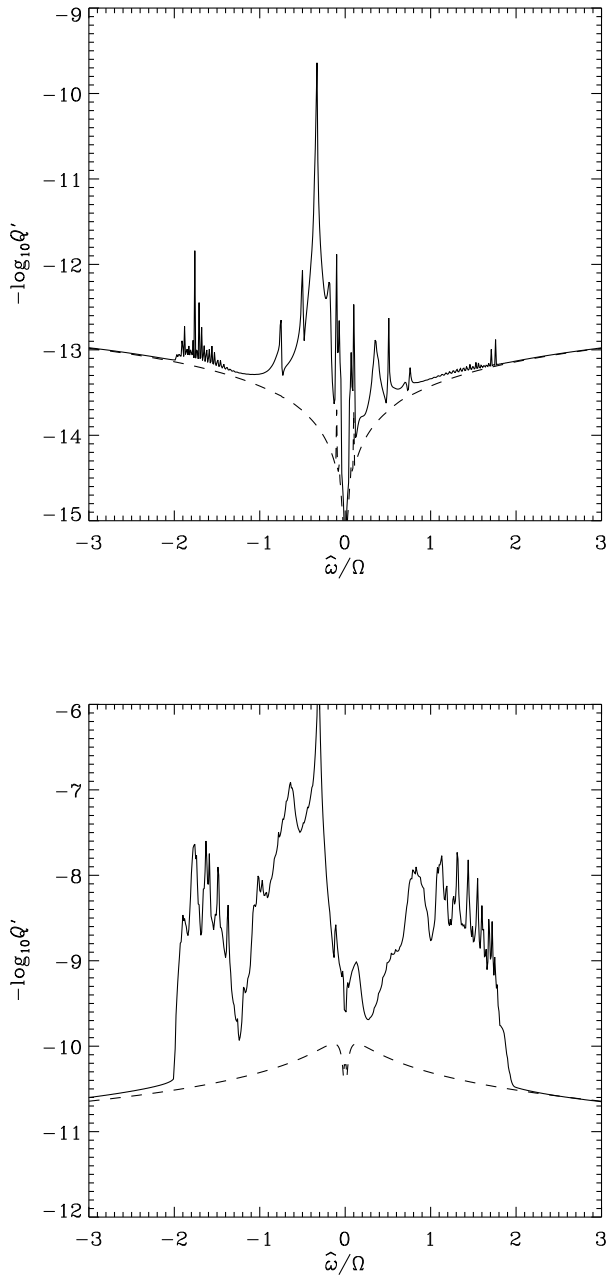

Figure 5.8: $Q'_\star$ as a function of the ratio of tidal frequency to spin frequency $\hat{\omega}/\Omega$, from dissipation of the $l = m = 2$ component (we find the behaviour of the $m = 0$ and 1 components is similar in magnitude) of the equilibrium tide, and dissipation of inertial modes, in the OCZ of two F-type star models. The dashed lines represent the effect of omitting the Coriolis force, and therefore inhibiting inertial waves. The top figure shows a high-mass $1.5\,M_\odot$ F-star, with solar metallicity and an age of 0.7 Gyr, assumed to be spinning with a period of 3 d. This has a very thin OCZ, and tidal dissipation is extremely weak. The bottom figure shows a low-mass $1.2\,M_\odot$ F-star, with solar metallicity and an age of 1.0 Gyr, assumed to be spinning with a period of 3 d. Tidal dissipation is much stronger in this star, though still smaller than that in Fig. 6 from OL07 for a $1.0\,M_\odot$ G-star. Together with Fig. 2.9 this shows that $Q'_\star$ can vary considerably between stars, even within the range of F-stars.

We consider the range of OCZ properties for F-stars, as the mass and metallicity are varied. A selection of illustrative examples will now be presented, which represent the range of properties expected for F-stars. Fig. 5.8 shows $Q'_\star$ as a function of tidal frequency for two F-stars, with different OCZ properties. The top panel in Fig. 5.8 shows that tidal dissipation in more massive F-stars, with very thin OCZs, is found to be extremely weak, with $Q'_\star \gtrsim 10^{12}$ for most tidal frequencies. This implies that tidal dissipation in such stars is probably negligible in contributing to the spin-orbit evolution of HJ systems. The bottom panel in Fig. 5.8 shows that tidal dissipation in lower mass F-stars with thicker convective envelopes, is similar to but slightly weaker than that for solar-type stars (OL07), since $Q'_\star \gtrsim 10^8$ for most tidal frequencies (even those in the range $|\hat{\omega}| < 2|\Omega|$).

A model with $1.3\,M_\odot$ star similar to XO-3, except that we choose supersolar metallicity ($Z = 0.03$), is found to have a similar OCZ to the $1.2\,M_\odot$ model in the bottom panel of Fig. 5.8, and has a very similar $Q'_\star$. The metallicity of the star affects the thickness of the OCZ, and therefore the efficiency of tidal dissipation.

From these examples, it is clear that assuming a single $Q'_\star$ applies for all stars is incorrect. Even within the mass range of F-stars there is considerable variation (for a given $\hat{\omega}$) in $Q'_\star \sim 10^8 - 10^{12}$ in our calculations, primarily as a result of the variation in the mass fraction contained in the OCZ. Lower mass stars, and those with higher metallicity, tend to have thicker OCZs than higher mass, low-metallicity stars. In addition, higher mass stars are more centrally condensed, so the mass fraction in their outer regions will be lower. This results in low-mass, high-metallicity stars having lower $Q'_\star$ then high-mass, low-metallicity stars. F-stars, in general, also have different $Q'_\star$ than solar-type stars, with radiative cores.

5.8 An explanation for the survival of all (currently observed) short-period planets

Our most important result is that this mechanism can potentially explain the survival of all short-period extrasolar planets around solar-type stars[4] with masses in the range

[4]Contained in the catalogue at http://www.exoplanet.hanno-rein.de/ or http://exoplanet.eu/catalog.php

$0.5 \leq m_\star/M_\odot \leq 1.1$. From using the closest fit stellar model to each of these stars, we find that no planet clearly satisfies Eq. 5.3.3 with a period $P \lesssim 3$ d (planets much further out may satisfy the criterion, though this tidal effect is then unimportant). All of these planets are insufficently massive (or orbit sufficiently young stars, with low values of $C/C_\odot$) that they are unlikely to cause wave breaking at the centre of their hosts. The dominant mechanism of tidal dissipation in these stars is therefore likely to be damping of the equilibrium tide by turbulent convection. This is likely to be relatively inefficient for these periods, since the turbulent viscosity must be reduced when the orbital period is shorter than the convective timescale, as we discussed in § 1.4 (see e.g. Zahn 1966; Goldreich & Nicholson 1977; Goodman & Oh 1997; Penev et al. 2007). This could be an important explanation for the survival of these planets.

As an example, WASP-19 b (Hebb et al. 2010) is the latest candidate for the shortest period massive transiting planet. This planet has mass $m_p = 1.15 M_J$, in an orbit of $P = 0.78$ d, around a star of mass $m_\star \approx 0.95 M_\odot$, and hence will contain a radiative core. The stellar age is poorly constrained, but we find that the IGWs excited by this planet will not have sufficient amplitude to cause wave breaking at the centre of the star, for all reasonably-aged stellar models of a similar mass star. This means that the planet will not be subject to accelerating tidal decay through critical layer absorption, perhaps explaining its survival. Constraints on the tidal $Q'_\star$ for this system would then give us information on alternative mechanisms of tidal dissipation, such as the dissipation of the equilibrium tide by turbulent convection. The existence of this planet on its observed orbit can be explained through the absence of wave breaking at the centre of its star.

The results of this thesis also allow us to propose an explanation for the survival of planets around F-type stars, with convective cores. This is because in these stars, the mechanism outlined in Part II of this thesis will not work in such stars, regardless of the mass of the planet. The reason for this is that IGWs do not propagate in convective regions, and will reflect from the top of the convective core before they reach the centre. Together with our results in § 5.7, this allows us to explain the survival of planets such as WASP-18 b (Hellier et al. 2009), WASP-12 b (Hebb et al. 2009) and OGLE-TR-56 b (Sasselov 2003). Taking the current values for the stellar

properties of the host stars in these systems, we find that they are each likely to have a convective core, which will prevent IGWs from reaching the centre of each star. In addition, these stars are slowly rotating, and so the relevant tidal frequencies are likely to be outside the range of inertial waves ($|\hat{\omega}| > 2|\Omega|$), which would imply that such waves are not excited by tidal forcing. This means that the resulting $Q'_\star$ is due only to damping of the equilibrium tide, which from Fig. 5.8 (in the limit in which $|\hat{\omega}| \gg |\Omega|$) is seen to be much larger than its value when inertial waves are excited. Therefore it is likely that the relevant $Q'_\star \gtrsim 10^{10}$ in these stars, which would imply that tidally-induced inspiral will not occur within the age of these systems. Weak dissipation in the star could therefore explain the survival of these planets, which all orbit F-stars.

Our mechanism can also explain why the most massive short-period planets (which still have smaller or comparable moments of inertia in the orbit as the RZ of the star), such as WASP-18 b (Hellier et al., 2009), WASP-14 b (Joshi et al., 2009) or CoRoT-14 b, are exclusively found around F-stars, which have convective cores, and in which critical layer formation induced by wave breaking at the centre is unable to operate. Note, however, that very massive perturbers around solar-type stars may have sufficient orbital angular momentum to be able to synchronise their stars and reach an approximate tidal equilibrium state, neglecting stellar magnetic braking, which would prevent orbital decay, even for planets in orbit around a solar-type star. This may be an explanation for the synchronisation of close-binary stars (e.g. Mazeh 2008).

Our results make several predictions, which will be tested by ongoing and future studies of transiting planets, such as WASP and Kepler. In particular, we make the prediction that fewer massive planets in the range $3 \lesssim M_J \lesssim 20$, in orbits with $P \lesssim 2 - 3$ d, that satisfy Eq. 5.3.3, will be found around solar-type stars.

5.9 Conclusion

In Part II of this thesis, a mechanism of tidal dissipation has been studied in which tidally excited IGWs break at the centre of a solar-type star, and form a critical layer. In this chapter, we considered the implications of this process for the survival of short-period planets around solar-type stars. We computed numerically the linearised adiabatic tidal response, in order to calculate the angular momentum flux of

the waves launched at the CZ/RZ interface. A semi-analytic model of this quantity was presented, and its validity was verified by numerical integrations.

We computed the tidal $Q'_\star$ that results from this process in an extensive set of stellar models. We found that Eq. 5.4.2 is a quite robust estimate, which was found to vary by no more than a factor of 5 throughout the range of G and K stars, within the mass range $0.5 - 1.1 M_\odot$, at any stage in their main-sequence lifetime, for a given planetary orbit. This results in a relatively rapid inspiral for planets on short-period orbits, if a critical layer is produced.

One important result of this work is to highlight the importance of the internal structure of the star on the magnitude of the tidal dissipation. We briefly discussed the tidal dissipation expected in F-stars, which contain convective cores. There are differences between the dissipation in G and F stars, due to differences in their internal structure – most notably the presence of a radiative core in a G-type star, which support IGWs, enabling more efficient dissipation if wave breaking (and critical layer formation) occurs. Taken together with a result of OLO7, that the spin period of the star also affects $Q'_\star$, we can conclude that it is certainly incorrect to assume $Q'_\star$ is identical for all stars.

We provided an explanation for the survival of all currently observed short-period planets around F, G or K stars, as a result of weak tidal dissipation in the star. Around G and K-type stars, planets can survive if their masses are insufficient to cause wave breaking at the centre (and therefore to satisfy Eq. 5.3.3). The stars are also slowly rotating, so it is likely that damping of the equilibrium tide by turbulent convection is the dominant mechanism of tidal dissipation, which has previously been found to be inefficient in the appropriate period range (e.g. Goldreich & Nicholson 1977; Goodman & Oh 1997). Around F-stars, planets can survive because the process of wave breaking will be prevented by reflection of the tidally excited IGWs from the convective core before they become nonlinear, together with weak dissipation of the equilibrium tide in the thin OCZ, as long as the stars are slowly rotating.

We predict that there will be very few massive planets (with masses $\lesssim 20 M_J$) orbiting G-stars (which satisfy Eq. 5.3.3) in orbits of less than 2 days, due to the rapid inspiral that results from critical layer absorption near the centre. We also predict that

the population of short-period HJs around G-stars will decrease with main sequence age, as a result of the increasing central condensation of the star, making breaking more likely. A corollary of these predictions is that there should be more massive planets in short-period orbits observed around F-stars. This appears to be the case from the current sample of extra-solar planets.

Chapter 6

Stability analysis of a standing internal gravity wave near the centre of a solar-type star in 2D

In Chapters 3 and 4 we have presented the results of numerical simulations of IGWs approaching the centre of a solar-type star, in both two and three dimensions. We found that the waves break if they overturn the isentropes near the centre, but they were not observed to undergo instability for smaller amplitudes. It has been proposed that parametric instabilities could be important for smaller amplitude waves (e.g. Kumar & Goodman 1996; GD98). Our simulations may not have the spatial resolution or have a sufficiently long run time for these instabilities to be observed. In this chapter we perform a stability analysis of our 2D exact wave solution. This work has two aims: to determine any instabilities that set in for small amplitude waves, and to understand the breaking process in more detail. Our results are compared with the stability of a plane IGW in a uniform stratification, and with previous work by Kumar & Goodman (1996) on a similar problem to our own. The astrophysical relevance of our results is then discussed.

6.1 Introduction

Many stability analyses of a plane IGW in Cartesian geometry with a uniform stratification have been performed (e.g. McEwan & Robinson 1975; Meid 1976; Drazin 1977; Klostermeyer 1982). These indicate that a monochromatic propagating plane IGW is always unstable to parametric instabilities, whatever its amplitude, in the absence of diffusion. In that problem such analyses were made possible for finite-amplitude (in addition to infinitesimal amplitude) waves because the solution is exact. This is a consequence of the fact that $\mathbf{k} \cdot \mathbf{u} = 0$, implying that the advective operator $\mathbf{u} \cdot \nabla$ annihilates any disturbance belonging to the same plane wave. These stability analyses allow a detailed understanding of the initial stages of the breaking process for these waves (e.g. Drazin 1977; Klostermeyer 1982; Lombard & Riley 1996).

When a small perturbation is added to a basic plane wave, the resulting evolutionary equations have periodic coefficients. This allows the possibility for parametric instability to occur. The first study of this problem was by McEwan & Robinson (1975), who considered perturbations with length scales much smaller than the primary IGW wavelength, in which case the problem can be reduced to the solution of Mathieu's equation. The motion of the fluid in the basic wave gives rise to unstable modes, just as parametric oscillations of a pendulum are excited by periodic changes of its length. The growth rates of these parametrically unstable modes increases (linearly) with the amplitude of the basic wave.

Subsequent analyses expanded the perturbation onto a Floquet basis, and relaxed the small-scale assumption. These studies all find that in a dissipationless fluid, the disturbances with the largest growth rates have the smallest spatial scales (e.g. Drazin 1977; Klostermeyer 1982). In viscous or radiative fluids, dissipative effects scale with the inverse square of the length scale of a given mode. This means that the most unstable wavelengths will no longer be those of the smallest spatial scale, but will be those for which the competing effects of dissipation and (nonlinear) growth favour the latter, and this will depend on the Reynolds number (also the Prandtl number when radiative diffusion is included).

Lombard & Riley (1996) performed a detailed stability analysis of a plane IGW which demonstrated that the instability that contributes to wave breaking is driven by

a combination of wave shear and wave entropy gradients. They find that wave-wave resonance interactions are the primary mode of instability for small amplitude waves, with the picture being much more complicated near overturning amplitudes. However, no difference in the type of instability is found for waves that do and do not overturn the stratification for some wave phase.

In our problem we have obtained an exact 2D standing wave solution representing IGWs near the centre of a solar-type star. This enables us to perform a stability analysis of this wave for any amplitude. This is the subject of the present chapter. One important difference between our problem and previous studies is that the nonlinearity is spatially localised in the innermost wavelengths, whereas the nonlinearity is present everywhere in the plane IGW problem.

In the centre of a star, viscous (molecular) damping is negligible, and the dominant linear dissipation mechanism is radiative diffusion, which is too inefficient to prevent the excitation of waves with scales not much smaller than the primary wavelength. This is true for the waves excited by planets orbiting solar-type stars with several-day periods. This means that parametrically excited modes with scales much shorter than the primary wave could be excited. These will then be damped by diffusion but not before they can draw energy the primary wave, and possibily contribute to wave breaking.

We have already demonstrated through direct numerical simulations that a wave with sufficient amplitude to overturn the stratification undergoes a rapid instability (with a growth time on the order of a wave period) which leads to wave breaking. We found that the wave overturns the stratification during part of its cycle if the angular velocity in the wave exceeds the angular pattern speed of the forcing, i.e. $u_\phi/r \gtrsim \Omega_p$. In these 2D simulations, the wave reflects perfectly from the centre of the star if its amplitude is insufficient to satisfy this criterion, and long-term integrations do not show that any instabilities act on the waves. The picture in 3D is very similar. In this chapter we perform a weakly nonlinear stability analysis of our 2D wave solution using a Galerkin spectral method. This work has two main aims:

- to better understand the early stages of the breaking process for large amplitude waves,

- to determine what (if any) instabilities may set in for waves that are unable to overturn the isentropes at any location in the wave.

The motivation for this study is that if the waves are subject to parametric instabilities, whatever their amplitudes, the reflection of waves from the centre of the star will not be perfect. This would stand in contrast to the prediction from linear theory, and the results of our numerical simulations. The simulations performed thus far may not have the spatial resolution or have long enough run time to be able to capture small-scale parametric instabilities. If they indeed occur, and the tidally excited waves are weakly nonlinearly damped by parametric instabilities, this could contribute to the tidal dissipation, and have implications for the survival of short-period planets with insufficient masses to cause breaking.

6.2 Internal gravity wave stability analysis

We start with the dimensionless Boussinesq-type system Eqs. 3.4.29–3.4.32, previously derived in Chapter 3. We consider a circular region with $r \in [0, r_{out}]$, taking $r_{out} = 1$, which is an impermeable outer boundary at constant entropy, i.e., $\psi(1, \phi, t) = b(1, \phi, t) = 0$, to confine the modes. Our inner boundary condition is a regularity condition[1] at $r = 0$, which is implicitly enforced through our choice of basis functions for the perturbation to the wave, as we describe below.

We use dimensionless units such that the unit of length $[L] = r_{out}$, the unit of time $[T] = N_{out} = C^{-1} r_{out}^{-1}$, and take $C = 1$. We then express the velocity field in terms of a (real) streamfunction ψ, defined by

$$u_r = \frac{1}{r}\partial_\phi \psi, \tag{6.2.1}$$

$$u_\phi = -\partial_r \psi, \tag{6.2.2}$$

which automatically enforces the solenoidality constraint on the velocity. We consider a stationary, stably stratified background containing a nonlinear wave (denoted by

[1] However, in the computation of the table of integrals described below, this is replaced by an inner boundary at $r_{in} = 10^{-4}$, to avoid the coordinate singularity at the origin.

subscript w), subject to a perturbation (denoted by primes). That is, we expand

$$b = b_w + b', \tag{6.2.3}$$

$$\psi = \psi_w + \psi'. \tag{6.2.4}$$

To eliminate the modified pressure variable q, we take the curl of the momentum equation

$$\partial_t(\nabla \times \mathbf{u}) = \nabla \times \mathbf{r}b - \nabla \times (\mathbf{u} \cdot \nabla \mathbf{u}), \tag{6.2.5}$$

which can be expanded to first order in the perturbed quantities. The z-component of this linearised equation expressed in terms of the streamfunction, together with the buoyancy equation, is

$$\partial_t(-\nabla^2\psi') + \partial_\phi b' = J(\psi_w, -\nabla^2\psi') + J(\psi', -\nabla^2\psi_w) \tag{6.2.6}$$

$$\partial_t b' + \partial_\phi \psi' = J(\psi_w, b') + J(\psi', b_w), \tag{6.2.7}$$

which is two equations for two unknowns (ψ', b'). The vorticity perturbation is $\zeta' = -\nabla^2\psi'$. The nonlinearities in this system provide coupling between different waves. We neglect the terms $J(\psi', -\nabla^2\psi')$ and $J(\psi', b')$, which is consistent with our weakly nonlinear approach.

6.2.1 Exact primary wave solution

In the frame in which the wave is steady and ϕ is the azimuthal coordinate, our primary wave is

$$\begin{aligned}\psi_w &= \mathrm{Re}\left[\frac{4}{k_{2,n_p}^3} A J_2(k_{2,n_p} r) e^{2i\phi}\right] \\ &= \frac{2}{k_{2,n_p}^3}\left[A J_2(k_{2,n_p} r) e^{2i\phi} + A^* J_2(k_{2,n_p} r) e^{-2i\phi}\right],\end{aligned} \tag{6.2.8}$$

which is an $m = 2$ wave with n_p radial nodes (to be chosen later), where $A \in \mathbb{C}$, in general, and is time-independent in this frame. From here on, we take $A \in \mathbb{R}$, without loss of generality. Note that $b_w = k_{2,n_p}\psi_w$ and $\nabla^2\psi_w = -k_{2,n_p}^2\psi_w$. We define k_{2,n_p} such that $J_2(k_{2,n_p}) = 0$. This is equivalent to confining the primary wave in a circular

region of unit radius with an impermeable outer boundary at constant entropy. We plot this wave with $n_p = 4$ in Fig. 6.1. Note that we define n_p so that $n_p = 2$ when there are no zeroes except at the boundaries, which is a nonstandard definition.

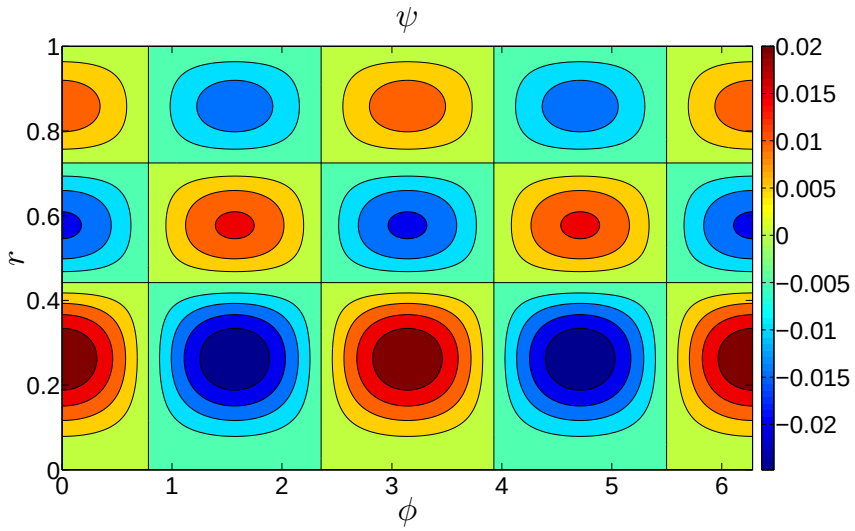

Figure 6.1: Streamfunction of the primary wave ψ_w for $n_p = 4$, with an arbitrary amplitude for illustration. Contours of constant ψ_w are the streamlines of the primary wave flow. The flow goes clockwise around the red streamlines and anticlockwise around the blue streamlines. Stagnation points are located at the radial nodes r where $J_2(k_{2,n_p} r) = 0$, at azimuthal locations $\phi = \frac{(2n+1)}{4}\pi$ for $n \in \mathbb{Z}$.

This wave overturns the stratification when $\partial_r s < 0$, where $s = (1/2)r^2 + b_w$. This is equivalent to $\frac{1}{r}\partial_r b_w < -1$. Note that overturning occurs only when $A > 1$, and is more likely for waves with large n and small m values. The size of the convectively unstable region can be illustrated for a given A and n_p, by calculating when

$$N^2 = g\partial_r s = r(r + \partial_r b) \tag{6.2.9}$$

$$= r^2 + \mathrm{Re}\left[\frac{2A}{k_{2,n_p}} r \left(J_1(k_{2,n_p} r) - J_3(k_{2,n_p} r) e^{2i\phi}\right)\right] < 0, \tag{6.2.10}$$

(where we take $c_p = 1$ for convenience). For illustration, we plot the 2D region that is convectively unstable for several A values when $n_p = 4$ in Fig. 6.2. An approximate size for the overturning region for small r when $A > 1$ is

$$r_{ov} \approx \sqrt{\frac{6}{k_{2,n_p}^2}\left(1 - \frac{1}{A}\right)}, \tag{6.2.11}$$

at the most unstable wave phase. When $A = 1$ the overturning region is the point $r = 0$, with the region expanding for larger A. If the instabilities that cause wave breaking are convectively driven, we would expect them to be strongly localised within the convectively unstable regions of the primary wave.

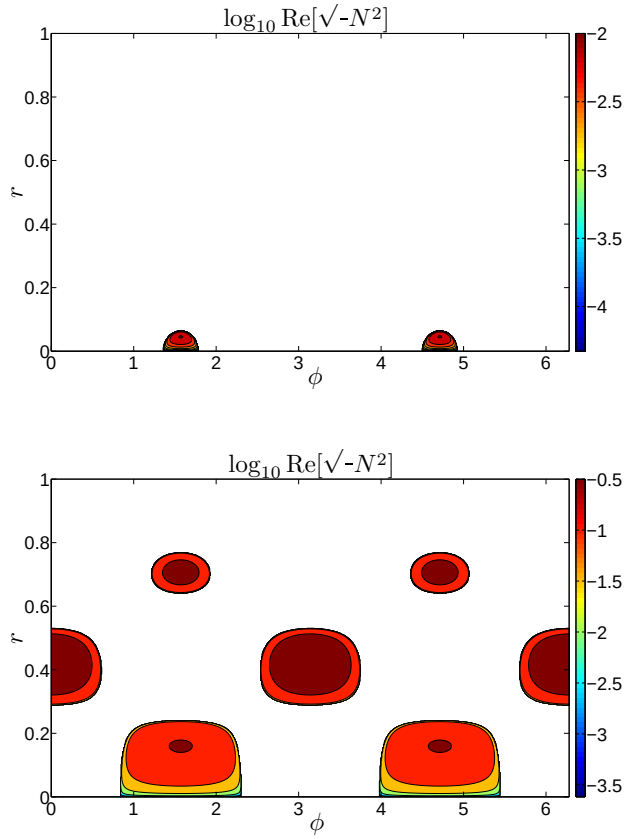

Figure 6.2: Spatial exent of the region that is made convectively unstable by the primary wave for $A = 1.1$ (top) and 10 (bottom), with $n_p = 4$. This regions expands from the point $r = 0$ when $A = 1$ to encompass the innermost few wavelengths for larger A.

6.2.2 Infinitesimal perturbations

We consider linear pertubations to this finite-amplitude primary wave, which we expand as (dropping the primes from now on)

$$\psi = \sum_{m=-\infty}^{\infty} \sum_{n=2}^{\infty} \psi_{m,n}(t) J_m(k_{m,n} r) e^{im\phi}, \tag{6.2.12}$$

$$b = \sum_{m=-\infty}^{\infty} \sum_{n=2}^{\infty} b_{m,n}(t) J_m(k_{m,n} r) e^{im\phi}, \tag{6.2.13}$$

where $k_{m,n}$ is chosen such that the solutions for each azimuthal wavenumber m, and radial node number $n \geq 2$, satisfy the outer boundary condition at $r = 1$, for which

$$J_m(k_{m,n}) = 0. \tag{6.2.14}$$

This condition forces $k_{m,n} \in \mathbb{R}$, for $|m|, n \in \mathbb{Z}^+$. The above expansion automatically enforces a regularity condition on the perturbations at $r = 0$. Eqs. 6.2.12 and 6.2.13 define our Galerkin basis. This basis is adopted for two reasons: the linear solutions ($A = 0$) take the same form, and it automatically ensures that the total energy of the perturbations is conserved, since the energy flux through the boundaries is always zero (because $u_r = b = 0$ at $r = 0, 1$).

Note that our spectral-space amplitudes $\psi_{m,n}(t), b_{m,n}(t) \in \mathbb{C}$, so we must take the real part at the end of the calculation to obtain physical quantities. For each m, there is an infinite number of components with different values of n. In our spectral representation of the solution, we truncate these infinite series at $1-M \leq m \leq M-1$, where M is an odd number, and $n = N$. This truncation is chosen so that we have an exactly equal number either side of $m = 0$ (and a similar number either side of the primary wave $m = 2$) which ensures that our mathematical realisation of the problem has the symmetry property that we discuss in § 6.5.3 below.

6.2.3 Derivation of the evolutionary equations

Evolutionary equations for the amplitudes $\psi_{m,n}(t)$ and $b_{m,n}(t)$ can be derived by projection through integration onto the Galerkin basis. To do this we substitute the above expansions into the weakly nonlinear system defined by Eqs. 6.2.6–6.2.7. An important orthogonality relation is

$$\int_0^{2\pi} \int_0^1 r J_m(k_{m,n'} r) J_m(k_{m,n} r) e^{i(m-m')\phi} dr d\phi = \pi \left[J_{m+1}(k_{m,n})\right]^2 \delta_{n,n'} \delta_{m,m'}, \tag{6.2.15}$$

where δ is the Kronecker delta. Note that this results in different normalisation factors for each m and n wave. Also note that

$$-\nabla^2 \left(J_m(k_{m,n} r) e^{im\phi}\right) = k_{m,n}^2 J_m(k_{m,n} r) e^{im\phi}. \tag{6.2.16}$$

6.2.4 Linear solutions (in the absence of the primary wave)

Consider $J(\dots,\dots) = 0$, which is equivalent to having a hydrostatic background with no primary wave flow. If we substitute the expansions Eq. 6.2.12–6.2.13 into Eqs. 6.2.6–6.2.7, and then multiply by $rJ_{m'}(k_{m'n'}r)e^{-im'\phi}$, and finally integrate over $\phi \in [0, 2\pi]$ and $r \in [0, 1]$, we obtain

$$k_{m,n}^2\dot{\psi}_{m,n} + imb_{m,n} = 0 \tag{6.2.17}$$

$$\dot{b}_{m,n} + im\psi_{m,n} = 0 \tag{6.2.18}$$

for each m, n, after redefining $m' \to m$, and $n' \to n$ after the integration. This system, together with the boundary conditions, can be solved to give

$$\psi_{m,n} = A_{m,n}e^{-i\omega_{m,n}t}, \tag{6.2.19}$$

which are oscillations if $A_{m,n} \in \mathbb{C}$, with frequency $\omega_{m,n} = m/k_{m,n}$ in the inertial frame. This is the dispersion relation for modes confined to a circular region of unit radius, and is the frequency of a non-interacting wave which is able to exist in the container in the absence of any primary wave flow, which can take any value in the range $[0, 1]$ (if we do not truncate the Galerkin basis at some finite values of N and M, then these modes would be dense in this frequency interval), since the maximum buoyancy frequency $N_{max} = 1$. In the frame rotating with the pattern speed of the primary wave with angular frequency $\omega_p/2 = 1/k_{2,n_p}$, the Doppler-shifted frequency is $\hat{\omega}_{m,n} = \omega_{m,n} - \omega_p$. Note that $k_{m,n}$ increases with both m and n, but $\omega_{m,n}$ decreases with n and increases with m. When substituting the above solution back into Eq. 6.2.12–6.2.13, we obtain the linear solutions of the system, which are Bessel functions of a given order m with n nodes in the radial direction. This motivated our choice of Galerkin basis.

6.2.5 Nonlinear terms

We obtain our weakly nonlinear system from Eqs. 6.2.6–6.2.7 through the same approach as in the previous section, to obtain for each m and n,

$$k_{m,n}^2\dot{\psi}_{m,n} + imb_{m,n} = \frac{1}{\pi\left[J_{m+1}(k_{m,n})\right]^2}\int_0^{2\pi}\int_0^1 \Big\{ rJ_m(k_{m,n}r)e^{-im\phi}$$

$$\times \left[J(\psi_w, -\nabla^2\psi) + J(\psi, -\nabla^2\psi_w)\right] \Big\} dr d\phi, \quad (6.2.20)$$

$$\dot{b}_{m,n} + im\psi_{m,n} = \frac{1}{\pi \left[J_{m+1}(k_{m,n})\right]^2} \int_0^{2\pi} \int_0^1 \Big\{ r J_m(k_{m,n} r) e^{-im\phi} \times \left[J(\psi_w, b) + J(\psi, b_w)\right] \Big\} dr d\phi, \quad (6.2.21)$$

where the Jacobians contain sums over n' and m'. The sum over m' is eliminated to a pair of terms through the ϕ integration, using Eq. 6.2.15. A set of coupling integrals of triple products of Bessel functions also results, for which there is a sum of such terms over n', i.e., an m, n wave is coupled through nonlinear terms to waves with $m \pm 2$ and (in principle) all node numbers $n \in \{2, \ldots, \infty\}$. The system reduces to

$$k_{m,n}^2 \dot{\psi}_{m,n} + imb_{m,n} = \sum_{n'=2}^{\infty} \Big\{ \alpha_{m,n,n'} \left(k_{m-2,n'}^2 - k_{2,n_p}^2\right) \tilde{A} \psi_{m-2,n'} + \beta_{m,n,n'} \left(k_{m+2,n'}^2 - k_{2,n_p}^2\right) \tilde{A}^* \psi_{m+2,n'} \Big\}, \quad (6.2.22)$$

$$\dot{b}_{m,n} + im\psi_{m,n} = \sum_{n'=2}^{\infty} \Big\{ \alpha_{m,n,n'} \tilde{A} \left(b_{m-2,n'} - k_{2,n_p} \psi_{m-2,n'}\right) + \beta_{m,n,n'} \tilde{A}^* \left(b_{m+2,n'} - k_{2,n_p} \psi_{m+2,n'}\right) \Big\}, \quad (6.2.23)$$

where

$$\tilde{A} = \frac{2}{k_{2,n_p}^3} A. \quad (6.2.24)$$

The coupling coefficients are

$$\alpha_{m,n,n'} = \underbrace{\frac{2}{\left[J_{m+1}(k_{m,n})\right]^2}}_{\text{normalisation}} \left(i(m-2)\mathcal{I}_{m,n,n'}^1 - 2i\mathcal{I}_{m,n,n'}^2\right), \quad (6.2.25)$$

$$\beta_{m,n,n'} = \underbrace{\frac{2}{\left[J_{m+1}(k_{m,n})\right]^2}}_{\text{normalisation}} \left(i(m+2)\mathcal{I}_{m,n,n'}^3 + 2i\mathcal{I}_{m,n,n'}^4\right), \quad (6.2.26)$$

with the integrals

$$\mathcal{I}_{m,n,n'}^1 = \int_0^1 J_m(k_{m,n} r) \left[\partial_r J_2(k_{2,n_p} r)\right] J_{m-2}(k_{m-2,n'} r) dr, \quad (6.2.27)$$

$$\mathcal{I}_{m,n,n'}^2 = \int_0^1 J_m(k_{m,n} r) J_2(k_{2,n_p} r) \left[\partial_r J_{m-2}(k_{m-2,n'} r)\right] dr, \quad (6.2.28)$$

$$\mathcal{I}^3_{m,n,n'} = \int_0^1 J_m(k_{m,n}r)\left[\partial_r J_2(k_{2,n_p}r)\right] J_{m+2}(k_{m+2,n'}r)dr, \tag{6.2.29}$$

$$\mathcal{I}^4_{m,n,n'} = \int_0^1 J_m(k_{m,n}r)J_2(k_{2,n_p}r)\left[\partial_r J_{m+2}(k_{m+2,n'}r)\right]dr. \tag{6.2.30}$$

Note that these are related by

$$\mathcal{I}^3_{m,n,n'} = \mathcal{I}^1_{m+2,n',n}\ , \tag{6.2.31}$$

$$\mathcal{I}^4_{m,n,n'} = \mathcal{I}^2_{m+2,n',n} - \mathcal{I}^1_{m+2,n',n}\ . \tag{6.2.32}$$

For use in the derivation of the spectral space energy equation in a subsequent section, we find it convenient to define

$$\tilde{\alpha}_{m,n,n'} = -i\pi\left[J_{m+1}(k_{m,n})\right]^2\alpha_{m,n,n'}, \tag{6.2.33}$$

and similarly for $\tilde{\beta}_{m,n,n'}$. This is because we then have the relation

$$\tilde{\beta}_{m,n,n'} = \tilde{\alpha}_{m+2,n',n}. \tag{6.2.34}$$

6.2.6 Diffusive terms

In the presence of viscosity and radiative diffusion (or hyperdiffusion) Eqs. 6.2.6–6.2.7 become

$$\partial_t(-\nabla^2\psi) + \partial_\phi b = J(\psi_w, -\nabla^2\psi) + J(\psi, -\nabla^2\psi_w) + (-1)^{2+\alpha}\nu\nabla^{2+2\alpha}\psi, \tag{6.2.35}$$

$$\partial_t b + \partial_\phi\psi = J(\psi_w, b) + J(\psi, b_w) + (-1)^{1+\alpha}\kappa\nabla^{2\alpha}b, \tag{6.2.36}$$

where α is chosen to give the standard diffusive operator ($\alpha = 1$), or hyperdiffusion ($\alpha = 2, 3$). In this case we obtain the (linearised) system

$$k^2_{m,n}\dot{\psi}_{m,n} + imb_{m,n} = -\nu k^{2+2\alpha}_{m,n}\psi_{m,n}, \tag{6.2.37}$$

$$\dot{b}_{m,n} + im\psi_{m,n} = -\kappa k^{2\alpha}_{m,n}b_{m,n}, \tag{6.2.38}$$

instead of Eq. 6.2.17–6.2.18. The dispersion relation is then

$$\left(\omega_{m,n} + i\nu k^{2\alpha}_{m,n}\right)\left(\omega_{m,n} + i\kappa k^{2\alpha}_{m,n}\right) = \frac{m^2}{k^2_{m,n}}, \tag{6.2.39}$$

indicating that the frequencies of the allowed solutions are modified in the presence of ν, κ. The growth rate expected in the presence of weak diffusion is therefore modified to be $\mathrm{Im}\,[\omega] - \frac{1}{2}(\nu+\kappa)k_{m,n}^{2\alpha}$, with $\mathrm{Im}\,[\omega]$ being the appropriate inviscid growth rate. To obtain growing modes, diffusion must be sufficiently weak so that it does not overcome nonlinear growth. Hyperdiffusion with $\alpha = 3$ is adopted since it better restricts the dissipation to the highest wavenumbers. This enables numerical convergence in the eigenvalue problem discussed below, but does not significantly perturb the growth rates of the lower wavenumber eigenmodes with the values of ν, κ that we adopt. From here on, we also take $\nu = \kappa$.

With the inclusion of diffusive terms we require $1 + 2\alpha$ additional boundary conditions at each boundary. These are regularity conditions at the centre, and at the outer boundary we can consider a variety of boundary conditions of the form $\nabla^{2n}\psi = 0$ for $n = 0, 1, \ldots, \alpha$ and $\nabla^{2n} b = 0$ for $n = 0, 1, \ldots, \alpha - 1$. These are automatically satisfied by our Galerkin basis Eq. 6.2.12–6.2.13 and the definition of $k_{m,n}$. With these boundary conditions (which force $k_{m,n}$ to be real), the Galerkin basis is therefore exact for the single-wave diffusive problem. Note that this is also true if hyperdiffusion is adopted, due to property Eq. 6.2.16. In the numerical solution of the eigenvalue problem in the following sections we include these diffusive terms to achieve numerical convergence. This is necessary because in the absence of diffusion, the most unstable modes are found to prefer the smallest spatial scales.

One important difference between this problem and that discussed in Chapter 7 is that in that case the solution with viscous and radiative damping is no longer exact. This makes sense physically because we are damping the wave, but the difference can be mathematically explained as follows. In that problem we force a particular wave, i.e., choose a wave with $\omega \in \mathbb{R}$. With diffusion $k_{m,n} \in \mathbb{C}$, so that $J_m(k_{m,n} r) \in \mathbb{C}$, in general. Since the real part of this is taken before computing the nonlinear terms, the property Eq. 6.2.16 no longer implies that the nonlinear terms vanish. In this section, we are forcing $k_{m,n} \in \mathbb{R}$ through the boundary conditions, thus each component of our Galerkin basis is exact with viscous and radiative damping, and the corresponding solutions will have a nonzero decay rate as a result of these diffusive processes. This further supports our choice of the Galerkin basis Eq. 6.2.12–6.2.13.

6.3 Method of solution

Our weakly nonlinear system Eqs. 6.2.20–6.2.21 can be written in the form of a generalised eigenvalue problem of the form

$$A\mathbf{U} = \omega B\mathbf{U}, \tag{6.3.1}$$

where $\mathbf{U}$ is the column vector whose components are the quantities $(\psi_{m,n}, b_{m,n})$ for each m and n. A is the block tridiagonal matrix representing the system. This is done by seeking normal mode solutions of the form $\psi_{m,n}(t) \propto e^{-i\omega t}$ for each m and n, and similarly for $b_{m,n}(t)$. B is the matrix that can be represented as

$$\mathrm{B} = -i \begin{pmatrix} k_{m,n}^2 & 0 \\ 0 & 1 \end{pmatrix}, \tag{6.3.2}$$

for a single m and n. We solve this problem using standard generalised eigenvalue solver routines, such as ZGGEV in the LAPACK libraries. This returns the eigenvalues $\{\omega\}$, and the spectral space eigenfunctions $\{\psi_{m,n}, b_{m,n}\}$ corresponding to each eigenvalue. The real space eigenfunctions can be reconstructed from these, using Eqs. 6.2.12–6.2.13.

We choose $N = 50$ and $M = 27$. With our choice of $\alpha = 3$ hyperdiffusion, it has been found from preliminary investigation that $10^{-11} \leq \nu \leq 10^{-14}$ is appropriate. This hyperdiffusion is found to give the numerical junk eigenvalues, whose eigenfunctions oscillate at the smallest scales, a large decay rate, and allows our growing modes to be adequately converged for the values of A and n_p that we consider.

6.3.1 Numerical computation of table of integrals

The tables of integrals defined by Eqs. 6.2.27–6.2.30 for each value of m, n, n' are computed using a 4th/5th order adaptive step Runge-Kutta integrator. To enable efficient computations, the Bessel functions are computed simultaneously with the integrals. This is desirable because using built-in Mathematica or Matlab routines for computing these functions is extremely slow when they are evaluated at every step.

Note that Bessel's equation

$$\partial_r(r\partial_r\psi) + r\left(k_{m,n}^2 - \frac{m^2}{r^2}\right)\psi = 0, \tag{6.3.3}$$

can be rewritten as the coupled set of first order ODEs

$$\frac{d\xi}{dr} = r\left(\frac{m^2}{r^2} - k_{m,n}^2\right)\psi, \tag{6.3.4}$$

$$\frac{d\psi}{dr} = \frac{\xi}{r}. \tag{6.3.5}$$

We also need the derivatives of various Bessel functions, so we compute

$$\frac{d^2\psi}{dr^2} = \frac{(m^2 - r^2k_{m,n}^2)\psi - \xi}{r^2}, \tag{6.3.6}$$

for each r. To compute the integrals, we solve $\frac{d\mathcal{I}^i_{m,n,n'}}{dr}$ for $i \in \{1,2,3,4\}$. This involves solving a system of 15 ODEs in total for each m, n, n'. Using our chosen resolution of $N = 50$, $M = 27$, this involves the computation of $M(N-1)^2 \sim 10^5$ integrals in total. These are computed for a given number of radial nodes in the primary wave in the range $2 \leq n_p \leq 12$. We impose an inner boundary at $r_{in} = 10^{-4}$ to avoid the coordinate singularity at the origin, and use initial conditions appropriate from considering the asymptotic behaviour of the Bessel functions. For small N and M values the numerical integrals have been checked to agree with those computed from Mathematica, and for large N and M, several integrals containing the highest n and m values were also checked. We use a relative error tolerance of 10^{-13}, which has been found to compute the most oscillatory integrals (corresponding to the highest n and m value) accurately (compared with Mathematica) to within at least 6 decimal places.

6.4 Kinetic and potential energy equations

The kinetic and potential energies can be computed from either the real-space or spectral-space eigenfunctions. This will enable a determination of the dominant source of free energy driving the instability (e.g. Lombard & Riley 1996), and will also provide an independent calculation of the growth rate, which can be used to check our numerical code. We derive an energy equation in spectral space, and compute the

volume-integrated terms using the numerically computed eigenfunctions, without converting to real space. This has been found to reduce numerical errors, resulting from large numerical cancellations in the most oscillatory Bessel functions, when the energy equations are instead computed in real space. In addition, it is simpler to construct the hyperdiffusion terms in spectral space, so that they can be fully taken into account in the energy budget.

We define $K = \frac{1}{2}|\mathbf{u}|^2$, $P = \frac{1}{2}b^2$ and $E = K + P$, as the kinetic, potential and total energy densities of the disturbance, respectively. We define a volume (strictly an area, since we are in 2D) integral by

$$\langle X \rangle = \int_0^{2\pi} \int_0^1 X r dr d\phi. \tag{6.4.1}$$

Note that

$$\langle K \rangle = \frac{1}{2} \sum_{m=-\infty}^{\infty} \sum_{n=2}^{\infty} k_{m,n}^2 |\psi_{m,n}|^2 \pi \left[J_{m+1}(k_{m,n}) \right]^2, \tag{6.4.2}$$

$$\langle P \rangle = \frac{1}{2} \sum_{m=-\infty}^{\infty} \sum_{n=2}^{\infty} |b_{m,n}|^2 \pi \left[J_{m+1}(k_{m,n}) \right]^2, \tag{6.4.3}$$

$$\langle E \rangle = \langle K \rangle + \langle P \rangle. \tag{6.4.4}$$

Evolutionary equations for the volume-integrated energy can be obtained from Eq. 6.2.22 & 6.2.23. After some rearrangement, these can be written

$$\langle \dot{K} \rangle = \langle \mathcal{N}_{sw} \rangle + \langle F_b \rangle + \langle F_\nu \rangle, \tag{6.4.5}$$

$$\langle \dot{P} \rangle = \langle \mathcal{N}_{bw} \rangle - \langle F_b \rangle + \langle F_\kappa \rangle, \tag{6.4.6}$$

$$\langle \dot{E} \rangle = \langle \mathcal{N}_{sw} \rangle + \langle \mathcal{N}_{bw} \rangle + \langle F_\nu \rangle + \langle F_\kappa \rangle, \tag{6.4.7}$$

where

$$\langle \mathcal{N}_{sw} \rangle = \mathrm{Re} \left\{ \sum_{m=-\infty}^{\infty} \sum_{n=2}^{\infty} \sum_{n'=2}^{\infty} i \tilde{\alpha}_{m,n,n'} \left(k_{m-2,n'}^2 - k_{m,n'}^2 \right) \tilde{A} \psi_{m,n}^* \psi_{m-2,n'} \right\}, \tag{6.4.8}$$

$$\langle \mathcal{N}_{bw} \rangle = \mathrm{Re} \left\{ \sum_{m=-\infty}^{\infty} \sum_{n=2}^{\infty} \sum_{n'=2}^{\infty} i \tilde{\alpha}_{m,n,n'} \tilde{A} k_{2,n_p} \left(b_{m,n}^* \psi_{m-2,n'} + \psi_{m,n}^* b_{m-2,n'} \right) \right\}, \tag{6.4.9}$$

$$\langle F_b \rangle = \mathrm{Re} \left\{ \sum_{m=-\infty}^{\infty} \sum_{n=2}^{\infty} im \psi_{m,n}^* b_{m,n} \pi \left[J_{m+1}(k_{m,n}) \right]^2 \right\}, \tag{6.4.10}$$

$$\langle F_\nu \rangle = \mathrm{Re}\left\{ \sum_{m=-\infty}^{\infty} \sum_{n=2}^{\infty} -\nu k_{m,n}^{2+2\alpha} |\psi_{m,n}|^2 \pi \left[J_{m+1}(k_{m,n}) \right]^2 \right\}, \tag{6.4.11}$$

$$\langle F_\kappa \rangle = \mathrm{Re}\left\{ \sum_{m=-\infty}^{\infty} \sum_{n=2}^{\infty} -\kappa k_{m,n}^{2\alpha} |b_{m,n}|^2 \pi \left[J_{m+1}(k_{m,n}) \right]^2 \right\}. \tag{6.4.12}$$

$\langle \mathcal{N}_{sw} \rangle$ represents the production of perturbation kinetic energy from the primary wave shear. $\langle \mathcal{N}_{bw} \rangle$ represents the production of perturbation potential energy from the primary wave entropy gradients. Whichever of $\langle \mathcal{N}_{sw} \rangle$ or $\langle \mathcal{N}_{bw} \rangle$ is dominant tells us whether this instability is driven by the wave shear or the wave entropy gradients. $\langle F_b \rangle$ is the buoyancy flux term, representing conversion between kinetic and potential energies of the disturbance.

After truncation at $|m| = M$ and $n = n' = N$, each of these terms are computed from the spectral space eigenfunctions, together with the numerically computed table of integrals. The growth rate can then be computed from

$$\mathrm{Im}[\omega'] = \frac{\langle \dot{E} \rangle}{2\langle E \rangle} = \frac{\langle \dot{K} \rangle}{2\langle K \rangle} = \frac{\langle \dot{P} \rangle}{2\langle P \rangle}. \tag{6.4.13}$$

We have checked that each of these equations are accurately satisfied to within at most a few percent for each of the unstable modes discussed in this chapter. This is an excellent check of our analytical derivations and numerical calculations, and should convince ourselves that our results are consistent.

6.5 Numerical tests

In this section we briefly mention several numerical tests which we have performed to validate our numerical code. Following this section, in § 6.6 and 6.7 we discuss the results of our stability analysis for waves with $A < 1$ and $A > 1$, respectively.

6.5.1 Linear

In the absence of nonlinear couplings ($A = 0$), we obtain a set of non-interacting modes with eigenfreqencies $\omega \in \{\omega_{m,n}\}$, where $\omega_{m,n} = m/k_{m,n}$ (in the inertial frame), as we predicted in § 6.2.4. In the absence of diffusion, these have zero growth rate, i.e., $\mathrm{Im}[\omega] = 0$, for all eigenmodes. When hyperdiffusion is included, the eigenmodes

each have a nonzero decay rate determined by the values of ν and κ, which is very accurately (to more than 10 decimal places) computed from considering only the terms $\langle F_\nu \rangle$ and $\langle F_\kappa \rangle$ in the energy equation. The real-space eigenfunctions that result are what is predicted from linear theory, in that they are Bessel functions of order m with n nodes in the radial direction.

6.5.2 Weakly nonlinear

We followed a typical eigenmode as A is gradually increased from zero, and found that for $|A| \ll 1$, the shift in the eigenfrequency $\mathrm{Re}[\delta\omega] \propto A^2$, as we would expect for modes not undergoing parametric resonance (e.g. Landau & Lifshitz 1969).

6.5.3 Symmetries

The real-space solutions can be represented in the form

$$\mathrm{Re}\left[\sum_m \sum_n c_{m,n} e^{i(m\phi - \omega t)}\right]. \tag{6.5.1}$$

This is symmetric under the transformations $c_{m,n} \rightarrow c^*_{m.n}$, $m \rightarrow -m$ and $\omega \rightarrow -\omega^*$. This symmetry should exist for all primary wave amplitudes, and results from the fact that only the sign of the pattern speed ω/m has meaning, and not the sign of the wavenumber or frequency. This means that when the eigenvalues are plotted on the complex frequency plane, they should be symmetric about $\mathrm{Re}\,[\omega] = 0$.

6.6 Results for waves with $A < 1$: parametric instabilities

We examine the unstable modes that exist when $0 < A < 1$, which is when the primary wave does not overturn the stratification at any location in the wave. The instability is a parametric instability, for which a simple model is briefly reviewed in Appendix A.7. When $A \neq 0$, the fraction of eigenmodes that are growing is nonzero (above a critical A set by the values of n_p and ν, which can be understood from Eq. A.7.7) and increases with A, as nonlinear growth starts to dominate over the decay due to diffusion for a

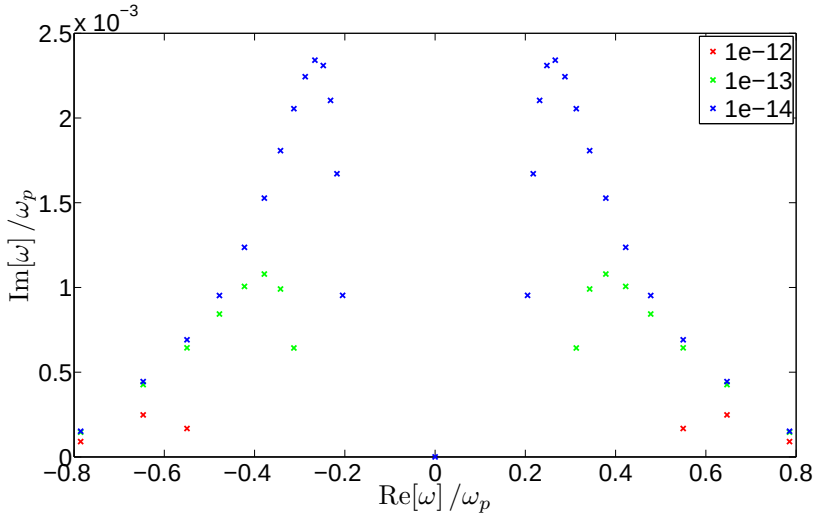

Figure 6.3: Distribution of unstable eigenvalues on the complex frequency plane for $A = 0.1$, $n_p = 4$ and $\nu = 10^{-12}, 10^{-13}, 10^{-14}$.

larger number of modes. For small A, the eigenvalues of the unstable modes displayed on the complex plane are distributed in two curves that are approximately equidistant from the origin at each location. This is illustrated in Fig. 6.3, and is a result of the symmetry described in § 6.5.3.

In the limit that $A \to 0$, the unstable modes can be identified as the parametrically excited free-wave modes. These are a pair of free wave modes that exist when $A = 0$, which undergo modifications to their complex frequencies at $O(A)$ that reinforce each other. As A is increased, the unstable modes consist of gradually more complicated superpositions of free wave modes, until for $A \gtrsim O(1)$, the eigenfunctions become localised in the convectively unstable regions. This will be studied in § 6.7. For $A \lesssim 1$, the eigenfunctions exist because of their confinement by the boundaries, though they interact quite strongly with the primary wave, and are generally not simply free wave modes with a nonzero growth rate. However, we have verified that the modes consist of a pair whose frequencies approximately add up to ω_p in the inertial frame, with a detuning $|\Delta|/\omega_p \lesssim 10^{-2}$ for most pairs of modes.

The number of unstable modes that exist in this amplitude range depends quite strongly on viscosity. This is illustrated in Fig. 6.3. The number is also found to decrease as n_p is increased. These two behaviours are related by the fact the wave

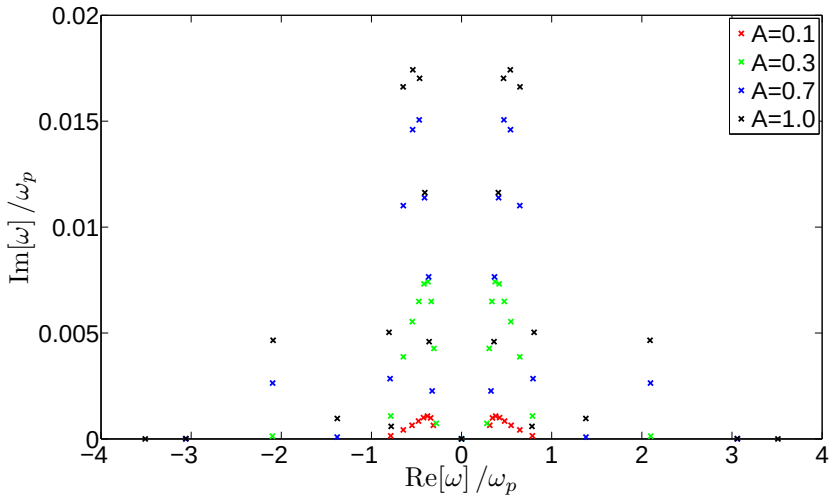

Figure 6.4: Distribution of unstable eigenvalues on the complex frequency plane for various values of A, with $n_p = 4$ and $\nu = 10^{-14}$.

should undergo parametric instabilities, which have largest growth rates when the resonant tuning is good, which is more likely to occur for perturbations with larger wavenumbers. However, these large wavenumber components are strongly damped by diffusion. Increasing n_p means that the "effective resolution" available to capture the unstable modes decreases. This is the same as increasing ν, hence the same trends exhibited in increasing n_p and ν.

The neat distribution of eigenvalues into two curves does not persist as A is increased, as illustrated in Fig. 6.4. The frequencies (in the rotating frame) are primarily smaller than the primary wave frequency in the inertial frame. However, a small number of modes exist for $A \gtrsim 0.3$ which have frequencies larger than ω_p. Nevertheless, in each case the frequencies of the unstable modes are always smaller than the maximum buoyancy frequency in the flow (which corresponds with $1/\omega_p \sim 6$ in the units of this figure, for $n_p = 4$). This makes sense if these are gravity wave-like disturbances, which are parametrically excited by the primary wave.

In Fig. 6.5, the growth rate for the most unstable mode is shown to scale approximately linearly with A for $A \leq 1$. A slope of 1 in this figure is predicted for $A \ll 1$ if the instability is due to a parametric resonance.

Our most important result of this section is illustrated in Fig. 6.6. This shows that

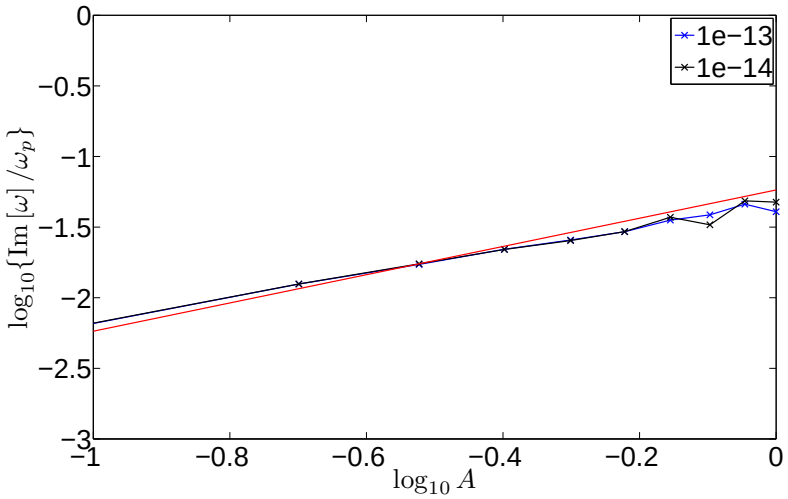

Figure 6.5: Im[ω] vs. A for the most unstable mode with $n_p = 4$ and $\nu = 10^{-13}, 10^{-14}$. The solid red line has slope 1. This shows that the instability approximately scales linearly with A for small A, indicating that the instability when $A < 1$ is due to a parametric resonance.

the growth rate scales inversely with the number of wavelengths within the domain (note that this is after normalising by ω_p). In this figure we plot the logarithm of the growth rate versus $\log_{10} n_p$ for $A = 0.5$ and 0.8, respectively. The slope is always approximately equal to -1 for low n_p. The tail-off at larger n_p is due to diffusion, and arises because modes with smaller spatial scales parametrically excite modes with even smaller spatial scales (as a result of the theorem proved by Hasselmann 1967), which are then more easily damped by diffusion. As we would expect from this interpretation, the value of n_p at which diffusion dominates moves to smaller n_p as ν is increased. The inverse dependence on n_p that is present when diffusion is unimportant is a key result. This suggests that although parametric instabilities exist for any amplitude in the absence of diffusion, in a sufficiently large domain they become unimportant. We discuss the relevance of this result in § 6.8.

6.6.1 Eigenfunctions

In the top panels of Figs. 6.7 & 6.8 we plot the real (blue solid lines) and imaginary parts (red dashed lines) along $\phi = 0$ of the spatial eigenfunctions of the most unstable mode for $A = 0.1$ and 0.5, respectively. We have taken $n_p = 4$ and $\nu = 10^{-13}$. These

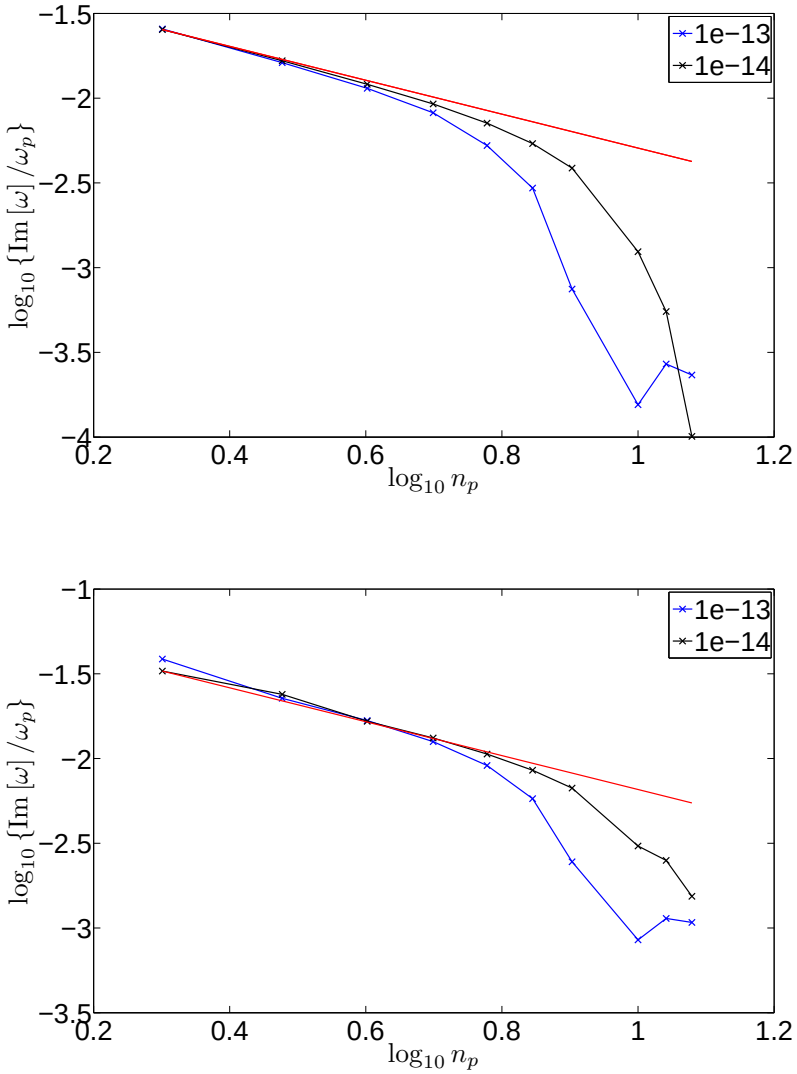

Figure 6.6: $\log_{10}\mathrm{Im}[\omega/\omega_p]$ vs. $\log_{10} n_p$ for the most unstable mode when $A = 0.5$ and 0.8 respectively, for $\nu = 10^{-13}$ and 10^{-14}. The red line has a slope -1. The tail-off at larger n_p is due to diffusion.

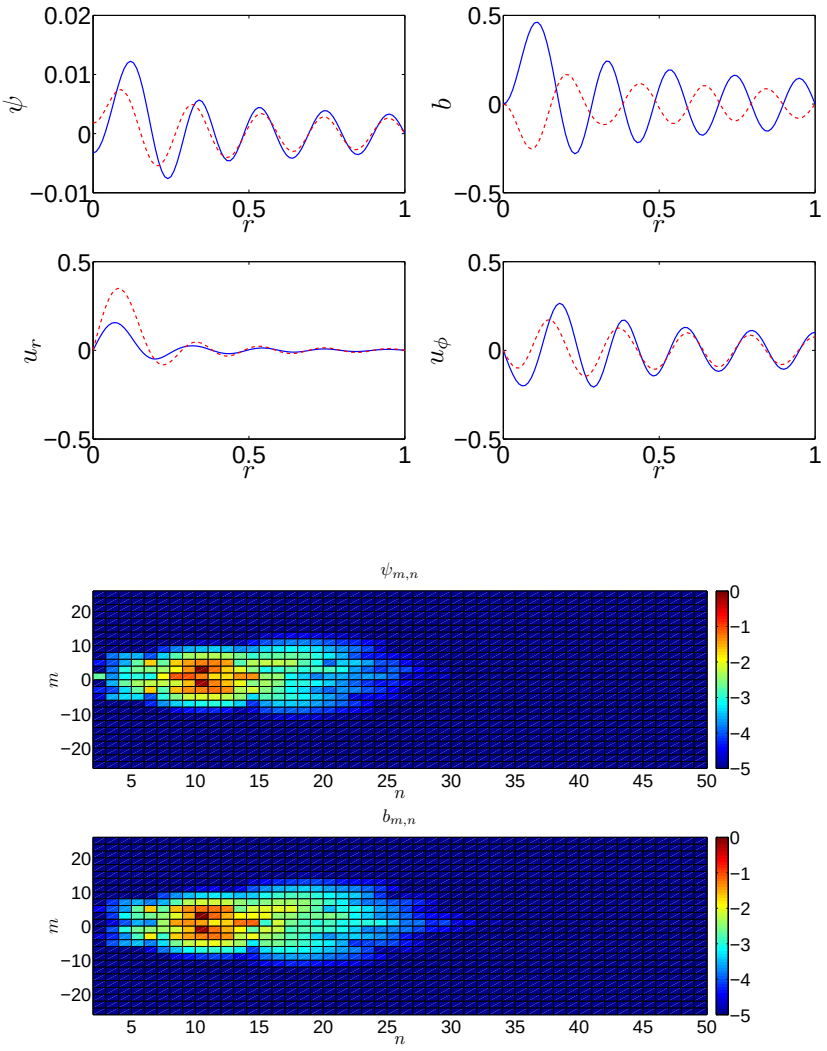

Figure 6.7: Top: Real (blue solid lines) and imaginary (red dashed lines) parts along $\phi = 0$ of the spatial eigenfunctions for the most unstable mode for $A = 0.1$, $n_p = 4$, $\nu = 10^{-13}$. The eigenfrequency is $\omega/\omega_p = 0.378 + 0.001i$. Bottom: Spectral space eigenfunction of the same mode. The colour scale represents $\log_{10} |\psi_{m,n}/\max\{\psi_{m,n}\}|$, and similarly for $b_{m,n}$.

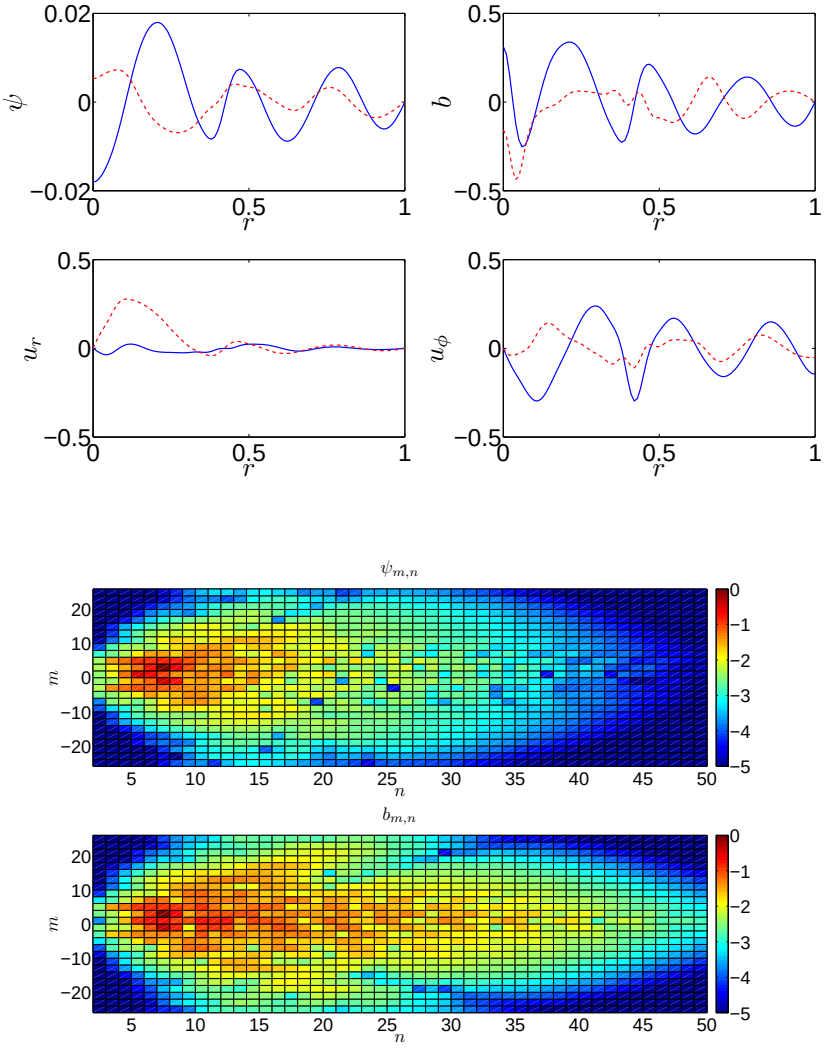

Figure 6.8: Top: Real (blue solid lines) and imaginary (red dashed lines) parts along $\phi = 0$ of the spatial eigenfunctions for the most unstable mode with $A = 1$, $n_p = 4$, $\nu = 10^{-13}$. The eigenfrequency is $\omega/\omega_p = 0.540 + 0.017i$. Bottom: Spectral space eigenfunction of the same mode. The colour scale represents $\log_{10} |\psi_{m,n}/\max\{\psi_{m,n}\}|$, and similarly for $b_{m,n}$.

modes exist throughout the box and are confined by the boundary. They become more distorted from the free wave modes as A is increased towards unity (and in fact also for $A > 1$, until the localised modes appear), especially in the innermost wavelengths of the primary wave. Note that the amplitude of the eigenfunctions is arbitrary since we are solving an eigenvalue problem. The bottoms panels of Figs. 6.7 & 6.8 show the spectral space eigenfunctions of the same unstable modes. We have normalised $\psi_{m,n}$ and $b_{m,n}$ to their maximum absolute values and taken the base 10 logarithm of each component to produce the figures. These show that growing modes for the chosen values of A are not simply a pair of free wave modes which are excited by the primary wave. They contain many n and m values localised around a particular n and m, and are therefore interacting strongly with the primary wave. Multiple n and m values are involved even when $A = 0.1$. For the value of ν adopted, these modes are well resolved, as is shown from the amplitude decay of the spectral space eigenfuntion, which occurs before the resolution limit is reached in n and m.

6.6.2 Energetics of the instabilities

When $A < 1$, the isentropes are never overturned by the primary wave, so a pure radial convective instability is not possible. However, these instabilities could be driven by the free energy resulting from the primary wave shear or entropy gradients, or a combination of the two. In this section, we compute the spectral space energy contributions outlined in § 6.4, for a sample of growing modes in this amplitude range. We have confirmed that the growth rate is accurately computed from Eq. 6.4.13, to within a few percent at most. In Table 6.1 we outline the contributions to the growth rate from each term in Eqs. 6.4.5–6.4.7 for the most unstable mode for $A = 0.1, 0.5$ and 1 with $n_p = 4$ and $\nu = 10^{-13}$. The eigenfunctions for two of these are plotted in Figs. 6.7 & 6.8. These examples are illustrative of every unstable mode that exists when $A < 1$ (and also the non-localised modes that exist when $A > 1$).

Firstly, we note that the integrated kinetic and potential energy of the modes are in approximate equipartition. A single wave can be shown to be in exact equipartition, so we would expect $\langle K \rangle \approx \langle P \rangle$ if these modes are parametrically excited gravity waves with a single n and m. That they are in approximate equipartition and include many

	$A = 0.1$	$A = 0.5$	$A = 1$
$\mathrm{Re}\,[\omega]$	0.065	0.080	0.093
$\mathrm{Im}\,[\omega]$	1.86×10^{-4}	1.97×10^{-3}	3.00×10^{-3}
$\langle K \rangle$	3.28×10^{-2}	3.82×10^{-2}	3.70×10^{-2}
$\langle P \rangle$	3.25×10^{-2}	3.87×10^{-2}	4.16×10^{-2}
$\langle \mathcal{N}_{sw} \rangle$	-3.20×10^{-7}	-3.98×10^{-5}	-9.55×10^{-5}
$\langle \mathcal{N}_{bw} \rangle$	3.57×10^{-5}	3.76×10^{-4}	6.62×10^{-4}
$\langle F_b \rangle$	1.81×10^{-5}	2.04×10^{-4}	3.51×10^{-4}
$\langle F_\nu \rangle$	-5.58×10^{-6}	-1.35×10^{-5}	-3.29×10^{-5}
$\langle F_\kappa \rangle$	-5.55×10^{-6}	-2.01×10^{-5}	-6.03×10^{-5}

Table 6.1: Energy components of the most unstable mode for $A = 0.1, 0.5$ and 1, with $n_p = 4$ and $\nu = 10^{-13}$. Note that $\omega_p \approx 0.17$.

n and m components indicates that these modes are the larger A generalisations of the parametrically excited free wave modes. The source of free energy driving these modes is entirely the potential energy resulting from primary wave entropy gradients. Somewhat surprisingly, the primary wave shear contribution is much smaller, and actually stabilises the modes. This instability converts primary wave potential energy to disturbance potential energy, and then converts approximately half of this input energy to the disturbance kinetic energy through the buoyancy flux term. This process results in approximate equipartition between $\langle K \rangle$ and $\langle P \rangle$. Note that the entropy gradients in the primary wave are insufficient to cause convective instability. These modes are driven by weaker entropy gradients in radius and azimuth.

6.7 Results for waves with $A > 1$: the initial stages of wave breaking

When $A > 1$, the primary wave overturns the stratification during part of its cycle. Our simulations have shown that an instability breaks the wave within a few wave periods once this first occurs. The initial stages of this breaking process are examined in this section by choosing $A > 1$. To resolve convectively unstable modes with the adopted values of N and M, we require the size of the overturning region to be sufficiently large. Since overturning occurs only at the point $r = 0$ when $A = 1$, this necessitates choosing values of A larger than unity to capture such instabilities. We are interested

in instabilities which act to break the waves in an (effectively) unbounded domain (the central regions of the RZ of a solar-type star), therefore the appropriate unstable mode should not rely on the boundaries for confinement, and should be localised within the innermost wavelength of the primary wave. This is because the presence of confining boundaries is artificial, and is imposed to specify the problem. With this in mind, we now discuss the results of our stability analysis for waves with $A > 1$.

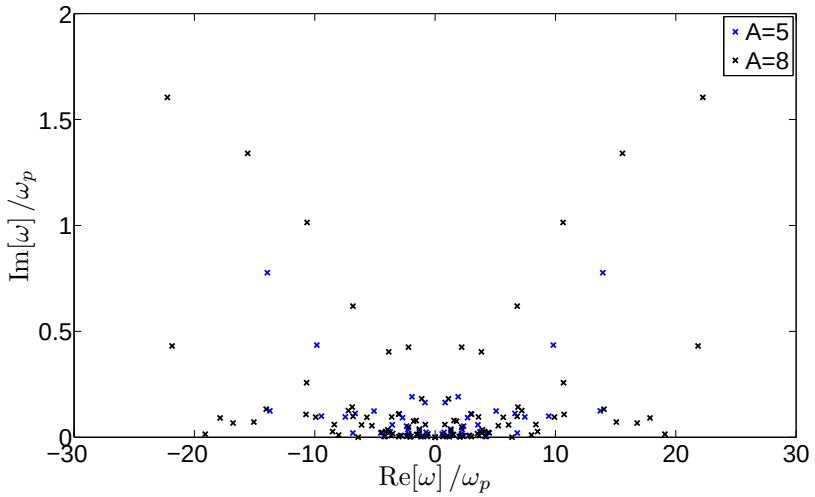

Figure 6.9: Distribution of unstable eigenvalues on the complex frequency plane for $n_p = 4$ and various A with $\nu = 10^{-13}$.

The eigenvalues of the unstable modes displayed on the complex plane are shown in Fig. 6.9 for $A = 5$ and $A = 8$, both with $n_p = 4$ and $\nu = 10^{-13}$. The most unstable modes are located on distinct branches, which stand above the continuation of the modes that exist when $A < 1$. From studying their eigenfunctions, we find that the modes on the branches are localised disturbances, unlike those below the main branches. The modes on the branches could therefore represent the type of mode that breaks the primary wave (this is discussed further in the next subsection). These branches extend further from the origin the greater the value of A. In Fig. 6.10 we plot the unstable modes for $A = 5$ for two values of n_p. This shows that the unstable modes on the branches do not move around significantly as n_p is varied. They therefore depend only weakly on the location of the outer boundary. Note, however, that the growth rate becomes smaller as we go to larger n_p because of the increasing importance

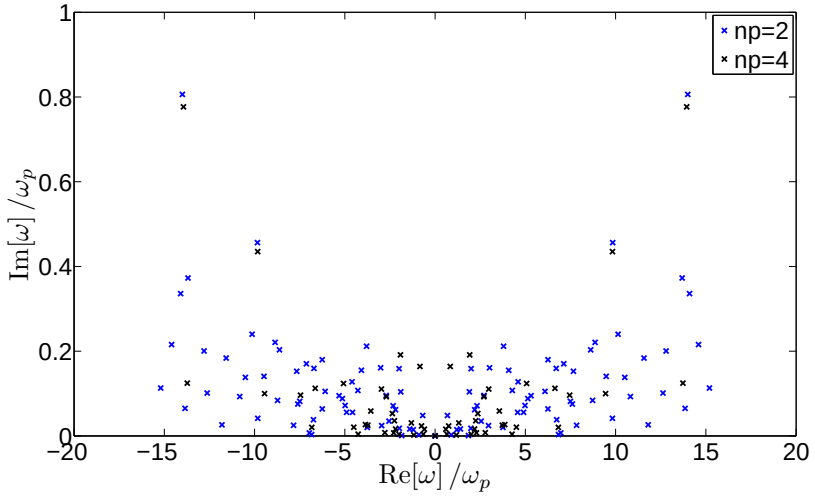

Figure 6.10: Distribution of unstable eigenvalues on the complex frequency plane for $A = 10$ and various n_p, with $\nu = 10^{-13}$.

of diffusion.

Note that the largest frequency of some growing modes is larger than the maximum buoyancy frequency $N_{max} = 1$ (which corresponds with $1/\omega_p \sim 6$ in the units of this figure, for $n_p = 4$). The nonzero frequencies of the modes in this frame indicate that they are oscillatory, and are non-steady. In addition, the growth rates of the most unstable modes are sufficiently fast compared with the primary wave frequency that the instability grows within several wave periods after onset.

The growth rate of the most unstable modes for a given n_p increases with A as illustrated in Fig. 6.11 for $n_p = 4$, where curves for $\nu = 10^{-13}$ and 10^{-14} have been plotted. There is an approximate square root dependence for $A \gtrsim 5$. If the instability is driven by convectively unstable entropy gradients, then we might expect

$$\begin{aligned} \mathrm{Im}\left[\omega'\right] &\lesssim \sqrt{\max\left[-N^2\right]} \\ &= \left(\max\left\{-r^2 - \mathrm{Re}\left[\frac{2A}{k_{2,n_p}} r \left(J_1(k_{2,n_p} r) - J_3(k_{2,n_p} r)\right) e^{2i\phi}\right]\right\}\right)^{1/2}. \quad (6.7.1) \end{aligned}$$

Thus, for large A the growth rate should scale with the square root of the primary wave amplitude. This behaviour is not observed when $1 \lesssim A \lesssim 5$. In this range, the square root dependence may not be exhibited partly because there is insufficient resolution to accurately capture the modes that contribute to breaking since the overturning region

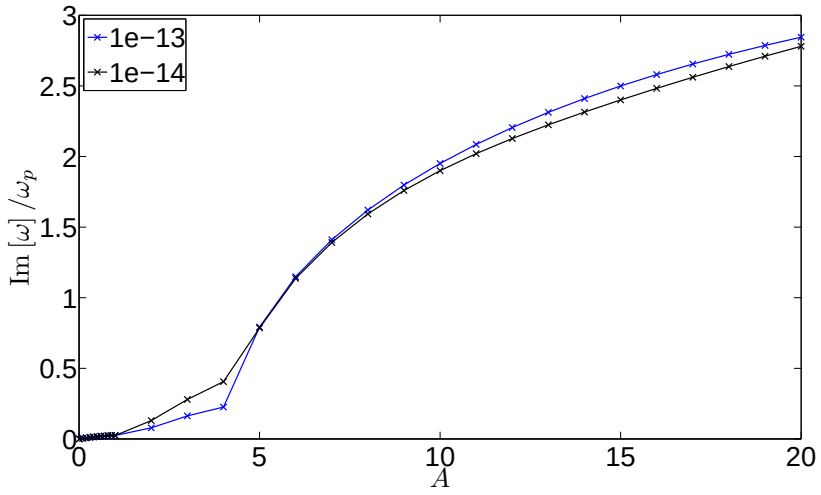

Figure 6.11: Im[ω] vs. A for the most unstable mode for $n_p = 4$, $\nu = 10^{-13}$ and 10^{-14}. The instability grows within a primary wave period when $A \gtrsim 5$, which is when the localised modes begin to appear.

is small compared with the box size. We have noticed that the growth rate does not significantly depend on ν (and therefore the resolution), for the most unstable modes, except in the range $1 \lesssim A \lesssim 5$, which supports this explanation.

The behaviour of the growth rate on n_p is illustrated in Fig. 6.12 for the most unstable mode when $A = 5$, for two values of ν. For large n_p, the unstable modes have sufficiently small spatial scales for diffusion to become important, so we expect a tail-off at large n_p. The important point that can be taken from this figure is that the (normalised) growth rate of the localised modes on the branches does not depend on the number of wavelengths within the domain, for modes that are not strongly affected by diffusion. This means that the instability can be important in a large domain, such as the RZ of a solar-type star, which contains many primary wavelengths.

6.7.1 Eigenfunctions

In the top panel of Fig. 6.13 we plot the real (blue solid lines) and imaginary parts (red dashed lines) along $\phi = 0$ of the spatial eigenfunctions of the most unstable mode for $A = 5$, $n_p = 4$ and $\nu = 10^{-13}$. The spectral-space eigenfunction of this mode is plotted in the bottom panel. The mode is strongly nonlinearly interacting with the

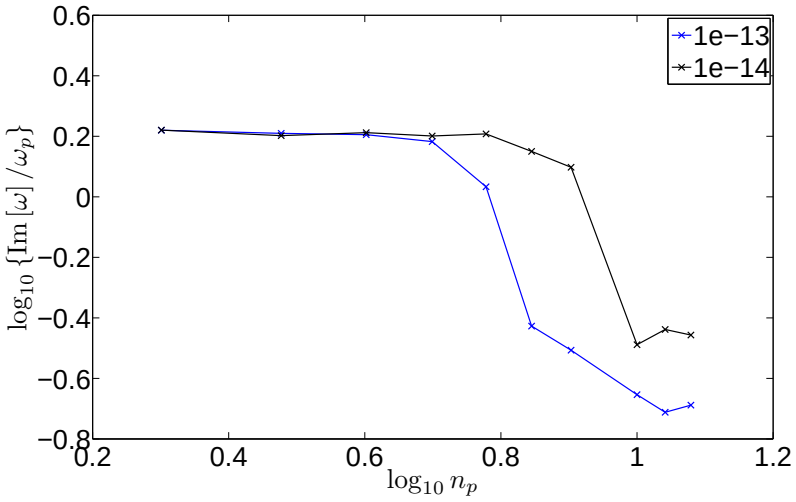

Figure 6.12: Im[ω] vs. n_p for the most unstable localised modes when $A = 5$ and $\nu = 10^{-13}$ and 10^{-14}.

primary wave, as shown by the number of different n and m values that appreciably contribute. The contribution to the eigenfunction is nonzero, but not maximal, near $|m| = M - 1$, and is negligible at $n = N$, which indicates that this mode is only just adequately resolved. The eigenfunction is spatially localised within the innermost wavelengths of the primary wave. Each of the several most unstable modes in the range $5 \leq A \leq 10$ which lie on the branches in Fig. 6.9 are localised modes, and have qualitatively different form to the type of modes that exist below the branches, which are a continuation of the modes that exist when $A < 1$. As we go to larger A for the same value of ν, the most unstable mode utilises an increasing number of n and m values up to the resolution limit. This means that to adequately resolve the modes we would have to either increase the resolution or the value of ν.

The components of the spatial eigenfunction of the most unstable mode when $A = 5$, $n_p = 4$ and $\nu = 10^{-13}$, is plotted in Fig. 6.14 on the (ϕ, r)-plane, to further illustrate the spatial dependence of this mode. In Fig. 6.15 we plot the region of negative N^2 for the same primary wave. A comparison of these figures makes clear that the eigenfunction is primarily localised within the regions made convectively unstable by the primary wave entropy perturbation. This adds further evidence to the conjecture that the instability is convective. We also find that any unstable mode on the branches

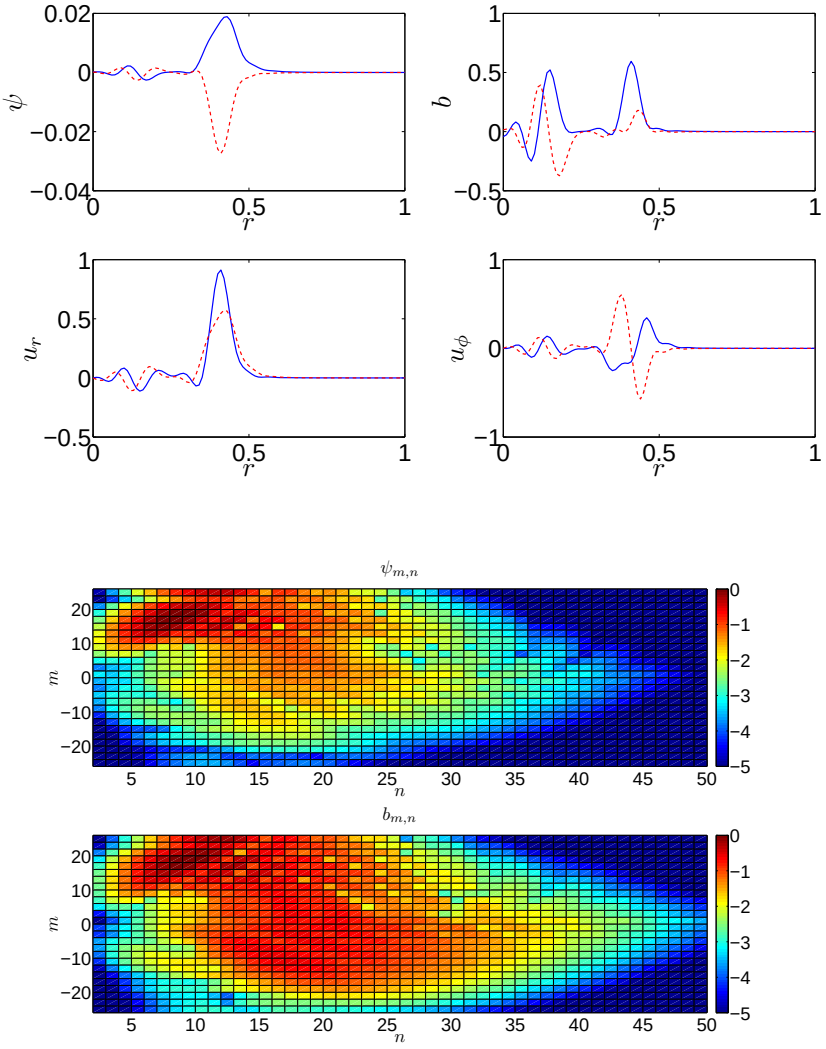

Figure 6.13: Top: Real (blue solid lines) and imaginary (red dashed lines) parts along $\phi = 0$ of the spatial eigenfunctions for the most unstable mode with $A = 5$, $n_p = 4$, $\nu = 10^{-13}$. The eigenfrequency is $\omega/\omega_p = 9.68 + 0.302i$. Bottom: Spectral space eigenfunction of the same mode. The colour scale represents $\log_{10} |\psi_{m,n}/\max\{\psi_{m,n}\}|$, and similarly for $b_{m,n}$.

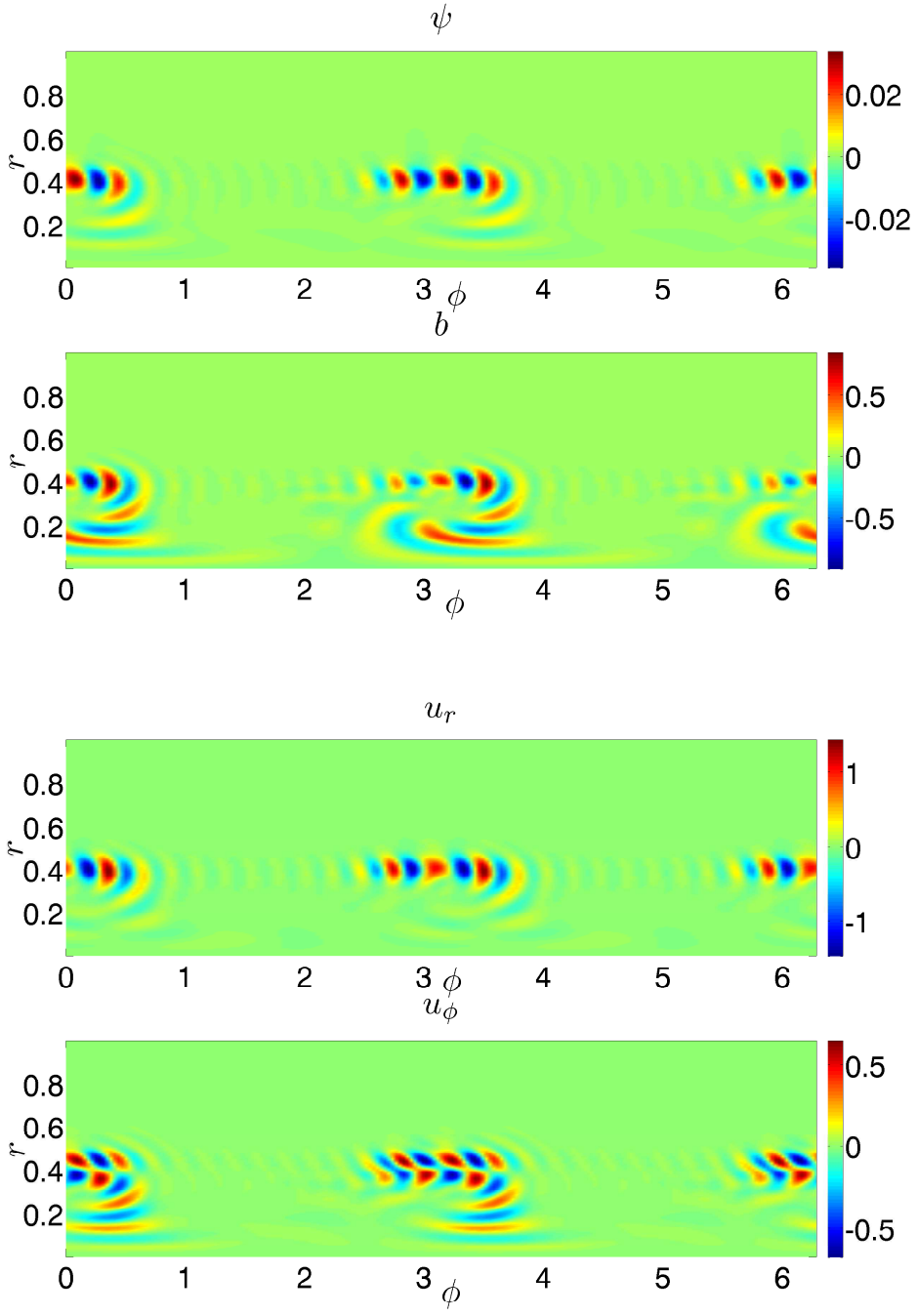

Figure 6.14: 2D Spatial eigenfunction of the most unstable mode for $A = 10$, $n_p = 4$ and $\nu = 10^{-13}$, plotted on the (ϕ, r)-plane.

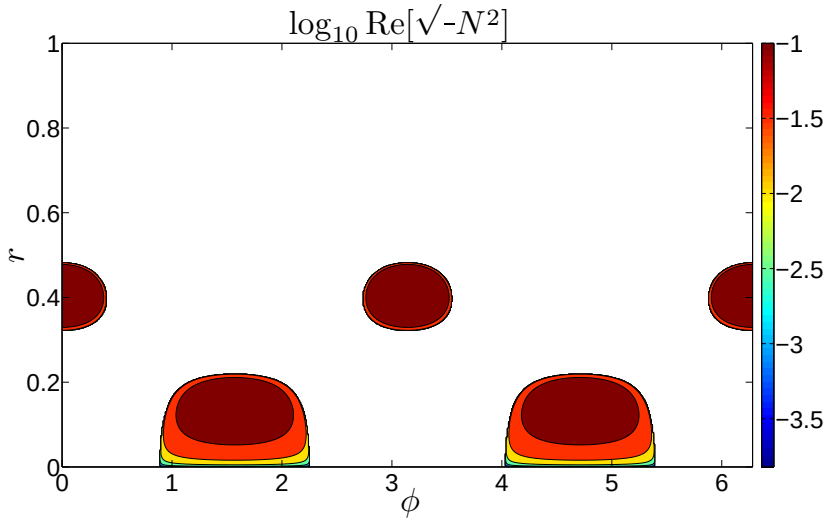

Figure 6.15: Unstable region for $A = 10$, $n_p = 4$. This can be compared with Fig. 6.14.

of Fig. 6.9 that are excited when $5 \leq A \leq 10$ are similarly localised and have a qualitatively similar appearance to the eigenfunction plotted in Fig. 6.14.

6.7.2 Energetics of the instabilities

In this section, we compute the spectral space energy contributions outlined in § 6.4 for a representative sample of the localised growing modes that exist when $A > 1$. We have confirmed that the growth rate is accurately computed from Eq. 6.4.13, to within a few percent for the modes considered in this analysis. However, it must be noted that the most unstable mode when $A \gtrsim 5$ is typically not fully resolved with our adopted resolution and ν, in that there is nonzero power in the highest n and m values. This can lead to errors in the energy analysis typically of order $10 - 30\%$, so we leave these modes out of this analysis, and only choose those that are adequately resolved for Table 6.2. In this table, we outline the contributions to the growth rate from each term in Eqs. 6.4.5–6.4.7 for several unstable modes that exist when $A \gtrsim 5$, each with $n_p = 4$ and $\nu = 10^{-13}$. The eigenfunction corresponding to the first of these is plotted in Figs. 6.13 & 6.14.

As in the case of the modes that exist when $A < 1$, the instability is driven by the free energy associated with primary wave entropy gradients, as is shown by the fact that $\langle \mathcal{N}_{bw} \rangle$ is the dominant contribution to the growth. This is indeed what would

	$A = 5$	$A = 7$
$\mathrm{Re}\,[\omega]$	1.67	2.40
$\mathrm{Im}\,[\omega]$	0.052	0.134
$\langle K \rangle$	6.95×10^{-2}	3.37×10^{-2}
$\langle P \rangle$	1.73×10^{-2}	1.02×10^{-2}
$\langle \mathcal{N}_{sw} \rangle$	-5.50×10^{-3}	-1.57×10^{-3}
$\langle \mathcal{N}_{bw} \rangle$	2.05×10^{-2}	1.55×10^{-2}
$\langle F_b \rangle$	1.82×10^{-2}	1.22×10^{-2}
$\langle F_\nu \rangle$	-2.10×10^{-3}	-1.33×10^{-3}
$\langle F_\kappa \rangle$	-0.517×10^{-3}	-0.80×10^{-3}

Table 6.2: Energy components of the most unstable mode for $A = 5$ and 7, with $n_p = 4$ and $\nu = 10^{-13}$. Note that $\omega_p \approx 0.17$.

be expected of a convectively driven instability. In addition, the primary wave shear is much weaker and tends to stabilise the modes. Unlike the modes that exist when $A < 1$, we do not necessarily have $\langle K \rangle \approx \langle P \rangle$, and examples have been found that do and do not satisfy approximate equipartition, so these modes do not appear to be gravity wave-like, unlike the parametrically excited modes that exist when $A < 1$.

The growth rates are always $\lesssim \mathrm{Re}\left[\sqrt{-N^2}\right]$, which is expected to be an upper limit if the instability is convective. The negative contribution of shear, as well as hyperdiffusion mean that the modes that we have calculated have somewhat smaller growth rates that this simple estimate would predict. The route of energy transfer that drives the instability is the same as for the parametric instabilities discussed in the previous section.

6.8 Summary and discussion of results

In the previous two sections we have analysed the instabilities that exist when $A < 1$ and $A > 1$.

6.8.1 Wave breaking

When $A > 1$ we have identified a class of localised modes that are driven by convectively unstable entropy gradients in the primary wave. These modes exist in the absence of an outer boundary, and are very likely to have initialised the wave break-

ing process in the simulations presented in Chapters 3 & 4. Subsequent stages in the breaking process are not studied using this stability analysis because these would involve nonlinear interactions between the perturbations to the wave, which we neglected in our weakly nonlinear approach. The instability growth time is of the order of a primary wave period, which is in agreement with the wave breaking times observed in our simulations.

6.8.2 Parametric instabilities

When $A < 1$, there exist pairs of parametrically excited modes driven by (convectively stable) primary wave entropy gradients, with wave shear playing a subordinate stabilising role. These modes exist because of their confinement by the outer boundary. Our most important result regarding these modes is the inverse dependence of the growth rate on n_p. This can be explained by considering the relative time the primary wave spends in the innermost regions, where its nonlinearity is strongest. The fraction of the total wave propagation time spent in the innermost regions, where growing modes are excited by the nonlinearity, scales with $k_{2,n_p}^{-1} \propto n_p^{-1}$, so the growth rate should also scale with n_p^{-1}. Combining this with our observation that the growth rate increases approximately linearly with wave amplitude, we can write

$$\mathrm{Im}\left[\omega\right] \propto \frac{A}{n_p}, \tag{6.8.1}$$

for the modes excited when $A < 1$.

Our simulations in Chapters 3 & 4 did not show any instabilities acting on the waves when $A < 1$. This can be neatly explained from Eq. 6.8.1 in the limit as $n_p \to \infty$, where the growth rate tends to zero. This limit is appropriate since the waves have effectively no outer boundary in the simulations, because we damp the waves before they reach the boundaries of the computational domain. The fact that we observed no instabilities in the simulations is therefore consistent with this stability analysis, and is not a consequence of limited run time or insufficient spatial resolution.

6.8.3 Comparison with the plane IGW problem

This problem has some important differences with the case of a plane IGW in a uniform stratification. For that problem, as we discussed in the introduction to this chapter, parametric instabilities act for any A, and always result in instability in the absence of diffusion. In addition, Lombard & Riley (1996) find that the presence or absence of isentropic overturning does not seem to play a dominant role in, and is not the cause of, the instability[2]. This is different from our problem, where we find that overturning results in the presence of a different class of localised modes, that are excited in the convectively unstable regions of the wave. However, we do find that the source of free energy driving the instability is the same whether $A < 1$ or $A > 1$. It is true that parametric instabilities exist for any A in our problem, like in the plane IGW problem, but these become unimportant in a large domain because the nonlinearity is spatially localised in the innermost wavelengths. This is different from the plane IGW problem, in which the nonlinearity is important everywhere in the wave.

The importance of overturning in our case could be because the primary wave shear does not drive the modes, and in fact typically acts to stabilise them. In the plane IGW problem, instabilities for any A are driven by a combination of $\langle \mathcal{N}_{sw} \rangle$ and $\langle \mathcal{N}_{bw} \rangle$, whereas in our problem instabilities are always driven solely by $\langle \mathcal{N}_{bw} \rangle$. Shear therefore does not play as important a role as for the instability of plane IGWs.

From the results of their stability analyses, Lombard & Riley (1996) and Sonmor & Klaassen (1997) state that wave stability is a three-dimensional problem. This might suggest that the picture we have outlined could differ in 3D. However, the simulations performed in Chapter 4 show a strong similarity with the 2D results. Performing a similar stability analysis in 3D would be somewhat involved, and would be restricted to studying the stability of small amplitude waves, because the wave solution is not exact in 3D. It would be possible to calculate higher order terms to the solution, which would make it valid for larger A, and then perform a stability analysis of this wave. Without performing such an analysis, it is difficult to quantify the importance of three-dimensional effects on the wave stability. Nevertheless, the excellent correspondence

[2]However, it is possible that in their calculations they have insufficient resolution to be able to resolve any localised convectively unstable modes. If they go to larger A, than the maximum they consider of 1.1, and/or consider larger resolutions, such localised modes may start to appear.

between the results of the simulations in 2D and 3D suggest that for our problem the inclusion of a third dimension would be unimportant, with regards to wave stability.

6.8.4 Implications for tidal dissipation

In Chapter 5, we discussed the implications of the wave breaking process for tidal dissipation in solar-type stars, and therefore to the survival of short-period planets. What more can we say in light of the results of this chapter?

One result is that parametric instabilities exist for waves with $A < 1$. These do not occur in an unbounded domain (the limit as $n_p \to \infty$), but will be present in the RZ of a solar-type star, since this does have an outer boundary, albeit many wavelengths from the centre of the star. We can roughly fit Eq. 6.8.1 to the results of our stability analysis, allowing us to give an upper bound to the expected growth rate of the strongest instability of a tidally excited gravity wave with $A < 1$. We write

$$\mathrm{Im}\left[\frac{\omega}{\omega_p}\right] = K\frac{A}{n_p}, \tag{6.8.2}$$

and calculate a value of K from the solutions to our eigenvalue problem, where we typically find $K \approx 0.1$. In the RZ of a solar-type star, tidally excited gravity waves have $10^2 \lesssim n_p \lesssim 10^3$, for orbital periods in the range $1 \lesssim P \lesssim 3$ days. We can therefore calculate an upper bound on the expected growth rate of a parametric instability in a real star from taking $A = 1$ and $n_p = 10^2$, giving $\mathrm{Im}\left[\omega/\omega_p\right] \approx 10^{-3}$, so that the resulting growth time,

$$t_{grow} = \frac{1}{\mathrm{Im}\left[\omega\right]} \approx 2.7 \text{ yrs.} \tag{6.8.3}$$

It is important to note that this estimate is likely to be an approximate lower bound on t_{grow}, and will not be strongly affected by the inclusion of the rest of the RZ, because the the amplitude of the waves, and therefore the nonlinearity, is much smaller away from the centre. (In addition, note that our Boussinesq-type model is only valid where $N \propto r$, which is only true near the centre of the star.) These calculations constrain the effects of nonlinear wave-wave interactions in the innermost regions, but do not take into account the rest of the RZ.

It is important to estimate the magnitude of the resulting tidal dissipation, so that we can evaluate its role in the evolution of short-period planets. Instead of considering the problem of continual forcing of the primary wave by the planet, we consider initialising the primary wave and ask how long it takes to be attenuated (and its energy dissipated), calling this timescale t_{nl} (this is similar to the highly eccentric binary problem discussed in Kumar & Goodman (1996), which we discuss in the next section). The torque on the star due to the gradual attenuation of the wave due to the combined action of these parametric instabilities at nonlinearly damping the wave, is

$$\frac{m}{\omega} F \left(1 - e^{-\alpha}\right), \tag{6.8.4}$$

with the attenuation factor $\alpha = t_{group}/t_{nl}$, and F being computed as outlined in Chapter 5. We define the global group travel time $t_{group} = 2\int_0^{r_b}(1/c_{g,r})dr \approx 25$ d, from a numerical calculation for the waves excited by a planet in a one-day orbit around the current Sun. The next question is: what is t_{nl}? To calculate this accurately is a very difficult problem, and involves many uncertainties, particularly those involving the saturation process for these nonlinear couplings. However, we note that a lower bound on t_{nl} can be obtained by the growth rate of the fastest growing parametric instability t_{grow}. This is because this will act as a bottleneck for the nonlinear cascade of energy from the primary wave, and so will limit the maximum decay rate of the primary wave. This is probably also true if we are continually forcing the wave. We can then estimate

$$\alpha \lesssim \frac{t_{group}}{t_{grow}} \approx 0.025. \tag{6.8.5}$$

This gives an upper bound on the torque resulting from the nonlinear damping of the primary wave. Using Eq. 5.1.2, this can be used to give a lower bound on the tidal quality factor resulting from nonlinear damping of the primary wave in the $A < 1$ regime,

$$Q'_\star \gtrsim \frac{10^5}{1 - e^{-\alpha}} \approx \alpha^{-1} 10^5 \approx 5 \times 10^6, \tag{6.8.6}$$

in the weak damping limit. The efficiency of this process is less than critical layer

absorption by a factor $\alpha^{-1} \gg 1$. Note that this gives a lower bound on $Q'_\star$, because t_{nl} is likely to be somewhat larger than t_{grow} (e.g. Kumar & Goodman 1996 take $t_{nl} = 10t_{grow}$). The resulting $Q'_\star$ may therefore be one or several orders of magnitude larger than this lower bound. Furthermore, it is interesting to note that this bound may not be sensitive to the number of wavelengths in the RZ, and therefore to the orbital period, because the dependences of t_{group} and t_{grow} on n_p cancel at leading order.

The parametric instabilities that exist when $A < 1$ are much slower than the rapid instabilities that onset when $A > 1$. The nonlinear outcome of the $A > 1$ instabilities is that the wave breaks and forms a critical layer, which then absorbs subsequent ingoing waves, and results in astrophysically efficient tidal dissipation. The estimate of this section indicates that the parametric instabilities that exist when $A < 1$ are much less efficient at dissipating energy in the tide, by several orders of magnitude. This important result supports the explanation outlined in Chapter 5 for the survival of short-period planets around solar-type stars.

6.8.5 Comparison with Kumar & Goodman

We can qualitatively compare our results with previous work by Kumar & Goodman (1996), who studied nonlinear damping of tidal oscillations in highly eccentric solar-type binaries. They used a truncated Hamiltonian approach to study parametric instabilities of tidally excited f and g-modes. In their model, stellar eigenmodes are coupled together from terms that exist at third order in displacement in the expansion of the Lagrangian density, i.e., they adopt a weakly nonlinear approach. They consider the evolution of a mode that has been tidally excited, but is no longer subject to forcing, due to nonlinear coupling with a large number of g-modes that are present in the RZ of the star (and exist because they have already been excited by turbulent convection, for example). Their result indicates that high order and high degree g-modes can be parametrically excited by low order quadrupolar f and g-modes, and can draw energy from the primary mode on a timescale that is much shorter than the radiative damping time of the primary mode.

A direct comparison of our work with theirs is not possible for several reasons.

Firstly, in their numerical work they mainly consider a primary f-mode coupling to many g-modes in the RZ. The f-mode eigenfunction has its largest magnitude at the surface and decays rapidly inwards, in contrast to the primary g-modes that we are considering, so the coupling strengths are likely to be different. Secondly, we only consider the nonlinear interactions in the central regions of the star, where they are likely to be most important for g-modes, whereas they consider these interactions throughout the whole star. Thirdly, our model is 2D, whereas their eigenfunctions are valid in 3D for a spherically symmetric background. This last point, however, is probably not going to be important.

One important point is that they neglect the possibility of wave breaking, which would provide an upper limit to the amplitude of a given mode. This would prevent modes with large amplitudes from coupling with the primary wave, and the nonlinear outcome of the breaking (most notably critical layer formation) would significantly modify the strength of tidal dissipation. Their results will therefore not be valid for primary or daughter waves that satisfy a breaking criterion, since weakly nonlinear theory is insufficient in this case. Indeed, the concept of parametric instability is no longer valid if the daughters break and cannot form standing modes.

Keeping in mind the differences between our approach and theirs, we now directly apply their results to our problem, and quantitatively compare the growth time of parametric instabilities with those found in this chapter. The growth time in their work

$$t_{grow} \approx 4 \left(\frac{E_{p,0}}{10^{35}\mathrm{J}} \right)^{-1/2}, \tag{6.8.7}$$

where $E_{p,0}$ is the initial energy in the primary wave. For the g-modes that we consider,

$$E_{p,0} = \int \int \int \mathcal{E} r^2 \sin\theta dr d\theta d\phi = F \int (1/c_{g,r}) dr = F t_{group}. \tag{6.8.8}$$

This can be computed to give $E_{p,0} \approx 2 \times 10^{29} J$ for a Jupiter-mass planet on a one-day orbit around the current Sun, which has $A \approx 0.3$. This means that $t_{grow} \approx 3$ yr when $A = 1$, which happens to agree surprisingly well our calculation in the previous section, given the differences in our approach. The total number of daughter modes which simultaneously interact with the primary in their model is $\sim 10^{10} \left(\frac{E_{p,0}}{10^{35}\mathrm{J}} \right)^{5/4} \sim 10^2$

for our fiducial case. We also find that there are many growing modes for a given set of parameters in our stability analysis, so these statements appear qualitatively consistent. They find that collectively, these modes absorb most of the energy of the primary wave after a time $\sim 10 t_{grow}$ (this is equivalent to assuming $\alpha \sim 10^{-3}$ in the previous section). This predicts $Q'_\star \sim 5 \times 10^7$ in their approach. We therefore conclude that our results are broadly consistent with Kumar & Goodman (1996).

6.9 Conclusions

In this chapter we have performed a stability analysis of the 2D exact wave solution derived in Chapter 3. The equations governing the evolution of the perturbations were written down in spectral space using a Galerkin spectral method, and then solved as an eigenvalue problem. This required the imposition of an artificial impermeable outer boundary.

We have identified the modes that initiate the breaking process when the wave overturns the stratification. This type of mode is strongly localised in the convectively unstable regions of the primary wave, and is driven by unstable entropy gradients. Its growth time is comparable with the primary wave period, which is consistent with the breaking time observed in the simulations of Chapters 3 and 4.

We have also studied the instabilities which exist for waves with insufficient amplitudes to overturn the stratification. We find that these are parametric instabilities driven by (convectively stable) entropy gradients in the primary wave. The growth rate of these modes scales inversely with the number of wavelengths within the domain, so they become less important for a real star than for the small container considered here. It is estimated that their growth times in a real star would be of the order of 3 yr, which is much longer than the orbital period of a short-period planet, though many such modes are excited. Rough estimates are made that provide a upper bound on the magnitude of the resulting tidal dissipation, for which we find $Q'_\star \gtrsim 10^7$ from this process. This is clearly much weaker than the dissipation resulting from critical layer absorption, and so is unlikely to change the picture outlined in Chapter 5 for the survival of short-period planets.

We discussed several differences between our problem and the stability of a plane

IGW in a uniform stratification (e.g. Lombard & Riley 1996). We have confirmed that when the wave is confined in a container with an outer boundary it is unstable whatever its amplitude, in the absence of diffusion. However, the inverse dependence of the growth rate on the number of wavelengths within the container is quite different, and results from the finite time of nonlinear interaction being much shorter than the group travel time across a large container.

We compared our results to Kumar & Goodman (1996), who studied the nonlinear damping of tidally excited oscillations in highly eccentric binaries, and found some agreement. They predict that many ($\sim 10^2$) modes collectively draw energy from the primary wave, which we have qualitatively confirmed from our stability analysis. The growth rates of parametric instabilities for the same problem in both of our approaches when $A < 1$ are of the same order of magnitude. They therefore predict a similar lower bound for $Q'_\star$ resulting from this process. This is promising, given the differences in our approach. It would be interesting to extend their numerical calculations by studying the parametric instabilities of g-modes including continual tidal forcing of the primary wave and nonlinear couplings involving many daughter and granddaughter modes, as well as taking into account the amplitude limiting effects of wave breaking. Weakly nonlinear theories such as ours and theirs are likely to be valid when considering the initial stages of the breaking process, and in studying whether any instabilities exist for suboverturning waves, which were the topics of study in this chapter. However, they should not be used to determine long-term behaviour for waves which overturn the stratification (such as for the close binary problem whenever $A > 1$).

It would be worthwhile to confirm the results of this chapter using 2D numerical simulations with SNOOPY. An artificial impermeable outer boundary could be implemented in the code, and the resulting instabilities then studied. Of particular importance is to determine the rate at which energy is lost from the primary wave due to the parametric instabilities for suboverturning waves that we studied in this chapter (i.e., to numerically calculate t_{nl}). This would enable a more accurate calculation of the magnitude of $Q'_\star$ and would provide a useful independent check of our results. We defer such calculations to future work.

Chapter 7

Critical layer formation by radiative diffusion

In Part II of this thesis, we have studied critical layer formation by wave breaking. This occurs if the tidally excited IGWs have sufficient amplitude when they reach the centre to overturn the stratification. This process only operates if the wave amplitudes exceed a critical value. In this section we consider a mechanism which could operate even if the waves are of too low amplitude to initiate breaking. This mechanism is critical layer formation through radiative damping of the tidally forced primary waves. This process could provide efficient tidal dissipation in solar-type stars perturbed by less massive companions. However, this mechanism results in a very slow deposition of angular momentum ($\sim$ Myr), in comparison to the relatively rapid deposition which occurs when the wave breaks ($\sim$ few days). This means that this process may be prevented by effects that resist the development of differential rotation, of which several are briefly discussed.

7.1 Order-of-magnitude estimate

Near the centre of a star, radiative diffusion is the dominant linear dissipation mechanism. If the waves are gradually attenuated by radiative diffusion on their reflection from the centre, over a sufficiently long time, they may be able to spin up the innermost regions of the star to the angular pattern speed of the tide Ω_p, hence producing

a critical layer. Radiative diffusion is much weaker near the centre than at the top of the RZ, but the central regions are more easily spun up by this gradual deposition of angular momentum, because of their small moment of inertia. We have already observed this process occuring in our simulations in Fig. 3.9, albeit with viscosity and not radiative diffusion acting on the waves. Later in this chapter we perform simulations with radiative diffusion, and confirm that this effect is present in our simulations. In this section we provide an order-of-magnitude estimate of the timescale for radiative diffusion to spin up a region, of size of the order of the central wavelength of the primary wave, to Ω_p.

If the wave is attenuated as it propagates from a radius R, to the centre, and back to R again, by a factor $e^{-\alpha/2}$, i.e., such that the outgoing energy flux is $Fe^{-\alpha}$, then the torque on this region of the star is given by the angular momentum transferred to the mean flow, and is

$$\Gamma = \frac{m}{\omega} F(1 - e^{-\alpha}). \tag{7.1.1}$$

Here we assume that F is that given in Eq. 5.2.24, which is reasonable when the response is non-resonant. The wave attenuation

$$\alpha \approx 2 \int_0^R \frac{\eta k^2}{c_{g,r}} dr, \tag{7.1.2}$$

where η is the thermal diffusivity and k is the wavenumber. We have $k \sim k_r$, except within the innermost wavelength, and the radial group velocity $c_{g,r} \approx \frac{\omega}{k_r}$. The thermal diffusivity can be calculated from the properties of the appropriate stellar model from

$$\eta = \frac{16\sigma T^3}{3\kappa\rho^2 c_p}, \tag{7.1.3}$$

where σ is the Stefan-Boltzmann constant, κ is the opacity, and c_p is the specific heat at constant pressure. This assumes N^2 is due only to entropy gradients, rather than a mixture of entropy and composition gradients, so the attenuation may be weaker in practice. However, the stratification at the stellar centre is composed of these in roughly equal parts, so this is unlikely to affect the attenuation significantly. We can take η to be constant over the inner $\sim 5\%$ of a star, to a first approximation, with a

value $\approx 16.7\mathrm{m}^2\mathrm{s}^{-1}$, in the case of the Sun. In addition, k_r is roughly constant with radius within this region, though formally diverges as $r \to 0$. We can reasonably estimate

$$\alpha \approx 2 \times 6^{\frac{3}{2}} \eta \frac{C^3}{\omega^4} R \approx 4 \times 10^{-4} \left(\frac{R}{R_\odot}\right) \left(\frac{P}{1\mathrm{d}}\right)^4, \tag{7.1.4}$$

where R is the size of the region spun up by this process. This is because $k_r \sim \frac{\sqrt{l(l+1)}N}{r\omega}$, if $\omega \ll N$, and $N = Cr$. We also note that the tidal frequency $\omega = 2\left(\frac{2\pi}{P}\right)$. This means that the attenuation by radiative diffusion within the innermost few percent of the star is small for waves excited by planets on one-day orbits. However, the wavelength of the waves becomes shorter for longer period orbits, so their attenuation by radiative diffusion is more efficient. Note that $\alpha \gtrsim 1$ only when $P \gtrsim 8$ days, even when radiative diffusion over the entire RZ is considered (in fact GD98, who made a more accurate calculation by including the radial dependence of the wavenumber and diffusivity, found that $\alpha \gtrsim 1$ for $P \gtrsim 11.6$ days). This means that the waves excited by planets on short-period orbits with $P \lesssim 3$ days, whose survival could be threatened by the process of wave breaking, will not be significantly attenuated in traversing the RZ, according to linear theory. It is therefore appropriate to ask whether they will break on reaching the stellar centre.

To a first approximation, the central $\sim 3\%$ of a star can be modelled as a uniform density sphere, with the central density ρ_c. Its moment of inertia is $I = \frac{4}{5}\pi R^5 \rho_c$. Using Eq. 7.1.1, we have the following differential equation describing the spin evolution of the central regions:

$$I\frac{d\Omega}{dt} = \frac{m}{\omega} F(1 - e^{-\alpha}). \tag{7.1.5}$$

Assuming that the system evolves slowly, which is probably true until breaking occurs, we can take F, ω, and α, to be constant in time as the central regions are spun up. This allows a straightforward solution, giving the resulting timescale to spin up the region of the central wavelength to Ω_p, in the case of Jupiter orbiting the Sun with a

one-day period (in which $R \sim 0.01 R_\odot$), of

$$t_{SU} = \frac{4}{5} \frac{\pi R^5 \rho_c \Omega_p^2}{F(1 - e^{-\alpha})} \approx 3 \text{ Myr}. \tag{7.1.6}$$

Note that this timescale strongly depends on the size of the region that is spun up. When $\alpha \ll 1$, which is valid for $P \lesssim 10$ days, $t_{SU} \propto P^{5/3}$.

In this estimate we have used Model S of the current Sun, so this value only applies to our star. However, we have repeated this calculation using the same set of stellar models discussed in Chapter 5, with masses in the range $0.5 \leq m_\star/M_\odot \leq 1.1$, and find that $t_{SU} \lesssim 1$ Gyr for each of these models, for Jupiter orbiting the star with a one-day period.

This striking estimate indicates that *all* gas giants on short-period orbits around G or K stars could eventually cause the formation of a critical layer near the centre of the star, given sufficient time $\lesssim O(1)$ Gyr. Once this has formed, we have found in our simulations in Chapters 3 & 4 that it is reasonable to assume that the IW angular momentum flux is entirely absorbed near the centre. Hence, our estimate of $Q'_\star$ in the previous chapter could apply to *all* slowly rotating G and K stars.

Unlike the mechanism of nonlinear wave breaking, which has so far been the main subject of this thesis, the formation of a critical layer by radiative diffusion requires the progressive spin-up of the region of the central wavelength by a gradual deposition of angular momentum. This angular momentum deposition is much slower than the rapid deposition that results from wave breaking (spin-up time of several days), so this process could be interrupted by mechanisms that resist the development of differential rotation, such as hydrodynamic instabilities or magnetic stresses. We briefly consider several such effects later in this chapter.

This section has only presented an order-of-magnitude estimate of the timescale for this process. One question that must be answered is whether a more detailed calculation will affect this process. In the next section, we study the effects of viscosity and radiative diffusion on our nonlinear primary wave in 2D.

7.2 IGWs subject to viscous and radiative damping in 2D

In this section, we perform a 2D calculation to study the effects of viscosity and radiative diffusion on the nonlinear wave derived in Chapter 3. Our aim is to check whether a more detailed calculation of the wave damping is consistent with our simple estimate of the previous section.

We are interested in the limit in which the wave reflects approximately perfectly from the centre of the star, which is appropriate for low-amplitude waves. In this case, global standing modes form in the RZ, which are damped over a long time by radiative diffusion. We consider a circular region of radius r_{out}, and analyse the effects of both viscosity and radiative diffusion on a primary wave

$$\psi_w(r,\xi) = \mathrm{Re}\left[AJ_2(r)e^{i\xi}\right], \tag{7.2.1}$$

by calculating the perturbed solutions

$$\psi = \psi_w + \delta\psi, \qquad b = b_w + \delta b. \tag{7.2.2}$$

We start from the vorticity and buoyancy equations (in the dimensionless units of § 3.5)

$$\partial_t(-\nabla^2\psi) + \partial_\phi b = J(\psi, -\nabla^2\psi) + F[\psi], \tag{7.2.3}$$

$$\partial_t b + \partial_\phi \psi = J(\psi, b) + G[b]. \tag{7.2.4}$$

The functionals $F[\psi]$ and $G[b]$ represent the effects of viscosity and radiative diffusion, respectively, and evaluate straightforwardly in Cartesian coordinates as

$$F[\psi] = (\nabla \times \nu\nabla^2\mathbf{u})\cdot\mathbf{e}_z = -\nu\nabla^4\psi, \tag{7.2.5}$$

$$G[b] = \kappa\nabla^2 b. \tag{7.2.6}$$

A forced wave equation can be derived by combining the vorticity and buoyancy equa-

tions, to give

$$\partial_t^2(-\nabla^2\psi) - \partial_\phi^2\psi = \partial_t J(\psi, -\nabla^2\psi) - \partial_\phi J(\psi, b) + \partial_t F[\psi] - \partial_\phi G[b]. \qquad (7.2.7)$$

We neglect nonlinear coupling Jacobians, i.e., we consider the perturbation to be produced only from viscous and radiative damping of the primary wave. This means that we assume $J(\delta\psi, -\nabla^2\psi_w) = J(\psi_w, -\nabla^2\delta\psi) = J(\delta\psi, b_w) = J(\psi_w, \delta b) = 0$. These nonlinearities would couple an $m = 2$ wave with $m = 0$ and $m = 4$ waves, though to first order, $\delta\psi$ has the same azimuthal form as the primary $m = 2$ wave. Since $|\delta\psi|$ is assumed small, we can neglect these couplings, to $O(A)$. Other wavenumbers grow due to these couplings at $O(A^2)$, competing with radiative and viscous damping of the perturbed solution, which we also neglect, i.e., we assume $F[\delta\psi] = G[\delta b] = 0$. Note that $\partial_t^2(-\nabla^2\psi_w) - \partial_\phi^2\psi_w = \partial_t J(\psi_w, -\nabla^2\psi_w) - \partial_\phi J(\psi_w, b_w) = 0$, since the adiabatic primary wave solution is exact. We make the assumption of linearity, that $J(\delta\psi, -\nabla^2\delta\psi) = J(\delta\psi, \delta b) = 0$. Substituting the perturbed solutions, under these assumptions, gives

$$\partial_t^2(-\nabla^2\delta\psi) - \partial_\phi^2\delta\psi = \partial_t F[\psi_w] - \partial_\phi G[b_w], \qquad (7.2.8)$$

which can be rewritten as (factoring out $e^{i\xi}$)

$$\tilde{L}_m\delta\psi = f(r), \qquad (7.2.9)$$

where the linear differential operator

$$\tilde{L}_m \equiv \frac{m^2}{r}L_m \equiv \frac{m^2}{r}\left[\partial_r r\partial_r - r(1 - \frac{m^2}{r^2})\right], \qquad (7.2.10)$$

and after simplification, we obtain the forcing

$$f(r)e^{i\xi} \equiv \partial_t F[\psi_w] - \partial_\phi G[b_w], \qquad (7.2.11)$$

$$= 2iA(\nu + \kappa)J_2(r)e^{i\xi}, \qquad (7.2.12)$$

which has its maximum near the centre, and oscillates with radius with an amplitude decaying asymptotically like $r^{-\frac{1}{2}}$. This can be obtained easily using the fact that

$\nabla^2\psi_w = -\psi_w = -b_w$. It makes sense that this has the same symmetry in azimuth and time as the primary wave. We also expect the forcing to have a similar form to the primary wave, but to be out of phase by $\pi/2$, i.e., to cause decay in wave amplitude at every location.

Note that radiative diffusion (κ) and viscosity (ν) have the *same* effects on the primary wave. This is results from the fact that $\psi_w = b_w$ for these waves, and that the ϕ and t dependence only comes through ξ (so the ϕ and t dependence is the same except for a phase shift of π). The waves also satisfy equipartition of kinetic and potential energies, when integrated over a multiple of half-wavelengths, as we will now prove.

If we rewrite Bessel's equation in the form

$$\frac{1}{r}\partial_r(r\partial_r J_m) - \frac{m^2}{r^2}J_m = -J_m, \tag{7.2.13}$$

multiply by rJ_m, and integrate over radius from r_1 to r_2, we obtain

$$\int_{r_1}^{r_2}\left[(\partial_r J_m)^2 + \frac{m^2}{r^2}J_m^2\right] r dr = \int_{r_1}^{r_2} J_m^2 dr + \left[rJ_m\partial_r J_m\right]_{r_1}^{r_2}. \tag{7.2.14}$$

Since $2P = J_m^2$ and $2K = (\partial_r J_m)^2 + \frac{m^2}{r^2}J_m^2$, where K and P are the kinetic and potential energies, respectively, this statement is telling us that equipartition holds if we integrate over a range where J_m or $\partial_r J_m$ are zero at the end points. Equipartition therefore holds when the energies are integrated over integer multiples of half a wavelength, which is $r_2 - r_1 = \frac{n}{2}\lambda_r$ for $n \in \mathbb{Z}$, in the WKB limit. This equipartition of kinetic and potential energies is only satisfied in an averaged sense, and not pointwise, as we can see from Fig. 7.1.

In the form of Eq. 7.2.9, we can solve the problem by finding Green's function, which is the solution of

$$\tilde{L}_m G(r, r') = \delta(r - r'). \tag{7.2.15}$$

This can be found by imposing the two-point BCs

$$\delta\psi(r_{in}) \;=\; 0, \tag{7.2.16}$$

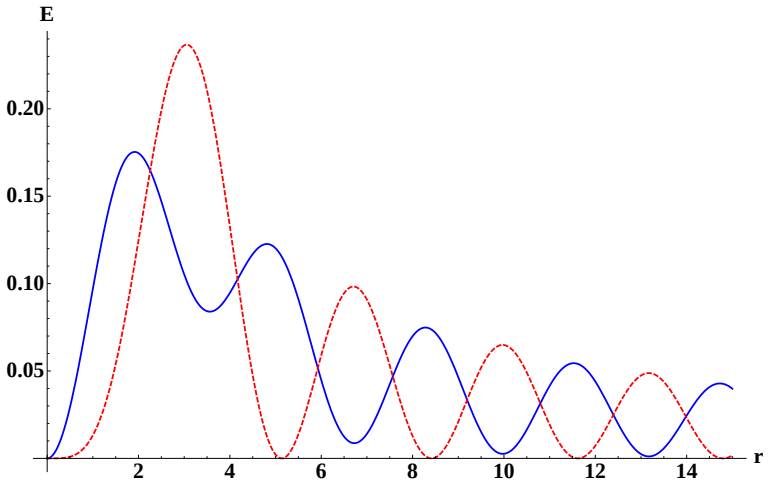

Figure 7.1: Kinetic (blue line) and potential (red line) energies in the primary wave as a function of radius. K increases first, and then the remaining part of the first wavelength has $P > K$. Equipartition holds in an averaged sense, but is not satisfied pointwise $\forall r$.

$$\delta\psi(r_{out}) \quad \propto \quad J_m(r_{out}) - iY_m(r_{out}), \tag{7.2.17}$$

which correspond to the physical condition of regularity at the centre ($r_{in} = 0$), and an OW BC at $r = r_{out}$. Note that we are assuming the solution is proportional to, and not equal to, the given OW, otherwise we would be forcing the solution at the outer boundary, and fixing the amplitude of the solution. Hence, we are looking for waves with an outgoing energy/angular momentum flux. We are required to choose r_{out} to be much closer than infinity, since the wave would entirely damp if $r_{out} = \infty$; $\delta\psi$ would also increase to no longer satisfy the requirement that $|\delta\psi/\psi_w| \ll 1$ for a linear analysis. We choose $r_{in} = 0$, and r_{out} to be several wavelengths from the centre.

Two linearly independent solutions of the homogeneous (unforced) wave equation are the standing wave and OW solutions, J_m and $J_m - iY_m$, respectively. Green's function is then

$$G(r,r') = \begin{cases} \frac{i\pi r}{2} J_m(r) \left[J_m(r') - iY_m(r')\right], & r_{in} \le r \le r', \\ \frac{i\pi r}{2} \left[J_m(r) - iY_m(r)\right] J_m(r'), & r' \le r \le r_{out}. \end{cases} \tag{7.2.18}$$

The solution is the real part of

$$\delta\psi(r,\xi) \quad = \quad \int_{r_{in}}^{r_{out}} G(r,r') f(r') dr' e^{i\xi}$$

$$
\begin{aligned}
= \quad & [J_m(r) - iY_m(r)]\, e^{i\xi} \int_{r_{in}}^{r} \frac{i\pi r'}{2} J_m(r') f(r') dr' \\
& + J_m(r) e^{i\xi} \int_{r}^{r_{out}} \frac{i\pi r'}{2} \left[J_m(r') - iY_m(r')\right] f(r') dr'.
\end{aligned} \tag{7.2.19}
$$

Note that as $r \to r_{out}$, the solution is an OW with amplitude $\delta A_{out} = \int_{r_{in}}^{r_{out}} \frac{i\pi r'}{2} J_m(r') f(r') dr'$, and as $r \to r_{in}$, the solution is a standing wave with amplitude $\int_{r_{in}}^{r_{out}} \frac{i\pi r'}{2} \left[J_m(r') - iY_m(r')\right] f(r') dr'$. The relevant part for the angular momentum transport is the part which is an OW, i.e., the first integral only. Note that the OW decays asymptotically like $r^{-\frac{1}{2}} e^{-ir}$, so at infinity, this wave decays to zero.

Using Mathematica to compute the integrals, we obtain the closed-form solution (for $m = 2$), which is the real part of

$$
\begin{aligned}
\delta\psi(r,\xi) = \frac{A}{2}(\nu+\kappa) e^{i\xi} \Bigg\{ & \pi r_{out} J_2(r) \left(r_{out} [J_1(r_{out})]^2 - 4 J_1(r_{out}) J_2(r_{out}) + r_{out} [J_2(r_{out})]^2 \right) \\
& + i\pi r Y_2(r) \left(r [J_1(r)]^2 - 4 J_1(r) J_2(r) + r [J_2(r)]^2 \right) \\
& - i\sqrt{\pi} J_2(r) G^{2,2}_{1,3} \left(r, \frac{1}{2} \,\middle|\, \begin{matrix} 1, \frac{3}{2} \ , & \frac{1}{2} \\ 1, 3 \ , & -1, 0, \frac{1}{2} \end{matrix} \right) \\
& + i\sqrt{\pi} J_2(r) G^{2,2}_{1,3} \left(r_{out}, \frac{1}{2} \,\middle|\, \begin{matrix} 1, \frac{3}{2} \ , & \frac{1}{2} \\ 1, 3 \ , & -1, 0, \frac{1}{2} \end{matrix} \right) \Bigg\}.
\end{aligned} \tag{7.2.20}
$$

Note that along $\xi = n\frac{\pi}{2}$, for $n \in \mathbb{Z}$, $\mathrm{Re}[\delta\psi] \propto J_2(r)$. The "$G$" functions above are Meijer-G functions (e.g. Lozier et al. 2010), which result from the second integral. They are written in Mathematica as, e.g.,

$$
G^{2,2}_{1,3} \left(r_{out}, \frac{1}{2} \,\middle|\, \begin{matrix} 1, \frac{3}{2} \ , & \frac{1}{2} \\ 1, 3 \ , & -1, 0, \frac{1}{2} \end{matrix} \right) \equiv \mathrm{MeijerG}[\{\{1, \frac{3}{2}\}, \{\frac{1}{2}\}\}, \{\{1, 3\}, \{-1, 0, \frac{1}{2}\}\}, r, \frac{1}{2}].
$$

Some care is needed to ensure that there are no large numerical cancellations when dealing with the Meijer-G function. This has been found to occur when the difference of the final two terms on top and bottom are integers (here, $\frac{1}{2}$ and any of $-1, 0, \frac{1}{2}$), particularly for large $r \gtrsim 20$. This is likely to be a numerical instability from the algorithm that evaluates these complicated functions in Mathematica.

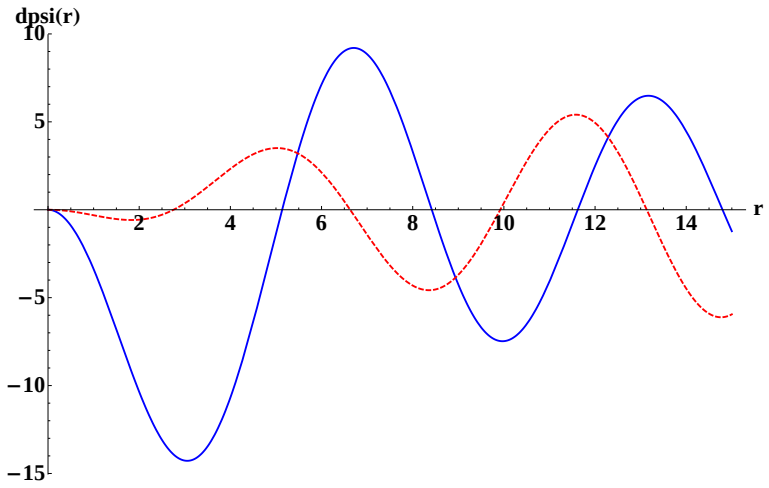

Figure 7.2: $\delta\psi$ along $\xi = 0$ for the perturbed solution, showing both the real (blue line) and imaginary (red line) parts. These are oscillatory functions of radius, out of phase by $\pi/2$. $|\mathrm{Re}[\delta\psi]|$ is largest in the centre. Further out, the amplitudes of oscillation of the real and imaginary parts are comparable.

7.2.1 Angular momentum flux

Since our aim is to determine whether our simple estimate of the spin-up due to radiative diffusion is confirmed by this calculation, we turn to compute the torque on the central regions. The perturbed angular momentum flux is

$$\delta F_r^L = \left(\frac{m\rho_0}{\omega}\right)\pi m r \mathrm{Im}\left[(\partial_r\delta\psi)\psi_w^* + \delta\psi^*(\partial_r\psi_w)\right], \tag{7.2.21}$$

which is proportional to $\nu + \kappa$ since $\delta\psi \propto \nu + \kappa$, as expected. For the above solution this evaluates (when $m = 2$) to

$$\begin{aligned}\delta F_r^L(r) \;=\; & \left(\frac{\rho_0}{\omega}\right)2\pi^2|A|^2(\kappa+\nu)r\Big\{r^2[J_1(r)]^3Y_2(r) - rJ_2(r)[J_1(r)]^2\left(rY_1(r)+4Y_2(r)\right) \\ & + r[J_2(r)]^2J_1(r)\left(4Y_1(r)+rY_2(r)\right) - r[J_2(r)]^3\left(rY_1(r)+2Y_2(r)\right) \\ & + 2\pi^{-1/2}[J_2(r)]^2 G^{2,1}_{2,4}\left(r,\frac{1}{2}\,\middle|\,\begin{matrix}1 & , & 0\\ \frac{1}{2},\frac{5}{2} & , & \frac{3}{2},0\end{matrix}\right)\Big\}.\end{aligned} \tag{7.2.22}$$

The main contribution to this is from $\delta A_{out}(r)$, because this corresponds to the amplitude of the OW. In fact, it can be shown that $\delta F_r^L \approx -m^2\delta A_{out}(r)$, which is easily confirmed by plotting these functions. The radial flux at a particular radius does not

(and should not) depend on the location of the outer boundary (which only comes into the second integral).

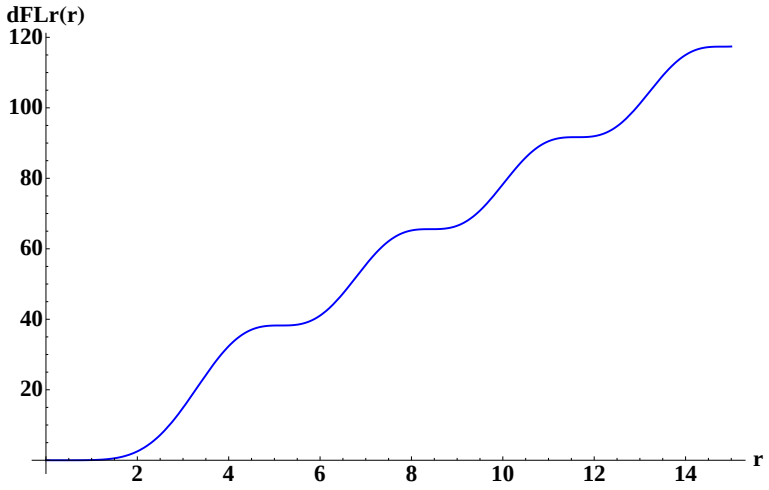

Figure 7.3: δF_r^L for the perturbed solution. This is equivalent to the total torque on the region inside a ring of radius r. This has approximately the same form as the first integral δA_{out}. Note that $\delta F_r^L \sim r^6$ as $r \to 0$, but $\delta F_r^L \sim r$ as $r \to \infty$.

In Fig. 7.3 we plot the perturbed angular momentum flux. This is equivalent to the torque on the region inside a ring of radius r. It makes physical sense for the torque to increase with radius from the centre. This is because the OWs have travelled further, and experienced more dissipation due to ν, κ, the larger the value of r.

The corresponding torque density per unit radius, defined such that the total torque

$$\Gamma \equiv \delta F_r^L \equiv \int_0^{r_{out}} \mathcal{T}(r) dr, \tag{7.2.23}$$

which results from viscous and radiative damping of the primary wave, is

$$\mathcal{T}(r) = \partial_r(\delta F_r^L). \tag{7.2.24}$$

The torque density $\mathcal{T}$ is plotted in Fig. 7.4. The torque density oscillations have roughly constant amplitude, outside of the innermost wavelength. This is what we would expect from the a simple calculation in the WKB approximation. In this approximation, the OW can be expressed as $(J_2 - iY_2)e^{i\xi} \sim \sqrt{\frac{2}{\pi r}} e^{-i(r+\xi-\frac{5\pi}{4})}$, for which the torque scales linearly with radius. In fact, it is only for the innermost wavelength that geometrical factors become important, where the solution is modified from that

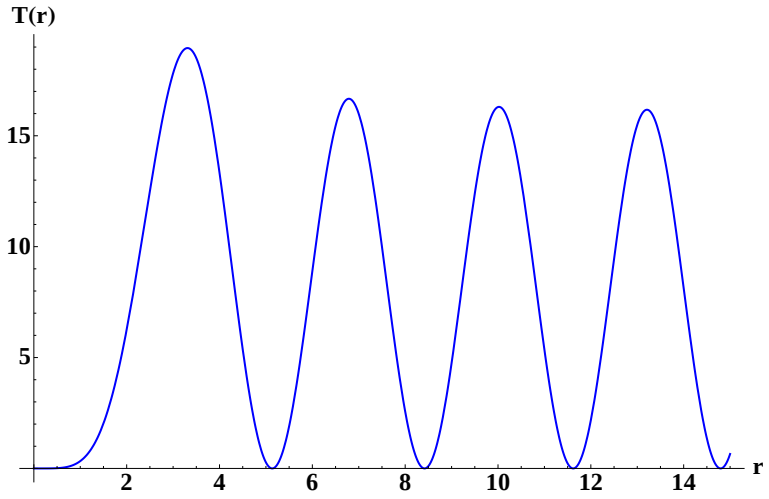

Figure 7.4: Torque density for the perturbed solution. This has roughly constant amplitude as a function of radius, as expected from a simple calculation in the WKB approximation. This is largest within the first wavelength, but not significantly, marking the only departure from WKB.

expected from this approximation.

The torque in the order-of-magnitude estimate of § 7.1 scales linearly with radius when $\alpha \ll 1$, for which $\alpha \sim R$. More precisely, we can express

$$\Gamma = F_r^L(1 - e^{-\alpha}) \approx F_r^L \alpha_1 R + O(R^2), \tag{7.2.25}$$

where $\alpha \approx \alpha_1 R = 16\eta \frac{C^3}{\omega^4} R$ in 2D, and F_R^L is the angular momentum flux in IWs. In dimensionless units we can express $\alpha = 2\frac{m}{\omega^2}(\nu + \kappa)r$, if we write $\eta = (\nu + \kappa)\frac{\Omega_p}{C^2}$. We then have

$$\frac{T}{F_r^L} \approx 4\frac{(\nu + \kappa)}{\omega^2} r. \tag{7.2.26}$$

This allows us to compare the magnitude of the torque with that from the calculation of this section.

For the detailed calculation, we find that $\delta A_{out}(r) \approx 2r$ outside of the first half-wavelength. This means that

$$\delta F_r^L \approx 2rm^2 \left(\frac{\rho_0}{\omega}\right) |A|^2(\nu + \kappa). \tag{7.2.27}$$

If we normalise this with respect to the angular momentum flux in the ingoing part of the primary standing wave solution, taking $F_r^L = \left(\frac{m\rho_0}{\omega}\right) 2m|A_{in}|^2$, with $|A_{in}| = |A|/2$ (to get the correct scaling for the IW), then

$$\frac{\delta F_r^L}{F_r^L} \approx 4\frac{(\nu+\kappa)}{\omega^2}r. \tag{7.2.28}$$

This demonstrates that the torque has a similar magnitude and scaling with radius as predicted from our simple estimate.

To summarise this section, we have performed a two-dimensional analysis, which has confirmed that our simple order-of-magnitude calculation of the torque on the central regions of the star due to radiative damping of the waves, has the correct magnitude and scaling with radius. We have also found that the effects of viscosity and radiative diffusion on the waves are the same, and would both be able, in principle, to spin up the central regions.

The resulting torque density is (slightly) largest within the innermost wavelength, and is oscillatory. Coupled with the fact that the moment of inertia of the central regions $\sim r^5$, because the density is approximately uniform in the innermost wavelengths, this implies that the central wavelengths are the most likely to be spun up by radiative diffusion (or viscosity). Note, that the torque is always positive, and only acts to spin up (and not down) the central regions, as expected when $\Omega < n$.

7.3 2D simulations

Motivated by the simulation presented in Fig. 3.9, in which viscosity acts to gradually transfer angular momentum from the wave to the mean flow, eventually producing a critical layer, we will now present similar simulations with radiative diffusion. We use the two-dimensional set-up of Chapter 3, except with $\nu = 0$, and choose various values of κ, ranging from $10^{-4} - 10^{-7}$. Neglecting viscosity is observed to result in numerical instability if any wave breaking occurs, but here we only follow the evolution until a critical layer forms by radiative diffusion. We use a forcing amplitude $\tilde{f}_r = 2.5$, which is insufficient to cause breaking, appropriate for considering the tidal evolution of lower-mass tidal perturbers.

We find that the waves are significantly attenuated on propagation to the centre, from the launching region, if $\kappa \gtrsim 10^{-4}$. This situation is that appropriate for waves excited by planets on orbits of around ten days, for which the attenuation α due to radiative diffusion is close to unity. The waves are gradually damped as they propagate, but in this case have deposited most of their angular momentum *before* they approach the central regions, which they reach with low amplitude. The result is that the central regions are negligibly spun up by the waves excited by planets on orbits of $P \gtrsim 8 - 11$ days, and therefore will not produce a critical layer. Regions farther out have larger moment of inertia, and so are harder to spin up by this process.

In Fig. 7.5 we plot the temporal evolution of the dominant Fourier components, $m = 2$ and $m = 0$, in the solution, in a simulation with $\kappa = 10^{-5}$. For this simulation, the attenuation by radiative difusion on propagation from the launching region is small to moderate, and the waves still have reasonable amplitudes near the centre. Over many wave crossing times, the gradual deposition of angular momentum results in appreciable spin-up of the central regions. Thus radiative diffusion has the same result as viscosity (see Fig. 3.9) acting on the waves, as predicted by our analysis in the previous section. In this simulation, a critical layer is eventually formed within the innermost wavelength. The resulting evolution would then be similar to that described in Chapter 3, except that in these simulations numerical instabilities set in since we neglect viscosity.

These simulations confirm the picture so far outlined in this chapter, that radiative diffusion can be responsible for the production of a critical layer near the centre. This outcome could occur for tidal perturbers with insufficient masses to be able to cause wave breaking, if they have short enough orbital periods for the waves to reach the centre with sufficient amplitude, i.e., for $P \lesssim 8$ days. Radiative diffusion preferentially spins up the central regions because these have smaller moment of inertia than regions farther out. Given the similarities between the two and three-dimensional problems, as observed in Chapter 4, we expect that this picture would be the unchanged in 3D.

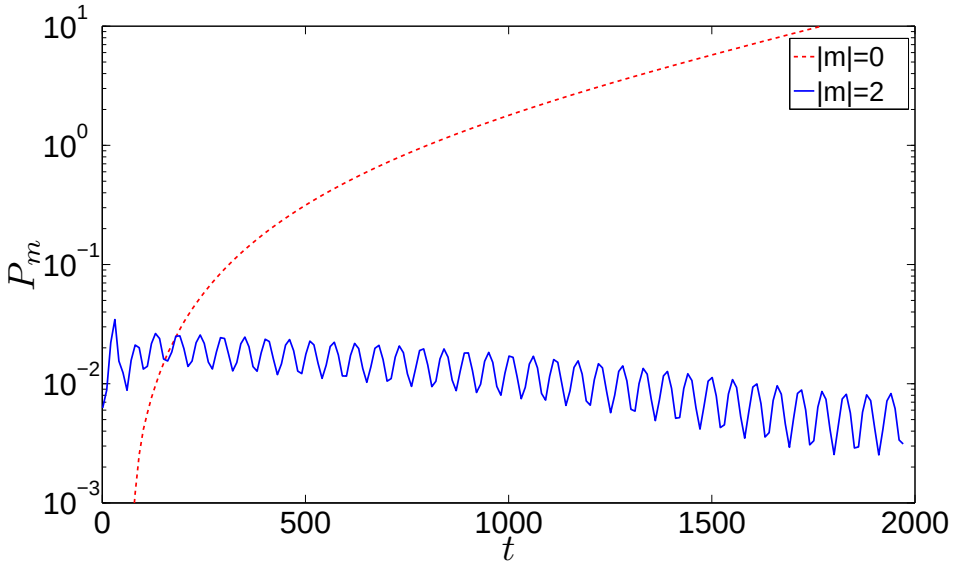

Figure 7.5: Temporal evolution of the power spectral density P_m, for $m = 0$ and $m = 2$, for a simulations with $\kappa = 10^{-5}$. Together with Fig. 3.9, this shows that radiative diffusion has the same effects on these waves as viscosity, and is able to gradually spin up the mean flow, to eventually produce a critical layer.

7.4 Discussion

The process that we have outlined in this chapter could provide efficient tidal dissipation in solar-type stars perturbed by less massive companions than wave breaking would require. However, this mechanism results in a very slow deposition of angular momentum ($\sim$ Myr), in comparison to the relatively rapid deposition which occurs when the wave breaks ($\sim$ few days). This process is therefore more likely to be prevented by effects that resist the development of differential rotation. In this section we discuss several of these possible mechanisms.

7.4.1 Magnetic fields in the RZ

It is well known that large-scale magnetic fields have the ability to hold fluids in uniform rotation. In particular, in ideal MHD, Ferraro's Law of Isorotation holds, which states that an axisymmetric steadily rotating system has constant angular velocity along each field line. Any shear in the component of the velocity transverse to the magnetic field generates a transverse field, which grows until the Lorentz force acts

back on the shear. This process generates Alfvén waves, leading to a torsional oscillation of the field with a period determined by the Alfvén travel time across the disturbance (Mestel & Weiss 1987):

$$\tau_A = \frac{R}{v_A} = \frac{R\sqrt{\mu_0 \rho}}{B_0}, \tag{7.4.1}$$

where v_A is the Alfvén speed, R is the spatial scale of the shear (i.e., the region forced into differential rotation by radiative diffusion or wave breaking), B_0 is the background magnetic field, ρ is the fluid density, and μ_0 is the magnetic permeability.

Indeed, the presence of a magnetic field in the RZ of the Sun has been invoked to explain why the differential rotation profile of the CZ has not been imposed on the interior (Gough & McIntyre 1998). It is not currently possible to measure the magnetic field beneath the solar surface, though calculations indicate that a poloidal field of only 10^{-2} G (with global Alfvén travel time $\sim 10^6$ years) would be sufficient to bring the Sun's RZ into uniform rotation. If such a field exists in the Sun, and in other solar-type stars, then magnetic stresses could inhibit the gradual development of differential rotation, and prevent the formation of a critical layer by radiative diffusion. The Alfvén travel time across a region of radial extent R, is

$$\tau_A \approx 10^4 \mathrm{yr} \left(\frac{R}{R_\odot}\right) \left(\frac{1\mathrm{G}}{B_0}\right) \left(\frac{\rho}{\rho_c}\right)^{\frac{1}{2}}, \tag{7.4.2}$$

where we have used the central density of the star, to give an upper limit, for a given field strength. Mestel & Weiss (1987) suppose that the strength of the field lies in the range 10^{-2} G $\lesssim B_p \lesssim 10^3$ G, so the global τ_A could be several orders of magnitude shorter than this estimate. In any case, this indicates that magnetic effects could be very important, since this timescale is probably much shorter than Eq. 7.1.6.

If the central $\sim 1\%$ of the star is rotating with angular speed Ω_p, then the ratio of the energy in the magnetic field to the energy in the shear is

$$\frac{B_0^2/(2\mu_0)}{(1/2)R^2\Omega_p^2} \approx 8 \times 10^{-9} \left(\frac{B_0}{1\mathrm{G}}\right) \left(\frac{0.01 R_\odot}{R}\right)^2 \left(\frac{P}{1\mathrm{d}}\right)^2. \tag{7.4.3}$$

This tells us that unless we have a magnetic field much larger than the proposed upper bound (which can probably be ruled out on empirical grounds; Friedland & Gruzinov

2004), then we are in the weak-field limit of Spruit (1999), in which the differential rotation winds up the poloidal field to produce a strong toroidal field. This toroidal field may then be subject to instabilities, such as the Tayler instability (Tayler 1973), which would set in on the Alfvén timescale to produce turbulence. However, the final nonlinear outcome of such instabilities on angular momentum redistribution is unclear.

7.4.2 Goldreich-Schubert-Fricke instability

Throughout the RZ, $\eta/\nu \gg 1$ (taking a value $\sim 10^6$ just below the convection zone). In this limit, a powerful hydrodynamic instability enabled by thermal diffusion results if the specific angular momentum decreases outwards from the rotation axis. In both of the mechanisms that we have outlined in this part of the thesis, a region in which

$$\partial_R R^2 \Omega(R) \leq 0, \tag{7.4.4}$$

is produced, where R is the cylindrical radius. This is unstable to the Goldreich-Schubert-Fricke (GSF) instability (Goldreich & Schubert 1967; Fricke 1968; also see Menou et al. 2004 for the inclusion of a weak magnetic field). The instability is axisymmetric, and the maximum growth rate is comparable with the local rotation period, which is approached for wavelengths $\lambda \lesssim 2\pi \left(\eta/N\right)^{1/2}$, where thermal diffusion can overcome the buoyant restoring force. In our simulations with thermal diffusion, $\lambda \lesssim 2\pi \left(\frac{\kappa\Omega_p}{\pi C^3 R}\right)^{1/2} \sim 10^{-4}$, so we would not be able to resolve such instabilities. (In the Sun, we expect $\lambda \lesssim 10^{-7} R_\odot$ near the centre.) The nonlinear outcome of this instability with regards to angular momentum redistribution and entropy mixing is unclear. In addition, the presence of compositional gradients may be able to stabilise the flow against such instabilities, so it is unclear how effective they will be at preventing the gradual spin-up by radiative diffusion that we have presented in this chapter.

7.5 Conclusions

In this chapter we have identified a further process by which efficient dissipation of IGWs could occur. If the waves are of too low amplitude to initiate breaking, but reach the centre without significant attenutation on one passage of the RZ, then the

weak deposition of angular momentum through radiative damping of the waves, can spin up the region of the central wavelength over a timescale of millions of years, until a critical layer is formed. The subsequent evolution of the system is that discussed in previous chapters of Part II of this thesis. This process could provide efficient tidal dissipation in solar-type stars perturbed by less massive companions. However, it may be prevented by hydrodynamic instabilities or magnetic stresses, that resist the development of differential rotation. Further work is required to study whether this remains a viable mechanism of tidal dissipation, in a detailed study including these effects.

Chapter 8

Conclusion

In this thesis we have studied two problems regarding tidal interactions between short-period extrasolar planets and their host stars.

In the first part, we adopted a simple model of tidal friction to understand the secular spin-orbit evolution of HJs on inclined orbits, due to tides. We also analysed the influence of stellar spin-down due to magnetic braking on the tidal evolution. We found that simple timescale estimates can be misleading, and it is essential to consider coupled evolution of the orbital and rotational elements, including dissipation in both the star and planet, to accurately model the evolution.

The most important result of Part I is that the timescale for stellar spin-orbit alignment is comparable with the inspiral time for HJs. This result was obtained using the constant lag time model, and is true if the ratio of the moments of inertia of the orbit to that of the fraction of the star which tidally exchanges angular momentum with orbit, is of order unity or smaller. This means that observed inclinations are likely to be a relic of the migration process that produced these extraordinary planets, thus highlighting the importance of RM effect observations of transiting planets, which can determine the sky-projected angle between the stellar spin and the orbit. Since different formation scenarios produce different distributions of this angle, these observations have the potential to determine the formative histories of HJs. In particular, they can distinguish between migration caused by planet-planet scattering or Kozai oscillations combined with tidal dissipation in the star, and that produced by tidal interaction with the gas disk.

The population of planets whose spin-orbit alignments have been observed with the RM effect can be statistically analysed to give a distribution of i for HJs (Fabrycky & Winn 2009). Such work indicates the surprising result that most HJs appear to be misaligned, possessing a wide variety of spin-orbit angles (Triaud et al. 2010). This distribution of i appears consistent with that predicted by the process of Kozai cycles with tidal friction (Fabrycky & Tremaine 2007). Together with our result that the spin-orbit angle is not likely to change appreciably over the lifetime of the system due to tides, *if future observations can confirm this i distribution*, this would be consistent with the hypothesis that Kozai migration may indeed be a primary formation mechanism of HJs. However, it is unlikely to be able to account for all of these planets. These observations do seem to reduce the importance of disk migration at producing HJs.

In the second part of this thesis, we studied the mechanisms of tidal dissipation in solar-type stars. In particular, IGWs are launched at the CZ/RZ interface of a such a star, by the tidal forcing of a short-period planet. The fate of these waves as they approach the centre of the star was studied, primarily using numerical simulations.

In Chapter 3 we first derived a Boussinesq-type model of the central regions of a solar-type star, together with a wave solution, which is exact in 2D. We then integrated this system of equations in 2D, using spectral methods, studying the instabilities of the wave as the amplitude of forcing was varied. We found that the waves undergo instability and break above a critical amplitude, below which the waves reflect perfectly from the centre of the star. Wave breaking leads to the formation of a critical layer, which absorbs subsequent ingoing waves. This process can spin the star up from the inside out, as the planet is pulled into the star.

In chapter 4 we extended these simulations to 3D. The wave solution valid near the centre is not exact in 3D, and nonlinearities, though small, do not vanish. Nevertheless, we confirmed that this process in 3D gives the same general picture as that in 2D. One exception, however, is that the deposition of angular momentum by the waves results in latitudinal differential rotation, though this is unlikely to significantly affect the critical layer absorption.

We studied the implications of the production of a critical layer by wave breaking,

for tidal dissipation in solar-type stars, in Chapter 5. We calculated the tidal quality factors $Q'_\star$ that result from this process, improving a model by Goodman & Dickson (1998). The validity of this model was verified by numerical integrations of the linearised tidal response, in an extensive set of solar-type stellar models. We found that, for a given planetary orbit, the dissipation resulting from critical layer absorption is very efficient, with

$$Q'_\star \approx 10^5 \left(\frac{P}{1 \text{ day}} \right)^{\frac{14}{5}}, \tag{8.0.1}$$

which varies by less than an order of magnitude between all solar-type stars, in the mass range $0.5 \leq m_\star/M_\odot \leq 1.1$, throughout their main-sequence lifetimes.

The critical amplitude required for wave breaking has been obtained, as a function of the mass of the planet, and the strength of the stable stratification at the stellar centre. This varies significantly between different stars, with breaking being more likely in massive and more highly evolved stars, with stronger central condensations. The implications of this mechanism for the survival of short-period extrasolar planets has been discussed. In particular, if wave breaking occurs, a close-in planet will rapidly spiral into its host star in only a few million years. However, this process only occurs if the planet is sufficiently massive, or the star is sufficiently evolved. In fact, none of the planets currently observed orbiting a solar-type star is likely to cause breaking at the centre. This could be an important explanation for their survival.

We studied the tidal dissipation in F-type stars, which have masses in the range $1.1 \lesssim m_\star/M_\odot \lesssim 1.8$. This is in general weaker than in solar-type stars, due to differences in their internal structure, most importantly the presence of a convective core prevents the wave breaking mechanism that we have described in Part II of this thesis. In addition, the convective envelopes of these stars are generally thinner than in solar-type stars, so the dissipation of the equilibrium tide (and inertial waves if they are excited) by turbulent convection is weaker. Contrary to common assumptions, $Q'_\star$ is found to vary with the internal structure of the star, with tidal frequency, and for solar-type stars, exhibits a dependence on the amplitude of the tide. It is therefore inappropriate to consider $Q'_\star$ as a constant, uniform across all stars, except in making qualitative statements about tidal evolution, or in constraining the magnitude of the

dissipation (such as we did in Chapter 2).

The results of this thesis were combined to propose a possible explanation for the survival of all of the extrasolar planets currently observed in short-period orbits around F, G and K stars. We provided several predictions, which will be tested in ongoing studies of transiting planets, such as WASP and Kepler. In particular, we predict that fewer massive planets will be found around G-stars in periods of less than 2 days, i.e., those massive enough to satisfy Eq. 5.3.3. We also predict that the fraction of short-period HJs in orbits shorter than 2 days around G-stars will decrease with stellar age.

Our simulations in Chapters 3 & 4 indicate that nonlinearities do not play an important role in preventing the reflection of the waves from the centre, unless the wave has sufficient amplitude to overturn the stratification. In Chapter 6 we performed a stability analysis of our 2D standing internal gravity wave near the centre of a solar-type star, to determine whether the waves are subject to weaker parametric instabilities below the critical amplitude required for wave breaking. We found that although the waves undergo parametric instabilities, driven by entropy gradients in the primary wave, at any amplitude, because the nonlinearity is spatially localised in the innermost wavelengths, the growth rate scales inversely with the number of wavelengths contained within the radiation zone. This means that the growth rates of these instabilities tend to be sufficiently small that they do not result in astrophysically important tidal dissipation. These results support our explanation for the survival of short-period planets that we have presented in this thesis. We also identified the instabilities that contribute to the early stages of wave breaking, and found that they are driven by the free energy associated with primary wave entropy gradients, and are strongly localised within the convectively unstable regions.

Finally, in Chapter 7, we proposed an alternative mechanism of tidal dissipation. This involves the formation of a critical layer by the gradual damping of the waves by radiative diffusion. Based on an order-of-magnitude estimate, which we followed up with analytical calculations and numerical simulations, we found that this process could operate for lower-mass planets. However, this mechanism is in conflict with current observations, since it would pose a threat to the survival of all short-period

planets in orbits of less than 2 days. We discussed some hydrodynamic instabilities and magnetic processes which may prevent this mechanism.

8.1 Future work

The subject of resonances has been avoided so far in this thesis. The probability of the tidal frequency exactly matching some normal mode of the star at any one time is tiny. However, evolution of the tidal frequency, due to changes in the stellar spin or the orbit, or evolution of the stellar g-mode eigenfrequencies, can result in the system passing through resonance. Simple estimates indicate that it is most likely for *at least* one resonance to be passed in the lifetime of a system. It is not yet understood whether this will result in the amplitude of the tide to grow sufficiently for wave breaking to occur, when both radiative damping and the gradual evolution of the frequencies is considered. I am currently performing some calculations to try to understand this problem.

Part II of this thesis has studied a promising mechanism of tidal dissipation, which may operate in stars with radiative cores. However, we have so far neglected the influence of magnetic fields and rotation. Future work is certainly required to understand in more detail the effects of magnetic fields. In particular, a strong toroidal magnetic field at the top of the RZ may be able to reduce the amplitude of the waves that are launched. Large-scale magnetic fields may also be able to prevent the spin-up of the interior by the process outlined in Chapter 7, though probably not the more rapid spin-up due to wave breaking. In addition, they could affect the picture that we have outlined for the long-term evolution of the RZ due to critical layer absorption. It is also of interest to consider the effects on the wave amplitude by differential rotation in the RZ.

Orbits with nonzero eccentricities, and inclinations with respect to the stellar equator, excite IGWs with different frequencies and azimuthal wavenumbers. In this thesis, we only considered the waves excited by planets in circular, coplanar orbits, which have $m = 2$. Future work is required to see whether the same process is efficient at circularising the orbits of short-period planets, or of aligning the stellar spin with the orbit. This could be studied in a straightforward extension of the simulations described in

this thesis.

Another route for further work regards core-envelope coupling in stars, and how this can be produced, and will affect, tidal evolution of HJs. It has been proposed by Winn et al. (2010), that the current population of misaligned planets can be explained as a result of inefficient tidal dissipation in their host stars. This is because most of the misaligned planets orbit F-stars, and we found in Chapter 5 that tidal dissipation in those stars is likely to be weaker than in solar-type stars. Such stars may thus be less likely to realign with the orbit than G-stars, which have stronger dissipation. However, it is uncertain whether core-envelope coupling can occur in such stars, and this is certainly an area which requires further study, since it is not yet understood, even for the Sun.

To conclude, tidal dissipation in stars requires much further work before we can say that we fully understand its effects in the evolution of short-period planetary systems. This thesis has presented a mechanism that is likely to be important in solar-type stars, but much further work is required. Hopefully myself and others will be able to continue to explore this avenue in the next few years.

Part III

Appendices

Appendix A

A.1 Additional secular perturbing accelerations

In Chapter 2.1, we ignored the contribution of any perturbing accelerations except tidal friction. In this section we list the remaining terms from Eggleton & Kiseleva-Eggleton (2001), which we have rewritten without reference to $\hat{\mathbf{e}}$, so that they are regular for a circular orbit. The resulting contributions to $\mathbf{f}$ are listed in Mardling & Lin (2002). Here we write down the additional contributions to the secular evolution of the system due to binary (outer body) perturbations (b), quadrupolar distortion of the star due to their spins and tidal bulges ($q1$), and general relativistic apsidal precession (GR):

$$\left(\frac{d\mathbf{h}}{dt}\right)_b = -3C_b h\left[\frac{(1-e^2)}{h^2}(\mathbf{n}\cdot\mathbf{h})(\mathbf{n}\times\mathbf{h}) - 5(\mathbf{n}\cdot\mathbf{e})(\mathbf{n}\times\mathbf{e})\right], \tag{A.1.1}$$

$$\left(\frac{d\mathbf{h}}{dt}\right)_{q1} = -\frac{\alpha_1}{h(1-e^2)^2}\left(\mathbf{\Omega}_1\cdot\mathbf{h}\right)\left(\mathbf{\Omega}_1\times\mathbf{h}\right), \tag{A.1.2}$$

$$h\left(\frac{d\mathbf{e}}{dt}\right)_b = 3C_b(1-e^2)\left[2(\mathbf{h}\times\mathbf{e}) - (\mathbf{n}\cdot\mathbf{h})(\mathbf{n}\times\mathbf{e}) + 5(\mathbf{n}\cdot\mathbf{e})(\mathbf{n}\times\mathbf{h})\right], \tag{A.1.3}$$

$$\begin{aligned} h\left(\frac{d\mathbf{e}}{dt}\right)_{q1} &= \frac{\alpha_1}{(1-e^2)^2}\left[\frac{1}{2}\left(\frac{3}{h^2}(\mathbf{\Omega}_1\cdot\mathbf{h})^2 - \Omega_1^2\right) + \frac{15Gm_2}{a^3}f_2(e^2)(1-e^2)^2\right](\mathbf{h}\times\mathbf{e}) \\ &\quad + \frac{\alpha_1}{h^2(1-e^2)^2}\left(\mathbf{\Omega}_1\cdot\mathbf{h}\right)\left(\mathbf{\Omega}_1\cdot\mathbf{h}\times\mathbf{e}\right)\mathbf{h}, \end{aligned} \tag{A.1.4}$$

$$h\left(\frac{d\mathbf{e}}{dt}\right)_{GR} = \frac{3Gm_{12}n}{ac^2(1-e^2)}\left(\mathbf{h}\times\mathbf{e}\right), \tag{A.1.5}$$

n is a unit vector normal to the binary (outer body) orbital plane, c is the speed of light, and

$$\alpha_{1,2} = \frac{R_{1,2}^2 k_{1,2} m_{2,1}}{2\mu n a^5}, \tag{A.1.6}$$

$$C_b = \frac{m_3}{(m_{12}+m_3)} \frac{n_{out}^2}{n} \frac{1}{4(1-e^2)^{1/2}(1-e_{out}^2)^{3/2}}. \tag{A.1.7}$$

Similar terms for the quadrupolar distortion of the planet ($q2$) can be obtained by including additional terms identical to Eqs. A.1.2 and A.1.4, with $1 \rightarrow 2$ (and $m_2 \rightarrow m_1$). These terms can be included on the right hand side of Eqs. 2.1.9–2.1.13. The integrator used in Part I has been extended with these additional contributions, and tested on the Kozai migration of HD-80606 b using the initial conditions of Wu & Murray (2003). The quantity C_b gives the magnitude of the binary (outer body) perturbation, and is related to the period of a Kozai oscillation (if one is induced), which is on the order of $(1/3C_b)(1-e^2)^{-1/2}$.

A.2 Stability of the synchronous state without MB

Here the stability of the equilibrium state $\tilde{\Omega} = \tilde{n}$ is analysed, in the absence of MB. We need to consider the energy (E) and total angular momentum (L) of the system, which we write in the dimensionless form

$$\tilde{L} = \tilde{n}^{-\frac{1}{3}} + \tilde{\Omega}, \tag{A.2.1}$$

$$\tilde{E} = -\tilde{n}^{\frac{2}{3}} + \tilde{\Omega}^2, \tag{A.2.2}$$

where

$$\tilde{L} = \frac{L}{(G m_{12} R_1)^{\frac{1}{2}} \mu} C^{\frac{1}{4}}, \tag{A.2.3}$$

$$\tilde{E} = \frac{2R_1 E}{G m_1 m_2} C^{-\frac{1}{2}}, \tag{A.2.4}$$

are dimensionless measures of the total angular momentum and total energy of the system, respectively. $\tilde{L}$ and $\tilde{E}$ represent the values that the total angular momentum and total energy would take for a Keplerian orbit at radius R_1, together with a factor

C involving the ratio of orbit to spin angular momentum at the stellar surface. These definitions allow the equations to be written in a very simple form.

It is straightforward to see from Eqs. 2.3.1 & 2.3.2 that there exists a curve of equilibrium points corresponding to spin-orbit synchronism ($\tilde{\Omega} = \tilde{n}$). This can also be shown by minimising the energy at constant total angular momentum

$$\frac{\partial \tilde{E}}{\partial \tilde{n}}\Big|_{\mathrm{const}\tilde{L}}^{\tilde{\Omega}=\tilde{n}} = 0. \tag{A.2.5}$$

The stability of the equilibrium curve as a function of $\tilde{n}$ follows from

$$\frac{\partial^2 \tilde{E}}{\partial \tilde{n}^2}\Big|_{\mathrm{const}\tilde{L}}^{\tilde{\Omega}=\tilde{n}} = \frac{2}{9}\tilde{n}^{-\frac{4}{3}}\left[\tilde{n}^{-\frac{4}{3}} - 3\right]. \tag{A.2.6}$$

A synchronous state is stable if $\tilde{n} \leq 3^{-\frac{3}{4}}$, which is equivalent to the criterion of Counselman (1973) & Hut (1980), who proved that an equilibrium state reached through tidal friction is stable if $\frac{I\Omega}{\mu h} \leq \frac{1}{3}$, i.e., no more than a quarter of the total angular momentum is in the form of spin angular momentum.

A.3 Tidal potential valid for any stellar obliquity

In this section we expand the tidal potential into its separate Fourier components. This is required to study which tidal frequencies are relevant for significantly inclined orbits, such as that of XO-3 b. We consider two bodies in mutual Keplerian orbit with semi-major axis a and mean motion n. Adopt a coordinate system with origin at the centre of body 1, and let this represent the star, and body 2 the planet. The tidal potential experienced at an arbitrary point P in body 1 is the nontrivial term of lowest order in r,

$$\Psi = \frac{Gm_2}{2R^5}\left[R^2r^2 - 3(\mathbf{R}\cdot\mathbf{r})^2\right], \tag{A.3.1}$$

where position vector of the point P in body 1 is $\mathbf{r}$, and the position vector of the centre of mass of body 2 is $\mathbf{R}(t)$. Body 2 is treated as a point mass, of mass m_2. We consider an inclined, circular orbit. Without loss of generality, we consider body 2 to orbit in a plane inclined to the (x, y)-plane by an angle i, so that its Cartesian

coordinates are

$$\mathbf{R} = a\left(\cos nt\cos i, \sin nt, \cos nt\sin i\right), \tag{A.3.2}$$

while the Cartesian coordinates of a point P are

$$\mathbf{r} = r\left(\sin\theta\cos\phi, \sin\theta\sin\phi, \cos\theta\right), \tag{A.3.3}$$

where (r, θ, ϕ) are the usual spherical polar coordinates. Then

$$\begin{aligned}\Psi &= \frac{Gm_2}{2a^3}r^2\left[1 - 3\left(\cos nt\cos i\sin\theta\cos\phi\right.\right.\\ &\qquad \left.\left. + \sin nt\sin\theta\sin\phi + \cos nt\sin i\cos\theta\right)^2\right]. \end{aligned}\tag{A.3.4}$$

Let

$$\tilde{P}_l^m(\cos\theta) = \left[\frac{(2l+1)(l-m)!}{2(l+m)!}\right]^{\frac{1}{2}} P_l^m(\cos\theta), \tag{A.3.5}$$

where $0 \le m \le l$ and $l \in \mathbb{Z}^+$, denote an associated Legendre polynomial normalised such that

$$\int_0^\pi \left[\tilde{P}_l^m(\cos\theta)\right]^2 \sin\theta d\theta = 1. \tag{A.3.6}$$

The tidal potential correct to arbitrary order in the stellar obliquity i can be expanded as a series of rigidly rotating spherical harmonics of second degree,

$$\Psi = \frac{Gm_2}{a^3}\left[\sum_{j=1}^{8} A_j(i) r^2 \tilde{P}_2^{m_j}(\cos\theta)\cos(m_j\phi - \omega_j t)\right], \tag{A.3.7}$$

where the azimuthal order m_j, frequency ω_j, tidal (Doppler shifted) forcing frequency $\hat{\omega}_j = \omega_j - m_j\Omega$, and the obliquity dependent amplitude $A_j(i)$ of each component are

$$m_1 = 0, \quad \omega_1 = 0, \quad \hat{\omega}_1 = 0, \quad A_1 = \sqrt{\frac{1}{10}}\left(1 - \frac{3}{2}\sin^2 i\right), \tag{A.3.8}$$

$$m_2 = 2, \quad \omega_2 = 2n, \quad \hat{\omega}_2 = 2n - 2\Omega, \quad A_2 = -\sqrt{\frac{3}{5}}\cos^4\frac{i}{2}, \tag{A.3.9}$$

$$m_3 = 0, \quad \omega_3 = 2n, \quad \hat{\omega}_3 = 2n, \quad A_3 = -\frac{3}{2}\sqrt{\frac{1}{10}}\sin^2 i, \tag{A.3.10}$$

$$m_4 = 1, \quad \omega_4 = 0, \quad \hat{\omega}_4 = -\Omega, \quad A_4 = \sqrt{\frac{3}{5}} \cos i \sin i, \tag{A.3.11}$$

$$m_5 = 1, \quad \omega_5 = 2n, \quad \hat{\omega}_5 = 2n - \Omega, \quad A_5 = \frac{1}{2}\sqrt{\frac{3}{5}} \sin i \left(\cos i + 1\right), \tag{A.3.12}$$

$$m_6 = 1, \quad \omega_6 = -2n, \quad \hat{\omega}_6 = -2n - \Omega, \quad A_6 = \frac{1}{2}\sqrt{\frac{3}{5}} \sin i \left(\cos i - 1\right), \tag{A.3.13}$$

$$m_7 = 2, \quad \omega_7 = 0, \quad \hat{\omega}_7 = -2\Omega, \quad A_7 = \frac{1}{2}\sqrt{\frac{3}{5}} \sin^2 i, \tag{A.3.14}$$

$$m_8 = 2, \quad \omega_8 = -2n, \quad \hat{\omega}_8 = -2n - 2\Omega, \quad A_8 = -\sqrt{\frac{3}{5}} \sin^4 \frac{i}{2}. \tag{A.3.15}$$

There are eight components of the tide that contribute for arbitrary stellar obliquity. For small inclination, the terms that are of first order in the obliquity are for $m = 1$ and are the $j = 4$ and $j = 5$ components above. For a coplanar orbit, only $j = 1$ and $j = 2$ components above contribute, and these reduce to the first two components in OL04.

For an orbit with significantly nonzero i, many components contribute to the tidal force. Thus, for XO-3, for example, it is important to calculate the resulting Q' for each of the $m = 0$, $m = 1$ and $m = 2$ components of the tide. The relevant tidal frequencies for this system cannot be calculated with any certainty, since the stellar spin period has not been accurately determined. If we assume that the angle of inclination of the stellar equatorial plane to the plane of the sky is $\sim 90°$, then we have $\Omega \sim n$ currently. The relevant tidal frequencies would then be $\hat{\omega} = 0, \pm\Omega, \pm 2\Omega, \pm 3\Omega, \pm 4\Omega$.

A.4 Ingoing/outgoing wave decomposition

Since we have an analytic solution to the Boussinesq-type problem (see §3.5 & §4.2), we can deconstruct the numerical solution into a sum of IWs and OWs. Doing this enables us to quantify the amount of angular momentum absorbed as these waves approach and/or reflect from the centre. The approach we use in 3D is now described (we use an analogous method in 2D).

At each location in the grid, i.e. every point with spatial coordinates (x, y, z), we have four pieces of information, namely, u_r, u_θ, u_ϕ and b. Thus, it is possible to compute the (complex) IW and OW amplitudes A_{in} and A_{out} for the $l = m = 2$

wave at a single point (note that this is not true in 2D, where we require two or more points for this calculation, because we only have the variables u_r, u_ϕ and b). This is, however, computationally expensive, since the routines for computing Bessel functions are relatively slow (typically several hundred times slower than a square root). In addition, this method would be subject to potentially significant round-off errors. A more efficient method, which also (in principle) allows a simple extension to calculate the amplitudes A_{in}^{lm} and A_{out}^{lm}, for several values of l and m, is described in this section.

We aim to fit the simulation output to a linear model, corresponding to an IW and an OW. Hence, our problem is an overdetermined system of linear equations in terms of the unknown wave amplitudes. Let us write our system as

$$y_i = \sum_{i=1}^{4M} A_{ij} x_i, \tag{A.4.1}$$

where $\mathbf{y} = (u_r, u_\theta, u_\phi, b)$ is a vector of data variables at each grid point, of size $4N$, where $N = N_x N_y N_z$ is the total number of grid points. M is the number of spherical harmonics for which we compute the wave amplitudes, which is usually taken to be one. $\mathbf{x} = (A_{in}, A_{out})$ is a vector of size $4M < 4N$, whose components are the (complex) IW/OW amplitudes (for each l and m value), whose values are to be determined. The matrix A contains the IW and OW radial functions and spherical harmonic functions, evaluated at the selected grid points, and has size $4N \times 4M$. Its components *at a single point* are

$$\mathrm{A} = \begin{pmatrix} \mathrm{Re}[u_r^{in}(r,\theta,\xi)] & \mathrm{Im}[u_r^{in}(r,\theta,\xi)] & \mathrm{Re}[u_r^{out}(r,\theta,\xi)] & \mathrm{Im}[u_r^{out}(r,\theta,\xi)] \\ \mathrm{Re}[u_\theta^{in}(r,\theta,\xi)] & \mathrm{Im}[u_\theta^{in}(r,\theta,\xi)] & \mathrm{Re}[u_\theta^{out}(r,\theta,\xi)] & \mathrm{Im}[u_\theta^{out}(r,\theta,\xi)] \\ \mathrm{Re}[u_\phi^{in}(r,\theta,\xi)] & \mathrm{Im}[u_\phi^{in}(r,\theta,\xi)] & \mathrm{Re}[u_\phi^{out}(r,\theta,\xi)] & \mathrm{Im}[u_\phi^{out}(r,\theta,\xi)] \\ \mathrm{Re}[b^{in}(r,\theta,\xi)] & \mathrm{Im}[b^{in}(r,\theta,\xi)] & \mathrm{Re}[b^{out}(r,\theta,\xi)] & \mathrm{Im}[b^{out}(r,\theta,\xi)] \end{pmatrix}, \tag{A.4.2}$$

where each component uses the solution from §4.2 for an IW/OW (before taking real parts). Taking only a single point, this matrix is non-singular for all radii, and is related to the Wronskian. M is the number of spherical harmonics for which we compute the wave amplitudes, which is usually taken to be one.

We use a method of least squares to fit our model to the data (Press et al., 1992). This finds the best fit between the linear model data and simulation data, and com-

putes the solution for which the sum of the squared residuals is its least value. We compute the coefficients $\mathbf{x}$, which fit the model to minimise the least squares residuals, i.e., find $\hat{\mathbf{x}}$ such that

$$||A\hat{\mathbf{x}} - \mathbf{y}||^2 \leq ||A\mathbf{x} - \mathbf{y}||^2, \qquad \forall \mathbf{x}. \tag{A.4.3}$$

This minimisation problem has a unique solution if the $4N$ columns of the matrix A are linearly independent, which is true in our case, since $W[J_\nu(kr) + iY_\nu(kr), J_\nu(kr) - iY_\nu(kr)] = \frac{4}{i\pi r} \neq 0$, $\forall r$. The solution is found by solving the normal equations

$$\hat{\mathbf{x}} = (A^T A)^{-1} A^T \mathbf{y}. \tag{A.4.4}$$

We take into account radial variations in the amplitudes by splitting up the region inside the forcing region into a set of concentric spherical shells of thickness $\delta r \sim \lambda_r/2$, after removing an inner region of a few grid cells. This approach assumes the solution is locally independent of r, hence we can ignore radial derivatives of the amplitudes within each shell. This is not valid in regions where the solution varies rapidly. In addition, we speed up computation by stepping over the grid points in each Cartesian direction, by factors $i_{step}, j_{step}, k_{step}$, chosen to take values between 1 and 10. We always ensure that sufficient grid points are available in each shell to accurately compute the amplitudes.

We checked our method with the analytic wave solutions using Mathematica, and wrote a Matlab routine, which reads in SNOOPY/ZEUS output and solves the linear least squares problem for the wave amplitudes. We also compute the reflection coefficient $\mathcal{R}$, which is defined in Eq. 3.7.3. For perfect standing waves, $A_{in} = A_{out}$, and $\mathcal{R} = 1$. If the IW is entirely absorbed at the centre, then $\mathcal{R} = 0$.

The main disadvantage of our approach is that $\omega \neq 1, l \neq 2, m \neq 2$ components also contribute to the amplitudes. This problem can be ignored if we trust the computed values of $\mathcal{R}$ only where the solution is well described by the linear solution, i.e., far from the wave breaking and forcing regions. We therefore reconstruct u_r, and plot it along the x-axis, u_θ along the line $y = z$, u_ϕ along the line $y = x$, and b along the line $y = x$. All components of the solution are not zero for all radii along these lines when $\xi = 0$ (this requires shifting the phase of the linear model solution when the

wave phase is nonzero in the simulation data). Comparing the reconstructed solution with the simulation data allows us to check whether the deconstruction has worked.

A.5 ZEUS comparison

We confirm that the results are not dependent on the numerical method by reproducing the basic results using a stripped down version of ZEUS–2D[1] (Stone & Norman, 1992). ZEUS solves the equations of ideal compressible hydrodynamics, using a simple Eulerian method based on finite-differences, implemented using a covariant formalism, enabling the use of non-cartesian orthogonal coordinate systems. For our problem we solve the problem using cylindrical (r, ϕ) coordinates, which are the most natural to use for our problem. However, the coordinate singularity at the origin requires that we cut out a small region at the centre, on which we impose reflecting boundary conditions. What may seem an advantage of this coordinate system, that is the higher resolution at the centre, which is automatically present when we use a uniform grid in r and ϕ, requires very short timesteps when the resolution is increased, as a result of the CFL stability constraint. This becomes prohibitive as we increase the resolution of the grid to above 100×150 in r, ϕ respectively, so only preliminary low resolution runs were performed using this code. This is also because this code solves the compressible equations, and therefore resolves sound waves. For our problem we require a ratio of sound speed to radial group velocity of gravity waves $\chi = c_s/c_{g,r} \sim 6 \times 10^3$ (χ^{-1} is a measure of the importance of effects of compressibility), in order to reproduce an equivalent set-up to that used in the SNOOPY code above, so most of the computational time is spent resolving sound waves. In the thesis we only analyse the SNOOPY results, since they are at a much higher resolution, but here describe our problem set-up in ZEUS, for completeness. We use a circularly symmetric parabolic density stratification, $\rho(r) = \rho_0 - \rho_2 r^2$, and calculate the pressure (p) profile from hydrostatic equilibrium. We solve the equations

$$D\rho = -\rho \nabla \cdot \mathbf{u}, \tag{A.5.1}$$

[1] which has kindly been made freely available by J.Stone at http://www.astro.princeton.edu/∼jstone/zeus.html

$$D\mathbf{u} = -\frac{1}{\rho}\nabla p + \mathbf{g} + \begin{cases} 0, & r_{inner} \leq r < r_{force}, \\ \mathbf{f}, & r_{force} \leq r < r_{damp}, \\ \mathbf{d}, & r_{damp} \leq r < r_{box}, \end{cases} \tag{A.5.2}$$

$$D\left(\frac{e}{\rho}\right) = -\frac{p}{\rho}\nabla \cdot \mathbf{u}, \tag{A.5.3}$$

where $e = (\gamma - 1)p$ is the specific internal energy of the gas, $\mathbf{f} = -f_r \cos(2\phi - \omega t)\,\mathbf{e}_r$, and $\mathbf{d} = -d(r)\mathbf{u}$. We choose $\gamma = 5/3$, as appropriate for a monatomic ideal gas. Radial gravity has been implemented as a source term in the radial momentum equation: $\mathbf{g} = -g_1 r \mathbf{e}_r$. Both the inner and outer boundaries have reflecting boundary conditions, and we also implement a linear frictional damping in a region adjacent to the outer boundary, to prevent the reflection of (most of) the outgoing wave energy. A parabolic smoothing function $d(r) = \left(\frac{r - r_{damp}}{r_{box} - r_{damp}}\right)^2$ is used in the damping terms. We choose $r_{box} = 1.0$, $r_{damp} = 0.9$, $r_{force} = 0.85$ and $r_{inner} = 0.01$. In the code we specify $\rho_0, \rho_2, \omega, \lambda_r \,\&\, \tilde{f}_r$; the other relevant parameters are calculated from these. Choosing $\rho_0 = 1.0, \rho_2 = 0.1, \omega = 1.0, \lambda_r = 0.1$ and a suitable value for $\tilde{f}_r$ is sufficient to fully specify the problem.

A minimum value of $\chi = 6285$ is found from these initial conditions. Such a high value is required for the wavelength of the gravity waves to be $\lambda_r \simeq 0.1$, which allows ~ 8 wavelengths to be resolved within the grid. This value is not much smaller than that appropriate at the centre of a solar-type stars ($\chi \sim 10^4 - 10^5$). We set up the initial conditions in such a way to minimise this value given the above input parameters.

Calculations were performed in an inertial frame, though the results were interpreted in a frame rotating with the angular pattern speed of the tide, $\Omega_p = \omega/2$. In this rotating frame, the linear wave solution is steady, which allows the instability to be easily recognised as departures from a steady state.

With this resolution, there are some numerical errors near the inner boundary. This results from the fact that we only remove a small region near the centre, which is comparable with the size of a grid cell. In addition, the code has no explicit viscosity or thermal conduction, so we have less control over the scales of dissipation, than in SNOOPY. Nevertheless, ZEUS reproduces the same basic results as the SNOOPY

code, which indicates both that the effects of nonzero compressibility are not important in this problem, and that our basic results are not dependent on the numerical method.

A.6 Analytic calculation of F in the launching region

In this section, we adopt the notation of OL04, to avoid reproducing the results in that paper, since we are simply extending the results of their §4.4. In the launching region, we want to match the solutions of the RZ and CZ. Near the boundary $r = r_b$, we assume $N^2 \propto (r_b - r)^\alpha$, where $\alpha \in \mathbb{R}^+$, for the moment left unspecified. The characteristic radial extent of the transition region is of order ϵ^β, where $\beta \in \mathbb{R}^+$, and ϵ is the ratio of the spin frequency to the dynamical frequency, which is much smaller than unity for slowly rotating bodies. We write

$$r = r_b - \epsilon^\beta x, \tag{A.6.1}$$

where x is an inner variable, which is of order unity in the launching region. We can write

$$N^2 = \epsilon^{\alpha\beta}\mathcal{D}x^\alpha + O(\epsilon^{2\alpha\beta}), \tag{A.6.2}$$

where $\mathcal{D} = \frac{dN^2}{dx^\alpha} > 0$. If we pose the perturbation expansions

$$u_r' \sim \epsilon^{3-\beta(1+\alpha)}\bar{u}_r'(x,\theta), \tag{A.6.3}$$

$$u_\theta' \sim \epsilon\bar{u}_\theta'(x,\theta), \tag{A.6.4}$$

$$u_\phi' \sim \epsilon\bar{u}_\phi'(x,\theta), \tag{A.6.5}$$

$$\rho' \sim \epsilon^{2-\beta}\bar{\rho}'(x,\theta), \tag{A.6.6}$$

$$p' \sim \epsilon^2\bar{p}'(x,\theta), \tag{A.6.7}$$

$$\Phi' \sim \epsilon^2\check{\Phi}'(r_b,\theta) + \epsilon^{2+\beta}\bar{\Phi}'(x,\theta), \tag{A.6.8}$$

then we obtain the linearised system of equations 111-116 from OL04, except that we replace x by x^α in the buoyancy equation (Eq. 115). A linearised equation for the

modified pressure ($\bar{W} = \frac{\bar{p}'}{\rho_0} - \frac{p'_{(e)}\rho_2}{\rho_0^2} + \check{\Phi}'$) in the launching region can now be derived, for which

$$\mathcal{L}\bar{W} + \frac{r^2}{\mathcal{D}}\partial_x\left(x^{-\alpha}\partial_x\bar{W}\right) = 0, \tag{A.6.9}$$

where all coefficients are evaluated at $r = r_b$. This equation can be solved using the separation of variables

$$\bar{W} = \sum_i f^{(i)}(z)w_i(\theta). \tag{A.6.10}$$

The operator $\mathcal{L}$ contains only angular derivatives, and $\mathcal{L}\bar{w}_i = \lambda_i\bar{w}_i$, where $\lambda_i = \frac{k^2r^2}{N^2}$, and k is the WKB wavenumber of the waves. We thus obtain the equation

$$f^{(i)}(z) + \partial_z\left(z^{-\alpha}\partial_z f^{(i)}(z)\right) = 0, \tag{A.6.11}$$

where we have defined $z = \kappa_i x$, and the length scale

$$\kappa_i^{-1} = \left(\frac{\mathcal{D}\lambda_i}{r^2}\right)^{-\frac{1}{2+\alpha}}. \tag{A.6.12}$$

In the text this lengthscale is referred to as L_{launch}. The solution of this equation can be written down as a linear combination of Bessel functions of the first and second kinds, of order $\frac{\alpha+1}{\alpha+2}$:

$$f^{(i)}(z) = a_i z^{\frac{\alpha+1}{2}}\left\{J_{\frac{\alpha+1}{\alpha+2}}\left(\frac{2}{2+\alpha}z^{\frac{2+\alpha}{2}}\right) + s_i iY_{\frac{\alpha+1}{\alpha+2}}\left(\frac{2}{2+\alpha}z^{\frac{2+\alpha}{2}}\right)\right\}, \tag{A.6.13}$$

so that the complete solution in the transition region is

$$\bar{W} = \sum_i a_i z^{\frac{\alpha+1}{2}}\left\{J_{\frac{\alpha+1}{\alpha+2}}\left(\frac{2}{2+\alpha}z^{\frac{2+\alpha}{2}}\right) + s_i iY_{\frac{\alpha+1}{\alpha+2}}\left(\frac{2}{2+\alpha}z^{\frac{2+\alpha}{2}}\right)\right\}w_i(\theta) \tag{A.6.14}$$

This solution should match onto the WKB solution in the RZ when $x \gg 1$, constraining β as a function of α. This arises from considering the asymptotic form of the phase at large z, whose radial derivative should match the WKB wavenumber in the RZ. From this we find $\beta = 2/(2+\alpha)$.

If we from now on restrict ourselves to $\alpha = 1/2$, then the corresponding complete

solution in the transition region is the sum

$$\bar{W} = \sum_i a_i z^{\frac{3}{4}} \left\{ J_{\frac{3}{5}} \left(\frac{4}{5} z^{\frac{5}{4}} \right) + s_i i J_{\frac{3}{5}} \left(\frac{4}{5} z^{\frac{5}{4}} \right) \right\} w_i(\theta). \tag{A.6.15}$$

Similarly we can write the radial displacement as

$$\bar{\xi}_r' = \sum_i b_i \sqrt{z} \left\{ J_{\frac{2}{5}} \left(\frac{4}{5} z^{\frac{5}{4}} \right) \pm i t_i J_{\frac{2}{5}} \left(\frac{4}{5} z^{\frac{5}{4}} \right) \right\} w_i(\theta), \tag{A.6.16}$$

for a superposition of wave solutions in this model.

Deep in the RZ, our solution should reduce to a wave with an inwardly directed group velocity, for which $s_i = \pm 1$ (sign depending on that of the frequency). The asymptotic forms of the radial part of this solution at large z is

$$z^{\frac{3}{4}} \left\{ J_{\frac{3}{5}} \left(\frac{4}{5} z^{\frac{5}{4}} \right) \pm i J_{\frac{3}{5}} \left(\frac{4}{5} z^{\frac{5}{4}} \right) \right\} \sim (-1)^{\frac{9}{20}} \sqrt{\frac{5}{2\pi}} z^{\frac{1}{8}} \exp \left\{ \mp i \frac{4}{5} z^{\frac{5}{4}} \right\}. \tag{A.6.17}$$

Matching of W at $r = r_b$ requires the solution in the CZ to be continuous with the solution in the transition region at $z = 0$. This determinines the amplitudes a_i. The inward energy flux in (inertia-)gravity waves is found from evaluating

$$\begin{aligned} F &= \pi \int_0^\pi \mathrm{Re} \left[\left(\frac{\omega}{\hat{\omega}} \right) p'^* u_r' \right] r^2 \sin\theta d\theta & \text{(A.6.18)} \\ &= \epsilon^{\frac{19}{5}} \frac{\left(\frac{2}{5}\right)^{\frac{1}{5}} \pi^2}{\left[\Gamma\left(\frac{3}{5}\right)\right]^2} \rho_0 \omega_{(1)} \mathrm{sgn}(\hat{\omega}) \left(\frac{r^2}{\mathcal{D}} \right)^{\frac{2}{5}} \\ &\quad \times \sum_i \lambda_i^{\frac{3}{5}} \frac{\left| \int_0^\pi w_i^* \left[\check{W}(r_b, \theta) - \bar{W}^{(p)} \right] \sin\theta d\theta \right|^2}{\int_0^\pi |w_i|^2 \sin\theta d\theta}, & \text{(A.6.19)} \end{aligned}$$

which can be compared with OL04 Eq. 124. We find in general that $F \propto \omega^{\frac{8+3\alpha}{2+\alpha}}$. Thus we see that the main change in the energy flux from modifying the profile of N^2 in the transition region is to change its frequency dependence. There are also $O(1)$ changes to the numerical factors.

A.7 Toy model: parametric instability of primary wave

Parametric instability is a type of resonant triad interaction in which the transfer of energy from a parent (subscript p) mode, with amplitude A_p, destabilises a pair of daughter (subscript $d1, d2$) modes (which exist when $A_p = 0$). These can then be damped or subject to further nonlinear interactions (to produce granddaughter modes, and so on). The frequencies of the modes must satisfy an approximate temporal resonance condition $\omega_p \approx \omega_{d1} + \omega_{d2}$, for parametric resonance to occur.

The equations governing the temporal evolution of the mode amplitudes take the form (e.g. Dziembowski 1982; Wu & Goldreich 2001)

$$\dot{A}_p = \gamma_p A_p - i\omega_p A_p + i\omega_p \sigma A_{d1} A_{d2}, \tag{A.7.1}$$

$$\dot{A}_{d1} = -\gamma_{d1} A_{d1} - i\omega_{d1} A_{d1} + i\omega_{d1} \sigma A_p A^*_{d2}, \tag{A.7.2}$$

$$\dot{A}_{d2} = -\gamma_{d2} A_{d2} - i\omega_{d2} A_{d2} + i\omega_{d2} \sigma A^*_{d1} A_p. \tag{A.7.3}$$

In these equations, γ_j is the linear growth/damping rate of mode j, and σ is the nonlinear coupling strength for these three modes. Here A_j is the amplitude of mode j, with the energy in that mode being proportional to $|A_j|^2$.

The coupling coefficient σ is largest when $\omega_{d1} \approx \omega_{d2} \equiv \omega$, and therefore $\omega_{d1} \approx \omega_p/2$. If the daughter modes have similar frequency, then we can assume that they have similar spatial scales. Hence we can take their damping rates to be the same, i.e., $\gamma_{d1} = \gamma_{d2} \equiv \gamma$. To consider the initial stages of the breaking process we take A_p to be approximately constant in time. In our problem the primary wave is maintained at a constant amplitude due to forcing, and is not unstable. The evolutionary equations reduce to

$$\dot{A}_{d1} = -\gamma A_{d1} - i\omega A_{d1} + i\omega \sigma A_p A^*_{d2}, \tag{A.7.4}$$

$$\dot{A}_{d2} = -\gamma A_{d2} - i\omega A_{d2} + i\omega \sigma A^*_{d1} A_p. \tag{A.7.5}$$

If we take $A_{d1} \propto \exp st$, then the growth rate is

$$\mathrm{Re}\,[s] = -\frac{\gamma}{2} + \frac{1}{2}\omega\sigma|A_p|. \tag{A.7.6}$$

The growth rate is reduced if the detuning $\Delta\omega = \omega_p - \omega_{d1} - \omega_{d2} \neq 0$, by changing the second term to $(1/2)\sqrt{\omega_{d1}\omega_{d2}\sigma^2|A_p|^2 - (\Delta\omega)^2}$. From this model, we expect $\gamma \neq 0$ to simply reduce the growth rate for a given mode. In addition the growth rate scales linearly with the amplitude of the primary (parent) mode. The threshold amplitude for instability in this simple model is

$$|A_p| \geq \frac{\gamma}{\omega\sigma}, \tag{A.7.7}$$

which depends on the coupling strength σ.

The spatial dependence of the interaction is contained in the coupling coefficient σ, which contains an integral of the product of the three eigenfunctions. This toy model of parametric instability is useful as a simple model to understand some of the results of § 6.6. It is interesting to note that in this model, $\omega \approx m/k_{m,n} \sim n_p^{-1}$ for $A \ll 1$, since in this limit the daughter modes have frequencies comparable with the linear mode frequencies. This results in a growth rate scaling inversely with n_p.

A.8 Acronyms and abbreviations

Several acronyms and abbreviations regularly used in this thesis are listed alphabetically below.

AU: Astronomical Unit

CZ: Convection Zone

HJ: Hot Jupiter

IGW: Internal Gravity Wave

IW: Ingoing Wave

MB: Magnetic Braking

OCZ: Outer Convection Zone

OW: Outgoing Wave

RM: Rossiter-McLaughlin

RV: Radial Velocity

RZ: Radiation Zone

Bibliography

Alexander M. E., 1973, Ap&SS, 23, 459

Appourchaux T., Belkacem K., Broomhall A., Chaplin W. J., Gough D. O., et al., 2010, A&A Rv, 18, 197

Balbus S. A., Hawley J. F., 1994, MNRAS, 266, 769

Barnes S. A., 2003, ApJ, 586, 464

Beck J. G., Giles P., 2005, ApJL, 621, L153

Beckwith S. V. W., 1996, Nature, 383, 139

Bodenheimer P., Lin D. N. C., Mardling R. A., 2001, ApJ, 548, 466

Booker J. R., Bretherton F. P., 1967, J. Fluid Mech., 27, 513

Boyd J. P., 2001, Chebyshev and Fourier Spectral Methods. Dover Publications Inc.

Breeding R. J., 1971, J. Atmos. Sci, 50, 545

Bühler O., 2009, Waves and Mean Flows. Cambridge University Press

Chapront J., Chapront-Touzé M., Francou G., 2002, A&A, 387, 700

Charbonneau D., Brown T. M., Burrows A., Laughlin G., 2007, in Reipurth B., Jewitt D., Keil K., eds, Protostars and Planets V When Extrasolar Planets Transit Their Parent Stars. pp 701–716

Charbonneau D., Brown T. M., Latham D. W., Mayor M., 2000, ApJL, 529, L45

Chatterjee S., Ford E. B., Matsumura S., Rasio F. A., 2008, ApJ, 686, 580

Christensen-Dalsgaard J., 2002, Reviews of Modern Physics, 74, 1073

Christensen-Dalsgaard J., 2008, ApSS, 316, 13

Christensen-Dalsgaard J., Dappen W., Ajukov S. V., Anderson E. R., Antia H. M., Basu S., Baturin V. A., Berthomieu G., Chaboyer B., Chitre et al., 1996, Science, 272, 1286

Cochran W. D., Redfield S., Endl M., Cochran A. L., 2008, ApJL, 683, L59

Collier Cameron A., 2002, in Gänsicke B. T., Beuermann K., Reinsch K., eds, The Physics of Cataclysmic Variables and Related Objects Vol. 261 of Astronomical Society of the Pacific Conference Series, Magnetic activity in low-mass stars: Do the brakes come off?. pp 11–+

Counselman III C. C., 1973, ApJ, 180, 307

Cresswell P., Dirksen G., Kley W., Nelson R. P., 2007, A&A, 473, 329

Darwin G. H., 1880, Philos. Trans. R. Soc. London, A171, 713

Dobbs-Dixon I., Lin D. N. C., Mardling R. A., 2004, ApJ, 610, 464

Donati J.-F., Moutou C., Farès R., Bohlender D., Catala C., Deleuil M., Shkolnik E., Cameron A. C., Jardine M. M., Walker G. A. H., 2008, MNRAS, 385, 1179

Drazin P. G., 1977, Proc. R. Soc. Lond. A., 356, 411

Durisen R. H., Boss A. P., Mayer L., Nelson A. F., Quinn T., Rice W. K. M., 2007, in Reipurth B., Jewitt D., Keil K., eds, Protostars and Planets V Gravitational Instabilities in Gaseous Protoplanetary Disks and Implications for Giant Planet Formation. pp 607–622

Dziembowski W., 1982, Acta Astronomica, 32, 147

Eggleton P. P., Kiseleva L. G., Hut P., 1998, ApJ, 499, 853

Eggleton P. P., Kiseleva-Eggleton L., 2001, ApJ, 562, 1012

Ellis A. N., 1984, in Liege International Astrophysical Colloquia Vol. 25 of Liege International Astrophysical Colloquia, The Base of the Solar Convection Zone. pp 290–292

Fabrycky D., Tremaine S., 2007, ApJ, 669, 1298

Fabrycky D. C., Winn J. N., 2009, ApJ, 696, 1230

Feynman R. P., 1963, Feynman lectures on physics - Volume 1. Reading, Ma.: Addison-Wesley, 1963, edited by Feynman, Richard P.; Leighton, Robert B.; Sands, Matthew

Ford E. B., Rasio F. A., 2008, ApJ, 686, 621

Fortney J. J., Marley M. S., Barnes J. W., 2007, ApJ, 659, 1661

Fricke K., 1968, Zeitschrift fur Astrophysik, 68, 317

Friedland A., Gruzinov A., 2004, ApJ, 601, 570

Fritts D., 1979, J. Atmos. Sci, 26, 12

García R. A., Turck-Chièze S., Jiménez-Reyes S. J., Ballot J., Pallé P. L., Eff-Darwich A., Mathur S., Provost J., 2007, Science, 316, 1591

Garcia Lopez R. J., Spruit H. C., 1991, ApJ, 377, 268

Gavrilov S. V., Zharkov V. N., 1977, Icarus, 32, 443

Goldreich P., Nicholson P. D., 1977, Icarus, 30, 301

Goldreich P., Nicholson P. D., 1989, ApJ, 342, 1079

Goldreich P., Schubert G., 1967, ApJ, 150, 571

Goldreich P., Soter S., 1966, Icarus, 5, 375

Goldreich P., Tremaine S., 1979, ApJ, 233, 857

Goodman J., Dickson E. S., 1998, ApJ, 507, 938

Goodman J., Lackner C., 2009, ApJ, 696, 2054

Goodman J., Oh S. P., 1997, ApJ, 486, 403

Gough D. O., McIntyre M. E., 1998, Nature, 394, 755

Greenberg R., 1974, Icarus, 23, 51

Hasselmann K., 1967, J. Fluid Mech., 30, 737

Hazel P., 1967, J. Fluid Mech., 30, 775

Hebb L., Collier-Cameron A., Loeillet B., Pollacco D., SuperWasp Consortium t., 2009, ApJ, 693, 1920

Hebb L., Collier-Cameron A., Triaud A., Lister T., Smalley B., Maxted P., Hellier C., Anderson D., Pollacco D., et al., 2010, ApJ, 708, 224

Hébrard G., Bouchy F., Pont F., et al., 2008, A&A, 488, 763

Hellier C., Anderson D. R., Cameron A. C., Gillon M., Hebb L., Maxted P. F. L., Queloz D., Smalley B., Triaud A. H. M. J., et al., 2009, Nature, 460, 1098

Holzwarth V., Jardine M., 2005, A&A, 444, 661

Hut P., 1980, A&A, 92, 167

Hut P., 1981, A&A, 99, 126

Ivanov P. B., Papaloizou J. C. B., 2004, MNRAS, 353, 1161

Ivanov P. B., Papaloizou J. C. B., 2007, MNRAS, 376, 682

Ivanova N., Taam R. E., 2003, ApJ, 599, 516

Jackson B., Greenberg R., Barnes R., 2008, ApJ, 678, 1396

Johnson J. A., Winn J. N., Albrecht S., Howard A. W., Marcy G. W., Gazak J. Z., 2009, PASP, 121, 1104

Joshi Y. C., Pollacco D., Cameron A. C., Skillen I., Simpson E., et al., 2009, MNRAS, 392, 1532

Jurić M., Tremaine S., 2008, ApJ, 686, 603

Kant I., 1755, Allgemeine Naturgeschichte und Theorie des Himmels. Zeitz, Bei W. Webel, 1798. Neue aufl.

Klostermeyer J., 1982, J. Fluid Mech., 119, 367

Klostermeyer J., 1991, Geophysical and Astrophysical Fluid Dynamics, 61, 1

Knobloch E., Spruit H. C., 1982, A&A, 113, 261

Koop C. G., 1981, J. Fluid Mech., 113, 347

Koop C. G., McGee B., 1986, J. Fluid Mech., 172, 453

Kumar P., Goodman J., 1996, ApJ, 466, 946

Kumar P., Talon S., Zahn J.-P., 1999, ApJ, 520, 859

Landau L. D., Lifshitz E. M., 1969, Mechanics

Laplace P.-S., 1796, Exposition du systme du monde. Imprimerie du Cercle-Social, Paris.

Lesur G., Longaretti P.-Y., 2005, A&A, 444, 25

Lesur G., Longaretti P.-Y., 2007, MNRAS, 378, 1471

Lin D. N. C., Bodenheimer P., Richardson D. C., 1996, Nature, 380, 606

Lin D. N. C., Papaloizou J., 1979, MNRAS, 186, 799

Lombard P. N., Riley J. J., 1996, Physics of Fluids, 8, 3271

Lozier D., Boisvert R., Clark C., 2010, NIST Handbook of Mathematical Functions. Cambridge University Press, 2010

Lubow S. H., Ogilvie G. I., 2001, ApJ, 560, 997

MacGregor K. B., Brenner M., 1991, ApJ, 376, 204

Marcy G. W., Butler R. P., Williams E., Bildsten L., Graham J. R., Ghez A. M., Jernigan J. G., 1997, ApJ, 481, 926

Mardling R. A., Lin D. N. C., 2002, ApJ, 573, 829

Maslowe S., 1986, Ann. Rev. Fluid Mech., 18, 405

Mayor M., Queloz D., 1995, Nature, 378, 355

Mazeh T., 2008, in Goupil M.-J., Zahn J.-P., eds, EAS Publications Series Vol. 29 of EAS Publications Series, Observational Evidence for Tidal Interaction in Close Binary Systems. pp 1–65

McEwan A. D., Robinson R. M., 1975, J. Fluid Mech., 67, 667

McIntyre M., 2000, in Batchelor G. K., Moffatt H. K., Worster M. G., eds, Perspectives in Fluid Dynamics: A Collective Introduction to Current Research On Global-Scale Atmospheric Circulations. Cambridge University Press

McLaughlin D. B., 1924, ApJ, 60, 22

Meibom S., Mathieu R. D., 2005, ApJ, 620, 970

Meid R. P., 1976, J. Fluid Mech., 78, 763

Menou K., Balbus S. A., Spruit H. C., 2004, ApJ, 607, 564

Mestel L., 1968, MNRAS, 138, 359

Mestel L., Weiss N. O., 1987, MNRAS, 226, 123

Moutou C., Hébrard G., Bouchy F., et al., 2009, A&A, 498, L5

Munk W. H., MacDonald G. J. F., 1960, The rotation of the earth; a geophysical discussion. Cambridge [Eng.] University Press, 1960.

Murray C. D., Dermott S. F., 1999, Solar system dynamics. Solar system dynamics by Murray, C. D., 1999

Nagasawa M., Ida S., Bessho T., 2008, ApJ, 678, 498

Narita N., Sato B., Hirano T., Tamura M., 2009, PASJ, 61, L35

Narita N., Sato B., Ohshima O., Winn J. N., 2008, PASJ, 60, L1+

Ogilvie G. I., Lin D. N. C., 2004, ApJ, 610, 477

Ogilvie G. I., Lin D. N. C., 2007, ApJ, 661, 1180

Papaloizou J. C. B., Ivanov P. B., 2005, MNRAS, 364, L66

Papaloizou J. C. B., Nelson R. P., Kley W., Masset F. S., Artymowicz P., 2007, in Reipurth B., Jewitt D., Keil K., eds, Protostars and Planets V Disk-Planet Interactions During Planet Formation. pp 655–668

Papaloizou J. C. B., Savonije G. J., 1985, MNRAS, 213, 85

Papaloizou J. C. B., Savonije G. J., 1997a, MNRAS, 291, 651

Papaloizou J. C. B., Savonije G. J., 1997b, MNRAS, 291, 651

Papaloizou J. C. B., Terquem C., 2006, Reports of Progress in Physics, 69, 119

Peale S. J., 1999, ARA&A, 37, 533

Peale S. J., Lee M. H., 2002, Science, 298, 593

Penev K., Sasselov D., Robinson F., Demarque P., 2007, ApJ, 655, 1166

Peyret R., 2002, Spectral Methods for Incompressible Viscous Flow. Springer Verlag

Pollack J. B., Hubickyj O., Bodenheimer P., Lissauer J. J., Podolak M., Greenzweig Y., 1996, Icarus, 124, 62

Pont F., 2009, MNRAS, 396, 1789

Press W. H., 1981, ApJ, 245, 286

Press W. H., Teukolsky S. A., Vetterling W. T., Flannery B. P., 1992, Numerical recipes in FORTRAN. The art of scientific computing. Cambridge: University Press, —c1992, 2nd ed.

Rasio F. A., Tout C. A., Lubow S. H., Livio M., 1996, ApJ, 470, 1187

Richard D., Zahn J., 1999, A&A, 347, 734

Rogers T. M., Glatzmaier G. A., 2006, ApJ, 653, 756

Rogers T. M., Glatzmaier G. A., Jones C. A., 2006, ApJ, 653, 765

Rogers T. M., MacGregor K. B., 2010, MNRAS, 401, 191

Rossiter R. A., 1924, ApJ, 60, 15

Safronov V. S., 1969, Evoliutsiia doplanetnogo oblaka.. 1969.

Sasselov D. D., 2003, ApJ, 596, 1327

Savonije G. J., Papaloizou J. C. B., 1983, MNRAS, 203, 581

Savonije G. J., Papaloizou J. C. B., 1997a, MNRAS, 291, 633

Savonije G. J., Papaloizou J. C. B., 1997b, MNRAS, 291, 633

Savonije G. J., Papaloizou J. C. B., Alberts F., 1995a, MNRAS, 277, 471

Savonije G. J., Papaloizou J. C. B., Alberts F., 1995b, MNRAS, 277, 471

Savonije G. J., Witte M. G., 2002, A&A, 386, 211

Schatzman E., 1962, Annales d'Astrophysique, 25, 18

Schatzman E., 1993, A&A, 279, 431

Skumanich A., 1972, ApJ, 171, 565

Sonmor L. J., Klaassen G. P., 1997, J. Atmos. Sci., 54, 2655

Spruit H. C., 1999, A&A, 349, 189

Staquet C., Sommeria J., 2002, Ann. Rev. Fluid Mech., 34, 559

Stone J. M., Norman M. L., 1992, ApJS, 80, 753

Swedenborg E., 1734, Opera Philosophica et Mineralia. Dresden and Leipzig: Friedrich Hekel

Taam R. E., Spruit H. C., 1989, ApJ, 345, 972

Tayler R. J., 1973, MNRAS, 161, 365

Terquem C., Papaloizou J. C. B., Nelson R. P., Lin D. N. C., 1998, ApJ, 502, 788

Triaud A., et al., 2010, A&A, 524, A25

Verbunt F., Zwaan C., 1981, A&A, 100, L7

Watson M., 1981, GApFD, 16, 285

Weber E. J., Davis L. J., 1967, ApJ, 148, 217

Winn J. N., Fabrycky D., Albrecht S., Johnson J. A., 2010, ApJL, 718, L145

Winn J. N., Johnson J. A., Albrecht S., Howard A. W., Marcy G. W., Crossfield I. J., Holman M. J., 2009, ApJL, 703, L99

Winn J. N., Johnson J. A., Fabrycky D., Howard A. W., Marcy G. W., Narita N., Crossfield I. J., Suto Y., Turner E. L., Esquerdo G., Holman M. J., 2009, ApJ, 700, 302

Winn J. N., Noyes R. W., Holman M. J., Charbonneau D., Ohta Y., Taruya A., Suto Y., Narita N., Turner E. L., Johnson J. A., Marcy G. W., Butler R. P., Vogt S. S., 2005, ApJ, 631, 1215

Winters K. B., D'Asaro E. A., 1994, J. Fluid Mech., 272, 255

Witte M. G., Savonije G. J., 1999, A&A, 350, 129

Witte M. G., Savonije G. J., 2001, A&A, 366, 840

Witte M. G., Savonije G. J., 2002, A&A, 386, 222

Wu Y., 2005, ApJ, 635, 688

Wu Y., Goldreich P., 2001, ApJ, 546, 469

Wu Y., Murray N., 2003, ApJ, 589, 605

Yoder C. F., Peale S. J., 1981, Icarus, 47, 1

Zahn J. P., 1966, Annales d'Astrophysique, 29, 489

Zahn J.-P., 1975, A&A, 41, 329

Zahn J.-P., 1977, A&A, 57, 383

Zahn J.-P., 2008, in EAS Publications Series Vol. 29 of EAS Publications Series, Tidal dissipation in binary systems. pp 67–90

Zahn J.-P., Talon S., Matias J., 1997, A&A, 322, 320